On the dynamics of continental rifting: a numerical modelling approach

Luke S Mondy

A thesis submitted in fulfilment of the requirements for the
degree of Doctor of Philosophy

Faculty of Science
School of Geosciences
Division of Geology and Geophysics
University of Sydney
2019

DECLARATION

I certify that the intellectual content of this thesis is the product of my own work and that all the assistance received in preparing this thesis and sources have been acknowledged. This thesis has not been submitted for any degree or other purposes.

Luke S. Mondy

PREFACE

This PhD thesis consists of a collection of papers that are published or prepared for submission with international peer-reviewed journals appropriate to the discipline of geology. The publications form part of an integrated project and are presented in an order that represents the related elements of a connected thesis. The thesis contains an introductory section that provides an outline of the thesis, a summary of the contribution of the work to the field of geology, and a critical evaluation of the role of the thesis in informing further research in the field. Common themes in the papers are tied together and a discussion and conclusion of the whole thesis is presented at the end. No animal or ethical approvals were needed during the completion of this study. Data and interpretations in the thesis are the work of the author except where stated in the text.

Abstract

Passive margins around the world commonly feature evidence of syn-rift small scale contractional deformation, such as reverse faulting and low amplitude folding, as well as evidence of basin depth inversions. Often, these features have no corresponding change in plate motion, and seem in conflict with the kinematic understanding that areas undergoing continental rifting should record only extensional deformation and subsidence. It has been proposed that syn-rift basin inversion may form as a result of gravitational body forces developing because of the upwelling asthenospheric dome beneath the rifted region, known as rift push. The aim of this thesis is to investigate the role these gravitational forces can play on the evolution of passive margins during rifting, and to quantify the role the upwelling asthenosphere plays in this process. To achieve this, we use high-resolution thermomechanical numerical modelling in both two and three dimensions, with non-linear, temperature, stress, and strain-dependent rheologies, to map the evolution of the stress regime throughout the lithosphere as the margins develop. Two dimensional numerical experiments show that the upwelling asthenosphere is capable of driving rift opening, and that transient compressional stress of up to 30 MPa develop within localized regions of the passive margin. When coupled with simplified surface processes allowing the formation of sedimentary basins, the experiments show that rift basins can undergo multiple phases of compression with no change to the applied rift kinematics, as they tend to localise compressive stress. We also explore the role of rift-push in the fundamentally three-dimensional context of continental rifting close to an Euler pole. It has been proposed that diachronous upwelling of the asthenosphere could induce compressional structures along the strike of the rift axis. Our experiments show that as the asthenosphere reaches break-up earlier at one end of the rift, a component of rift-push force is orthogonal to the rift axis (as per the previous experiments), and a second component is parallel to the rift axis, as the relatively unthinned areas of lithosphere are juxtaposed against the upwelled asthenospheric dome along the strike of the rift. In combination, these force components produce transcurrent and compressional stress within the developing passive margins, which matches earthquake focal mechanism data from similar real-world examples. Finally, to facilitate the access of thermo-mechanical modelling to a broader community of structural geologists and tectonicists, we have designed a pre-built toolbox named the *Lithospheric Modelling Recipes* which includes a customizable 2D and 3D lithospheric model. In doing so, we aim to a) give structural geologists and tectonicists a user-friendly self-consistent framework to test their conceptual ideas, b) expand the pool of expertise and ideas tapping into geodynamic modelling, and c) enable a large number of geoscientists to critically assess geodynamic models, and d) contribute to the reproducibility of thermo-mechanical modelling.

This thesis is based on the following three articles:

Article 1.   Mondy, L. S., Rey, P. F., Duclaux, G., *ready for submission*, Interplay between tectonic extension, surface processes, and gravitational stress explains syn-rift basin inversions.

Article 2.   Mondy, L. S., Rey, P. F., Duclaux, G., Moresi, L., 2018. The role of asthenospheric flow during rifting propagation and breakup. *Geology, 46(2), pp. 103-106.*

Article 3.   Mondy, L. S., Rey, P. F., Duclaux, G., *ready for submission*, Lithospheric Modelling Recipe: A numerical modelling workflow of lithospheric processes for geologists.

Included in the appendices are three co-authored articles:

Appendix I.   Rey, P.F., Mondy, L., Duclaux, G., Teyssier, C., Whitney, D.L., Bocher, M. and Prigent, C., 2017. The origin of contractional structures in extensional gneiss domes. *Geology, 45(3), pp.263-266.*

Appendix II.   Korchinski, M., Rey, P.F., Mondy, L., Teyssier, C. and Whitney, D.L., 2018. Numerical investigation of deep-crust behavior under lithospheric extension. *Tectonophysics, 726, pp.137-146.*

Appendix III.   Beucher, R., Moresi, L., Giordani, J., Mansour, J., Sandiford, D., Farrington, R., Mondy, L., Mallard, C., Rey, P., Duclaux, G. and Kaluza, O., 2019. UWGeodynamics: A teaching and research tool for numerical geodynamic modelling. *Journal of Open Source Software.*

Finally, an article written for the EGU Geodynamics blog is included:

Appendix IV.   Mondy, L., 2018, Finding the forces within continental rifting, EGU Geodynamics 101 Blog, <https://blogs.egu.eu/divisions/gd/2018/02/28/finding-the-forces-in-continental-rifting/>

Table of Contents

Introduction

All tectonic activity on the Earth's surface is fundamentally attributable its thermal cooling under gravity. This relatively simple statement belies the underlying complexity at work, since its expression is determined by the dynamic interaction of a wide range of processes. Specific to continental rifting, we see that: subduction processes drive the far-field tectonic force; the asthenosphere ascent and decompression is driven by its buoyancy and convection patterns of the mantle; surface processes transport mass away from the rift flanks, which impacts on gravitational body forces controlling the surface topography and mantle upwelling via isostatic compensation - all of which is mediated through deformation controlled by the potentially non-linear, stress-, strain-, and temperature-dependent rheology of rocks.

To better understand the complexities of Earth dynamics, geoscientists have broken down these processes into many sub-disciplines: petrophysicists study rheology, structural geologists study deformation processes, tectonicists focus on kinematics and large scale deformation patterns, and geomorphologists study surface processes, etc.. This specialisation aims to allow the study of specific dynamics, while minimising confounding or second-order influences and effects. An example of this is kinematic modelling of tectonic plate motions, where plates are mapped through time and treated as rigid blocks that move according to Euler pole rotations. This very successful model underpins plate tectonics and provides great insight into paleogeography and the subduction history leading to the present day plates distribution and mantle structure - despite the fact this model largely ignores the deformation of plates.

As useful as these models are, by definition, they are not truly reflective of, or able to capture, the complexities of reality. From a kinematic point of view, geologists should only observe extensional structures where plates diverge, and contractional structures where plates converge. However, for example, the occurrence of extensional structures in convergent tectonic contexts is well documented - but following the acceptance of plate tectonics, it took our community another two decades to understand and accept the concept of gravitational collapse to explain them (England and Houseman, 1989; Rey et al., 2001). We have known since Newton's laws of motion that a better description of the world must incorporate both dynamics and kinematics into one physical framework.

Understanding plate tectonics from a dynamic perspective has been frustratingly difficult. Analogue modelling, which has provided useful insights from a kinematic and structural perspective has difficulty incorporating coupled gravitational body forces and thermal processes on the correct scales. Conversely, analytical descriptions of natural processes, such as the governing equations of Stokes flow (Stokes, 1851), energy diffusion (Fourier, 1822), and rheological behavior (Bingham, 1922) have been known for over a century, and yet the amount of computation required has meant that their application to geodynamics has been

very limited. However, in the past 30 years, the advent of accessible computational power has enabled solving these equations for the complex rheologies governing rock behaviour. This has spawned the field of numerical geodynamic modelling, allowing geoscientists to investigate the interplay between kinematics and dynamic processes.

This thesis aims to apply these new numerical techniques to the context of continental rifting, to explore why many passive margins show contractional syn-rift deformation, despite forming in a plate divergent setting. Syn-rift and break-up contractional structures, such as reverse faults, basin inversions, and folds are observed on passive margins around the world (Boldreel and Andersen, 1993; Withjack et al., 1998; Schlische et al., 2003; Cloetingh et al., 2008; Lundin and Doré, 2011; Holford et al., 2014). These inversion structures are typically associated with a small amount of shortening, with many inverted faults retaining a net normal throw, and low fold amplitudes of ~100 m (Holford et al., 2014). These structures develop often with no corresponding convergent plate motion change to account for their formation. The common development of these structures therefore suggests that gravitational forces are at play, as recently shown in metamorphic core-complexes (Rey et al., 2011).

Much work has been done on understanding gravitational forces within continental rifting, particularly focusing on the role the upwelling asthenosphere plays in controlling overall rift dynamics and its influence on the margins. Early work focused on studying the pressure changes induced by lateral variations in crust and lithospheric thicknesses. With the crust in isostatic equilibrium, areas of higher crustal and/or lithospheric thickness have an excess of gravitational potential energy (GPE) (Artyushkov, 1973). These variations in GPE impart lateral stresses, putting areas of relatively high thickness into extension, and areas of relatively low thickness into compression.

Investigation of the role of the convective mantle in continental rifting predicted that a mantle plume impinging on the lithosphere could have a similar impact, by inducing a higher pressure at the base of the lithosphere (Sengör and Burke, 1978). In contrast to 'passive' rifting, where far-field tectonic forces drive lithospheric thinning, the higher pressure from the 'active' mantle, coupled with the induced surface uplift, generates lateral pressure out toward the margins, sufficient to drive rifting, and place the margins into compression (Sengör and Burke, 1978).

Further investigation of mechanisms via which the upwelling mantle within a rift could apply force to the margins lead to the term "rift-push" being defined (Le Pichon et al., 1982; Turcotte and Emerman, 1983; Le Pichon and Alvarez, 1984). The rift-push force is driven by the difference in lithostatic pressure between the mantle in the rift centre and the flank. As the lithosphere thins, hot asthenospheric material is juxtaposed against the much cooler, and therefore more dense, lithospheric mantle in the rift flanks, generating a buoyancy force. As the asthenospheric dome forms beneath the thinning crust, the GPE in the centre of the rift becomes larger than the surrounding areas, generating a lateral force comparable in magnitude to ridge push. The magnitude and duration of the rift-push force is largely dependent on the temperature of the asthenospheric upwelling as it domes, with cooler upwellings generating a smaller buoyancy force (Buck, 1991; Davis and Kusznir, 2002). The rift-push force is somewhat countered by crustal buoyancy forces, where the unthinned crust in the rift flanks

sits isostatically higher than the thinned crust in the centre of the rift, and induces a lateral pressure gradient toward the centre of the rift, reducing the overall gradient of GPE across the margin.

With the introduction of advanced numerical modelling, it was demonstrated that the effect of the rift-push force, and the associated crustal buoyancy force, changes dynamically as the rift evolves (e.g., Bassi, 1991; Bott, 1992; Newman and White, 1999; Huismans et al., 2001; Burov, 2007), both as a function of the rifting conditions (e.g., mantle temperature, strain-rate) changing the magnitude, and due to the rift evolution itself (e.g., faulting and weakening of the lithosphere during rifting) changing the distribution of stress. In particular, Huismans et al. (2001), used numerical models to confirm that rifts could become self-propagating - essentially the system transforming from passive to active rifting - due to the rift-push force, aligning with predictions made originally by Turcotte and Emerman (1983). Further quantification of the role of buoyancy forces at passive margins around the Earth (Pascal and Cloetingh, 2009; Bellahsen et al., 2013) showed that the countering effect of crustal buoyancy is only relevant in relatively low rifting velocities, and is generally overwhelmed by the rift-push force (Davis and Kusznir, 2002), though it may help contribute to the formation of the contractional structures observed.

However, despite this work, it has remained somewhat unclear what impact the magnitude and timing of rift-push has on the development of contractional structures during passive margin evolution. To address this, the thesis begins with **Chapter 2**, which gives an overview of the important thermal and mechanical aspects of continental rifting, and how they are relevant to the numerical modelling done in this thesis.

Chapter 3 uses high resolution 2D numerical models to study the impact of the buoyant upwelling of the asthenosphere on passive margin development. We investigate the role of rift velocity in controlling the magnitude of rift-push, and specifically its impact on the stress state within the developing passive margin. We introduce simplified surface processes to form sedimentary basins, and analyse how this process competes with the upwelling asthenosphere, and how the basins themselves respond to the rift-push force. Our models show good agreement with previous works, e.g., showing a switch from passive to active rifting, but reveal that syn-rift compressional stress within the upper crust can reach up to 30 MPa in certain areas of the margin. Sedimentary basins tend to localise this stress, and can experience strong depth inversions as response to the upwelling asthenosphere.

Chapter 4 extends on this work by investigating the dynamics of rift push in a fundamentally three-dimensional setting. It has been proposed that contractional structures could form along a rift margin if break-up (and the corresponding asthenospheric upwelling) occurs diachronously (Withjack et al., 1998; Schlische et al., 2003). To test this, we use similar models to Chapter 3, extended into three-dimensions to model continental rifting when close to an Euler pole. Rifting close to an Euler pole presents a tectonic setting with dynamic changes along the rift axis, with slow spreading close to the pole, and fast spreading away from it, implying diachronous break up and asthenospheric upwelling. We again investigate the role of the upwelling asthenosphere in producing excess GPE and how it interacts with the applied tectonic forces. We demonstrate that the asymmetric rise of the mantle can produce both

compressional and trans-current tectonic stresses both ahead of the propagating rift tip and in the rift flanks, with the models also predicting the pattern of earthquake focal mechanisms found in areas such as the Woodlark Basin and the Galapagos Rise (Taylor et al., 1995; Floyd et al., 2002). **Appendix IV** adds additional context to this study, containing a blog post about the work done, published on the EGU Geodynamics Division website.

Continuing on the theme of investigating the formation of contractional structures within kinematically extensional settings, both **Appendix I** and **Appendix II**, co-authored publications, apply similar numerical modelling methods to a metamorphic core-complex setting. Appendix I explains the formation of coeval extensional and contractional structures within metamorphic core complexes, by showing that the weak lower crust flows into a double-dome structure as it is unloaded during extension. Appendix II explores the role of buoyancy forces in forming metamorphic core-complexes via a suite of 2D geodynamic models, exploring how varying lower crustal strength and density controls the conditions in which these double dome structures can form.

To enable the work done in Chapter 4, Appendix I, and Appendix II, a new methodological approach was designed and built to encourage and empower more tectonicists and structural geologists to use numerical geodynamic modelling tools. In **Chapter 5**, we identify a number of areas which block new users to numerical modelling, and present a framework, called the *Lithospheric Modelling Recipe* (*LMR*), which attempts to remove these blocks when using a particular modelling software, *Underworld*. While numerical modelling brings with it the promise of repeatable and reproducible science, often model data, codes, and input files are not published. This chapter provides guidance for other modelling codes in how to attract and retain users from a more diverse subsection of geoscience, and how this can encourage reproducible science.

This is followed up by a co-authored paper in **Appendix III**, which describes a similar methodology for the latest version of *Underworld* (version 2), called *UWGeodynamics*, which directly attributes inspiration and data from the *LMR*.

A discussion and conclusion summarises the main contributions presented in this thesis, and contextualises how they have contributed to explaining the formation of contractional and transcurrent structures in extensional settings, and how expanding the tools used to do this to more structural geologists and tectonicists can help accelerate research in these areas.

References

Artyushkov, E.V., 1973. Stresses in the lithosphere caused by crustal thickness inhomogeneities. Journal of Geophysical Research, 78(32), pp.7675-7708.

Bassi, G., 1991. Factors controlling the style of continental rifting: insights from numerical modelling. Earth and Planetary Science Letters, 105(4), pp.430-452.

Bellahsen, N., Husson, L., Autin, J., Leroy, S. and d'Acremont, E., 2013. The effect of thermal weakening and buoyancy forces on rift localization: Field evidences from the Gulf of Aden oblique rifting. Tectonophysics, 607, pp.80-97.

Bingham, E.C., 1922. Fluidity and plasticity (Vol. 2). McGraw-Hill.

Boldreel, L.O. and Andersen, M.S., 1993, January. Late Paleocene to Miocene compression in the Faeroe–Rockall area. In Geological Society, London, Petroleum Geology Conference series (Vol. 4, No. 1, pp. 1025-1034). Geological Society of London.

Bott, M.H.P., 1992. Modelling the loading stresses associated with active continental rift systems. Tectonophysics, 215(1-2), pp.99-115.

Buck, W.R., 1991. Modes of continental lithospheric extension. Journal of Geophysical Research: Solid Earth, 96(B12), pp.20161-20178.

Burov, E., 2007. The role of gravitational instabilities, density structure and extension rate in the evolution of continental margins. Geological Society, London, Special Publications, 282(1), pp.139-156.

Clark, M.K. and Royden, L.H., 2000. Topographic ooze: Building the eastern margin of Tibet by lower crustal flow. Geology, 28(8), pp.703-706.

Cloetingh, S., Beekman, F., Ziegler, P.A., van Wees, J.-D., and Sokoutis, D., 2008. Post-rift compressional reactivation potential of passive margins and extensional basins, in Johnson, H., et al., eds., The Nature and Origin of Compression in Passive Margins. Geological Society of London Special Publication 306, p. 27–70, https://doi.org/10.1144/SP306.2.

Davis, M., and Kusznir, N., 2002, Are buoyancy forces important during the formation of rifted margins?: Geophysical Journal International, v. 149, p. 524–533, 205 https://doi.org/10.1046/j.1365-246X.2002.01666.x.

England, P. and Houseman, G., 1989. Extension during continental convergence, with application to the Tibetan Plateau. Journal of Geophysical Research: Solid Earth, 94(B12), pp.17561-17579.

Fourier, J.B.J., 1822. Théorie analytique de la chaleur. F. Didot.

Holford, S.P., Tuitt, A.K., Hillis, R.R., Green, P.F., Stoker, M.S., Duddy, I.R., Sandiford, M., and Tassone, D.R., 2014. Cenozoic deformation in the Otway Basin, southern Australian margin: Implications for the origin and nature of post breakup compression at rifted margins. Basin Research, v. 26, p. 10–37, https://doi.org/10.1111/bre.12035.

Huismans, R.S., Podladchikov, Y.Y. and Cloetingh, S., 2001. Transition from passive to active rifting: Relative importance of asthenospheric doming and passive extension of the lithosphere. Journal of Geophysical Research: Solid Earth, 106(B6), pp.11271-11291.

Le Pichon, X., Angelier, J. and Sibuet, J.C., 1982. Plate boundaries and extensional tectonics. Tectonophysics, 81(3-4), pp.239-256.

Le Pichon, X. and Alvarez, F., 1984. From stretching to subduction in back-arc regions: Dynamic considerations. Tectonophysics, 102(1-4), pp.343-357.

Lundin, E.R. and Doré, A.G., 2011. Hyperextension, serpentinization, and weakening: A new paradigm for rifted margin compressional deformation. Geology, 39(4), pp.347-350.

Newman, R. and White, N., 1999. The dynamics of extensional sedimentary basins: constraints from subsidence inversion. Philosophical Transactions of the Royal Society of London. Series A: Mathematical, Physical and Engineering Sciences, 357(1753), pp.805-834.

Pascal, C. and Cloetingh, S.A., 2009. Gravitational potential stresses and stress field of passive continental margins: Insights from the south-Norway shelf. Earth and Planetary Science Letters, 277(3-4), pp.464-473.

Rey, P., 2001. From lithospheric thickening and divergent collapse to active continental rifting. Geological Society, London, Special Publications, 184(1), pp.77-88.

Rey, P.F., Teyssier, C., Kruckenberg, S.C. and Whitney, D.L., 2011. Viscous collision in channel explains double domes in metamorphic core complexes. Geology, 39(4), pp.387-390.

Schlische, R.W., Withjack, M.O., and Olsen, P.E., 2003. Relative timing of CAMP, rifting, continental breakup, and basin inversion: Tectonic significance, in Hames, W.E., et al., eds., The Central Atlantic Magmatic Province: Insights from Fragments of Pangea. American Geophysical Union Geophysical Monograph 136, p. 33–59, https://doi.org/10.1029/136GM03.

Sengör, A.M. and Burke, K., 1978. Relative timing of rifting and volcanism on Earth and its tectonic implications. Geophysical Research Letters, 5(6), pp.419-421.

Stokes, G.G., 1851. On the effect of the internal friction of fluids on the motion of pendulums (Vol. 9, p. 8). Cambridge: Pitt Press.

Turcotte, D.L. and Emerman, S.H., 1983. Mechanisms of active and passive rifting. In Developments in Geotectonics (Vol. 19, pp. 39-50). Elsevier.

Withjack, M.O., Schlische, R.W., and Olsen, P.E., 1998. Diachronous rifting, drifting, and inversion on the passive margin of central eastern North America: An analog for other passive margins. American Association of Petroleum Geologists, Bulletin, v. 82, p. 817–835.

Important thermal and mechanical aspects of continental rifting

To investigate the dynamics of the buoyant asthenosphere during rifting, we use the numerical modelling software *Underworld*. Within each chapter of this thesis, the specific details of the models are described, including the version of *Underworld*, the setup of the model domain, the rheologies used, the boundary conditions applied, and other additional processes implemented. Additionally, the supplements to Article 1 (Chapter 3) and Article 2 (Chapter 4) describe the key physical principles underpinning the numerical calculations used in *Underworld*, detailing the Stokes flow equations of the conservation of mass, momentum, and energy. However, as discussed in Article 3 (Chapter 5), if the details of the physics at play, together with the intricacies of the numerical framework used to solve it, goes beyond the common expertise of geologists, the key thermal and mechanical concepts controlling the deformation of the lithosphere are still within reach of field geologists. In this chapter, we describe the forces driving deformation, including far-field tectonics and internal body forces; the role of temperature changes; the rheology of rocks; and additional processes such as partial melting and surface processes.

Far-field tectonic forces

A far-field tectonic force is one derived from some other tectonic process, such as ridge-push at mid-oceanic ridge and slab-pull at subduction zone, where the force is transmitted through a tectonic plate. Within the context of passive continental rifting, slab-pull is the main driver of lithospheric deformation (Sengör and Burke, 1978). As oceanic lithosphere cools down over time, it becomes more dense, and eventually sinks into the mantle, creating a subduction zone. As gravity acts on this dense and strong slab, the force is transmitted through it,

along the oceanic plate, and across the continental margin to continent interior (Forsyth and Uyeda, 1975). This force, proportional to the difference in density between the subducting material and the surrounding mantle, is a buoyancy force, and is defined as

$$F_b = \Delta\rho \cdot v \cdot g \qquad (1.1)$$

where $\Delta\rho$ is the difference in density between the material and its surrounding medium, v is the volume of the material, and g is gravity. However, the evolving density and thickness of the slab, due to the changing temperature and pressure (phase changes), complicates the analytical calculation of this force.

For the slab to sink, and therefore transmit the force into a continental interior, the slab-pull force must exceed the viscous coupling between the oceanic lithosphere and the asthenosphere, both in the subduction zone and along the base of the oceanic plate. Once the far-field tectonic force acts upon a continental interior, if it exceeds the strength of the continental lithosphere at any location, deformation occurs. This deformation weakens the continental lithosphere further, both from the damage caused by faulting as well as the upwelling of hot and weak material (Huismans and Beaumont, 2002). This leads to a self-propagating process, where the weakened area localises more deformation, and thus resulting in continued lithospheric thinning until the continent breaks apart (Brune et al., 2016).

Within a numerical model of continental rifting, most commonly the far-field tectonic force is introduced by imposing a velocity boundary condition, rather than applying a set force magnitude. A velocity (which can vary through time and space) is
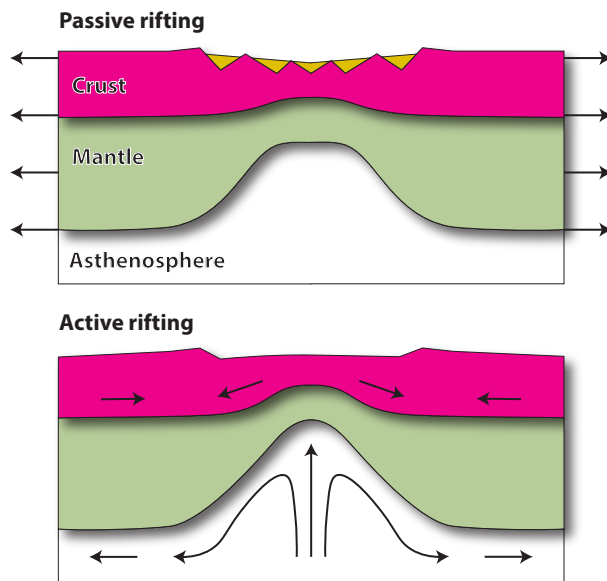
Passive rifting

Active rifting

Figure 1. Schematics of passive and active rifting, derived from Sengor and Burke (1978). Arrows indicate flow driving the thinning of the lithosphere.

set at the vertical boundaries of the computational grid. This velocity dictates an appropriate force to drive the flux of material through the walls. Along the vertical boundaries, the velocity along the depth axis can be either fixed (i.e. no-slip), or let to evolve in a self-consistent manner (i.e. free slip).

Forces from the convective mantle

Mantle convection is driven by the buoyancy of colder and denser regions sinking into hotter and lighter mantle which rises up. The convection of the mantle is able to impart forces on the continental lithosphere via both the viscous coupling of the asthenosphere and the lithosphere as a lateral traction, and through vertical forces related to the push or pull from a mantle upwelling or downwelling respectively. It was proposed by Sengör and Burke (1978) that a deep mantle upwelling could be capable of rifting the lithosphere without far-field tectonic forces, both via the thermal erosion of the lithospheric mantle (where hot mantle material replaces colder, denser lithospheric material) and via the induced surface uplift in the rift centre causing a gravitational collapse - all aided by the increased heat-flow, which weakens the lithosphere through increased temperature, volcanism and dyking. This mode of rifting was termed 'active

rifting', since the mantle is the driving component, as opposed to 'passive rifting' driven by far-field tectonics (Figure 1).

The concept of active and passive rifting has been very successful, though in reality all rifts experience some components of far-field tectonic force and mantle forcing (e.g. Koptev et al., 2018). Indeed, Huismans et al., (2001) used numerical models to show that rifts created via passive rifting can switch to become 'active' rifts, as the upwelling asthenosphere interacts with the rift flanks, highlighting the importance of the internal buoyancy forces and their role in mediating deformation.

Internal lithospheric gravitational forces

Gravitational forces internal to the lithosphere are body forces derived from pressure gradients induced by changes in rock density, either from different mineralogical composition, temperature, or by changes in the thickness of the crust and the lithospheric mantle. Here, we discuss isostatic equilibrium, changes in lithostatic pressure, gravitational potential energy, and its role within continental rifting.

Isostasy

Isostasy is the geological term for Archimedes' principle, that a mass partially or fully immersed in a liquid is acted upon by a buoyancy force equal to the weight of the fluid it has displaced. Analogous to icebergs floating on the ocean, this means in a geological context that the less dense continental lithosphere is partially immersed in, and floating above, the denser asthenospheric mantle. When the lithosphere is in isostatic equilibrium the buoyancy force balances the weight of the lithosphere (zero net force). When material is removed from the lithosphere e.g, via erosion or lithospheric delamination; or material is added to the lithosphere e.g., via sedimentation or thickening of the lithosphere via cooling; then the lithosphere raises or subsides to re-equilibrate the system.

Determining the topographic change caused by isostasy is typically calculated via either the

concepts of Airy isostasy or Pratt isostasy. Airy isostasy assumes that the crust and lithospheric mantle have fixed densities, and so accounting for topographic changes is done by varying the thickness of each layer. Pratt isostasy assumes the density of the crust and lithospheric mantle varies laterally instead. In reality, both cases are true, as mineralogical changes and tectonic forces vary both the density of rock and the thickness of the lithospheric layers - but each provide a simple means of estimating surface topography caused by isostasy. Both models rely on the notion of compensation depth - a depth at or below which there is no lateral variation of pressure. At or below this depth, the total lithostatic pressure of any two columns of rock can be equated, and used to determine the topography as a function of the rock density and layer thicknesses (Figure 2). However, both models assume local compensation - that is, there is no flexural support laterally across the lithosphere.

In numerical geodynamic modelling, isostatic equilibration can be considered implicit to the model, since the Stokes flow equations rely on the pressure gradient to determine flow. As such, Stokes flow under gravity will naturally seek the appropriate topography to produce a laterally constant pressure at the compensation depth. However, in models of continental rifting, where the velocity boundary conditions constantly remove rock material out the sides of the domain, the overall surface topography will sink as the mass is removed. To avoid this, it is common to use specialised boundary conditions to ensure the overall mass in the computational domain stays constant, and the surface does not sink artificially through time. In the models presented in this thesis, a constant-pressure boundary condition is maintained at the bottom boundary of the model by injecting or removing asthenospheric material.

Lithostatic Pressure, Gravitational Potential Energy, and Rift Push

A section of continental lithosphere being in isostatic equilibrium does not necessarily imply that no internal gravitational forces are at work. Isostatic equilibrium states that all columns in the section must be at the same lithostatic pressure at the compensation depth - but above this depth, the pressure within each column may be different.

As shown in Figure 3 (left), a column of normal lithosphere (column A) has a higher lithostatic pressure in the crust, when compared to a column of thinning lithosphere (column B), or a column of asthenospheric material after break up (column C). However, the opposite is true in the lithospheric mantle of column A, which has a lower lithostatic pressure compared to the other columns at the same depth. Comparing the lithostatic pressure through depth of two columns down to the compensation depth reveals that lateral pressure gradients develop, induced by the changing thickness of the lithosphere as it rifts (Figure 3, right). Areas with excess pressure are under extensional stress, while areas with a pressure deficit are under compressional stress. During continental rifting, it is therefore clear that a single column of rock may be under different tectonic stress regimes depending on the
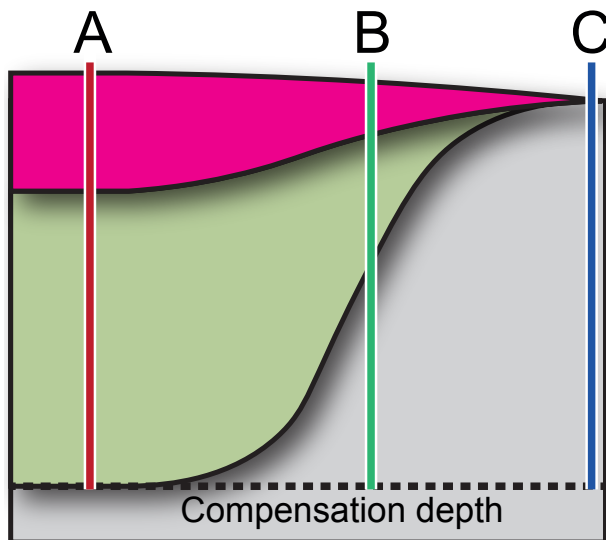

Figure 2: A diagrammatic representation of continental lithosphere at the point of breakup: column A is unthinned lithosphere (40 km thick crust, 140 km thick lithosphere), column B is stretched lithosphere (20 km thick crust, 70 km thick lithosphere), and column C is where the lithosphere is completely thinned. The surface topography is 0 km at column A, -3.18 km at column B, and -6.36 km at column C. The total lithostatic pressure at the compensation depth in each column is, by definition, equal.
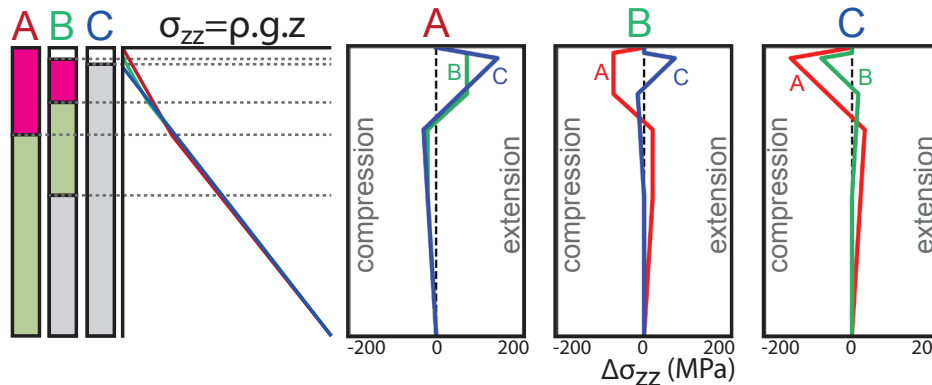
Figure 3. Left: columns A, B, and C taken from Figure 2, with their lithostatic pressure plotted through depth. Right: Graphs of the difference in lithostatic pressure between columns - for example, the graph labelled 'A' shows the lithostatic pressure of column A, minus each column B and C.

depth. If the difference in pressure between two locations exceeds the strength of the lithosphere, deformation will occur.

The gravitational potential energy, or GPE, of a column of rock is the depth integration of the lithostatic pressure. Therefore, areas with high GPE exert a net force toward areas of low GPE, with the force magnitude being calculated via the depth integration of the difference in lithostatic pressure between them (e.g., the area beneath the curves in Figure 3, right) (Artyushkov, 1973).

The term 'rift-push' describes this gravitational force during rifting and before the onset of seafloor spreading. This force acts between the centre of the rift axis and the adjacent unthinned rift flanks (Davis and Kusznir, 2002). The 'rift-push' becomes the 'ridge-push' when break-up is reached and a mid-oceanic ridge has formed. Similar to isostasy, these processes are implicit to the geodynamic calculations performed within numerical modelling, and are dependent on the density and thermal conditions.

Thermal processes

The gravitational forces are dependent on the density of rocks, which changes as a function of its mineralogical make up; on the local temperature, due to thermal expansion; the local pressure, due to compaction; and other processes, such as a phase change. Within the context of continental rifting, thermal processes have a large impact on the resulting gravitational forces at work, since the thermal expansion of rocks can reduce their density

on the order of ~10 kg.m^{-3} per increase of 100 ºK. This change is important particularly within the asthenospheric upwelling, since the higher temperature/lower density results in a lower lithostatic pressure, and therefore a corresponding higher neutral buoyancy level (e.g., Davis and Kusznir, 2002). This change can also result in other processes, such as Rayliegh Taylor instabilities at the base of the lithospheric mantle, or small-scale convection within the rising dome.

Geodynamic models take into account the processes of thermal diffusion and advection, within the imposed temperature boundary conditions (e.g., 20 ºC at the surface, 1330 ºC at the base of model), as well as other heat producing or consuming processes, including radiogenic heat production, heat absorbed via partial melt processes, or released via shear heating from mechanical deformation. The evolution of the temperature field derives from solving an energy equation of the form:

$$\frac{\partial T}{\partial t} = \kappa v^2 T - v \cdot \Delta T + H + \frac{\partial X}{\partial t} \cdot L \quad (1.2)$$

The right end side of the energy equation above includes four processes, from left to right: heat diffusion, heat advection, radiogenic heat production, and heat changes from partial melt processes (derived from equation 1c, Moresi et al., 2007).

Thermo-mechanical models are usually started with a realistic initial geotherm, which can be derived analytically or by allowing a model to reach a thermal steady-state over a long time period.

The geodynamic models used in this thesis are considered 'incompressible' and use the Boussinesq approximation (Boussinesq, 1897), which states that the density change induced by thermal expansion is incorporated as part of the buoyancy force, but the corresponding volume change is ignored - that is, volume changes in rocks do not affect the flow calculated by the Stokes equations. Similarly, we do not incorporate density changes due to pressure, and we do not model any mineralogical phase changes, and so any volume changes from these processes therefore are not accounted for.

Rheology

Rheology describes the mechanical response of materials to applied forces. Rocks exhibit brittle, viscous, and elastic mechanical behaviors, with the properties determined by the mineralogical makeup of the rock, its porosity and pore fluid saturation, and the pressure and temperature conditions. The rheology of rocks results in a resistive force (with respect to the effective force driving deviatoric stresses) that must be overcome for deformation to occur. For example, grains cohesion and the friction along faults plane must be overcome for faulting to happen. In the ductile domain, flow at a given rate can only occur when the viscosity at this particular rate is overcome.

Our knowledge of rock rheology largely derives from laboratory experiments, in which a volume of rock is submitted to a deviatoric stress under controlled pressure, temperature and fluid conditions. In the ductile regime, rheological properties are measured when the strain rate reaches a steady state; and in the brittle domain when an unstable frictional sliding occurs. From these experiments, various flow laws and parameters are derived.

In the ductile domain, the flow law expresses a relationship between the applied deviatoric stress (σ) and the resulting strain rate ($\dot{\varepsilon}$). The fundamental relationship is defined as:

$$\dot{\varepsilon} = \frac{\sigma}{2\eta} \qquad (1.3)$$

where η is the viscosity. The viscosity term represents a measure of the resistance to flow, mediating the relationship between stress and strain. For a Newtonian fluid this term is constant, expressing a linear relationship between deviatoric stress and strain rate. Most natural rocks display non-Newtonian behavior, meaning the required deviatoric stress change for a resulting change in strain rate is not linear:

$$\dot{\varepsilon} = A\sigma^n \qquad (1.4)$$

where A is the pre-exponential factor, and n is the deviatoric stress exponent. The stress exponent controls the non-linearity of the rock's behavior. The pre-exponential factor ($MPa^n.s^{-1}$) is a constant that varies significantly with rocks composition. Other controlling parameters, such as water fugacity and grain size, may be included in this formula, either implicitly as part of the measurement of A, or explicitly as separate terms.

An Arrhenius equation is used to account for the influence of pressure (P), temperature (T), activation energy and activation volume of the dominant deformation mechanism (A and V respectively):

$$\dot{\varepsilon} = A\sigma^n \exp(-\frac{E + PV}{nRT}) \qquad (1.5)$$

where R is the gas constant. For the geodynamic modelling performed in this thesis, this equation is used to determine the viscosity of rock materials in the Stokes flow calculations.

For a typical continental geotherm and lithostatic pressure (Figure 4), the flow law above predicts that the differential stress needed to achieve a given strain rate strongly varies with depth, and with applied strain-rate, as shown in Figure 4.

Figure 4 documents the sensitivity of the differential stress to temperature, with extremely and unrealistically strong rocks predicted at low temperature. In reality, in these regions of high-viscosity, it requires less energy for rocks to deform via brittle deformation. Brittle deformation is another form of
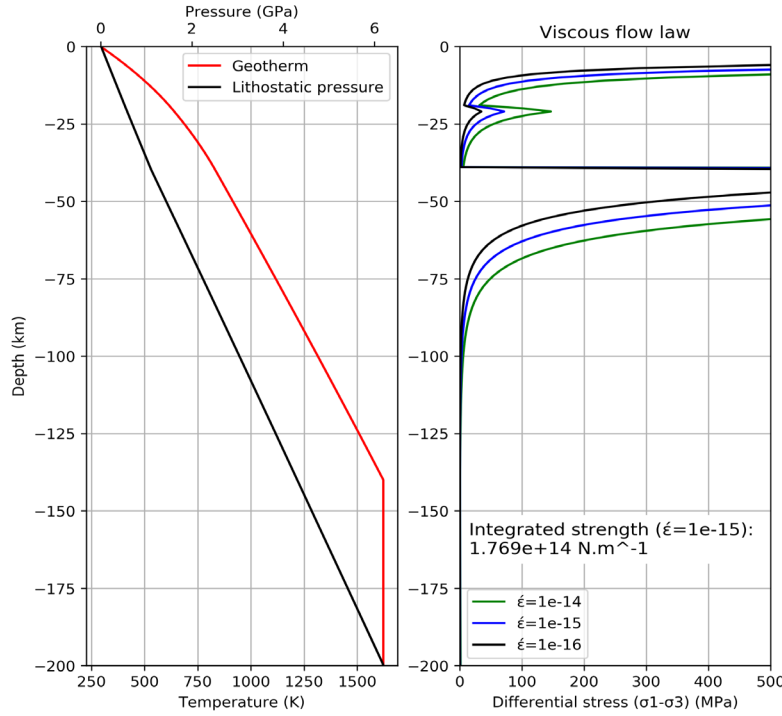
Figure 4. Left: The geotherm and pressure profile used to calculate the viscous flow law shown in the right panel. The lithosphere is made up of 20 km thick upper crust (ρ = 2800 kg.m⁻³, A (radiogenic heat production) = 1.2e-6 W.m⁻³), 20 km thick lower crust (ρ = 2900 kg.m⁻³, A = 0.6e-6 W.m⁻³), and the remainder is mantle material (ρ = 3330 kg.m⁻³, A = 0.02e-6 W.m⁻³). The base of the continental lithosphere is defined at -140 km, where the geotherm hits 1632 K. Right panel: A graph of the viscous flow law in an average section of continental lithosphere. The figure is clipped to 500 MPa, since the maximum value reaches 59,348 MPa. The calculations using different strain-rates shows the flow law's response to deformation. The upper crust uses a wet quartzite flow law (Paterson and Luan 1990), the lower crust uses a dry mafic granulite flow law (Wang et al., 2012), and the mantle uses a wet olivine flow law (Hirth and Kohlstedt, 2003)

plastic deformation. This mechanism accounts for faulting and fracturing, and involves the formation of discontinuous breaks to relieve stress. Notably, most geodynamic modelling uses the approximation of a continuous medium - that is, there can be no discontinuous breaks or gaps within the model, only continuous flow. The brittle laws used in the geodynamic modelling in this thesis faulting is approximated by instead generating narrow zones of low viscosity to represent faults.

A common model of brittle failure is the Drucker-Prager model, similar to Mohr-Columb, which accounts for the confining pressure (which opposes faulting) and the frictional properties of the rock including the cohesion (the strength of the "glue" keeping grains together) and the friction coefficient (which measures the resistance to sliding once a discontinuous break has formed). It is defined as:

$$\sqrt{J_2} = Ap + B \qquad (1.6)$$

where $\sqrt{J_2}$ is the second invariant of the deviatoric stress tensor, p is the pressure, and A and B are defined as:

$$A = \frac{2\sin\phi}{\sqrt{3}(3 - \sin\phi)} \qquad (1.7)$$

$$B = \frac{6C\cos\phi}{\sqrt{3}(3 - \sin\phi)} \qquad (1.8)$$

where C is the cohesion, and Φ is the friction coefficient.

In both viscous and brittle laws, additional complexities can lead to more realistic models of rock behaviors. In the modelling done in this thesis, we also incorporate strain weakening within the brittle laws, such that the cohesion and friction coefficient get smaller as a function of the accumulated strain (Huismans & Beaumont, 2002). This leads to more strain localization and more realistic brittle deformation. Other processes can be included, such as incorporating dynamic grain-size changes in viscous flow laws (e.g., Dannberg et. al., 2017) or taking into account partial melting which significantly reduces the viscosity of rocks (e.g., Whitney et. al., 2013).

Since rocks have the potential to deform via either viscous, brittle, or elastic behaviors, calculating which law governs deformation at a particular
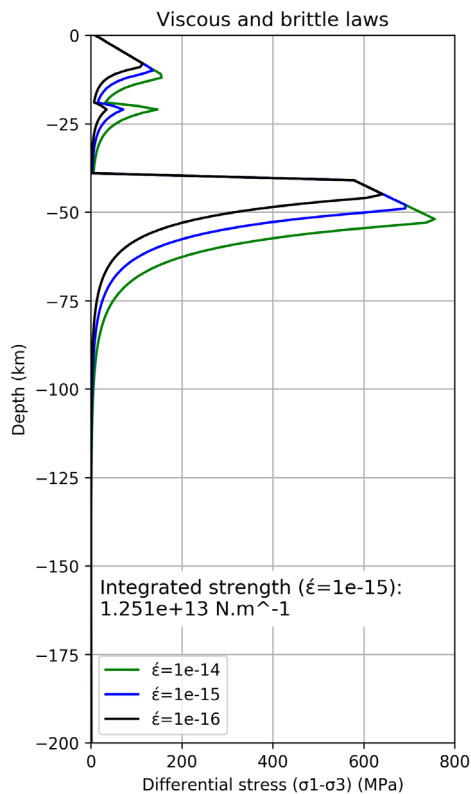
Figure 5. The same as the right panel of Figure 4, with both brittle and viscous laws.

Figure 6. The same differential stress diagram from Figure 5, with a differential stress clipping law applied.

depth requires figuring out which one requires the least differential stress. The role of long-term elastic behaviors in rifting has recently been shown to play a role in controlling individual fault dynamics, fault block rotation, and therefore to some extent, topography (Olive et al., 2016). However, the geodynamic models used in this thesis do not model elastic behavior, as it requires additional computational complexity and compressible materials to model accurately (Choi et al., 2013), with minor differences in first-order rift structures. Therefore the models use only brittle and viscous rheologies (so called 'visco-plastic' models). Figure 5 shows the differential stress profile, which combines the brittle branches and ductile branches described above.

Integrating the differential stress profiles gives a measure of the lithospheric strength, and helps determine if a given force would be enough to induce rifting in a given section of lithosphere. However, performing this calculation on, for
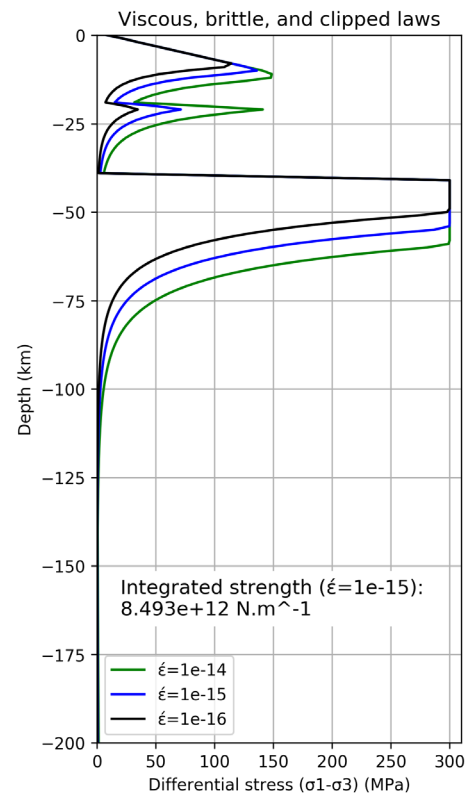
example, the lithosphere portrayed in Figure 5, produces a total lithospheric strength that is quite high. Evidence from Demouchy et al. (2013) and Zhong and Watts (2013) shows that the maximum deviatoric stress that a lithosphere can support does not exceed 300 MPa. This mismatch between nature and experimental data can be attributed to the limitations of laboratory experiments, as the strain rates used in experiments are many orders of magnitude faster than natural strain rate, and/ or additional deformation mechanisms may not be active in experimental tests under laboratory conditions (e.g. pseudo-plasticity (Ord & Hobbs, 1989); peierls creep (Kameyama et al., 1999)). One way to ensure that the strength of the lithosphere in our model is not unrealistically strong is to impose a deviatoric stress upper-bound as shown in Figure 6 (Watremez et al., 2013). The geodynamic modelling in this thesis uses the viscous, brittle, and stress upper-bound laws on all rock materials.

Additional geodynamic processes

A number of other geodynamic processes are incorporated into the numerical models detailed in this thesis. Here we discuss briefly both partial melting, and surface processes, and their impact on rift development.

Partial melting

Partial melting has a strong thermal and mechanical effect impacting on the dynamics of continental rifting. Partial melting occurs at different temperature and pressure conditions depending on the mineralogical composition and fluid content of rocks. Melting begins at the solidus and continues until the liquidus where the rock is fully melted. In between the solidus and liquidus the melt fraction is calculated following the parameterization from McKenzie and Bickle (1988):

$$M_f = 0.5 + T_{ss} + (T_{ss}^2 - 0.25) \cdot$$
$$(0.4256 + 2.988 \cdot T_{ss}) \quad (1.9)$$

where T_{ss} is the supersolidus temperature:

$$T_{ss} = \frac{T - (T_{sol}(z) + T_{liq}(z)/2)}{T_{liq}(z) - T_{sol}(z)} \quad (1.10)$$

where *Tsol(z)* and *Tliq(z)* are respectively the solidus and liquidus temperatures at depth *z*. As the melt fraction increases, it reaches a critical threshold value at which the melt phase forms an interconnected network. At the critical melt fraction, the viscosity of rocks decreases significantly by many orders of magnitude (e.g. Rosenberg and Handy, 2005). Furthermore, the melted material has a lower density than the remaining material, inducing buoyancy forces within the partially melted area, as well as driving the segregation of the melt phase from its source via porous flow. As melting occurs, latent heat energy is consumed as the phase change from solid to liquid occurs, which impacts on the geotherm.

Incorporating realistic melt processes within long-term tectonic thermo-mechanical codes is difficult, due to the large contrast between the small length and time scales of melting and porous flow,

compared to length and time scales of continental rifting. Within this thesis, the first order thermal and mechanical effects of partial melt are accounted for by reducing the viscosity, density and heat of partially melted rock as a function of the melt fraction (Rey et al., 2009). We disregard melt segregation and we assume that the melt phase remains in its source. This is a reasonable assumption as long as the melt fraction remains below 20-30% in the crust, and 2-3% in the mantle where melt interconnectivity is reached for a very small melt fraction (Teyssier and Whitney, 2002).

Surface processes

The transport of mass via erosion and sedimentation has a number of key mechanical and thermal feedbacks on continental rifts. Mechanically, mass transfer from the topographically higher rift flanks to the subsiding rift axis has an isostatic effect, leading to rift flank uplift and crust exhumation, and subsidence within the axis as the sediments weigh down on the stretching lithosphere. This increases the overall topographic relief of the rift region, and so enhance further erosion and deposition in a positive feedback loop (Burov and Poliakov, 2001, and references therein). On a smaller scale, a similar process also acts on individual normal faults, with the total fault heave increasing as the erosion of the footwall and loading of the hanging wall from sediments leads to a higher extensional force along the fault (Olive et al., 2014). From a thermal perspective, the influx of sediments to the rift axis can lead to a thermal blanketing effect, where the increased heat from the upwelling asthenosphere is trapped, further weakening the continental lithosphere and localising deformation.

For numerical modelling of continental rifting with surface processes, again a similar challenge of contrasting length and time scales exists. For 3D tectonic models, it is possible to use an external 3D surface process code, where each model performs its specialised task, and shares data at discrete intervals (e.g., Thieulot et al., 2014; Salles, 2016; Salles and Hardiman, 2016; Salles et al., 2018). Within

the context of 2D models, mass transport through surface processes can only be approximated through simple rules, as no sediments can flux in and out of the plane of the computational grid. For instance, some studies have used a diffusion law over the surface topography and/or one-dimensional stream power-law equations to approximate mass transport and maintain mass balance (e.g., Kooi and Beaumont, 1994). However, there is no strong rationale for maintaining mass balance on a 2D model, since in the natural world sediments are transported over a 3D surface. In the models used in this thesis, a simple approach is used to account for the first order effect of mass transfer during rifting. In this approach, when the surface of the model subsides below an imposed elevation (typically sea-level or a few 100's of meters below) sediments are deposited up to that elevation. A similar approach is used for erosion, and any rock material reaching an imposed maximum elevation is 'eroded' by being converted to air material.

References

Artyushkov, E.V., 1973. Stresses in the lithosphere caused by crustal thickness inhomogeneities. Journal of Geophysical Research, 78(32), pp.7675-7708.

Boussinesq, J., 1897. Théorie de l'écoulement tourbillonnant et tumultueux des liquides dans les lits rectilignes a grande section (Vol. 1). Gauthier-Villars.

Buck, W.R., 1991. Modes of continental lithospheric extension. Journal of Geophysical Research: Solid Earth, 96(B12), pp.20161-20178.

Buck, W.R., Lavier, L.L. and Poliakov, A.N., 1999. How to make a rift wide. Philosophical Transactions-royal Society of London Series a Mathematical Physical and Engineering Sciences, pp.671-689.

Burov, E. and Poliakov, A., 2001. Erosion and rheology controls on synrift and postrift evolution: Verifying old and new ideas using a fully coupled numerical model. Journal of Geophysical Research: Solid Earth, 106(B8), pp.16461-16481.

Brune, S., Williams, S.E., Butterworth, N.P. and Müller, R.D., 2016. Abrupt plate accelerations shape rifted continental margins. Nature, 536(7615), p.201.

Choi, E., Tan, E., Lavier, L.L. and Calo, V.M., 2013. DynEarthSol2D: An efficient unstructured finite element method to study long-term tectonic deformation. Journal of Geophysical Research: solid earth, 118(5), pp.2429-2444.

Copley A. (2012). The formation of mountain range curvature by gravitational spreading. Earth and Planetary Science Letters 351–352:208–214.

Dannberg, J., Eilon, Z., Faul, U., Gassmöller, R., Moulik, P., & Myhill, R. (2017). The importance of grain size to mantle dynamics and seismological observations. Geochemistry, Geophysics, Geosystems.

Davis, M., and Kusznir, N., 2002, Are buoyancy forces important during the formation of rifted margins?: Geophysical Journal International, v. 149, p. 524–533, 205 https://doi.org/10.1046/j.1365-246X.2002.01666.x.

Demouchy, S., Tommasi, A., Ballaran, T. B., & Cordier, P., 2013, Low strength of Earth's uppermost mantle inferred from tri-axial deformation experiments on dry olivine crystals: Physics of the Earth and Planetary Interiors, v. 220, p. 37-49.

Forsyth, D., & Uyeda, S. (1975). On the relative importance of the driving forces of plate motion. Geophysical Journal International, 43(1), 163-200.

Hirth, G. and Kohlstedt, D., 2003. in Inside the Subduction Factory (ed. Eiler, J.) 83–105 (Geophysical Monograph no. 138, American Geophysical Union, 2003).

Huismans, R.S., Podladchikov, Y.Y. and Cloetingh, S., 2001. Transition from passive to active rifting: Relative importance of asthenospheric doming and passive extension of the lithosphere. Journal of Geophysical Research: Solid Earth, 106(B6), pp.11271-11291.

Huismans, R. S., & Beaumont, C. (2002). Asymmetric lithospheric extension: The role of frictional plastic strain softening inferred from numerical experiments. Geology, 30(3), 211-214.

Kameyama, M., Yuen, D.A. & Karato, S.I., 1999. Thermal-mechanical effects of low-temperature plasticity (the Peierls mechanism) on the deformation of a viscoelastic shear zone. Earth and Planetary Science Letters, 168(1-2), pp.159-172.

Kooi, H. and Beaumont, C., 1994. Escarpment evolution on high-elevation rifted margins: Insights derived from a surface processes model that combines diffusion, advection, and reaction. Journal of Geophysical Research: Solid Earth, 99(B6), pp.12191-12209.

Koptev, A., Calais, E., Burov, E., Leroy, S. and Gerya, T., 2018. Along-axis Variations of Rift Width in a Coupled Lithosphere-Mantle System, Application to East Africa. Geophysical Research Letters.

McKenzie, D. and Bickle, M.J., 1988. The volume and composition of melt generated by extension of the lithosphere. Journal of petrology, 29(3), pp.625-679.

Moresi, L., Quenette, S., Lemiale, V., Meriaux, C., Appelbe, B., & Mühlhaus, H. B. (2007). Computational approaches to studying non-linear dynamics of the

crust and mantle. Physics of the Earth and Planetary Interiors, 163(1-4), 69-82.

Paterson, S. and Luan, F. C., 1990. Quartzite rheology under geological conditions, in Knipe, R. J. & Rutter, E. H. (eds), Deformation Mechanisms, Rheology and Tectonics, Geological Society, London, Special Publications, 54, 299-307.

Olive, J.A., Behn, M.D. and Malatesta, L.C., 2014. Modes of extensional faulting controlled by surface processes. Geophysical Research Letters, 41(19), pp.6725-6733.

Olive, J.A., Behn, M.D., Mittelstaedt, E., Ito, G. and Klein, B.Z., 2016. The role of elasticity in simulating long-term tectonic extension. *Geophysical Journal International*, *205*(2), pp.728-743.

Ord, A. & Hobbs, B.E., (1989). The strength of the continental crust, detachment zones and the development of plastic instabilities: Tectonophysics 158 (1-4), 269-289.

Rey, P. F., Teyssier, C., and Whitney, D.L., 2009. The Role of Partial Melting and Extensional Strain Rates in the Development of Metamorphic Core Complexes, in Chardon, D., Rey, P., Teyssier, C., and Whitney, D.L., eds., Hot Orogen: Tectonophysics, 477, p. 135–144.

Rosenberg, C.L. and Handy, M.R., 2005. Experimental deformation of partially melted granite revisited: implications for the continental crust. Journal of metamorphic Geology, 23(1), pp.19-28.

Salles, T., 2016. Badlands: A parallel basin and landscape dynamics model, SoftwareX, 5, 195–202, doi:10.1016/j.softx.2016.08.005.

Salles, T. & Hardiman, L., 2018. Badlands: An open-source, flexible and parallel framework to study landscape dynamics. Computers & Geosciences, 91, 77-89, doi:10.1016/j.cageo.2016.03.011.

Salles, T., Ding, X. and Brocard, G., 2018. pyBadlands: A framework to simulate sediment transport, landscape dynamics and basin stratigraphic evolution through space and time, PLOS ONE 13(4): e0195557.

Teyssier, C. and Whitney, D.L., 2002. Gneiss domes and orogeny. Geology, 30(12), pp.1139-1142.

Thieulot, C., Steer, P. and Huismans, R.S., 2014. Three-dimensional numerical simulations of crustal systems undergoing orogeny and subjected to surface processes. Geochemistry, Geophysics, Geosystems, 15(12), pp.4936-4957.

Wang, Y. F., Zhang, J. F., Jin, Z. M. and Green, H. W., 2012. Mafic granulite rheology: implications for a weak continental lower crust. Earth Planetary Science Letters, 353–354, 99–107.

Watremez, L., Burov, E., d'Acremont, E., Leroy, S., Huet, B., Pourhiet, L., and Bellahsen, N., 2013,

Buoyancy and localizing properties of continental mantle lithosphere: Insights from thermomechanical models of the eastern Gulf of Aden: Geochemistry, Geophysics, Geosystems, v. 14, no. 8, p. 2800-2817.

Whitney, D.L., Teyssier, C., Rey, P. and Buck, W.R., 2013. Continental and oceanic core complexes. Bulletin, 125(3-4), pp.273-298.

Zhong, S., and Watts, A., 2013, Lithospheric deformation induced by loading of the Hawaiian Islands and its implications for mantle rheology: Journal of Geophysical Research: Solid Earth, v. 118, no. 11, p. 6025-6048.

Article 1

Interplay between tectonic extension, surface processes, and gravitational stress explains syn-rift basin inversions

Luke S. Mondy[1], Patrice F. Rey[1], Guillaume Duclaux[2]
[1]*Earthbyte Group, School of Geosciences, The University of Sydney, Sydney NSW 2006, Australia*
[2]*Université Côte d'Azur, CNRS, OCA, IRD, Géoazur, 06560 Valbonne, France.*

ABSTRACT

Continental rifting is the result of divergent forces acting on a plate. Yet within rift zones and passive margins, small-scale contractional structures are frequently observed with no corresponding change in plate dynamics. The change in gravitational potential energy during the rifting process has been predicted to provide compressional force, but the nature and timing of it remains unclear. Using high-resolution 2D numerical experiments of the full rifting process allows us to track the dynamic interplay between the far-field tectonic forces and the internal gravitational body forces, and how it is modulated via rheology and faulting. We find that compressive stresses around 10-20 MPa commonly occur during rifting. We also introduce simple surface processes to investigate the role mass transport can play, and we show that sedimentary basins tend to experience transient phases of compression, localise compressive stresses, and experience depth inversions. Basin depth inversions may explain the formation of the break-up unconformity (BU).

INTRODUCTION

Continental divergence leads to extension, continental rifting and subsidence, which provides the space for the accumulation of sediments, and eventually to the formation of conjugated continental margins. Tectonic subsidence and lithospheric thinning are typically accommodated by grabens bounded by normal faults. In this divergent tectonic context, it is surprising to frequently observe transient episodes of basin inversion in the form of uplift, contractional re-activation of normal faults, or long-wavelength, shallow-angle unconformities and broad low-amplitude folds (e.g., Withjack et al., 1998; Schlische et al., 2003, Cloetingh et al., 2008; Holford et al., 2014). Often, these transient episodes of basin inversion cannot easily be related to far field compressional stresses. Along the passive margins of the North Atlantic for instance, a phase of contractional inversion has been documented during the rift-to-drift transition and early stage of sea-floor spreading (Withjack et al., 1998; Lundin and Doré, 2002, 2011). In the absence of

nearby active margin or collisional processes, the rift-push force, a gravitational body force caused by the buoyant asthenosphere upwelling beneath the rift, is often invoked as a possible driver (Le Pichon et al., 1982; Turcotte and Emerman, 1983; Le Pichon and Alvarez, 1984; Dewey, 1989; Bott, 1992; Boldreel and Andersen, 1993; Kelemen and Holbrook, 1995; Withjack et al., 1998; Huismans et. al., 2001; Davis and Kusznir, 2002; Bellahsen et al., 2013; Dias et al., 2015; Balazs et al., 2017; Mondy et al., 2017). According to this hypothesis, the interaction of far-field tectonic and local gravitational forces on rift margins is able to produce short-term, spatially localised episodes of compression, within a setting of ongoing divergent plate motion. Understanding the cause and timing, and spatial pattern of inversions in sedimentary rift basins along passive margins is critical for hydrocarbon exploration, given their role in the formation of structural traps. Here, we use 2D self-consistent thermo-mechanical numerical experiments

of lithospheric scale extension to document the dynamic evolution of a divergent setting from continental rifting to sea-floor spreading. We track through time the stress and strain rate fields, as well as the vertical motion of the topographic surface and that of the pre-rift basement. The results show that sedimentary basins along rifted margins display temporally and spatially variable patterns of extension and compression of similar magnitude and length scale to that described in nature. The magnitude of compressional stress, in excess of 20 MPa, is large enough to reactivate normal faults, and possibly to buckle the sedimentary basins into long-wavelength low amplitude folds. In addition, our experiments document the inversion, from subsidence to uplift, of the basement surface. The magnitude of this inversion depends on the extensional velocity, and is driven by the isostatic doming of the asthenosphere under the thinned lithosphere.

NUMERICAL EXPERIMENTS AND SETUP

We quantify, via 2D coupled thermo-mechanical experiments, the evolving stress field during the formation of continental margins. We use *Underworld 2.0*, an open source finite-element numerical framework (Moresi et al., 2003, 2007), with the *UWGeodynamics* module (Beucher et al., 2019), to solve the Stokes equation for a very low Reynolds number to obtain velocity and pressure fields from which strain rate and stress tensors are derived. All experiments use a 600 km wide (*x* axis) by 215 km deep (*y* axis) Cartesian grid, with a cell resolution of ~1 km (608 by 224 elements), onto which we map a model of continental lithosphere overlying the asthenospheric mantle. The model is

laterally homogeneous, except for i/ a 200 km wide zone in the centre of the model where the crust is pre-weakened with random damage, and ii/ a 10 km wide and 2 km deep small notch of additional lower crust placed in the centre (Figure 1). Both heterogeneities facilitate localisation of deformation in the centre of the domain, hence mitigating boundary effects and ensuring differing model runs are not controlled by numerical noise.

All materials are visco-plastic, with the viscosity dependent on stress, strain rate and melt-fraction. The upper crust is defined as a 20 km thick layer of wet-quartzite (Paterson and Luan, 1990), the lower crust as a 20 km thick layer of mafic granulite (Wang et al., 2012), and the mantle is made of wet olivine (Hirth and Kohlstedt, 2003). In all experiments, the asthenosphere and the lithospheric mantle have the same rheological parameters. Above the crust, a "sticky-air" layer of 20 km thickness, with viscosity of 1e18 Pa.s, simulates a free surface (Crameri et al., 2016). For all rock materials, we use Drucker-Prager plasticity with linear strain-weakening, reaching its peak at 20% accumulated strain. We also impose a stress limiter of 300 MPa to the entire lithosphere, to approximate additional rheological processes such as peierls creep, which limits the strength of the lithosphere within observational range (Demouchy et al., 2013; Zhong and Watts, 2013).

The initial geotherm for all experiments derives from imposing a surface temperature of 20 ºC, and a temperature of 1350 ºC from -140 km down to the bottom of the domain. The upper crust and sediments have a radiogenic heat production of 1.2 e-6 W.m^{-3}, twice as large as that of the lower crust, and
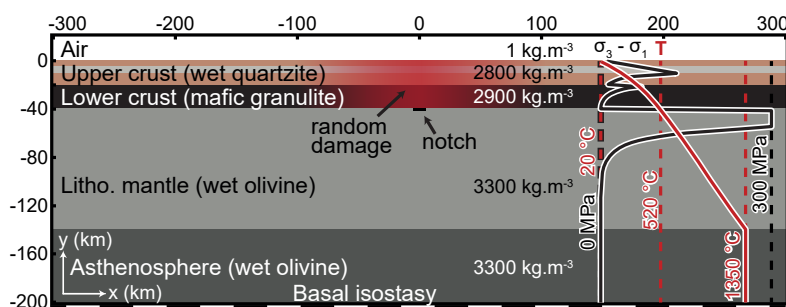
Figure 1. Experiment setup: Kinematic boundary conditions are applied to the vertical walls. The graphs show the differential stress and geotherm at the start of all experiments. The random damage is a gaussian distribution of the amount of accumulated brittle strain. The notch is a section of lower crust that is 10 km wide and 2 km deeper than the rest of the Moho.

the mantle has a radiogenic heat production of 0.02 e-6 W.m^{-3}. Before experiments are run, this system is allowed to reach a thermal steady state resulting in a temperature at the Moho of 545 ºC. During the experiments, the imposed temperatures are only applied to the air material and bottom boundary of the domain. To simulate the drop in viscosity due to partial melting, we impose a viscosity decrease by 3 orders of magnitude as melt fraction increases from the solidus to liquidus. Partial melting also impacts on the geotherm as latent heat energy is consumed in the process. Our experiments do not allow partially melted material to escape from the source (i.e. no porous flow), the maximum melt-fraction is limited to 30% in the crust and 2% in the mantle, and for simplicity we impose that the density of partial melted regions does not change. All rheological and thermal parameters are listed in Supplementary Table 1. We also run a suite of experiments with no melt, to ensure it does not confound our analysis.

Extensional deformation is driven by applying a total divergent velocity of 1, 2, 3, or 4 cm/yr, equally partitioned between the left and right vertical walls. To model isostatic compensation at the base of the domain, we calculate the lithostatic pressure at the beginning of the experiment, and impose it as a vertical stress boundary condition. The vertical walls use no-slip boundary conditions, in part to stabilise the isostatic basal condition. We apply a simple infilling rule to approximate surface processes. According to this rule when air particles fall below an imposed height, they inherit the sediment properties, and record time of 'deposition'. Conversely, when a particle of rock material exceeds a given height, it is "eroded" by switching its properties to air material. The experiments do not conserve mass in regard to surface processes. Since surface processes are inherently three-dimensional, we assume sediment material is sourced from outside the plane of the experiment domain. To prevent having sediments far from the continent margins, the in-filling rule is switched off when the distance between the two margins

reaches an imposed 'gap' distance (e.g., 100 km gap between margins). The supply of sediments and the effectiveness of erosion can therefore be controlled by adjusting both the threshold heights and the distance between margins at which surface processes stop. In our experiments, the deposition threshold is set to y = -1 km, and the margin distance is varied between 30 km, 60 km, 80 km, and 100 km. There is no long-term post-rift sedimentation in our experiments.

To document tectonic stress regimes throughout the lithosphere, we determine which principal stress axis is within 30º of vertical, and classify it into the appropriate Andersonian stress regime (Zoback, 1992, Mondy et al., 2017). While a particular state of stress is only strictly Andersonian at the surface, this method allows these familiar regimes (extensional and compressional, in a 2D context) to be mapped throughout the lithosphere.

RESULTS
Impact of sedimentation and divergence velocity on continental rifting

Figure 2a shows result of experiments under a moderate divergence velocity (2 cm/yr, averaged strain rate of 1e-15 s^{-1}) with and without sedimentation. In both cases deformation starts with a broad zone of near pure shear lithospheric thinning centered on the damaged region. As extension and thinning proceeds, the crustal notch at the Moho localizes deformation in the lithospheric mantle. Once this necking has initiated, the mantle upwells to one side of the crustal notch, and significant faulting in the crust leads to runaway lithospheric thinning and partial melting in the upwelling asthenosphere. Rifting occurs at around 10 myr and 35% extension, at which stage steady-state oceanic spreading accommodates continental divergence, and deformation of the continental margins largely ceases. In experiments with sediment input, rifting is delayed as sediments accumulation mitigates the effective thinning of the crust. In these experiments, rifting is reached at ca. 15 myr and 50% extension. This favors the accumulation of
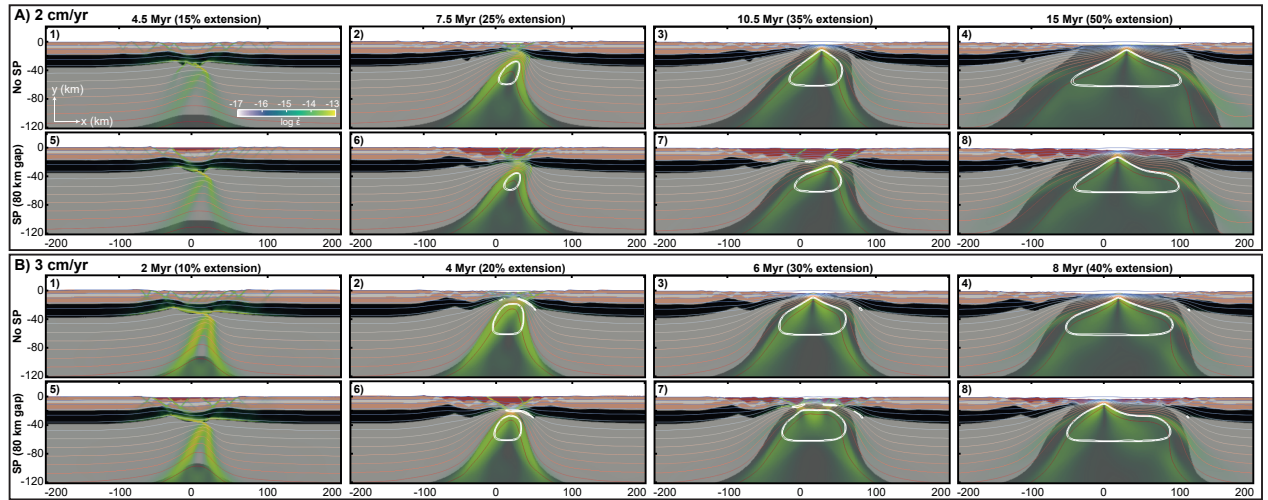
Figure 2. A) Evolution of extension model at 2 cm/yr total extension velocity. A1-4 have no sedimentation, while A5-8 have sedimentation from 1 km depth until the margins reach 80 km apart. Material colours are the same as Figure 1. Sediments are dark red. Semi-transparent blue-green colours show strain-rate. White contours show the 1% and 2% melt fraction. Coloured contours show 100 C isotherms, starting from 20 C. B) The same as A, but with 3 cm/yr extension velocity.

extensional deformation and therefore the formation of extended margins. Furthermore, experiments with sediment input have a tendency to develop slightly more asymmetric extension, as a result of the sediment loading forcing the migration of the proto mid-oceanic ridge.

Figure 2b shows that the depth of sedimentary basins is sensitive to the divergence velocity. As the divergence velocity is increased from 2 to 3 cm/yr (averaged strain rate of ~1.6e-15 s^{-1}) the maximum depth of sedimentary basins is reduced by a factor of ~2, and the impact of sedimentation on the timing of the rifting is much reduced. We conclude that whereas sedimentation lengthens the duration of pre-rifting extension which favours the formation of extended continental margins, divergence velocity limits the impact of sediment input in the evolution of continental rifting.

The role of sedimentation on stress inversion

Despite the constant far-field velocity applied to the domain boundaries, our experiments reveal a very dynamic stress field, with regions shifting from extension to compression as the rift evolves (Figure 3). In the lithospheric mantle, all experiments (with or without sedimentation) exhibit stress regime inversion from extension to compression. This inversion initiates when the Moho at the rift

axis is exhumed by ~10 km, and rapidly propagates to affect most of the lithospheric mantle (Suppl. Data Figure SF2). The crust shows an even more dynamic stress field. In experiments with no sediments, the crust shows regions of transient syn-rift compression from the surface down to ~20 km depth, developing most clearly in experiments with faster divergent velocities. In experiments with sediments, transient syn-rift inversion has a strong tendency to localise on rift basins instead of being more broadly distributed in the upper crust (Figure 3). In these basins, the magnitude of compressional stresses is ~10-20 MPa on average, and can reach up to ~30 MPa. The basin stress inversions occur after the lithospheric mantle stress inversions, and fluctuate in magnitude and depth, with some experiments showing two distinct phases of compressional stress.

At the time of oceanisation, all experiments show a change in the stress patterns, with a number of new zones of compressional stress forming in the crust and rift basins (see Supplementary Figure 2, 3).

Basement depth inversion

In experiments with no sediment input (the 'n/a' lines on Figure 4), the surface subsides monotonously until rifting is complete and seafloor
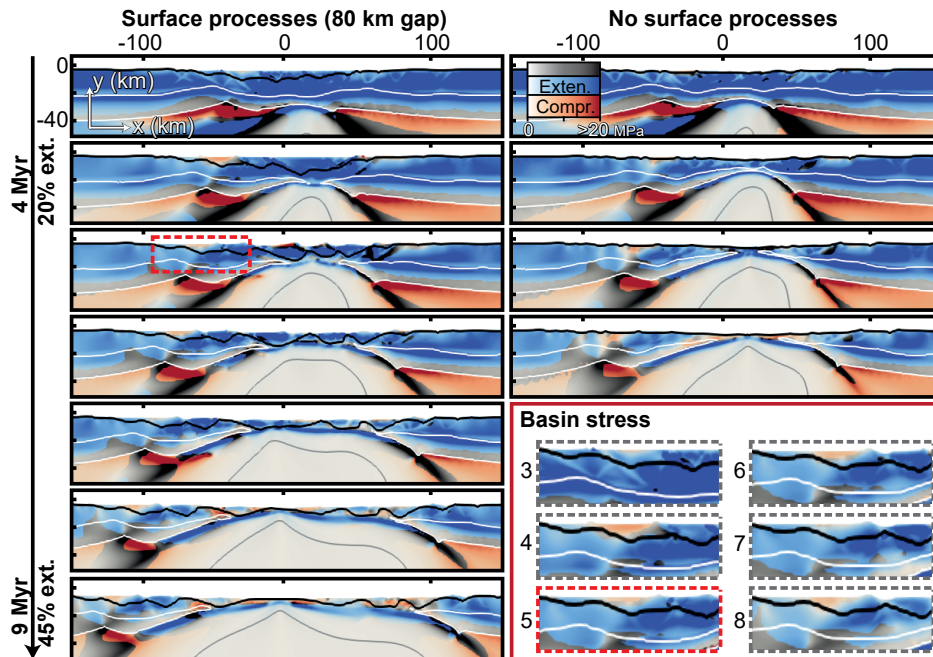
Figure 3. Tectonic stress regimes through time for 3 cm/ yr total extension experiment with (left) and without surface processes (right) until oceanisation. The red inset in the bottom right shows a zoomed in view of a basin from the experiment with surface processes (red dashed outline at t = 5 Myr indicates the location). The thick black contour follows the basement surface, the white contour delineates the outline of the lower crust, and the grey contour follows the 1350 ºC isotherm. Colour intensity shows the deviatoric stress magnitude, with red colours being in compression, and blue colours being in extension. Grey areas do not have a definable Andersonian stress.

spreading occurs. In contrast, in experiments with sediment input, the buried surface experiences a syn-rift inversion from subsidence to uplift (Figure 4). At the onset of divergence, deformation is broadly distributed, and the surface of the basement subsides slowly. As strain localises towards the centre of the rift, the rate of basement subsidence increases, enhanced by the weight of the sediment infill (Burov and Poliakov, 2001). We observe that the magnitude and duration of subsidence is controlled by the volume and the duration of sediment supply (controlled via the sedimentation depth threshold, and the margin gap parameter), and by extension velocity (Figure 4). As the conjugated margins move apart, sedimentation ceases (shown as circles on Figure 4), and all experiments record a switch from basement subsidence to uplift. During this inversion, the maximum, median, and average depths of all basins decreases by about 1 to 2 km (Supplementary Figure 4). This is more clearly documented in experiments with moderate divergence velocities (2 to 3 cm/yr). This strong phase of basement depth inversion correlates with the cessation of sedimentation, which in turn facilitates the exhumation of the asthenosphere eventually leading to rifting and seafloor spreading (triangle markers in Figure 4). As the asthenosphere rises to reach its

neutral buoyancy level (~3000 m below sea level), the maximum basin depth tends to remain steady or slowly decrease (Figure 4). We observe that the largest basement depth inversions occur in experiments where a thick sediment pile covers the central rift zone, impeding asthenospheric upwelling. As the sediment supply stops, the sediment pile is thinned by normal faulting and fault block rotation. The resulting isostatic uplift and exhumation of the asthenosphere pushes the thinning basins upward, some basins being profoundly stretched during this process. When breakup occurs away from the deepest basin, the maximum depth inversion is reduced, though still present.

DISCUSSION: BASIN STRESS AND BASEMENT DEPTH INVERSIONS

We follow others (e.g., Withjack et al., 1998; Huismanns et al., 2001; Davis and Kusznir, 2002) and attribute the stress and basin depth inversions to the doming of the upwelling asthenosphere, and its associated increase in gravitational potential energy (GPE). At the scale of the lithosphere, analytical calculations of the GPE during extension and rifting predict the stress regime switch from extension to compression within the crust of the stretched margin due to the interaction between

Average Basin Depth
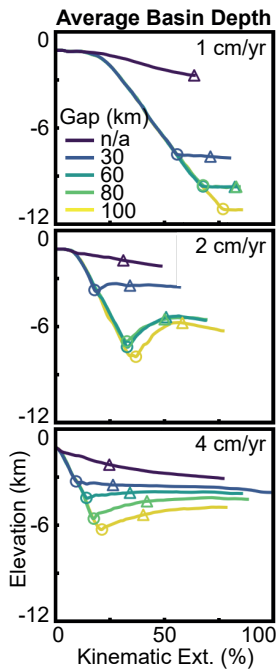
Figure 4. *Average depth of all basins, showing the impact of the cessation of sedimentation. "Gap" represents a control on the amount of sedimentation - when the gap between two margins reaches the gap distance, sedimentation ceases (n/a refers to the reference experiment with no sedimentation). Circles mark when sedimentation stops, triangles mark when break-up occurs. Not all experiments reach both sedimentation cessation and/ or breakup. See Supplementary Figure 4 for more data.*

crustal and asthenospheric buoyancy forces (Supplementary Figure 5). The contrasting GPE across the extended lithosphere leads to the progressive build up of horizontal gravitational stress (Turcotte and Emerman, 1983; Buck, 1991; Huismans et al., 2001; Rey, 2001; Davis and Kusznir, 2002). The experiments presented here document the role of sedimentation and its interference with the exhumation of the asthenospheric mantle, in mediating the transmission and distribution of gravitational compressive stress across a stretched margin (Pascal and Cloetingh, 2009; Bellahsen et al., 2013). In what follows we briefly discuss how the interplay between the exhumation of the asthenosphere and sedimentation impacts on basin inversion, the breakup unconformity and the dynamic evolution of deep basins.

Basin inversions

Along the eastern margin of North America, spatio-temporal patterns of basin inversion have been shown to correlate with the timing of breakup (Withjack et al., 1998; Schlische et al., 2003), and transient basin inversions structurally confined to sub-basins have been documented in many margins (Holford et al., 2014; Cloetingh et al., 2008). Our experiments document and quantify these basin

inversions, with the clearest signals coming from intermediate extension rates and syn-rift sedimentation. This 'Goldilocks zone' results from the optimum interplay between sedimentation and the upwelling asthenosphere. With fast extension (4 cm/yr), the asthenosphere rises more quickly, and remains hot, which enhances the compressional gravitational stresses it imposes on the continental margins. However, fast extension also results in shallower basins (Balazs et al., 2017). In contrast, slower extension (1 cm/yr) leads to deeper basins but the upwelling asthenosphere gets cooler and more dense, which reduces the compressional gravitational stresses and the potential for basin inversion (Keen, 1987; Davis and Kusznir, 2002). The potential for basin inversion is therefore optimum at intermediate extension rates (2-3 cm/yr).

Break-up unconformity

Typically associated to continental break-up, and before the onset of sea-floor spreading, there is a well-documented phase of regional uplift and erosion called break-up unconformities (Falvey, 1974). Processes that have been proposed to contribute to the formation of the break-up unconformity include flexural or isostatic uplift of the lithosphere as it thins, small-scale convection inducing vertical movements (Braun and Beaumont, 1989; Franke, 2013), or a rapid cessation of extension (Balazs et al., 2017). In our experiments, we observe a sharp switch in basement vertical motion from subsidence to uplift, similar to those found in Dias et al., (2015). This inversion is induced by the reduction in sediment supply (Figure 4) allowing for the acceleration of the doming of the asthenosphere and a change to compressional stress at the time of break-up. This basement depth inversion provides a new explanation for the break-up unconformity.

Dynamic evolution of deep basins

Our experiments show that rift basins tend to localise compressive stress. This contrast to experiments with no surface processes in which regions of compressive stress are more broadly distributed often reaching beyond the Moho (Figure 3,

Supplementary Figure 2,3). Although the modelled sediments have otherwise identical rheological properties to the upper crust, they are 100 kg.m-3 lighter. Consequently, deep basins led to small compressive gravitational stresses acting from the surrounding crust toward the basins (Le Pichon and Alvarez, 1984). In addition, the lower density of the rift basin reduces the resistance to faulting via the reduction of the confining pressure by about ~1 MPa/km compared to the confining pressure acting on the adjacent crust. These factors may explain why basins have the tendency to localize contractional deformation. The interaction of the asthenospheric buoyancy forces with these crustal buoyancy forces over time may also explain why multiple phases of extension and compression occur in some basins.

Deep basins that form on the inboard side of the margins that do not experience compressional stresses tend to localise extensional deformation away from the centre of the rift zone, in some cases so much so that thinning occurs simultaneously on both margins (e.g., Figure 3B7). This is a function of partial melting occurring under deeper basins, since the confining pressure is reduced in these areas, and creating very weak zones that focus deformation, which may indicate that this occurs more commonly on volcanic margins.

CONCLUSIONS

During continental extension and rifting, rift basins experience transient periods of compressional stresses, as well as an important episode of basement depth inversion. Our coupled thermal and mechanical experiments, with and without sediments supply, reveal that these are outcome of competing processes. On one hand, the asthenosphere is under the isostatic imperative to reach its neutral buoyant level (~ the elevation of mid-oceanic ridges). On the other hand, this imperative is contradicted by the loading due to the growing sedimentary pile, which mitigates crustal thinning and delays the exhumation of the asthenosphere.

A third important process is the stretching and thinning of rift basin themselves, which, as extension proceeds, facilitates the rapid isostatic exhumation of asthenosphere and the initiation of sea-floor spreading. These processes lead to gravitationally induced compressional stresses in excess of a few 10's of MPa. These results, in broad agreement with previous work on the 'rift-push' force (e.g. Davis and Kusznir, 2002; Huismanns et al., 2001; Balazs et al., 2017; Mondy et al., 2017), reveals that surface processes contribute to the complexity of margin development and that of the structural geology of rift basins.

ACKNOWLEDGEMENTS

REFERENCES CITED

Balazs, A., Burov, E., Matenco, L., Vogt, K., Francois, T. and Cloetingh, S., 2017. Symmetry during the syn- and post-rift evolution of extensional back-arc basins: The role of inherited orogenic structures. Earth and Planetary Science Letters, 462, pp.86-98.

Bellahsen, N., Husson, L., Autin, J., Leroy, S. and d'Acremont, E., 2013. The effect of thermal weakening and buoyancy forces on rift localization: Field evidences from the Gulf of Aden oblique rifting. Tectonophysics, 607, pp.80-97.

Beucher, R., Moresi, L., Giordani, J., Mansour, J., Sandiford, D., Farrington, R., Mondy, L., Mallard, C., Rey, P., Duclaux, G. and Kaluza, O., 2019. UWGeodynamics: A teaching and research tool for numerical geodynamic modelling. Journal of Open Source Software, 4(36), p.1136.

Boldreel, L.O. and Andersen, M.S., 1993, January. Late Paleocene to Miocene compression in the Faeroe–Rockall area. In Geological Society, London, Petroleum Geology Conference series (Vol. 4, No. 1, pp. 1025-1034). Geological Society of London.

Bott, M.H.P., 1992. Modelling the loading stresses associated with active continental rift systems.

Tectonophysics, 215(1-2), pp.99-115.

Buck, W.R., 1991. Modes of continental lithospheric extension. Journal of Geophysical Research: Solid Earth, 96(B12), pp.20161-20178.

Burov, E. and Poliakov, A., 2001. Erosion and rheology controls on synrift and postrift evolution: Verifying old and new ideas using a fully coupled numerical model. Journal of Geophysical Research: Solid Earth, 106(B8), pp.16461-16481.

Braun, J. and Beaumont, C., 1989. A physical explanation of the relation between flank uplifts and the breakup unconformity at rifted continental margins. Geology, 17(8), pp.760-764.

Crameri, F., Schmeling, H., Golabek, G.J., Duretz, T., Orendt, R., Buiter, S.J.H., May, D.A., Kaus, B.J.P., Gerya, T.V. and Tackley, P.J., 2012. A comparison of numerical surface topography calculations in geodynamic modelling: an evaluation of the 'sticky air' method. Geophysical Journal International, 189(1), pp.38-54.

Davis, M., and Kusznir, N., 2002, Are buoyancy forces important during the formation of rifted margins?: Geophysical Journal International, v. 149, p. 524–533, 205 https://doi.org/10.1046/j.1365-246X.2002.01666.x.

Dewey, J.F., 1989. Kinematics and dynamics of basin inversion. Geological Society, London, Special Publications. 44 (1): 352. doi:10.1144/gsl.sp.1989.044.01.20.

Demouchy, S., Tommasi, A., Ballaran, T. B. & Cordier, P., 2013. Low strength of Earth's uppermost mantle inferred from tri-axial deformation experiments on dry olivine crystals. Physics of Earth and Planetary Interior, 220, 37–49.

Dias, A.E.S., Lavier, L.L. and Hayman, N.W., 2015. Conjugate rifted margins width and asymmetry: The interplay between lithospheric strength and thermomechanical processes. Journal of Geophysical Research: Solid Earth, 120(12), pp.8672-8700.

Falvey, D.A., 1974. The development of continental margins in plate tectonic theory. Journal of Australian Petroleum Exploration Association, 14, 95–107.

Franke, D., 2013. Rifting, lithosphere breakup and volcanism: Comparison of magma-poor and volcanic rifted margins. Marine and Petroleum geology, 43, pp.63-87.

Hirth, G. and Kohlstedt, D., 2003. in Inside the Subduction Factory (ed. Eiler, J.) 83–105 (Geophysical Monograph no. 138, American Geophysical Union, 2003).

Holford, S.P., Tuitt, A.K., Hillis, R.R., Green, P.F., Stoker, M.S., Duddy, I.R., Sandiford, M., and Tassone, D.R., 2014. Cenozoic deformation in the Otway Basin, southern Australian margin: Implications for the origin and nature of post breakup compression at rifted margins. Basin Research, v. 26, p. 10–37, https://doi.org/10.1111/bre.12035.

Huismans, R.S., Podladchikov, Y.Y. and Cloetingh, S., 2001. Transition from passive to active rifting: Relative importance of asthenospheric doming and passive extension of the lithosphere. Journal of Geophysical Research: Solid Earth, 106(B6), pp.11271-11291.

Keen, C.E., 1987. Some important consequences of lithospheric extension. Geological Society, London, Special Publications, 28(1), pp.67-73.

Kelemen, P.B. and Holbrook, W.S., 1995. Origin of thick, high-velocity igneous crust along the US East Coast Margin. Journal of Geophysical Research: Solid Earth, 100(B6), pp.10077-10094.

Le Pichon, X., Angelier, J. and Sibuet, J.C., 1982. Plate boundaries and extensional tectonics. Tectonophysics, 81(3-4), pp.239-256.

Le Pichon, X. and Alvarez, F., 1984. From stretching to subduction in back-arc regions: Dynamic considerations. Tectonophysics, 102(1-4), pp.343-357.

Lundin, E. and Doré, A.G., 2002. Mid-Cenozoic post-breakup deformation in the 'passive' margins bordering the Norwegian–Greenland Sea. Marine and Petroleum Geology, 19(1), pp.79-93.

Lundin, E.R. and Doré, A.G., 2011. Hyperextension, serpentinization, and weakening: A new paradigm for rifted margin compressional deformation. Geology, 39(4), pp.347-350.

Mondy, L.S., Rey, P.F., Duclaux, G. and Moresi, L., 2017. The role of asthenospheric flow during rift propagation and breakup. Geology, 46(2), pp.103-106.

Moresi, L., Dufour, F. and Mühlhaus, H.B., 2003. A Lagrangian integration point finite element method for large deformation modeling of viscoelastic geomaterials. Journal of computational physics, 184(2), pp.476-497.

Moresi, L., Quenette, S., Lemiale, V., Meriaux, C., Appelbe, B. and Mühlhaus, H.B., 2007. Computational approaches to studying non-linear dynamics of the crust and mantle. Physics of the Earth and Planetary Interiors, 163(1-4), pp.69-82.

Pascal, C. and Cloetingh, S.A., 2009. Gravitational potential stresses and stress field of passive continental margins: Insights from the south-Norway shelf. Earth and Planetary Science Letters, 277(3-4), pp.464-473.

Paterson, S. and Luan, F. C., 1990. Quartzite rheology under geological conditions, in Knipe, R. J. & Rutter, E. H. (eds), Deformation Mechanisms, Rheology and Tectonics, Geological Society, London, Special

Publications, 54, 299-307.

Rey, P., 2001. From lithospheric thickening and divergent collapse to active continental rifting. Geological Society, London, Special Publications, 184(1), pp.77-88.

Turcotte, D.L. and Emerman, S.H., 1983. Mechanisms of active and passive rifting. In Developments in Geotectonics (Vol. 19, pp. 39-50). Elsevier.

Wang, Y. F., Zhang, J. F., Jin, Z. M. and Green, H. W., 2012. Mafic granulite rheology: implications for a weak continental lower crust. Earth Planetary Science Letters, 353–354, 99–107.

Withjack, M.O., Schlische, R.W., and Olsen, P.E., 1998. Diachronous rifting, drifting, and inversion on the passive margin of central eastern North America: An analog for other passive margins. American Association of Petroleum Geologists, Bulletin, v. 82, p. 817–835.

Zhong, S. and Watts, A. B., 2013. Lithospheric deformation induced by loading of the Hawaiian Islands and its implications for mantle rheology. Journal of Geophysical Research, 118, 1–24.

Zoback, M.L., 1992. First- and second-order patterns of stress in the lithosphere: The World Stress Map Project. Journal of Geophysical Research: Solid Earth, 97(B8), pp.11703-11728.

Supplements to: Interplay between tectonic extension, surface processes, and gravitational stress explains syn-rift basin inversions

Luke S. Mondy[1], Patrice F. Rey[1], Guillaume Duclaux[2]

[1]*Earthbyte Group, School of Geosciences, The University of Sydney, Sydney NSW 2006, Australia*

[2]*Department of Earth Science, University of Bergen, 5020 Bergen, Norway.*

Contents:

SUPPLEMENTAL METHODS

We solve the problem of conservation of mass, momentum and energy for incompressible mantle flow and lithosphere deformation, using *Underworld2* - an open source particle-in-cell finite-element code (freely available at underworldcode.org) - in conjunction with the *UWGeodynamics* library, an open-source python library for more user-friendly interaction with *Underworld2*. The input files used in this work can be found here: https://github.com/LukeMondy/Continental_Rifting

We assume a visco-plastic rheology depending on temperature, stress, strain, strain rate, and in some experiments melt fraction (see Table SM1). The densities of all rocks depend on temperature (see Table SM1).

Experimental setup

The experiments are run within a Cartesian box of 600 km (x-axis) by 220 km (y-axis), which is defined from -300 km to 300 km (x), and -200 km to 20 km (y). The computational grid dimensions for solving the visco-plastic Stokes problem is 608×224 (~1 km cells). A 10 km wide and 2 km deep rectangle of lower crust is defined at the top of the lithospheric mantle (centred around x = 0 km), to preferentially localise deformation in the centre of the domain (Van Wijk and Blackman, 2005). An initial random plastic strain (up to 5%) is imposed the crust to model existing damage and faulting.

Fundamental equations

Underworld solves the incompressible equations of continuity for momentum, energy, and mass as below:

$$\frac{\partial \tau_{ij}}{\partial x_j} - \frac{\partial \rho}{\partial x_i} = -\rho g \lambda_i$$

$$\frac{\partial T}{\partial t} + u_i \frac{\partial T}{\partial x_i} = \frac{\partial}{\partial x_i}\left(\kappa \frac{\partial T}{\partial x_i}\right) + Q$$

$$\frac{\partial u_i}{\partial x_i} = 0$$

Where x_i are the spatial coordinates, u_i is the velocity, T is temperature, ρ is density, g is gravity, λ_i is the unit vector in the direction of gravity, t is time, κ is thermal diffusivity, and Q is a source term for the energy equation. Summation on repeated indices is assumed.

Additional terms can be incorporated into the above equations. In the experiments presented, only radiogenic heating is added, unless explicitly mentioned otherwise - however, an additional experiment was run with partial melting, and so the associated terms and values are described below.

Both radiogenic heating and the thermal aspects of partial melting are incorporated into the energy equations as:

$$Q_{\text{radiogenic}} = \frac{A}{\rho C_p}$$

$$Q_{\text{partial melt}} = -1 \times \frac{L_f}{C_p} \frac{\delta M_f}{\delta t}$$

Where A is the rate of radiogenic heat production, C_p is heat capacity, L_f is latent heat of fusion, and M_f is the melt fraction.

The density of a material is defined via a function that depends on temperature and the melt fraction:

$$\rho = \rho_r \times (1 - \alpha(T - T_r) - (M_f \times M_{\Delta\rho_r}))$$

Where ρ_r is reference density, α is thermal expansivity, T_r is reference temperature, and $M_{\Delta\rho_r}$ is the fraction of density change when melted.

The melt fraction is calculated dynamically as part of the experiment, by using the super-solidus formula given by McKenzie and Bickle (1988):

$$SS = \frac{(T - T_s)}{(T_l - T_s)} - 0.5$$

$$M_f = 0.5 + SS + (SS^2 - 0.25) \times (0.4256 + 2.988 \times SS)$$

Where SS is the normalised super-solidus temperature, T_s is the solidus, and T_l is the liquidus.

The solidus and liquidus are defined as:

$$T_s = t_1 + t_2 P + t_3 P^2$$

Where P is pressure, t_1, t_2, and t_3 are defined Table DR1.

The constitutive behaviour is assumed to be visco-plastic rheologies. For the viscous component, flow is computed using dislocation creep (Hirth and Kohlstedt, 2003):

$$\dot{\varepsilon}_{\text{disc}} = A\sigma^n d^{-p} f_{H_2O}^r \exp\left(-\frac{E + PV}{nRT}\right)$$

Where $\dot{\varepsilon}$ is the effective strain-rate, A is the pre-exponential factor, n is the stress exponent, d is the grain-size, p is the grain-size exponent, f_{H2O} is the water fugacity, r is the water fugacity exponent, E is the activation energy, P is the pressure, V is the activation volume, R is the gas constant, and T is the temperature.

For the plastic component, failure is determined using the Drucker-Prager model:

$$\sqrt{J_2} = Ap + B$$

Where $\sqrt{J_2}$ is the second invariant of the deviatoric stress tensor, p is the pressure, and A and B are defined as:

$$A = \frac{2sin\phi}{\sqrt{3}(3 - sin\phi)}$$

$$B = \frac{6Ccos\phi}{\sqrt{3}(3 - sin\phi)}$$

Where C is the cohesion, and ϕ is the friction coefficient.

A linear strain-softening function is applied to the plastic component. As strain is accumulated from 0 to 20%, the material linearly weakens from its original cohesion and friction coefficient to their softened equivalents (defined in see Table SM1). Once fully weakened, the cohesion and friction coefficient remain constant at the softened values.

A stress limiter is applied to all rheologies, to limit the total strength of the lithosphere. The stress limiter is based on the work flow from Watremez et al. (2013), where a Von Mises criterion is applied, where:

$$\sqrt{J_2} = C$$

All materials are limited to 300 MPa in strength via this method, to account from pseudo-plastic processes, such as Peierls creep, and to ensure the lithosphere does not become artificially strong (Demouchy et. al., 2013; Zhong and Watts, 2013). To ensure numerical stability, all rock materials also have a minimum and maximum viscosity range of 1e19 Pa.s to 5e23 Pa.s.

Partial melting has a mechanical effect, whereby material undergoing melt will reduce in viscosity, within a given melt fraction range (defined in Table SM1), based on the following model:

$$\eta_{melted} = \eta \times (1 \times M_{f\%} + \eta_{factor} \times (1 - M_{f\%}))$$

Where η_{melted} is the viscosity after melting, η is the viscosity calculated from the flow law, $M_{f\%}$ is a normalised linear interpolation of the melt fraction between the lower and upper limits of the melt fraction range, and η_{factor} is the melt viscous softening factor the material undergoes once fully melted.

Rheologies

The rheologies used are based on published work: the upper crust flow law is a wet quartzite from Paterson and Luan (1990); the lower crust flow law is a mafic granulite from Wang et. al (2012); and the lithospheric mantle flow law is a wet olivine from Hirth and Kohlstedt (2003). Viscous flow laws that use 0 for the water fugacity exponent typically have this effect incorporated into the pre-exponential factor. Radiogenic heat production values are from Hasterok and Chapman (2011). Melt and other parameters derived from Rey and Müller, (2010). The air material uses an isoviscous 1e18 Pa.s flow law, with a density of 1 kg m-3, thermal expansivity of 0 K-1m, and a heat capacity of 1000 J K-1. See Table SM1 for detailed parameters values.

Boundary conditions

Isostatic bottom
A constant pressure boundary condition is defined along the bottom wall to model isostatic equilibrium. The pressure applied is calculated at the beginning of the experiments by calculating the lithostatic pressure across the entire domain, and using the average pressure from along the bottom wall. This value is then applied throughout the entire experiment.

Using a constant pressure boundary condition on the base of the model removes a significant constraint on the vertical position of the material in the domain, which can lead to instabilities and large artificial vertical velocities. To help stabilise the experiments, the vertical walls use a no-slip velocity boundary condition, and the top wall has a free-slip, no flux boundary condition (that is, no material can pass through the top wall).

Free surface and top wall boundary condition
To emulate a free surface, the experiments all use an air layer. The air material cannot be modelled at natural values of viscosity or thermal expansivity, since it would be numerically very expensive and unstable. A common substitute is to use a "sticky-air" layer, which has unrealistically high viscosity, but is low enough to not interfere with underlying geodynamics. The isostatic criterion formula from Crameri et. al, 2012 (eq 12) gives a criterion for determining the thickness and viscosity of a good sticky-air layer. Based on this, our experiments use an air-layer with a viscosity of 1e18 Pa.s, and a thickness of 20 km.

The top wall has a free-slip, no flux boundary condition. The no flux condition helps stabilise the isostatic boundary condition on the wall, since it fixes the vertical position of the material in the domain. However, it also means that air material cannot flow in or out of the domain as topographic highs and lows form. Therefore, we give the air a high compressibility, so that it can expand or contract as required.

Thermal boundary conditions
The top wall of the model domain is held constant at 293.15 K (20°C) along with any air material, and the bottom wall is held at 1623.15 K (1350°C). Before the experiment is run, the asthenosphere has an additional boundary condition, so that it too is held at 1623.15 K (1350°C). The model is then thermally equilibrated to achieve a steady state geotherm.

Once the experiment start, the asthenospheric boundary condition is removed.

Surface processes
Sedimentation and erosion are computed by a simple elevation threshold calculation. Air particles that reach a certain elevation are converted into sediment material, and any rock material particles that certain elevation are converted into air material. This process occurs at the end of each timestep. Surface processes cease when a 'gap' condition is met. At the beginning of the experiment, a line of passive tracer particles are distributed along the moho at 2 km spacing. As the experiment evolves, the largest gap between particles is evaluated, and if it exceeds the 'gap' parameter set (in our experiments, either: 30 km, 60 km, 80 km, or 100 km), then any surface processes are stopped. Functionally this results in the biggest gap being between the two margins that form, as the upwelling asthenosphere splits both the crust and the line of passive tracers.

This method of surface processes is both not physically accurate, and does not conserve mass. However, we believe this method is sufficient our experiments, since: a) the details of the process of basin formation is not necessarily the focus of this work, and b) the experiments are in a 2D setting. Since surface processes are fundamentally a three dimensional process, any mass-balancing methods of surface processes used in 2D would be similarly artificial.

Numerical parameters

Time stepping

Time stepping in Underworld uses the Courant-Friedrichs-Lewy (CFL) condition to ensure stable convergence. The CFL is a function of grid size, absolute maximum velocity, and maximum diffusivity. On top of this, to ensure a numerically efficient and temporally stable model run, the computed CFL timestep is multiplied by a factor of 0.1.
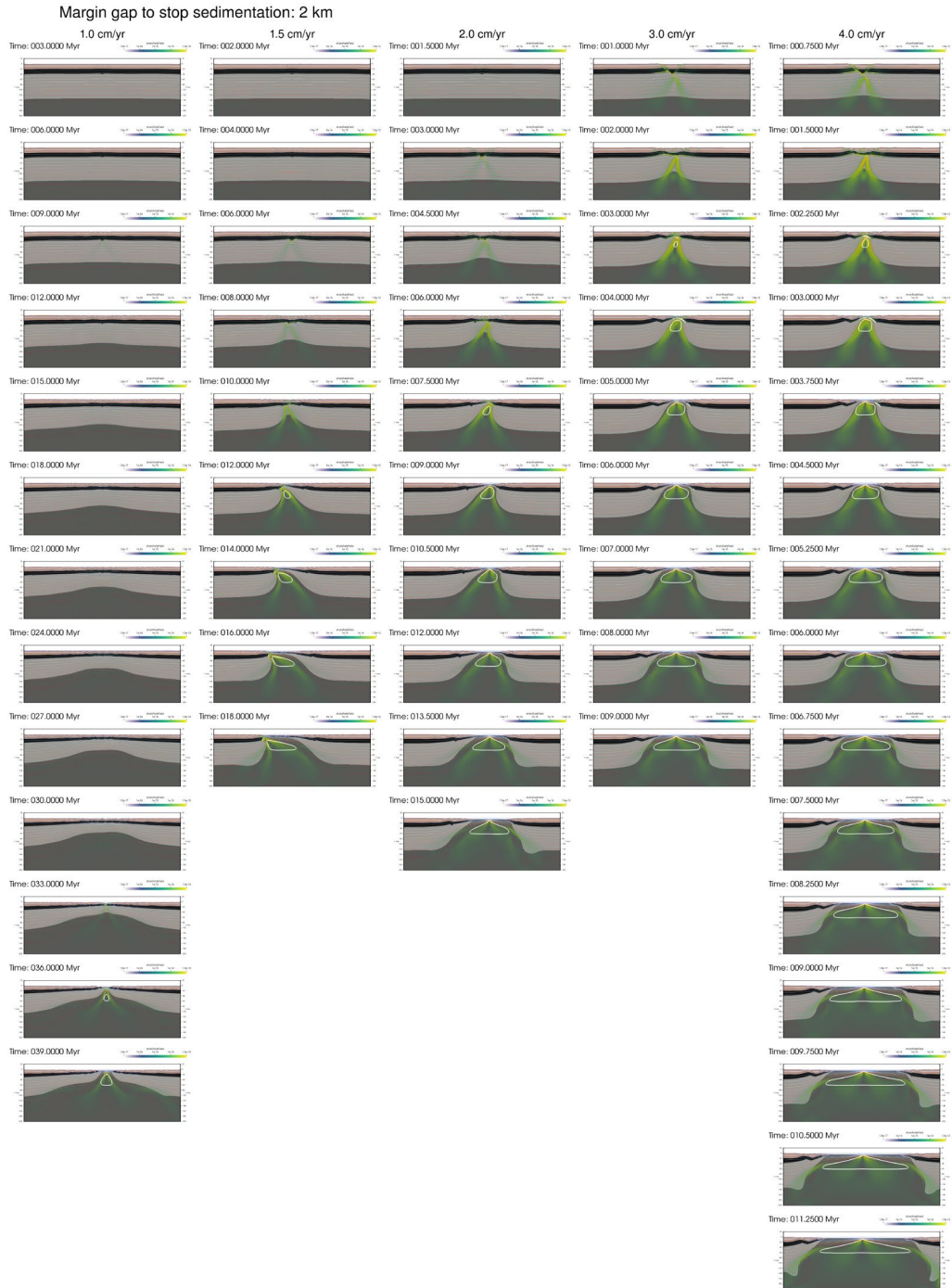
Solver parameters

The isostatic boundary condition used in these experiments is particularly sensitive to both the timestep size, and the solver parameters used. Underworld2 provides a tool called the penalty method, which is effective in solving difficult nonlinear problems - however, it is not compatible with compressible materials. Instead, we use stricter tolerances on the direct solver, with the nonlinear tolerance at 5e-4, and the linear solver tolerance at 1e-8. These parameters (along with the reduced CFL factor) produce very stable experiments, with very little velocity jumps and the associated strain-rate 'oscillating'.

SUPPLEMENTAL FIGURES

Figures SF1-SF3 show the evolution of different aspects of all experiments. In each figure, the columns represent a single experiment with a particular imposed extension velocity. Each row represents a 5% increase in the applied kinematic extension, starting from 5%, and increasing until the experiment finishes. Each set of experiments is grouped by the gap distance, which is defined as how large the distance between the two rifted margins can get before surface processes are turned off.

Figure SF1

Mechanical evolution of all experiments. Colours are the same as defined in Figure 2 from the main text.

Margin gap to stop sedimentation: 2 km

Margin gap to stop sedimentation: 30 km

Margin gap to stop sedimentation: 60 km

Margin gap to stop sedimentation: 80 km
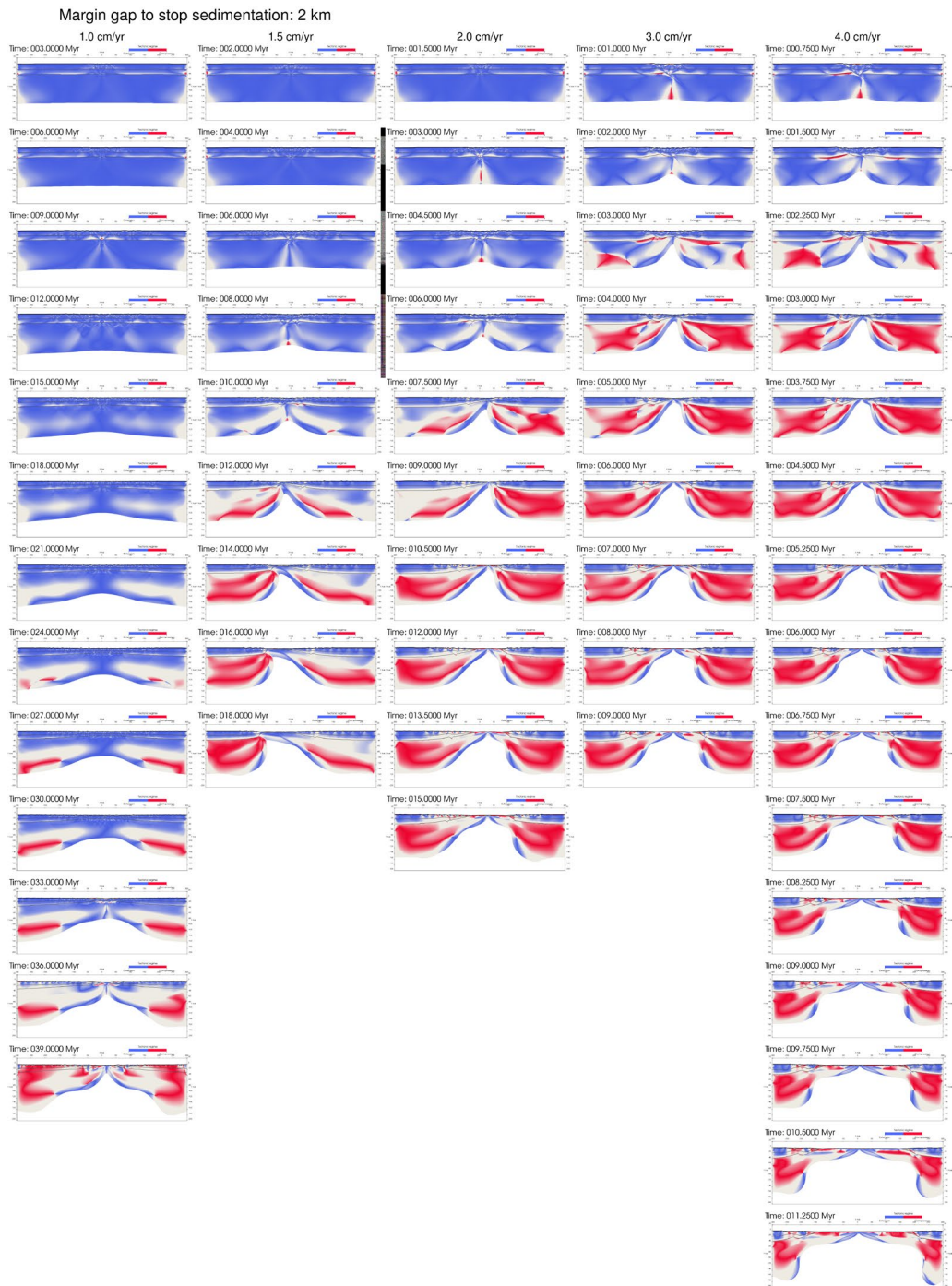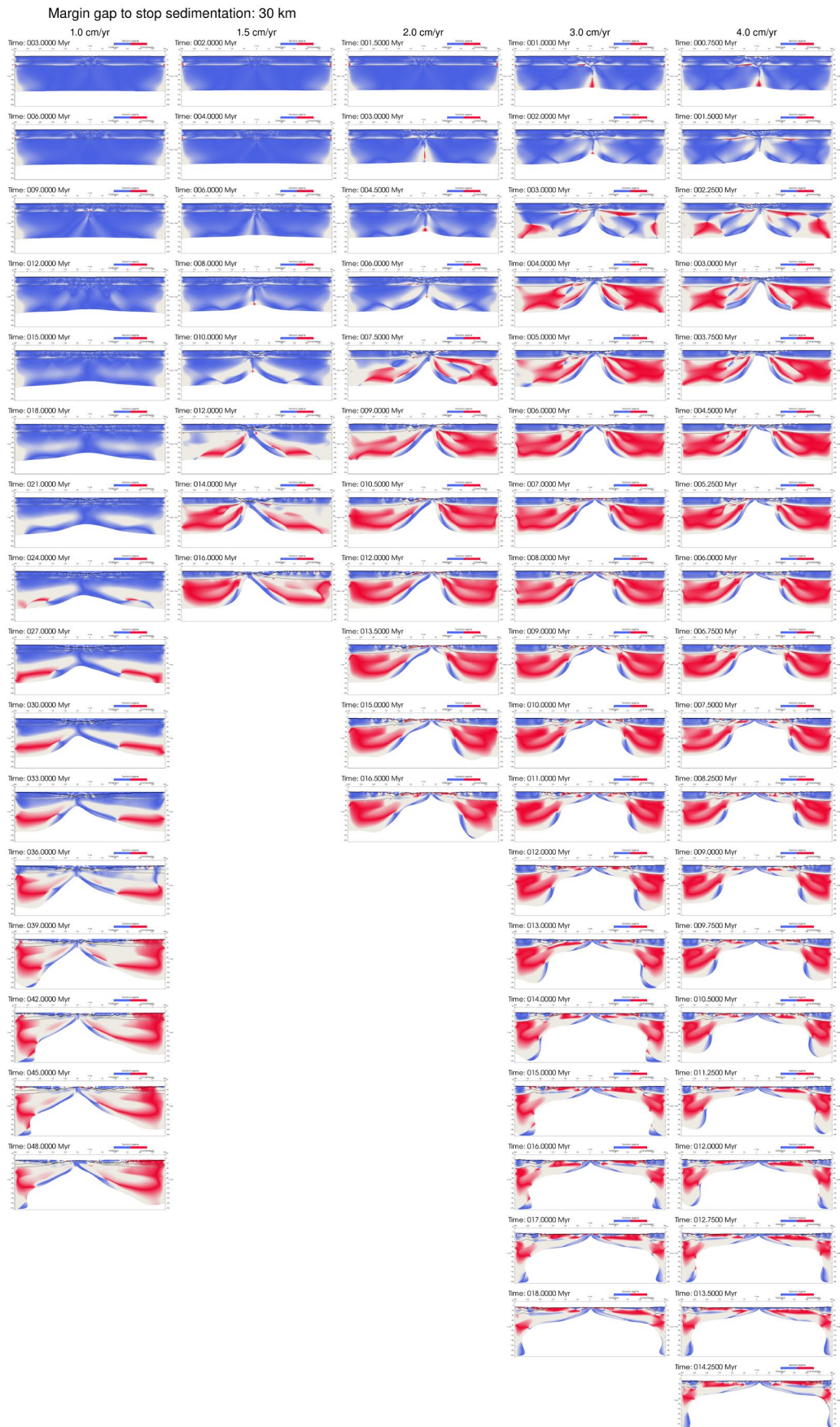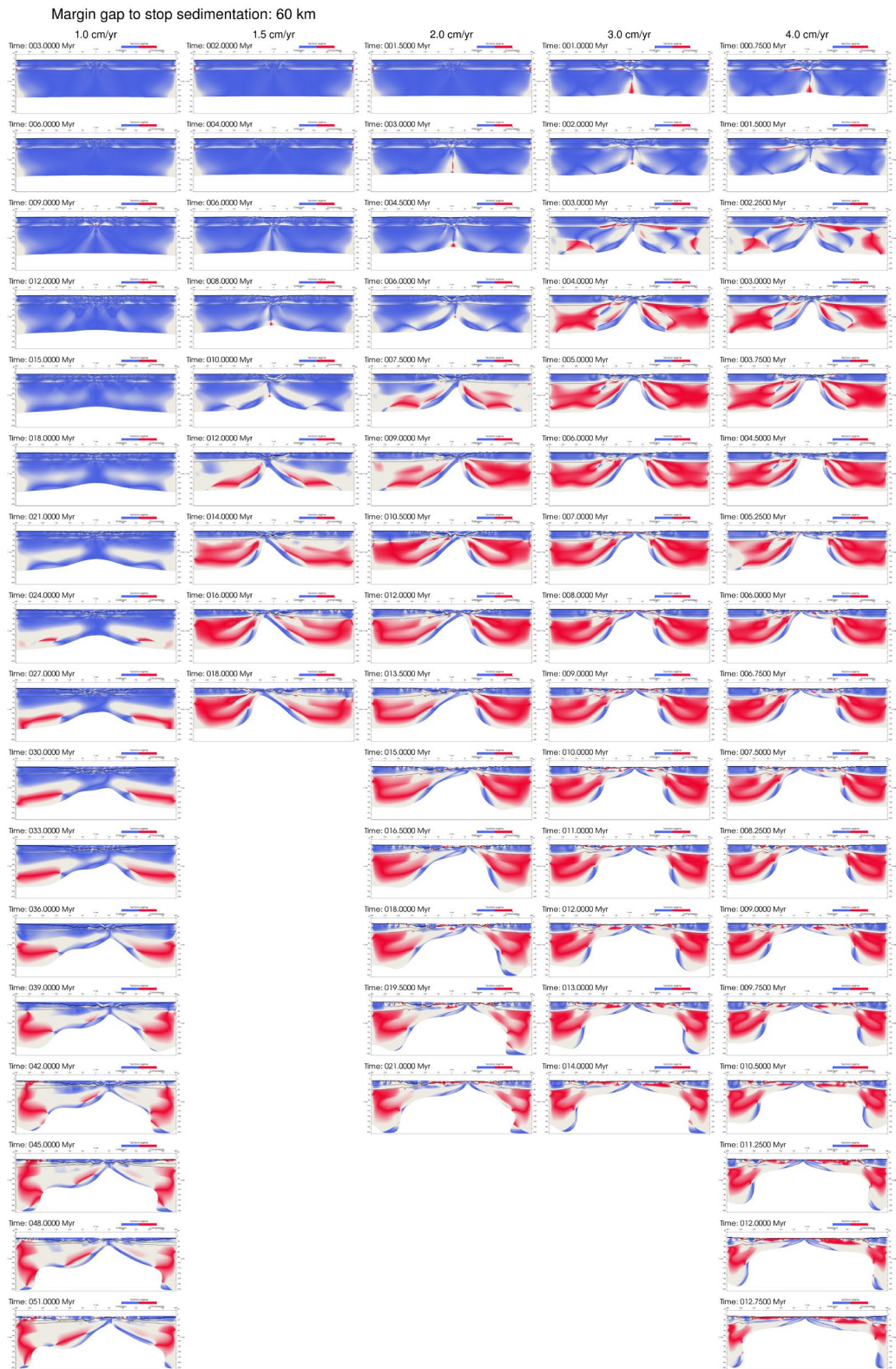
Margin gap to stop sedimentation: 100 km
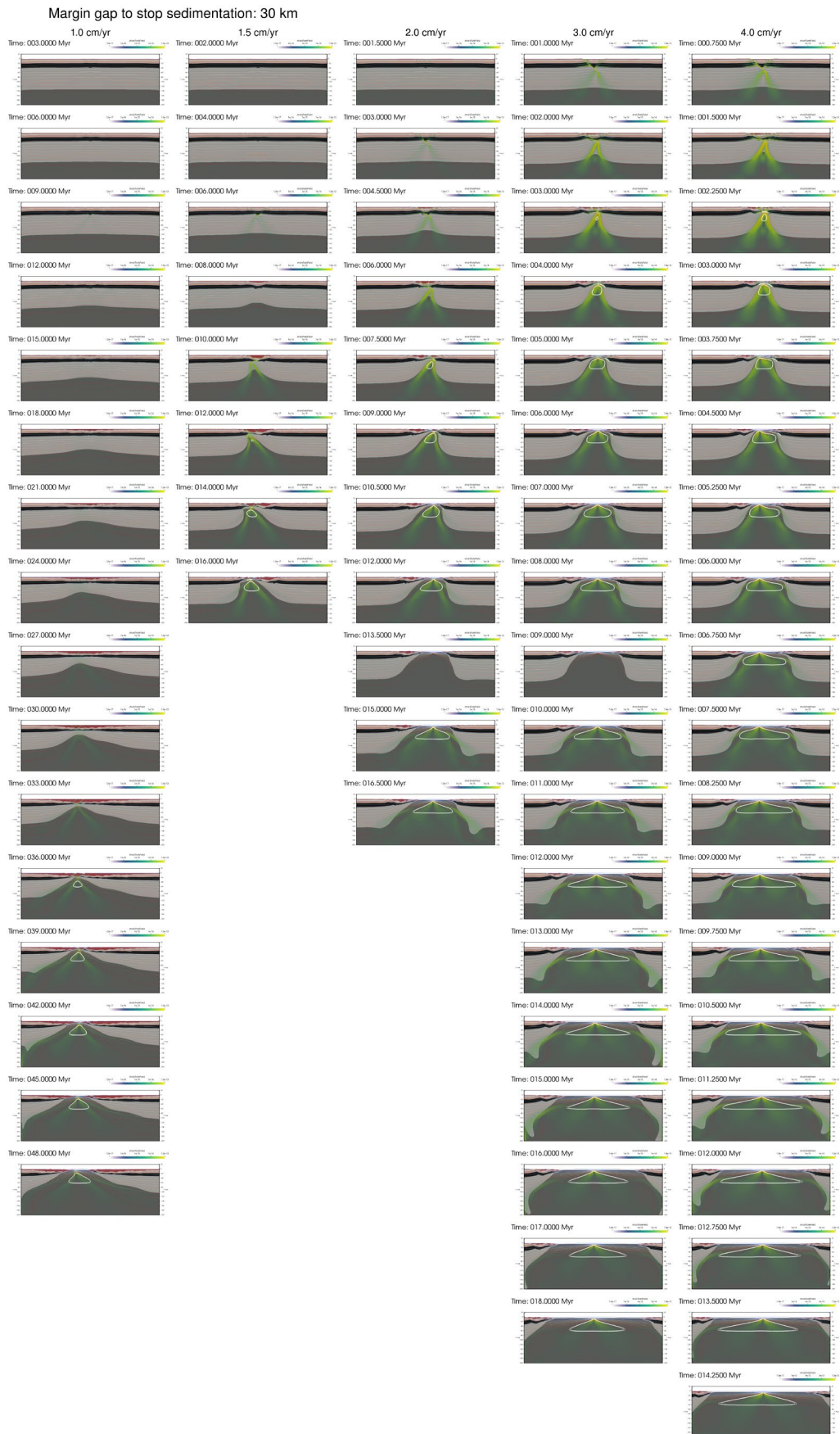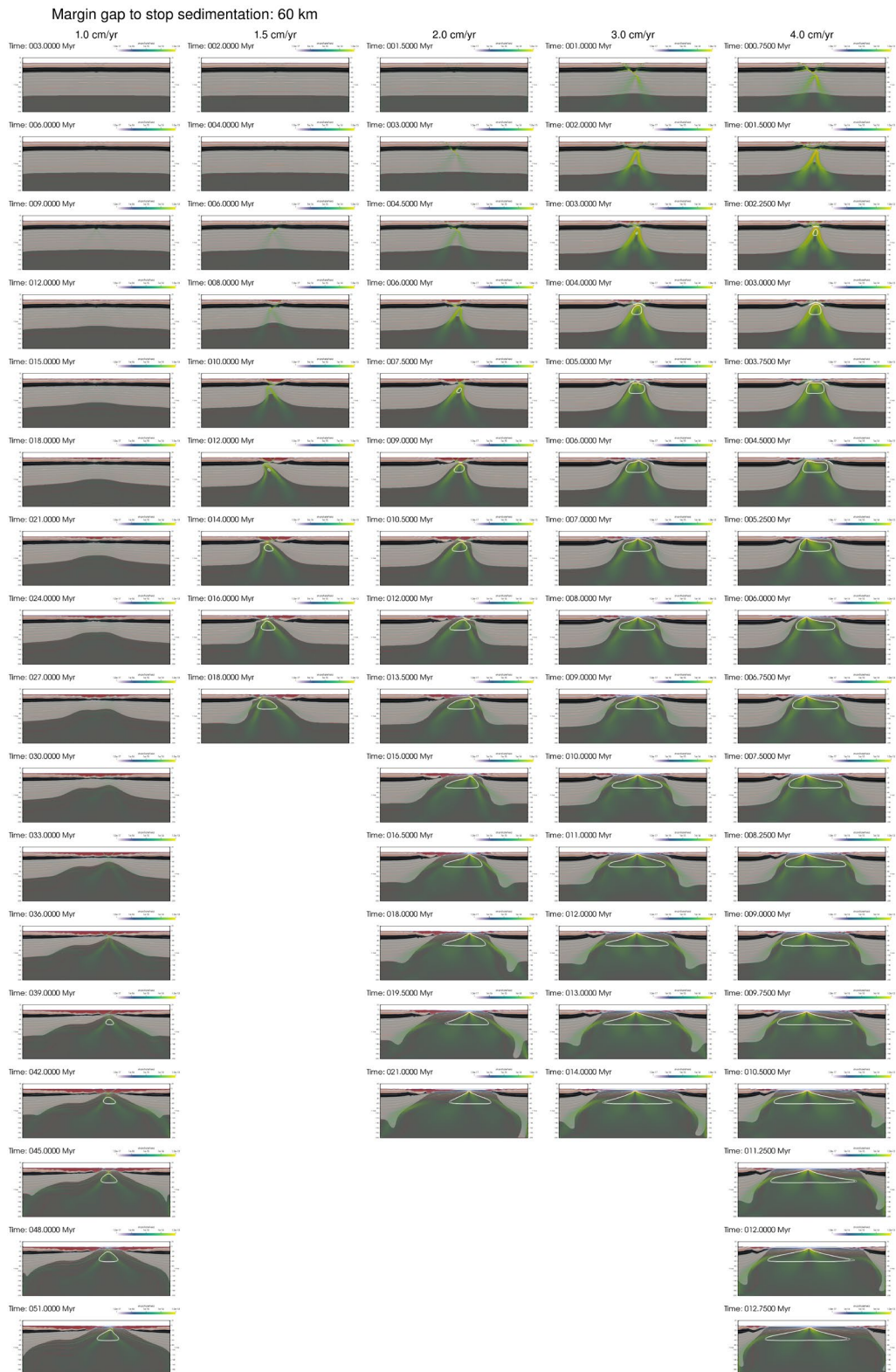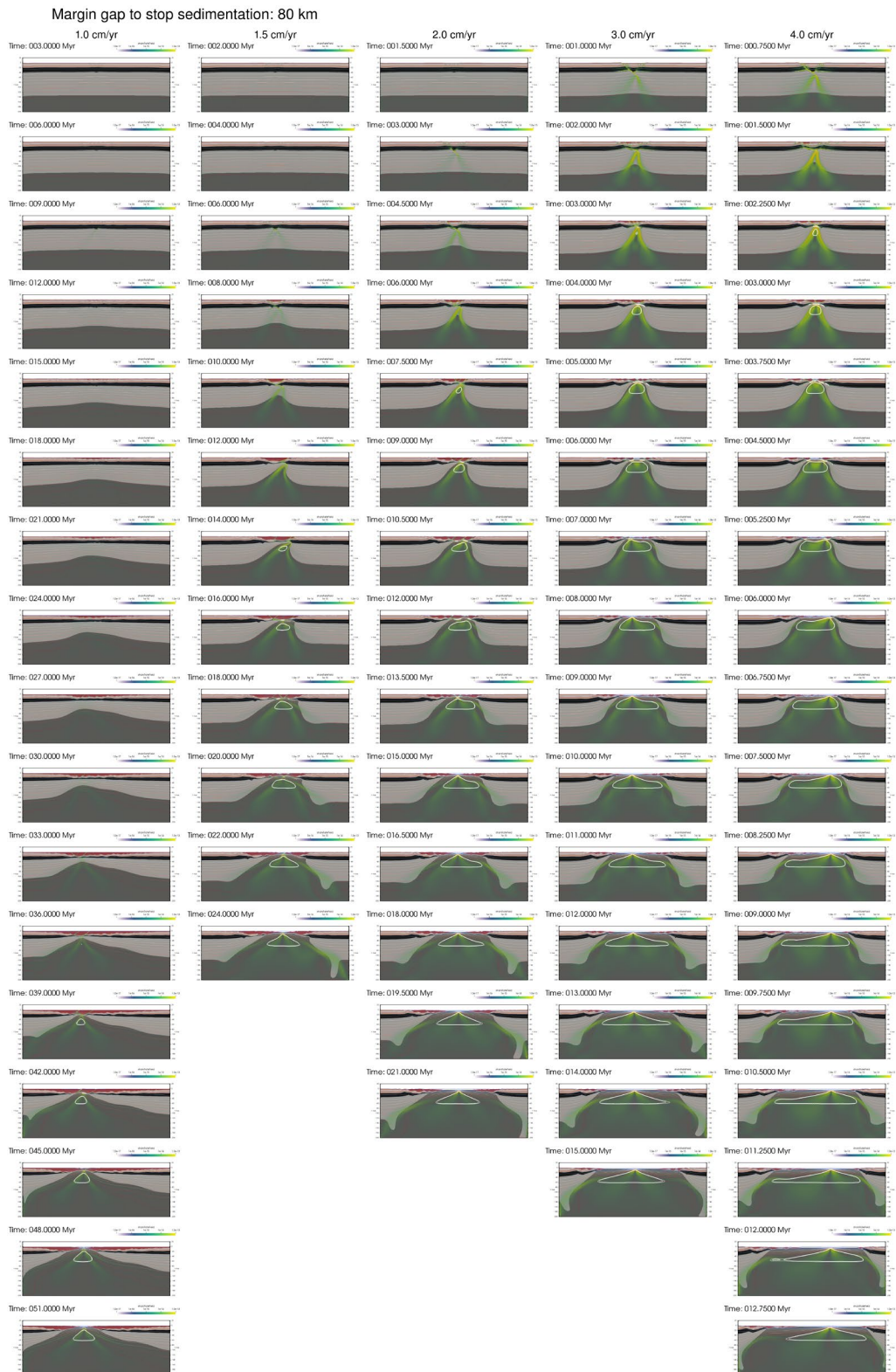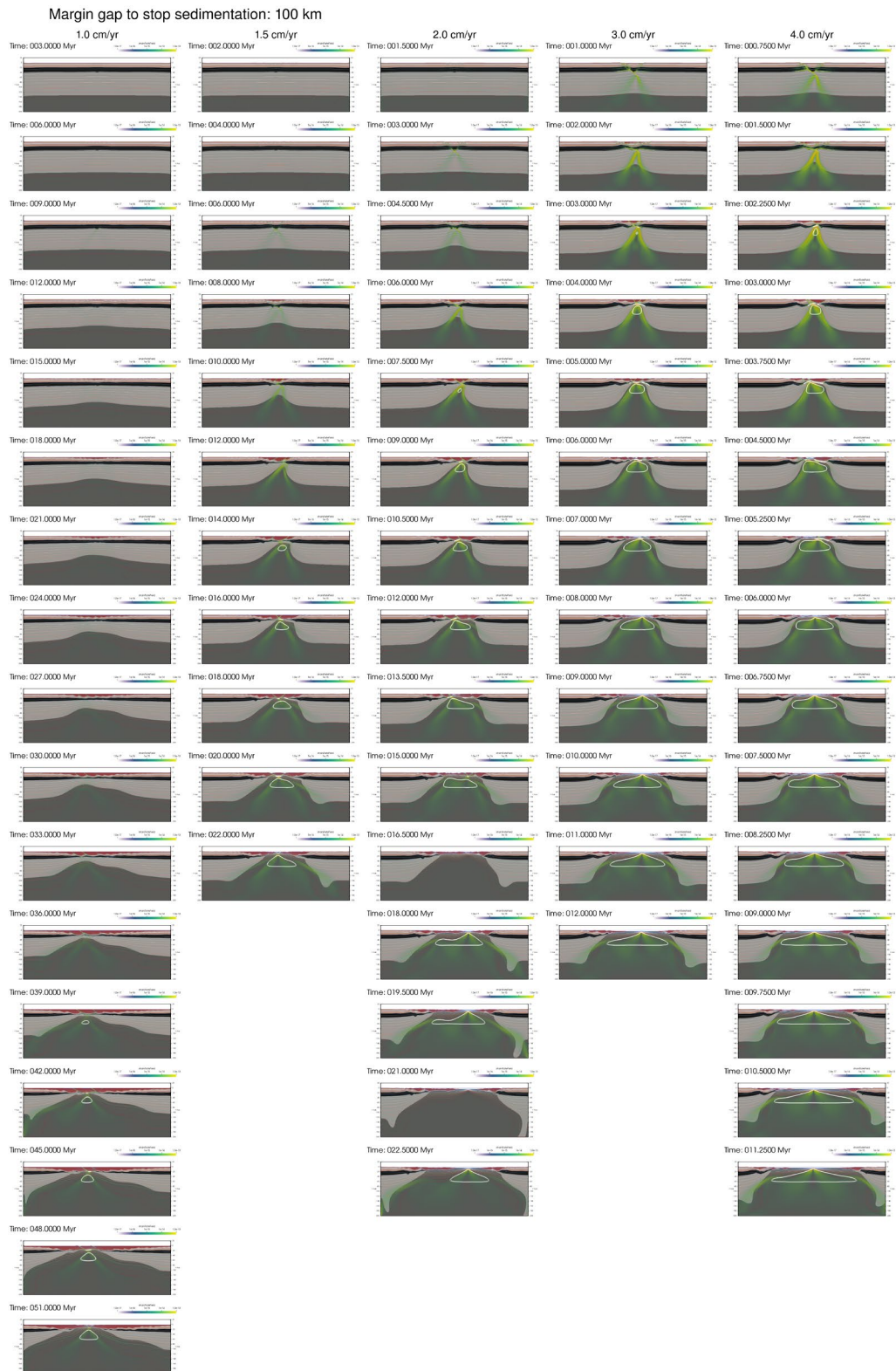
Figure SF2

Tectonic regime evolution of all experiments. Blue colours show regions in extension, red colours show regions in compression. Solid colours are where the plunge of the relevant principal stress is 90 degrees (vertical), which fades to white as the plunge reaches 60 degrees. Areas in white have no defined Andersonian stress.
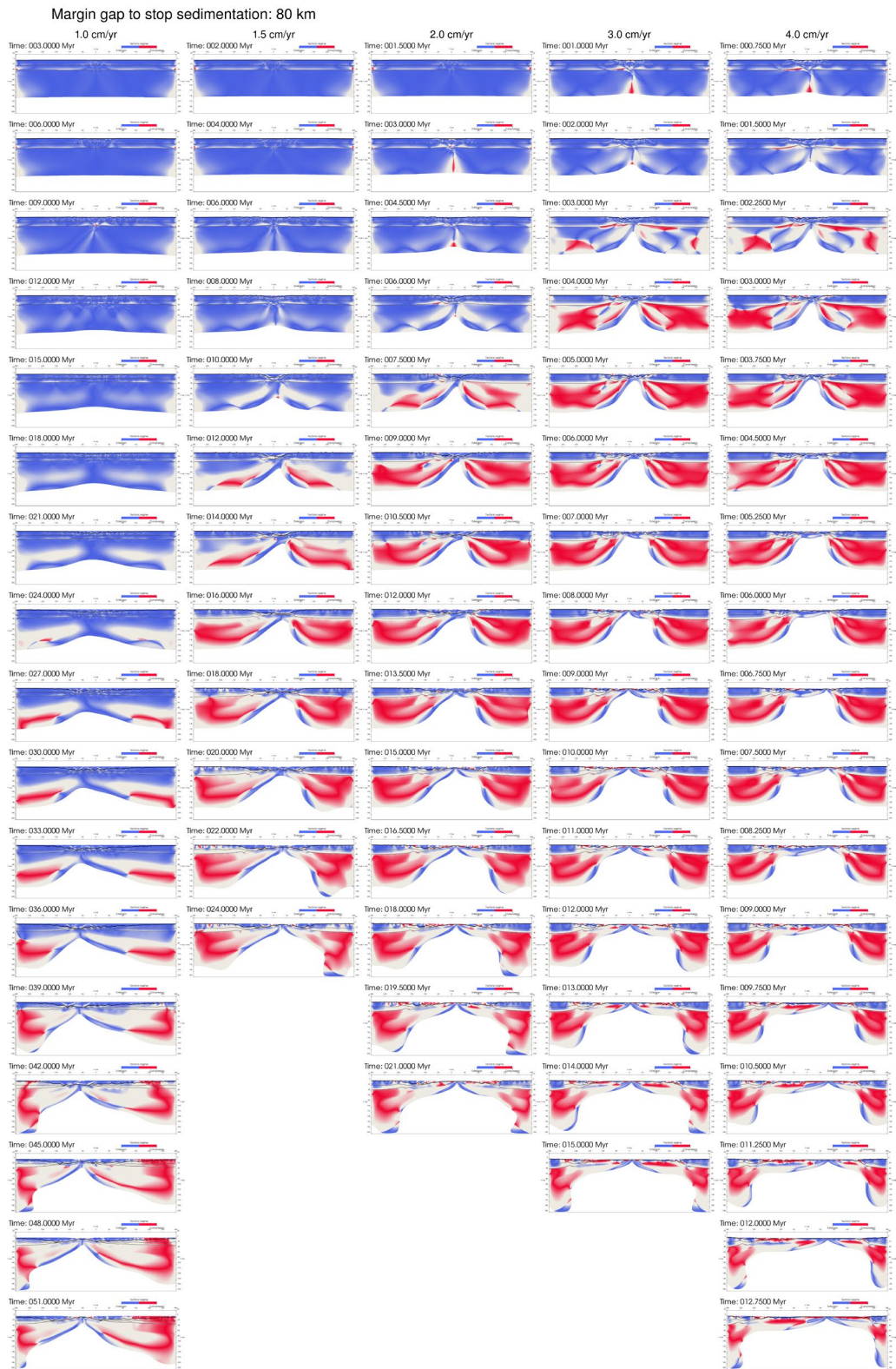
Margin gap to stop sedimentation: 2 km

Margin gap to stop sedimentation: 30 km

Margin gap to stop sedimentation: 60 km

Margin gap to stop sedimentation: 80 km
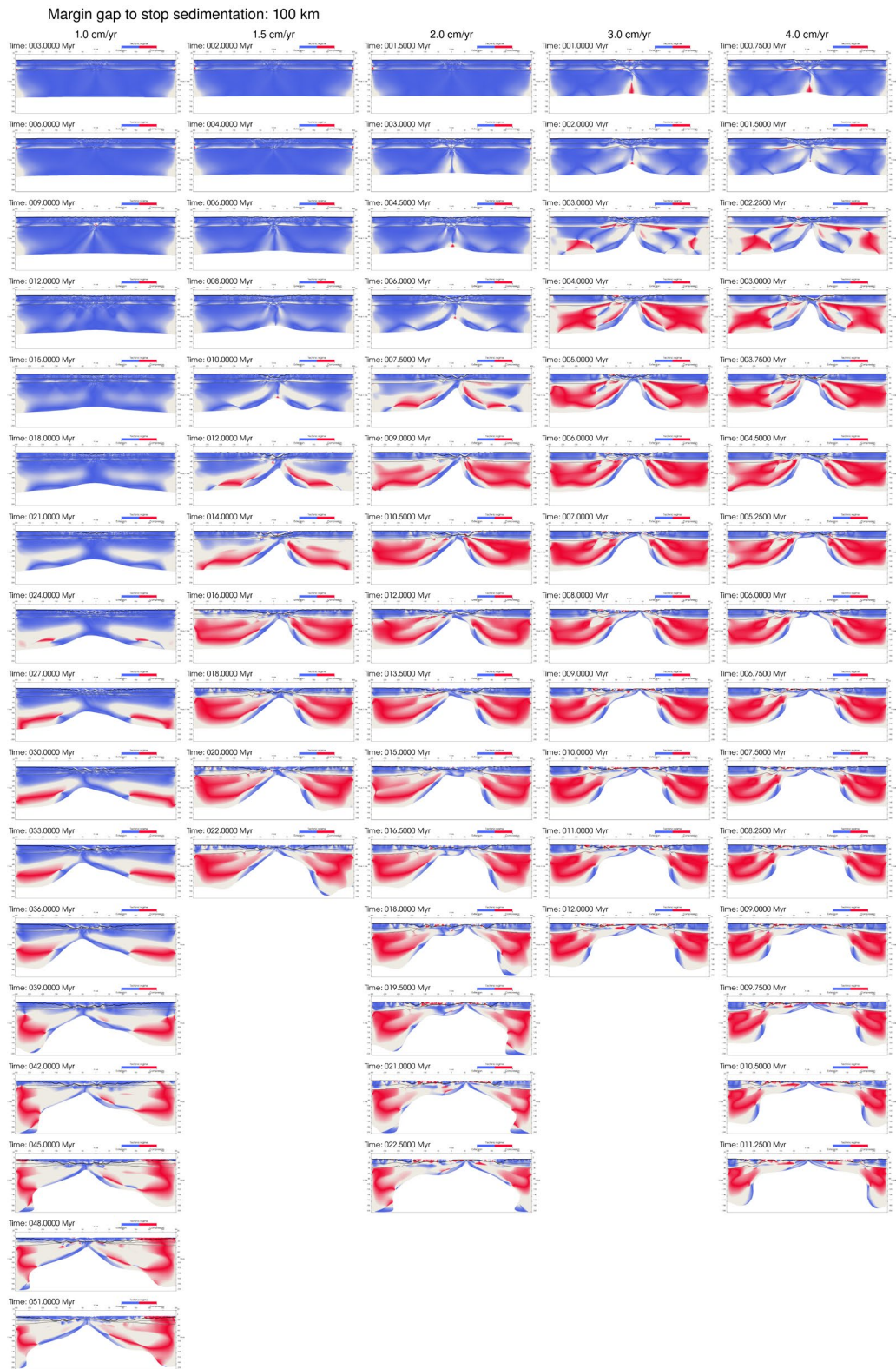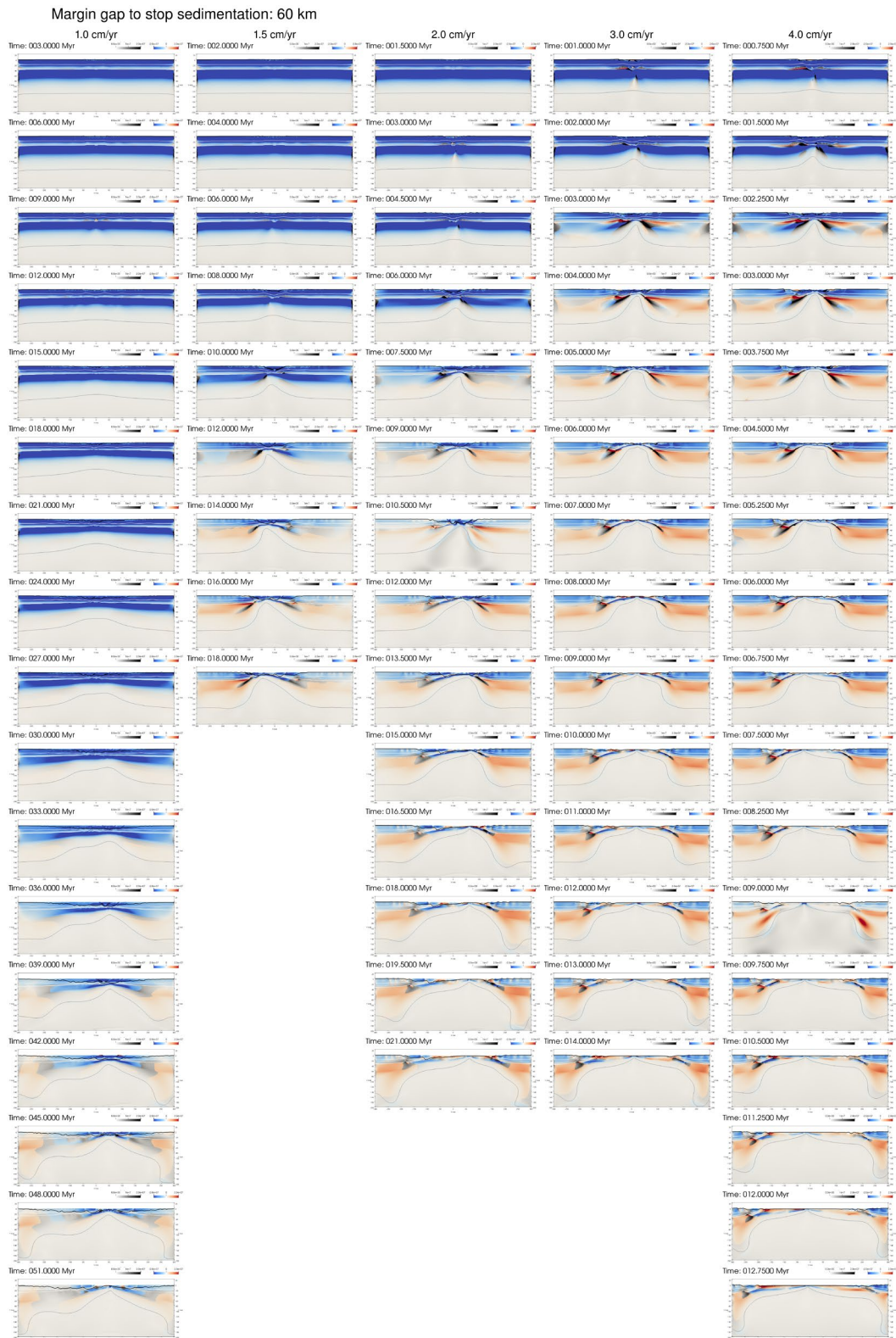
Margin gap to stop sedimentation: 100 km

Figure SF3

Tectonic regime mediated by deviatoric stress evolution of all experiments. Colours are defined in the same way as Figure 3 from the main text.
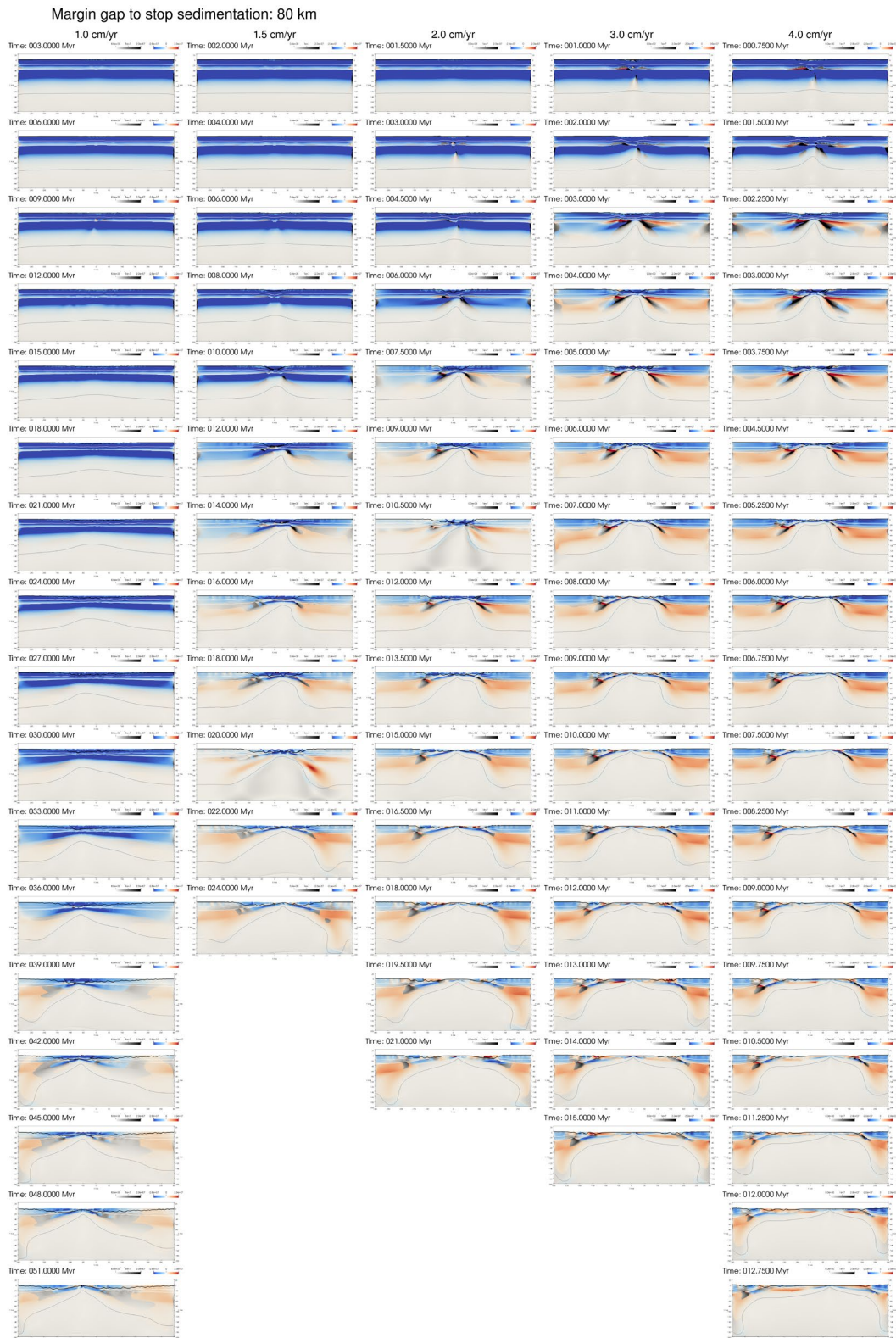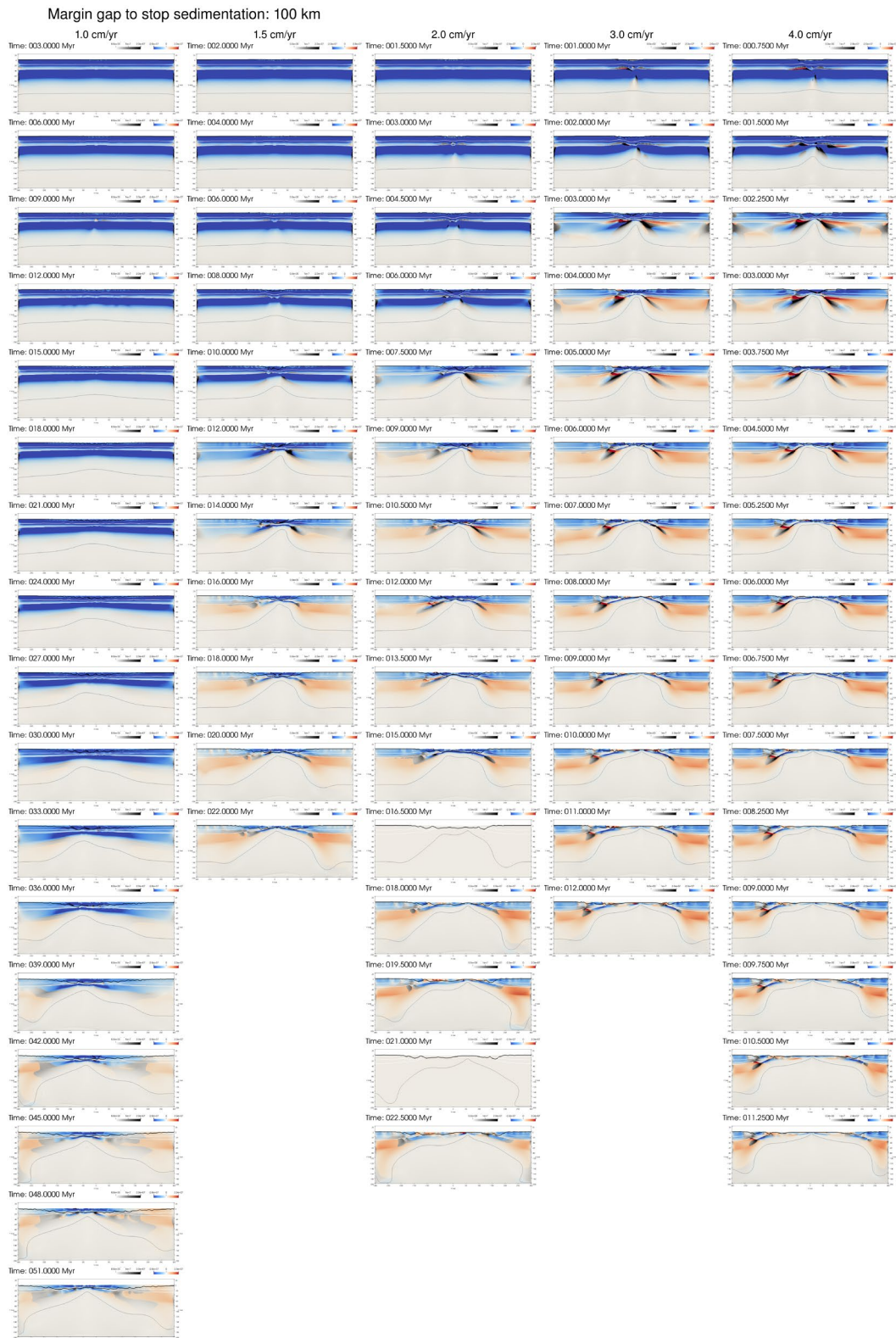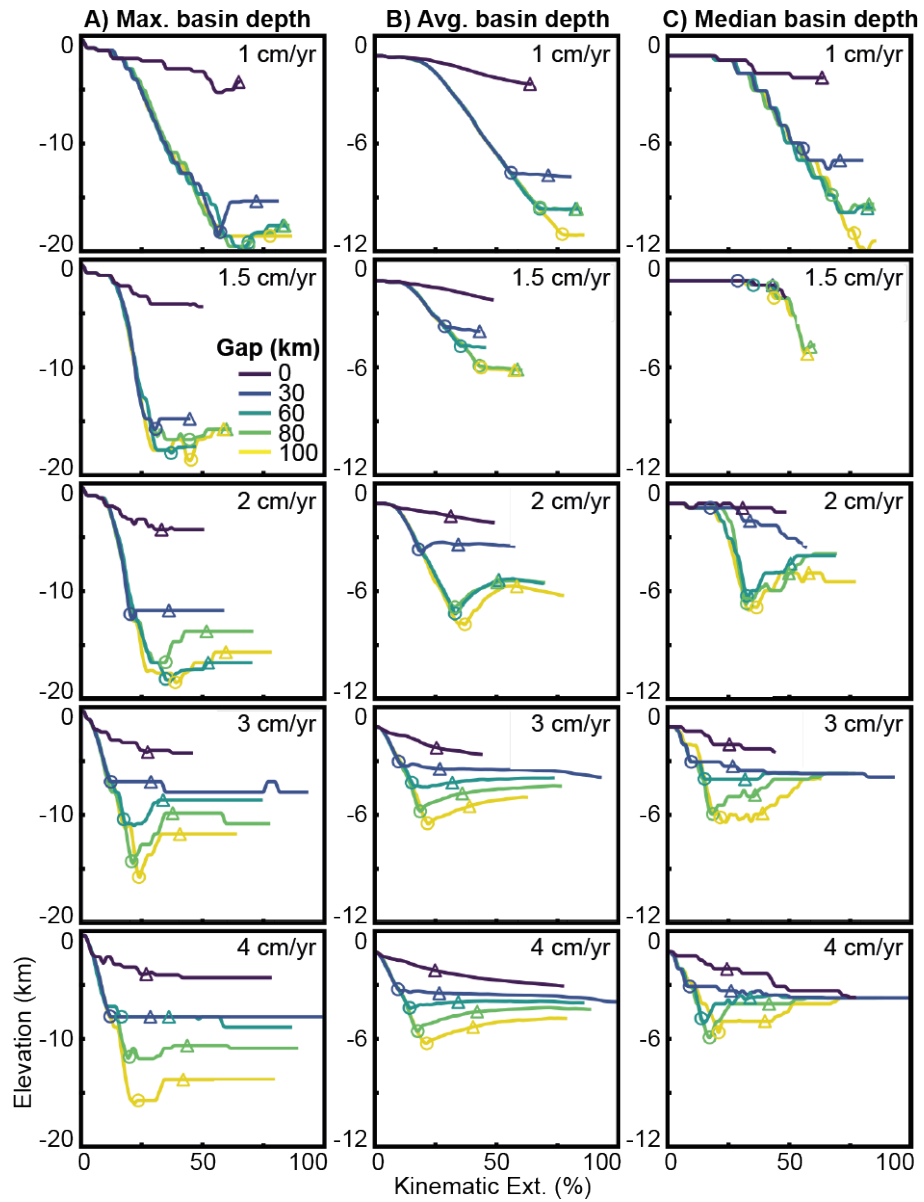
Margin gap to stop sedimentation: 2 km

Margin gap to stop sedimentation: 30 km

Margin gap to stop sedimentation: 60 km

Margin gap to stop sedimentation: 80 km

Margin gap to stop sedimentation: 100 km

Figure SF4

Statistics of basement depth through all experiments. Colours and symbols are the same as described in Figure 4 of the main text.

Figure SF5

Left: A simplified model of rifting in isostatic equilibrium, with three columns defined. **A** has unthinned crust (40 km thick) and lithosphere (140 km total thickness), **B** has crust and lithospheric thickness halved, and **C** has the crust and lithosphere completely thinned at a Mid Ocean Ridge (MOR). The crust is 2700 kg.m^{-3}, the lithosphere is 3330 kg.m^{-3}, and the asthenosphere is 3300 kg.m^{-3} to model thermal expansion. Column A is at 0 km depth, Column B is at 3.182 km depth, and Column C is at 6.363 km depth. There is no water in this calculation.

Right: shows the pressure difference between each column, based on colour, e.g., panel A has a green line, showing the pressure difference from column A to column B, and a blue line showing the difference from column A to column C. Grey areas show the summation of the pressure differences.

Even with a simple model, column B experiences a complex differential stress pattern through depth, as the pressure difference derives from both column A and C interact. Experiments shown in the main text with no sediments demonstrate a similar pattern (though more complex) in the transition from unthinned lithosphere to the MOR.
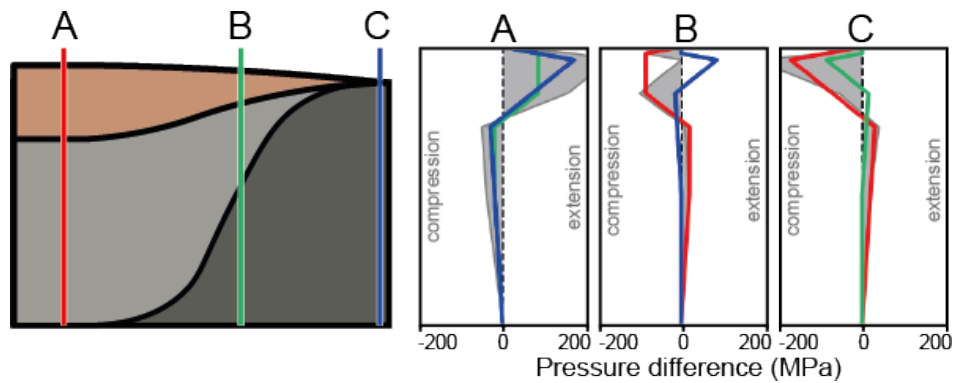
Table SM1

Parameter	Sediment	Upper Crust	Lower Crust	Mantle/Astheno
Reference density, ρ_r (kg m^{-3}) at 293.15 K	2700	2800	2900	3370
Thermal expansivity, α (K^{-1})	3e-5			
Heat capacity, C_p (J K^{-1} kg^{-1})	1000			
Thermal diffusivity, α (m^2 s^{-1})	1e-6			
Latent heat of fusion, L_f (kJ kg^{-1})	250			450
Radiogenic heat production, A (W m^{-3})	1.2e-6		0.6e-6	0.02e-6
Melt density change fraction, $M_{\Delta\rho_r}$	0			
Liquidus term 1, t_1 (K)	1493			2013
Liquidus term 2, t_2 (K Pa^{-1})	-1.2e-7			6.15e-8
Liquidus term 3, t_3 (K Pa^{-2})	1.6e-16			3.12e-18
Solidus term 1, t_1 (K)	993			1393.661
Solidus term 2, t_2 (K Pa^{-1})	-1.2e-7			1.32899e-7
Solidus term 3, t_3 (K Pa^{-2})	1.2e-16			-5.104e-18
Friction coefficient	0.55		0.577	0.577
Softened friction coefficient	0.055		0.2308	0.02308
Cohesion, C (MPa)	10		20	10
Softened cohesion, C (MPa)	2		0.8	0.4
Pre-exponential factor, A (MPa^{-n} s^{-1})	6.60693e-8		10e-2	1600
Stress exponent, n	3.1		3.2	3.5
Activation energy, E (kJ mol^{-1})	135		244	520
Activation volume, V (m^3 mol^{-1})	0		0	23e-6
Water fugacity	0		0	1000
Water fugacity exponent	0		0	1.2
Melt viscous softening factor	1e-3		1e-3	1e-1
Melt fraction range for viscous softening	0.15 - 0.3		0.15 - 0.3	0 - 0.02

REFERENCES

Crameri, F., Schmeling, H., Golabek, G., Duretz, T., Orendt, R., Buiter, S., May, D., Kaus, B., Gerya, T., and Tackley, P., 2012, A comparison of numerical surface topography calculations in geodynamic modelling: an evaluation of the 'sticky air' method: Geophysical Journal International, v. 189, no. 1, p. 38-54.

Demouchy, S., Tommasi, A., Ballaran, T. B., & Cordier, P., 2013, Low strength of Earth's uppermost mantle inferred from tri-axial deformation experiments on dry olivine crystals: Physics of the Earth and Planetary Interiors, v. 220, p. 37-49.

Hasterok, D., and Chapman, D., 2011, Heat production and geotherms for the continental lithosphere: Earth and Planetary Science Letters, v. 307, no. 1, p. 59-70.

Hirth, G. and Kohlstedt, D., 2003. Rheology of the upper mantle and the mantle wedge: A view from the experimentalists. Inside the subduction Factory, pp.83-105.

McKenzie, D. and Bickle, M.J., 1988. The volume and composition of melt generated by extension of the lithosphere. Journal of petrology, 29(3), pp.625-679.

Paterson, M., and Luan, F., 1990, Quartzite rheology under geological conditions: Geological Society, London, Special Publications, v. 54, no. 1, p. 299-307.

Rey, P., and Müller, R., 2010, Fragmentation of active continental plate margins owing to the buoyancy of the mantle wedge: Nature Geoscience, v. 3, no. 4, p. 257-261.

Van Wijk, J.W. and Blackman, D.K., 2005. Dynamics of continental rift propagation: the end-member modes. Earth and Planetary Science Letters, 229(3-4), pp.247-258.

Watremez, L., Burov, E., d'Acremont, E., Leroy, S., Huet, B., Pourhiet, L., and Bellahsen, N., 2013, Buoyancy and localizing properties of continental mantle lithosphere: Insights from thermomechanical models of the eastern Gulf of Aden: Geochemistry, Geophysics, Geosystems, v. 14, no. 8, p. 2800-2817.

Zhong, S., and Watts, A., 2013, Lithospheric deformation induced by loading of the Hawaiian Islands and its implications for mantle rheology: Journal of Geophysical Research: Solid Earth, v. 118, no. 11, p. 6025-6048.

Article 2

THE GEOLOGICAL SOCIETY
OF AMERICA®

The role of asthensopheric flow during rift propagation and breakup

Luke S. Mondy[1], Patrice F. Rey[1], Guillaume Duclaux[2]*, and Louis Moresi[3]
[1]Earthbyte Research Group, School of Geosciences, The University of Sydney, Sydney, NSW 2006, Australia
[2]Department of Earth Science, University of Bergen, 5020 Bergen, Norway
[3]School of Earth Sciences, Melbourne University, Victoria 3010, Australia

ABSTRACT

Continental rifting precedes the breakup of continents, leading to the formation of passive margins and oceanic lithosphere. Although rifting dynamics is classically described in terms of either active rifting caused by active mantle upwelling, or passive rifting caused by far-field extensional stresses, it was proposed that a transition from passive to active rifting can result from changes in buoyancy forces due to localized thinning of the lithosphere. Three-dimensional numerical experiments of rifting near an Euler pole allow the quantification of these buoyancy forces and show that gravitational stresses are strong enough not only to sustain rifting and drive axis-parallel motion in the asthenosphere dome, but also to promote along-axis asthenospheric flow and to drive the propagation of the rift tip toward its rotation pole. We show that gradients of gravitational potential energy due to the presence of the dome of asthenosphere induce time-dependent phases of compressional and transcurrent stress regimes, despite an overall divergent plate setting. Our experiments predict overdeepened bathymetry at the tip of the propagating rift, as well as the variability of focal mechanisms of shallow seismic events similar to those observed in such a setting. We also explain the episodes of basin inversion documented in many rifted continental margins.

INTRODUCTION

For many years, the dynamics of rifting was described in terms of active rifting caused by active mantle upwelling, or passive rifting caused by far-field extensional stresses, in which case the asthenosphere rises passively to accommodate the thinning of the lithosphere (Sengör and Burke, 1978; Turcotte and Emerman, 1983). It was subsequently proposed that buoyancy forces due to localized thinning of the lithosphere could sustain continued rift development following an episode of passive rifting (Huismans et al., 2001), or an episode of convective thinning of a thickened lithosphere (Rey, 2001).

The style of continental rifting, including strain and fault patterns (Buck, 1991; Manatschal, 2004), subsidence or uplift patterns (Mulugeta and Ghebreab, 2001), and magmatism (Pérez-Gussinyé et al., 2006), is strongly controlled by rheological layering of the lithosphere (Bassi et al., 1993) and the velocity of extension and its direction with respect to the rift axis (Brune et al., 2014). It also depends on the active and dynamic involvement of the convective mantle underneath the rift axis (Turcotte and Emerman, 1983; Huismans and Beaumont, 2008; Koptev et al., 2017).

Rifting near an Euler pole is therefore of particular interest because the divergent velocity between the two conjugate margins increases rapidly as the cosine of the angular distance from

the pole (Morgan, 1968; Lundin et al., 2014), and because the asthenospheric dome that raises diachronously along the rift axis results in an evolving dynamic balance between far-field stresses and local buoyancy. Extension near an Euler pole offers a simple three-dimensional (3-D) setting to explore the relative importance of this dynamic interaction, in driving both spatiotemporal stress-strain partitioning within the lithosphere and rift propagation.

Modeling provides a way to explore the evolving kinematics and dynamics of complex 3-D thermomechanical continental rifting systems. Analytical and physical modeling has investigated the implications of rifting close to an Euler

pole on the kinematics of rifting, rift propagation, crustal thinning, and melt production (Molnar et al., 2017). To capture rift dynamics, recent 3-D numerical studies have explored orthogonal rifting (Liao and Gerya, 2015), oblique rifting (Brune and Autin, 2013), rift linkage (Allken et al., 2012), segmented rift opening (Koopmann et al., 2014), and exhumation processes (Ellis et al., 2011). However, no studies have focused on the dynamics of rotational opening near an Euler pole, though it is the best setting to explore and understand the along-strike interaction between passive to active rifting processes.

NUMERICAL EXPERIMENTS AND RESULTS

We compare an experiment of rotational rifting with an experiment of orthogonal rifting, using 3-D Cartesian thermomechanical modeling with temperature- and strain-rate–dependent viscous and frictional-plastic rheologies involving strain weakening (see Fig. 1; see also the supplemental methods in the GSA Data Repository[1]). We identify the stress regime by determining which of the principal stress axes is closest to vertical.

---

[1]GSA Data Repository item 2018022, the methods used in this work, and additional supporting results, is available online at http://www.geosociety.org/datarepository/2018/ or on request from editing@geosociety.org.
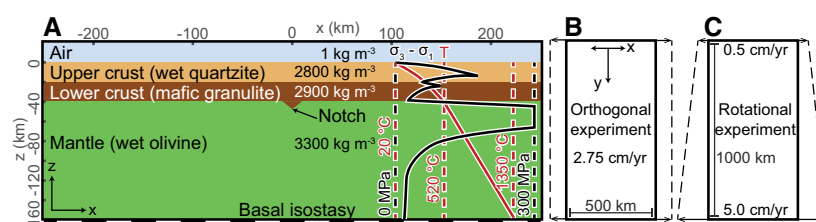
Figure 1. A: Vertical cross section showing initial rheological conditions of experiments; the rheological profile $\sigma_3-\sigma_1$ is shown in black, and the geotherm in red. B: Map view of the boundary conditions of orthogonal experiment. Constant total divergent velocity of 2.75 cm yr^{-1} is imposed on left and right walls, with free slip conditions applied on all other boundaries. C: Boundary conditions of rotational experiment. To approximate extension close to pole of rotation, constant kinematic boundary condition is imposed such that material along left and right walls move apart perpendicular to walls at velocity increasing linearly along rift axis—with total velocity from 0.5 cm yr^{-1} at $y = 0$ km ("slow end") to 5 cm yr^{-1} at $y = 1000$ km ("fast end"). This a rotation of 2.6° m.y.$^{-1}$ about Euler pole located at $x = 0$ km, $y = -111$ km (outside experiment domain).

The orthogonal experiment shows that strain and strain-rate histories evolve through successive and distinct phases (Figs. 2A–2D) (Lavier and Manatschal, 2006), with no segmentation or partitioning along the rift axis. Similarly, the stress regimes follow a time-dependent pattern. Asthenospheric flow is dominated by vertical flow into the rift axis, with some material sourced from beneath the flanks of the margins (Fig. DR2 [A1 and A2]). There is no net flow parallel to the rift axis.

In contrast to orthogonal extension, the rotational experiment shows strong strain and strain-rate partitioning along the rift axis (Figs. 2E–2H), similar to analogue modeling (Molnar et al., 2017). The phases, as defined for the orthogonal experiment, appear in succession at the fast-opening end of the experiment and migrate along the rift axis toward the Euler pole. The strain history (i.e., the appearance of the successive phases) at different locations along the rift axis is therefore diachronous. The stress evolution also shows time- and space-dependent partitioning (Figs. 2E–2H). Extensional stresses largely dominate at the early stages (Fig. 2E). As extension

proceeds, regions of transcurrent stress become prominent along the rift axis, delimiting a region where the axial graben is under compression (Fig. 2F). As continental breakup occurs along the rift axis, the surrounding regions return to a dominantly extensional stress regime, though a small region of transcurrent stress persists in front of the rift-propagating tip (Fig. 2G). At the fast-opening end of the rift, two narrow bands where compression dominates develop on both sides of the rift and within a region dominated by transcurrent stress directly adjacent to the central graben (Fig. 2H). A wave of transcurrent and compressional stress regimes (Figs. 2F–2H$_1$) and a narrow topographic deep (Fig. 2H$_2$; Fig. DR1) moves ahead of the tip of the propagating rift.

Figure 3A illustrates the rift-parallel asthenospheric flow pattern during rifting. While the total flow is dominated by upward motion, the magnitude of the rift-parallel velocity component—which is almost entirely absent in the orthogonal experiment—reaches up to a third of the magnitude of the far-field velocity. At the beginning of the experiment, the rift-parallel component of asthenospheric flow is directed

toward the fast end, feeding material to the rapidly thinning lithosphere (Fig. 3A). As extension and thinning continues, the flow reverses direction, and the asthenosphere flows toward the slow end. The peak velocity of the axial counterflow follows the tip of the propagating rift as it migrates along the margin, and its magnitude increases through time (see Fig. DR1).

SIGNIFICANCE OF STRESS REGIME CHANGES

The experiments document significant differences between rotational and orthogonal extension, most notably the large regions of transcurrent stress regime in the rotational experiment, which are absent in the orthogonal experiment. The primary driver of this large-scale change in stress regime can be attributed to the exhumation of the asthenosphere into a dome. This dome induces gradients of gravitational potential energy (GPE) by juxtaposing denser asthenospheric material in the rift center against relatively unthinned crustal material within the margins (Figs. 3B and 3C) (Turcotte and Emerman, 1983; Buck, 1991; Huismans et al., 2001; Rey, 2001; Davis and Kusznir, 2002). As the asthenospheric dome increases in size, the corresponding GPE high (see Figs. DR3 and DR6) progressively interferes with the driving plate boundary forces that emerge from our imposed kinematic boundary conditions. In the orthogonal experiment, exhumation of the asthenosphere is synchronous along the rift, and therefore induces GPE gradients perpendicular to its axis. When the gravitational force exceeds that imposed by the kinematic boundary conditions, the stress switches to a compressional regime within the lithospheric mantle (see Fig. DR2). In contrast, the rotational experiment shows GPE gradients in all directions away from the asthenospheric high, including in the direction of the rift axis. This leads to stress components acting both parallel and perpendicular to the rift axis, forcing the maximum stress axis σ_1 and the minimum stress axis σ_3 to be sub-horizontal, and thus explaining why rift-bounding faults transition progressively from extensional regime to transcurrent as shown in Figures 2F–2H. The asthenospheric doming also controls the along-axis component of counterflow (Fig. 3A), with the early lithospheric thinning inducing a suction force at the fast end of the domain (Van Wijk and Blackman, 2005; Koopmann et al., 2014), which is then reversed by the gravitational collapse down-axis of the uplifted asthenospheric dome. The magnitude of the along-axis component of counterflow is only weakly dependent on the magnitude of the imposed boundary velocities (see Fig. DR4), suggesting that this flow is driven by gravitational force. To quantify the gravitational stress induced by the differential uplift of the asthenosphere along the rift axis, the driving velocity boundary conditions were
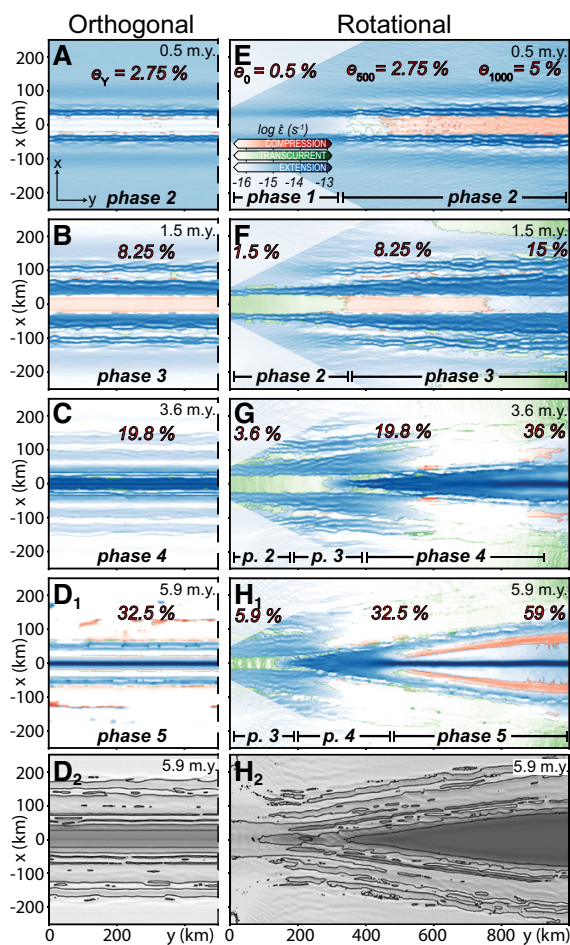
Figure 2. Evolution of orthogonal (A–D) and rotational (E–H) experiments. Strain-rate patterns show five consecutive phases highlighting changing stress regimes during rift propagation: phase 1—distributed faulting; phase 2—formation of rift-border faults and axial graben; phase 3—distributed faulting dies off, and second set of rift bounding normal faults initiates; phase 4—strain focuses on rift axis and detachment of two continental blocks; phase 5—oceanic spreading with strong strain localization at mid-ocean ridge. Extensional, transcurrent, and compressional stress regimes are mapped in blue, green, and red, respectively. Color saturation is a function of strain rate ($\dot{\varepsilon}$). Red percentages represent total extension at different locations along the y axis. e_y is extension in the x-direction for all y; e_0, e_{500}, and e_{1000} are extension in the x-direction at y = 0, 500, and 1000 km, respectively. D_2 and H_2 show shaded-relief surface elevation contoured at 1000 m intervals at end of experiments.

Figure 3. Gravitational deviatoric stress and velocity field for rotational model. A: Evolution of flow component parallel to rift axis (V_y). Flow is measured at base of lithosphere, along rift axis at 3.6 m.y., shortly after velocity boundary conditions were reduced to 0 cm yr^{-1}. Two profiles at 3.6 m.y. show magnitude of V_y before and after velocity conditions were removed. B,C: Transversal (B) and longitudinal (C) cross sections. Gravitational potential energy (GPE) is calculated at gray columns.
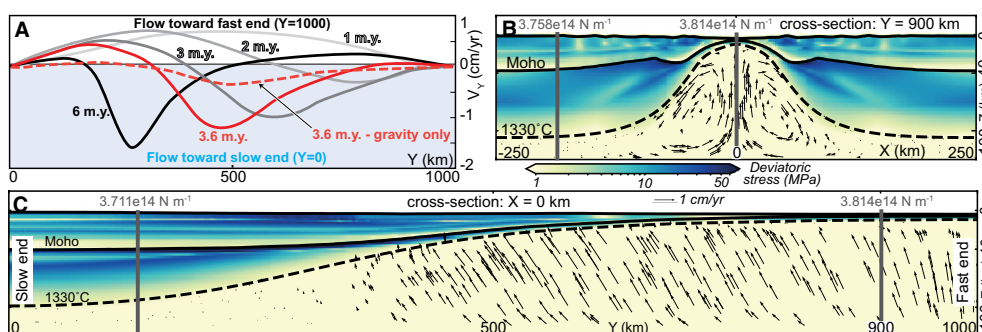
switched off (velocity set to 0 cm yr^{-1}) after 3.6 m.y. (Figs. 3B and 3C). Ahead of the propagating rift tip, the magnitude of the gravitational stress exceeds 110 MPa, and reaches 60 MPa in the rift flanks. This experiment reveals that the gravitational stress associated with the asthenospheric doming is large enough to drive rift-parallel flow and continental breakup.

FIELD EXAMPLES

The asthenospheric doming described here plays an active role in the evolution of rifting. This dome explains why the rifted margins in both the orthogonal and rotational experiments experience at least some transient periods of compression and/or transcurrent stress. Small, transient periods of basin inversions that correlate temporally with breakup have been documented on seaward-dipping reflectors along the eastern margins of North America (Withjack et al., 1998; Schlische et al., 2003). More generally, minor transient basin inversions structurally confined to sub-basins are very common and have been documented in many margins (Cloetingh et al., 2008; Holford et al., 2014). We join others to propose that the asthenospheric doming is the source of gravitational stresses responsible for small episodes of basin inversions (Withjack et al., 1998), but without necessarily invoking a mantle plume (Lundin and Doré, 2002).

Examples of rifting close to an Euler pole include the Woodlark Basin in Papua New Guinea, propagating westward into the Papuan Peninsula (Fig. 4A) (Taylor et al., 1995), and the Galapagos Rise propagating westward toward the East Pacific Rise and into 1 Ma oceanic crust (Fig. 4B) (Floyd et al., 2002). Each show characteristic V-shaped ridges, troughs, and scarps, with a trough preceding the tip of the propagating rift, where stress increase favors the activation of normal faults as well as strike-slip faults (Taylor et al., 1995; Floyd et al., 2002). The evolution of the above examples is affected by various local complications, including the proximity of the New Britain Trench and the proximity of the East Pacific Rise, respectively.

Bearing in mind these local complexities, we note some remarkable similarity between the spatial patterns that develop in the rotational experiment (Figs. 2F–2H) and these natural examples (in particular, matching earthquake focal mechanisms from the Woodlark Basin in Papua New Guinea; Fig. 4A; Taylor et al., 1995). Furthermore, the Galapagos spreading ridge shows both shallow zones of transcurrent and compressional tectonic regimes, as well as a topographic deep—the Hess Deep—ahead of the propagating tip (Fig. 4B) (Floyd et al., 2002).

CONCLUSIONS

On a sphere, where rigid plates rotate around fixed Euler poles, velocity gradients develop
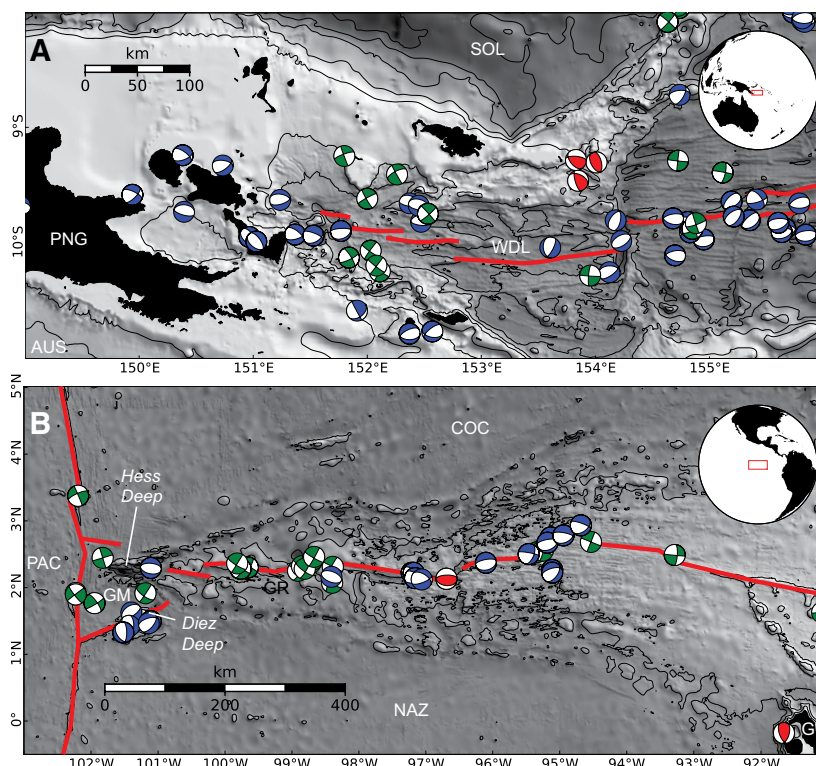
Figure 4. Natural examples of rifting near Euler pole. A: Woodlark Basin, Papua New Guinea; Euler pole ~500 km away from rift tip. B: Galapagos Rise; Euler pole ~1500 km away from rift tip. Shaded-relief bathymetric data are from General Bathymetric Chart of the Oceans (GEBCO) 30 arc-second grid (version 20150318; https://www.gebco.net), contoured at 1000 m intervals. Focal mechanisms for earthquakes with Mw > 5.0 are from Global Centroid Moment Tensor (CMT) Catalog (http://www.globalcmt.org/CMTsearch.html); thrust faults in red, strike-slip faults in green, and normal faults in blue. PNG—Papua New Guinea; AUS—Australian plate; SOL—Solomon plate; WDL—Woodlark Basin; PAC—Pacific plate; COC—Cocos plate; NAZ—Nazca plate; GM—Galapagos microplate; G—Galapagos archipelago; GR—Galapagos Rise.

along divergent plate boundaries, and as such, the structure along passive margins must vary too. Our 3-D numerical experiments document this evolution while also revealing regional, time-dependent stress changes in the lithosphere in response to differential exhumation (i.e., doming) of the asthenosphere. The associated 3-D gradients of GPE are sufficient to place significant compressional gravitational stresses on the adjacent continental margins, changing the stress regime from extensional to transcurrent or compressional, as well as driving rift propagation toward the Euler pole. Our models show that in a passive rifting setting, the asthenosphere has an active role in driving lateral propagation of the breakup front, thus calling for a revision of the classical active rift versus passive rift dichotomy. Gravitational stresses in response to asthenospheric doming can explain transient, low-magnitude basin inversions documented in many continental margins.

REFERENCES CITED
Allken, V., Huismans, R.S., and Thieulot, C., 2012, Factors controlling the mode of rift interaction in brittle-ductile coupled systems: A 3D numerical study: Geochemistry Geophysics Geosystems, v. 13, Q05010, https://doi.org/10.1029/2012GC004077.
Bassi, G., Keen, C.E., and Potter, P., 1993, Contrasting styles of rifting: Models and examples from the eastern Canadian margin: Tectonics, v. 12, p. 639–655, https://doi.org/10.1029/93TC00197.
Brune, S., and Autin, J., 2013, The rift to break-up evolution of the Gulf of Aden: Insights from 3D numerical lithospheric-scale modelling: Tectonophysics, v. 607, p. 65–79, https://doi.org/10.1016/j.tecto.2013.06.029.
Brune, S., Heine, C., Pérez-Gussinyé, M., and Sobolev, S.V., 2014, Rift migration explains continental margin asymmetry and crustal hyper-extension: Nature Communications, v. 5, 4014, https://doi.org/10.1038/ncomms5014.
Buck, W.R., 1991, Modes of continental lithospheric extension: Journal of Geophysical Research, v. 96, p. 20,161–20,178, https://doi.org/10.1029/91JB01485.
Cloetingh, S., Beekman, F., Ziegler, P.A., van Wees, J.-D., and Sokoutis, D., 2008, Post-rift compressional reactivation potential of passive margins and extensional basins, *in* Johnson, H., et al., eds., The Nature and Origin of Compression in Passive Margins: Geological Society of London Special Publication 306, p. 27–70, https://doi.org/10.1144/SP306.2.
Davis, M., and Kusznir, N., 2002, Are buoyancy forces important during the formation of rifted margins?: Geophysical Journal International, v. 149, p. 524–533, https://doi.org/10.1046/j.1365-246X.2002.01666.x.
Ellis, S.M., Little, T.A., Wallace, L.M., Hacker, B.R., and Buiter, S.J.H., 2011, Feedback between rifting and diapirism can exhume ultrahigh-pressure rocks: Earth and Planetary Science Letters, v. 311, p. 427–438, https://doi.org/10.1016/j.epsl.2011.09.031.
Floyd, J.S., Tolstoy, M., Mutter, J.C., and Scholz, C.H., 2002, Seismotectonics of mid-ocean ridge propagation in Hess Deep: Science, v. 298, p. 1765–1768, https://doi.org/10.1126/science.1077950.
Holford, S.P., Tuitt, A.K., Hillis, R.R., Green, P.F., Stoker, M.S., Duddy, I.R., Sandiford, M., and Tassone, D.R., 2014, Cenozoic deformation in the Otway Basin, southern Australian margin: Implications for the origin and nature of post-breakup compression at rifted margins: Basin Research, v. 26, p. 10–37, https://doi.org/10.1111/bre.12035.
Huismans, R.S., and Beaumont, C., 2008, Complex rifted continental margins explained by dynamical models of depth-dependent lithospheric extension: Geology, v. 36, p. 163–166, https://doi.org/10.1130/G24231A.1.
Huismans, R.S., Podladchikov, Y.Y., and Cloetingh, S., 2001, Transition from passive to active rifting: Relative importance of asthenospheric doming and passive extension of the lithosphere: Journal of Geophysical Research, v. 106, p. 11,271–11,291, https://doi.org/10.1029/2000JB900424.
Koopmann, H., Brune, S., Franke, D., and Breuer, S., 2014, Linking rift propagation barriers to excess magmatism at volcanic rifted margins: Geology, v. 42, p. 1071–1074, https://doi.org/10.1130/G36085.1.
Koptev, A., Cloetingh, S., Burov, E., François, T., and Gerya, T., 2017, Long-distance impact of Iceland plume on Norway's rifted margin: Scientific Reports, v. 7, 10408, https://doi.org/10.1038/s41598-017-07523-y.
Lavier, L.L., and Manatschal, G., 2006, A mechanism to thin the continental lithosphere at magma-poor margins: Nature, v. 440, p. 324–328, https://doi.org/10.1038/nature04608.
Liao, J., and Gerya, T., 2015, From continental rifting to seafloor spreading: Insight from 3D thermomechanical modeling: Gondwana Research, v. 28, p. 1329–1343, https://doi.org/10.1016/j.gr.2014.11.004.
Lundin, E., and Doré, A.G., 2002, Mid-Cenozoic post-breakup deformation in the 'passive' margins bordering the Norwegian-Greenland Sea: Marine and Petroleum Geology, v. 19, p. 79–93, https://doi.org/10.1016/S0264-8172(01)00046-0.
Lundin, E.R., Redfield, T.F., and Péron-Pindivic, G., 2014, Rifted continental margins: Geometric influence on crustal architecture and melting, *in* Sedimentary Basins: Origin, Depositional Histories, and Petroleum Systems: Proceedings of the 33rd Annual Gulf Coast Section of the Society for Sedimentary Geology (SEPM) Foundation, Bob F. Perkins Conference, p. 26–28.
Manatschal, G., 2004, New models for evolution of magma-poor rifted margins based on a review of data and concepts from West Iberia and the Alps: International Journal of Earth Sciences, v. 93, p. 432–466, https://doi.org/10.1007/s00531-004-0394-7.
Molnar, N.E., Cruden, A.R., and Betts, P.G., 2017, Interactions between propagating rotational rifts and linear rheological heterogeneities: Insights from three-dimensional laboratory experiments: Tectonics, v. 36, p. 420–443, https://doi.org/10.1002/2016TC004447.
Morgan, W.J., 1968, Rises, trenches, great faults, and crustal blocks: Journal of Geophysical Research, v. 73, p. 1959–1982, https://doi.org/10.1029/JB073i006p01959.
Mulugeta, G., and Ghebreab, W., 2001, Modeling heterogeneous stretching during episodic or steady rifting of the continental lithosphere: Geology, v. 29, p. 895–898, https://doi.org/10.1130/0091-7613(2001)029<0895:MHSDEO>2.0.CO;2.
Pérez-Gussinyé, M., Morgan, J.P., Reston, T.J., and Ranero, C.R., 2006, The rift to drift transition at non-volcanic margins: Insights from numerical modelling: Earth and Planetary Science Letters, v. 244, p. 458–473, https://doi.org/10.1016/j.epsl.2006.01.059.
Rey, P., 2001, From lithospheric thickening and divergent collapse to active continental rifting, *in* Miller, J.A., et al., eds., Continental Reactivation and Reworking: Geological Society of London Special Publication 184, p. 77–88, https://doi.org/10.1144/GSL.SP.2001.184.01.05.
Schlische, R.W., Withjack, M.O., and Olsen, P.E., 2003, Relative timing of CAMP, rifting, continental breakup, and basin inversion: Tectonic significance, *in* Hames, W.E., et al., eds., The Central Atlantic Magmatic Province: Insights from Fragments of Pangea: American Geophysical Union Geophysical Monograph 136, p. 33–59, https://doi.org/10.1029/136GM03.
Sengör, A.M.C., and Burke, K., 1978, Relative timing of rifting and volcanism on Earth and its tectonic implications: Geophysical Research Letters, v. 5, p. 419–421, https://doi.org/10.1029/GL005i006p00419.
Taylor, B., Goodliffe, A., Martinez, F., and Hey, R., 1995, Continental rifting and initial sea-floor spreading in the Woodlark Basin: Nature, v. 374, p. 534–537, https://doi.org/10.1038/374534a0.
Turcotte, D.L., and Emerman, S.H., 1983, Mechanisms of active and passive rifting: Tectonophysics, v. 94, p. 39–50, https://doi.org/10.1016/0040-1951(83)90008-2.
Van Wijk, J.W., and Blackman, D.K., 2005, Dynamics of continental rift propagation: The end-member modes: Earth and Planetary Science Letters, v. 229, p. 247–258, https://doi.org/10.1016/j.epsl.2004.10.039.
Withjack, M.O., Schlische, R.W., and Olsen, P.E., 1998, Diachronous rifting, drifting, and inversion on the passive margin of central eastern North America: An analog for other passive margins: American Association of Petroleum Geologists Bulletin, v. 82, p. 817–835.

GSA Data Repository 2018022

The role of asthenospheric flow during rift propagation and breakup

Luke S. Mondy[1], Patrice F. Rey[1], Guillaume Duclaux[2], Louis Moresi[3]

Contents

SUPPLEMENTAL METHODS

We solve the problem of conservation of mass, momentum and energy for incompressible mantle flow and lithosphere deformation, using Underworld - an open source particle-in-cell finite-element code (freely available at underworldcode.org), in conjunction with the *Lithospheric Modelling Recipe* (https://github.com/OlympusMonds/lithospheric_modelling_recipe), an open-source python wrapper developed within the EarthByte group to quickly and easily setup and run *Underworld* models in both 2D and 3D.

We assume a visco-plastic rheology depending on temperature, stress, strain, strain rate, and in some experiments melt fraction (see Table DR1). The densities of all rocks depend on temperature (see Table DR1).

Experimental setup

The experiments are run within a Cartesian box of 500 km (x-axis) by 1000 km (y-axis) and 180 km vertically (z-axis). The computational grid dimensions for solving the visco-plastic Stokes problem is 254×512×96 (~2 km cells). A 20 km wide and 8 km deep wedge of lower crust runs along the entire length of the experiment, to preferentially localise deformation in the centre of the domain (Van Wijk and Blackman, 2005). A free-slip boundary condition is imposed to the front and back walls, while a constant pressure is maintained at the bottom of the experiment to simulate the conditions of isostatic equilibrium. The topographic surface, which stands at sea level before rifting, evolves freely beneath a 20 km thick "sticky-air" layer (Crameri et. al., 2012). An initial random plastic strain (up to 5%) is imposed the upper crust to promote strain localisation near the surface.

Fundamental equations

Underworld solves the incompressible equations of continuity for momentum, energy, and mass as below:

$$\frac{\partial \tau_{ij}}{\partial x_j} - \frac{\partial \rho}{\partial x_i} = -\rho g \lambda_i$$

$$\frac{\partial T}{\partial t} + u_i \frac{\partial T}{\partial x_i} = \frac{\partial}{\partial x_i}\left(\kappa \frac{\partial T}{\partial x_i}\right) + Q$$

$$\frac{\partial u_i}{\partial x_i} = 0$$

Where x_i are the spatial coordinates, u_i is the velocity, T is temperature, ρ is density, g is gravity, λ_i is the unit vector in the direction of gravity, t is time, κ is thermal diffusivity, and Q is a source term for the energy equation. Summation on repeated indices is assumed.

Additional terms can be incorporated into the above equations. In the experiments presented, only radiogenic heating is added, unless explicitly mentioned otherwise - however, an additional experiment was run with partial melting, and so the associated terms and values are described below.

Both radiogenic heating and the thermal aspects of partial melting are incorporated into the energy equations as:

$$Q_{\text{radiogenic}} = \frac{A}{\rho C_p}$$

$$Q_{\text{partial melt}} = -1 \times \frac{L_f}{C_p} \frac{\delta M_f}{\delta t}$$

Where A is the rate of radiogenic heat production, C_p is heat capacity, L_f is latent heat of fusion, and M_f is the melt fraction.

The density of a material is defined via a function that depends on temperature and the melt fraction:

$$\rho = \rho_r \times (1 - \alpha(T - T_r) - (M_f \times M_{\Delta\rho_r}))$$

Where ρ_r is reference density, α is thermal expansivity, T_r is reference temperature, and $M_{\Delta\rho_r}$ is the fraction of density change when melted.

The melt fraction is calculated dynamically as part of the experiment, by using the super-solidus formula given by McKenzie and Bickle (1988):

$$SS = \frac{(T - T_s)}{(T_l - T_s)} - 0.5$$

$$M_f = 0.5 + SS + (SS^2 - 0.25) \times (0.4256 + 2.988 \times SS)$$

Where SS is the normalised super-solidus temperature, T_s is the solidus, and T_l is the liquidus.

The solidus and liquidus are defined as:

$$T_s = t_1 + t_2 P + t_3 P^2$$

Where P is pressure, t_1, t_2, and t_3 are defined Table DR1.

The constitutive behaviour is assumed to be visco-plastic rheologies. For the viscous component, flow is computed using dislocation creep (Hirth and Kohlstedt, 2003):

$$\dot{\varepsilon}_{\text{disc}} = A\sigma^n d^{-p} f_{H_2O}^r \exp\left(-\frac{E + PV}{nRT}\right)$$

Where $\dot{\varepsilon}$ is the effective strain-rate, A is the pre-exponential factor, n is the stress exponent, d is the grain-size, p is the grain-size exponent, f_{H2O} is the water fugacity, r is the water fugacity exponent, E is the activation energy, P is the pressure, V is the activation volume, R is the gas constant, and T is the temperature.

For the plastic component, failure is determined using the Drucker-Prager model:

$$\sqrt{J_2} = Ap + B$$

Where $\sqrt{J_2}$ is the second invariant of the deviatoric stress tensor, p is the pressure, and A and B are defined as:

$$A = \frac{2\sin\phi}{\sqrt{3}(3 - \sin\phi)}$$

$$B = \frac{6C\cos\phi}{\sqrt{3}(3 - \sin\phi)}$$

Where C is the cohesion, and ϕ is the friction coefficient.

A linear strain-softening function is applied to the plastic component. As strain is accumulated from 0 to 20%, the material linearly weakens from its original cohesion and friction coefficient to their softened equivalents (defined in see Table DR1). Once fully weakened, the cohesion and friction coefficient remain constant at the softened values.

A stress limiter is applied to all rheologies, to limit the total strength of the lithosphere. The stress limiter is based on the work flow from Watremez et al. (2013), where a Von Mises criterion is applied, where:

$$\sqrt{J_2} = C$$

All materials are limited to 300 MPa in strength via this method, to account from pseudo-plastic processes, such as Peierls creep, and to ensure the lithosphere does not become artificially strong (Demouchy et. al., 2013; Zhong and Watts, 2013). To ensure numerical stability, all rock materials also have a minimum and maximum viscosity range of 1e19 Pa.s to 5e23 Pa.s.

Partial melting has a mechanical effect, whereby material undergoing melt will reduce in viscosity, within a given melt fraction range (defined in Table DR1), based on the following model:

$$\eta_{melted} = \eta \times (1 \times M_{f\%} + \eta_{factor} \times (1 - M_{f\%}))$$

Where η_{melted} is the viscosity after melting, η is the viscosity calculated from the flow law, $M_{f\%}$ is a normalised linear interpolation of the melt fraction between the lower and upper limits of the melt fraction range, and η_{factor} is the melt viscous softening factor the material undergoes once fully melted.

Time stepping

Time stepping in *Underworld* uses the Courant-Friedrichs-Lewy (CFL) condition to ensure stable convergence. The CFL is a function of grid size, absolute maximum velocity, and maximum diffusivity. On top of this, to ensure a numerically efficient and temporally stable model run, the computed CFL timestep is multiplied by a factor of 0.33.

Rheologies

The rheologies used are based on published work: the upper crust flow law is a wet quartzite from Paterson and Luan (1990); the lower crust flow law is a mafic granulite from Wang et. al (2012); and the lithospheric mantle flow law is a wet olivine from Hirth and Kohlstedt (2003). Viscous flow laws that use 0 for the water fugacity exponent typically have this effect incorporated into the pre-exponential factor. Radiogenic heat production values are from Hasterok and Chapman (2011). Melt and other parameters derived from Rey and Müller, 2010. The air material uses an isoviscous 1e18 Pa.s flow law, with a density of 1 kg m^{-3}, thermal expansivity of 0 K^{-1}m, and a heat capacity of 1000 J K^{-1}. See Table DR1 for detailed parameters values.

Boundary conditions

Kinematic boundary conditions

At the time of writing, *Underworld1* is only capable of modelling Cartesian domains, which therefore imposes that it cannot natively model the natural system of rifting near a pole of rotation on a sphere. To apply a velocity boundary condition only to the walls of the domain, and allow the internal geodynamics to react freely, the mesh must be projected from spherical to Cartesian as shown in Figure DR5. The stereographic projection of the mesh shows that divergent velocity increases as a linear function of distance from the Euler pole, and small

circles have constant divergent velocity along their length. Imposed velocities applied at the boundary of the model are parallel to the small circles. When the mesh is projected into the Cartesian coordinates in *Underworld*, these properties are preserved - divergent velocities increase as a function of distance from the pole, and are parallel to small circles. Note that the approximation of a linear increase of velocity from the pole is valid when close to the Euler pole - over the model domain, the linear gradient deviates from the Euler pole derived velocity by less than 2%.

Other Cartesian numerical experiments featuring nearby Euler poles of rotation, e.g., Ellis et. al., 2011, differ from our method by instead applying boundary conditions with a velocity component along the *y* axis (that is, the imposed velocities have an *x* and *y* component), consistent with flattening the small circle onto a 2D plane. We did not take this approach, since it both enforces a flow towards the Euler pole of rotation to maintain the same amount of volume in the model domain, and does not necessarily impose velocities parallel to the small circles. Our approach avoids these issues, but instead suffers from implicit mesh distortion nearer to the Euler pole (as shown in the Figure DR5B stereographic projection). Therefore, we ignore the results shown overly distorted cells, shown in faded blue.

Another issue caused by this approximation is an induced shear velocity component that comes from the stretching of the boundary over time (Figure DR5A). This stretching is minimal, accounting for less than 1% of stretching during the experiment runtime. Additional experiments run further away from the Euler pole (see section "Experiment Sensitivity and Robustness", experiment AE5) suffer even less from this distortion and observer the same behaviours, and so the effect is ignored.

Top-surface boundary condition

To emulate a free surface, the models all use an air layer. The air material cannot be modelled at natural values of viscosity or thermal expansivity, since it would be numerically very expensive and unstable. A common substitute is to use a "sticky-air" layer, which has unrealistically high viscosity, but is low enough to not interfere with underlying geodynamics. The isostatic criterion formula from Crameri et. al, 2012 (eq 12) gives a criterion for determining the thickness and viscosity of a good sticky-air layer. Based on this, our experiments use an air-layer with a viscosity of 1e18 Pa.s, and a thickness of 20 km.

Thermal model setup

The top wall of the model domain is held constant at 293.15 K (20°C), and the bottom wall is held at 1623.15 K (1350°C). The model is then thermally equilibrated for ~1 billion years to achieve a steady state geotherm. The experiments use a sticky-air layer to allow the topographic surface to evolve freely. The thermal diffusivity of the air is 2.2e-5 $m^2 s^{-1}$, versus 1e-6 $m^2 s^{-1}$ for rock materials. The high thermal diffusivity of air limits the energy solver time stepping as follows:

$$\Delta t < C \frac{(\Delta x)^2}{K},$$

where Δt is the timestep in seconds, C is the courant factor, Δx is the minimum width of an element, and K is the maximum value of the thermal diffusivity. This implies that using a thermal diffusivity of 2.2e-5 $m^2 s^{-1}$ for the air would impose a Δt of 4.5% the potential maximum if the air material was not present. Since this approach imposes a large computational cost, we instead allow the air material to have a thermal diffusivity of 1e-6 $m^2 s^{-1}$, and then impose an internal thermal boundary condition of 293.15 K in the initial shape of the air material. This approach has been validated with 2D experiments of rifting under

similar conditions and has a negligible effect on model results.

Experiment Sensitivity and Robustness

To ensure the results presented are robust, a number of additional experiments were run. The experiments presented in the main body are very computationally demanding, with each experiment taking ~50,000 CPU hours. Therefore, to enable more rapid exploration of the parameter space, most of the additional experiments were run at 4 km grid cell resolution (half that of the original experiment). To be able to compare the lower resolution experiments to those in the main body (shown on Figure DR4 as **O1**), a 4 km grid cell version of the experiment (**AE1**) was run to confirm that the processes presented are not a function of numerical resolution. All experiments are shown in Figure DR4.

AE2 - Testing the basal boundary condition (4 km resolution): Underworld models isostasy via a function that calculates the local Pratt isostasy at each grid node along the bottom boundary, and applies the appropriate velocity to maintain a constant pressure. To ensure that the boundary condition is not overwhelming the internal geodynamics, an experiment with a 60 km deeper domain (originally 160 km extended to 220 km) was run, with the assumption that the hot, weak asthenosphere will act as a buffer to the basal boundary condition. The thermal initial condition is modified so that additional asthenosphere included in the domain is set to 1623.15°K.

AE3 - With partial melting (4 km resolution): To ensure the thermo-mechanical effects of partial melt (density change, viscosity change, and latent heat of fusion) were not a critical controlling factor, the partial melt functions were enabled in this experiment.

AE4 - No-slip velocity on kinematic walls (4 km resolution): To identify the significance of the velocity boundary conditions on the kinematically driven walls, an experiment where no shear motion along the kinematically driven boundaries was allowed was run.

AE5/AE6 - Halving/Doubling the angular velocity of the Euler pole (2 km resolution): To test if this effect is robust between different velocities, the O1 experiment was modified by halving and doubling the angular rate of extension – functionally increasing or decreasing the distance to the Euler pole. The linear velocities are 0.25 to 2.5 cm/yr for AE5, and 1.0 to 10.0 cm/yr for AE6. The results presented on Figure DR4 are scaled in time so that each timestep displays the same amount of kinematic extension, so they are comparable to other experiments.

To verify the basal boundary condition was behaving appropriately, two post-processing tests were done. The first test was to ensure the pressure across the bottom surface of the domain remained constant, given the Pratt isostasy condition. To check this, the variation of pressure of the bottom surface of the model domain was computed through time. The result was a maximum variation of total lithostatic pressure of 0.4% through the model evolution, which we deemed acceptable. The second test was to ensure that the same amount of material entering the model domain from the basal isostasy condition was equivalent to the amount of material leaving the domain from the kinematic boundary conditions. If any deviation exists, it may imply that the basal boundary condition is forcing some aspect of the geodynamics, rather than reacting to them. The result was a deviation less than 0.063% over the experiment lifetime, once the topographic evolution was taken into account, which we deemed acceptable.

Earthquake Focal mechanisms

Earthquake focal mechanisms displayed on Figure 4 were extracted from the Global CMT Catalogue (http://www.globalcmt.org/CMTsearch.html) (Dziewonski et. al., 1981; Ekström et. al., 2012). We selected events with a magnitude larger than 5.0 between 1976 and 2017. We did subset the catalog records using the tension and null axis plunge search fields. Thrust faults (in red) have large plunge (> 45) of tension axis, strike-slip faults (green) have large plunge of null axis, and normal faults (blue) have small plunge (< 45) for both tension and null axes.
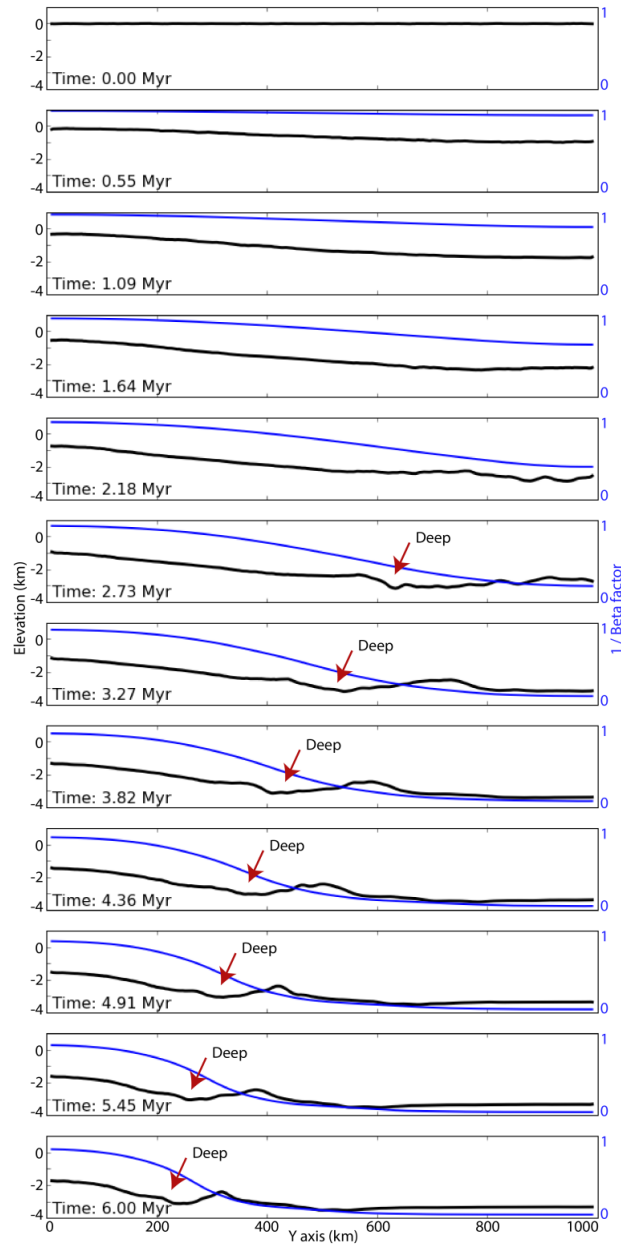
Figure DR1. Temporal evolution of topography and crustal thinning along the rift of the rotational experiment. The elevation along the rift axis shows the formation and migration of a "Deep", a localized topographic dip ahead of the rift tip. The formation of the deep begins when the lithospheric thickness is reduced by half, and tends to follow this point up the margin (towards y = 0 km). Once break-up has occurred (where 1/Beta is ~0), the elevation stabilises around 3.6 km depth. The deep ahead of the rift tip is similar to the Hess Deep described by Floyd et al., 2002 in the Galapagos Rise.
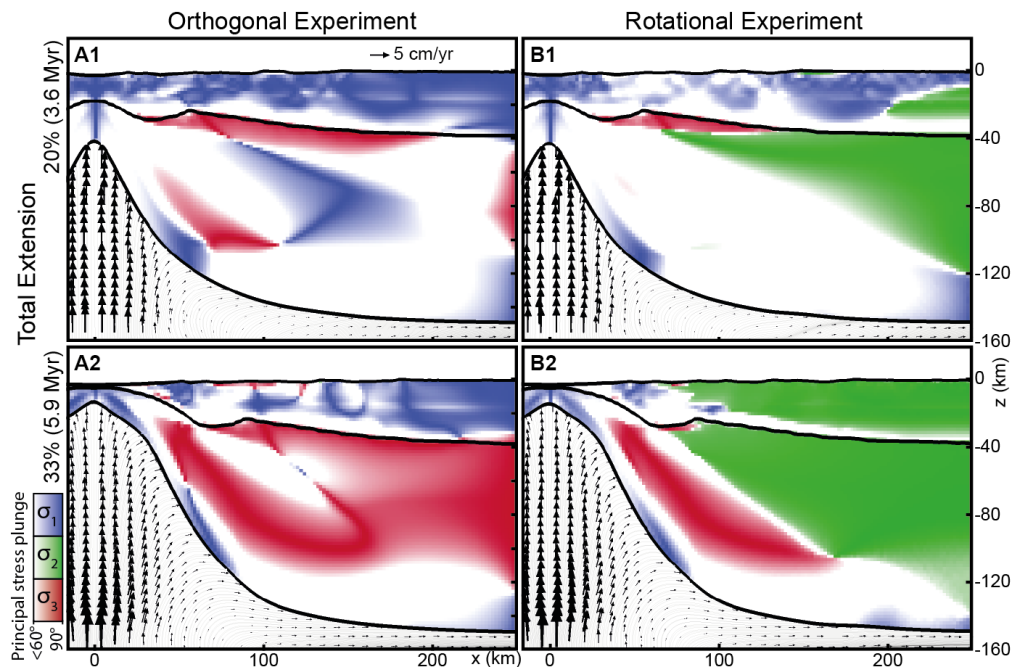
Figure DR2. Stress regime changes throughout the lithosphere. Mapping of Andersonian-like stress regimes (i.e. the plunge of one of the principal stress axes is > 60°) on cross-sections perpendicular to rift axis at y = 500 km. The **orthogonal** experiment shows that extensional stress regime (in blue) largely dominates the lithosphere in the early stages of the experiment **(A1)**, with only the surficial part of the axial rift graben and the very base of the lithosphere, directly above the upwelling asthenospheric dome, under compression. As the lithosphere continues to thin and reaches breakup **(A2)** the stress regime becomes strongly partitioned. Compression (in red) dominates in the lithospheric mantle, whereas extension dominates in the crust, though some compression persists along the continental margins. The **rotational** experiment (**B1** and **B2**) shows similar lithospheric structure, but instead with large areas dominated by strike-slip stress regime.
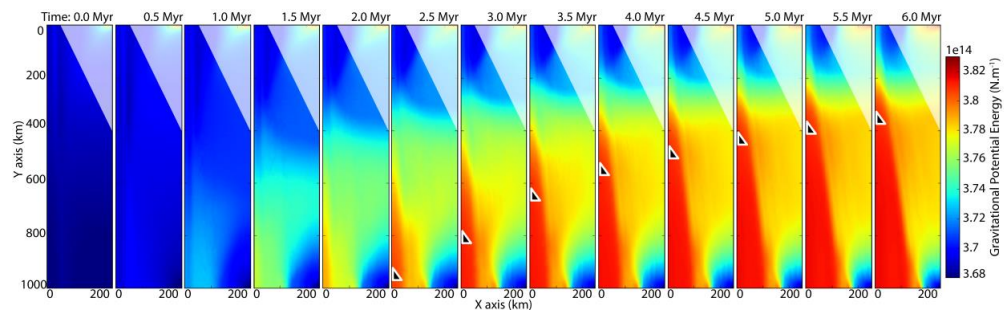
Figure DR3. Mapping the evolution of gravitational potential energy (GPE) during rotational rifting. As lithospheric thinning occurs, an excess of GPE within the rift centre builds as heavier mantle material displaces the lighter crust. Since the rifting occurs much faster further from the Euler pole, it produces a gradient of GPE along the x and y axes away from the forming asthenospheric dome. Only half the domain is shown (X = 0 to X = 250 km), since it is symmetrical. GPE was calculated by vertical integration of the lithostatic pressure. Black triangles represent the rift tip, where $1/\beta < 0.2$ (see Fig. DR1).
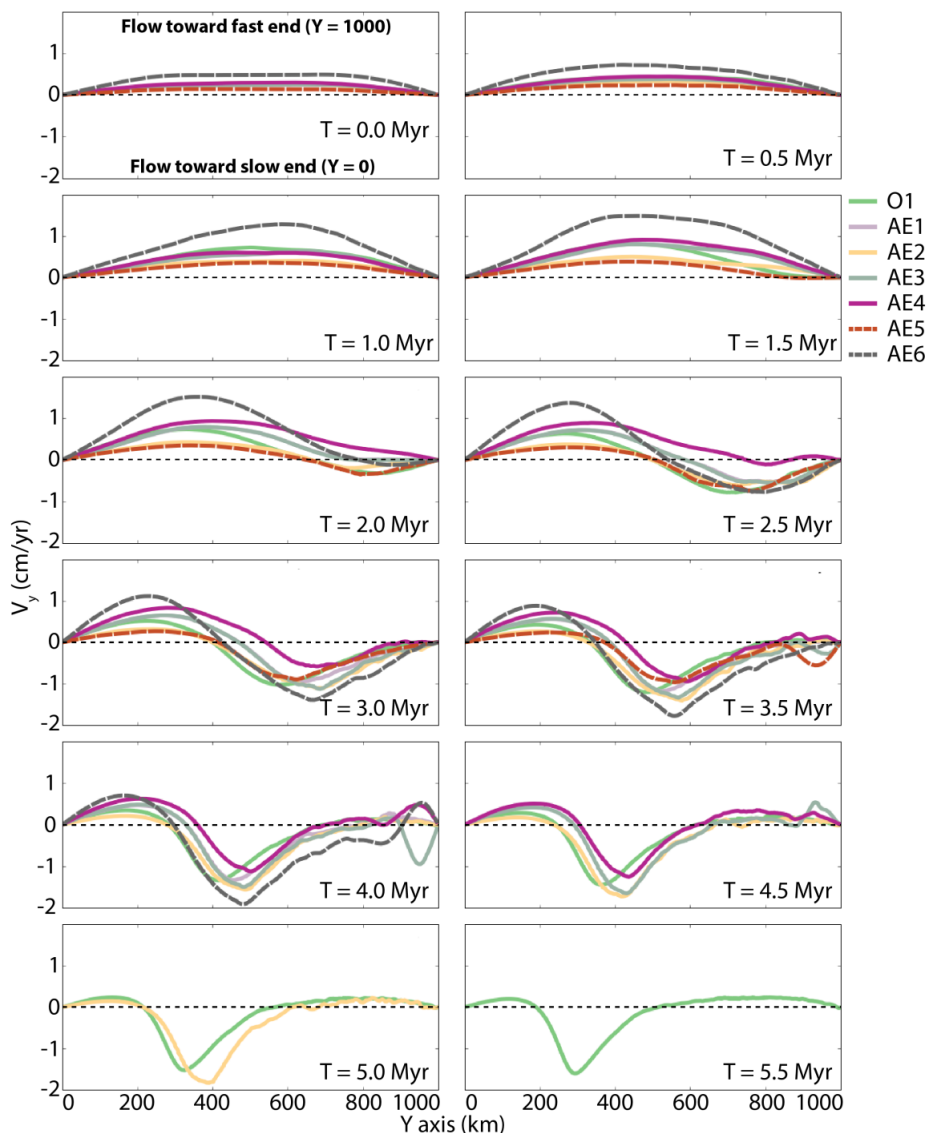
Figure DR4. Sensitivity analyses testing the role of resolution, boundary conditions, and partial melt. The profiles show the velocity component parallel to the rift-axis at the LAB (similar to Figure 4C) of additional experiments run to explore the robustness of experiment setup (see Supplemental Methods for details of each experiment). The additional experiments are all able to reproduce the results from the main text. All models show a similar pattern of initial flow away from the Euler pole, followed by a switch in direction when the asthenosphere approaches its peak height near y = 1000 km. This implies that the large scale mantle dynamics within the models are not dependent on resolution, the boundary conditions, or melt processes. Experiments AE5 (imposed velocities halved) and AE6 (imposed velocities doubled) in particular reinforce the conclusion from the main body of the text. The pattern of initial flow towards the fast end of the model is driven by tectonics (Van Wijk et. al., 2005; Koopmann et. al., 2014): AE5 shows reduced velocities; AE6 shows increased velocities. However, once the asthenosphere has reached its peak, the return flow velocity of

both AE5 and AE6 are relatively consistent with all other experiments, since it is driven by the difference in gravitational potential energy along the rift axis. The larger return flow for AE6 compared to AE5 can be attributed to thermal effects, where the faster rifting leads to weaker asthenospheric material, and hence easier flow, and vice versa. Note that AE5 and AE6 have had their times scaled to match the amount of kinematic extension in each panel.
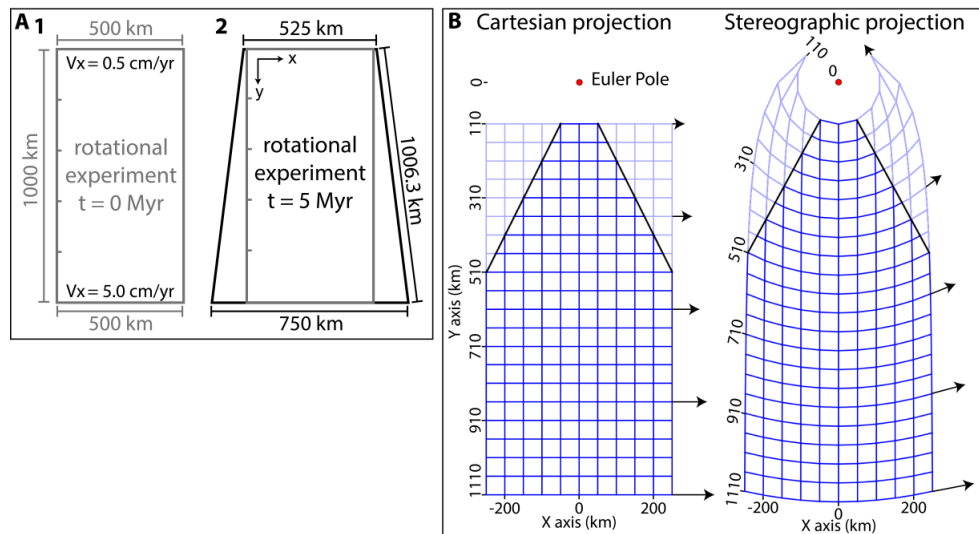
Figure DR5. Consequences of mapping a spherical velocity field onto a Cartesian domain. **A,** Map view of the model domain at t = 0 Myr, (**A1**), and after 5 Myr of extension (**A2**), The north-south walls are stretched from 1000 to 1006.3 km. **B,** The blue mesh shows the model domain projected in Cartesian (as Underworld models it), and the spherical equivalent (as would be on Earth) shown in a stereographic projection. The red point shows the location of the Euler pole. Black arrows representing the velocity boundary conditions are only shown for the right wall. Notably, in both cases, the applied velocity boundary conditions are parallel to the small circles, as rotation around an Euler pole enforces. The mesh distortion near the Euler pole is evident in the stereographic projection, hence its exclusion from analysis. The Y axis has been adjusted so the Euler pole is at y = 0 km for this figure.
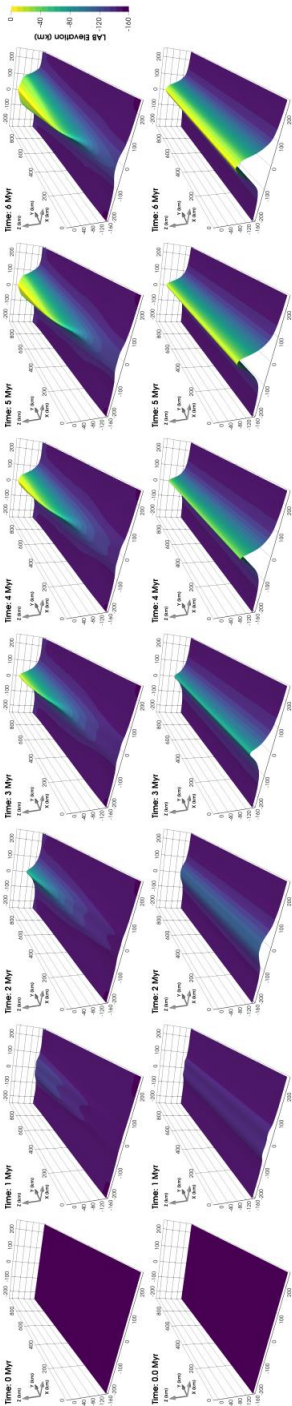
Figure DR6. 3D view through time of the elevation of the lithosphere-asthenosphere boundary (LAB) in the rotational experiment (top) and orthogonal experiment (bottom).

Table DR1

Parameter	Upper Crust	Lower Crust	Mantle
Reference density, ρ_r (kg m^{-3}) at 293.15 K	2800	2900	3300
Thermal expansivity, α (K^{-1})	3e-5	3e-5	3e-5
Heat capacity, C_p (J K^{-1} kg^{-1})	1000	1000	1000
Thermal diffusivity, α (m^2 s^{-1})	1e-6	1e-6	1e-6
Latent heat of fusion, L_f (kJ kg^{-1})	300	300	300
Radiogenic heat production, A (W m^{-3})	1.2e-6	0.6e-6	0.02e-6
Melt density change fraction, $M_{\Delta\rho_r}$	0.13	0.13	0.13
Liquidus term 1, t_1 (K)	1493	1493	2013
Liquidus term 2, t_2 (K Pa^{-1})	-1.2e-7	-1.2e-7	6.15e-8
Liquidus term 3, t_3 (K Pa^{-2})	1.6e-16	1.6e-16	3.12e-18
Solidus term 1, t_1 (K)	993	993	1393.661
Solidus term 2, t_2 (K Pa^{-1})	-1.2e-7	-1.2e-7	1.32899e-7
Solidus term 3, t_3 (K Pa^{-2})	1.2e-16	1.2e-16	-5.104e-18
Friction coefficient	0.577	0.577	0.577
Softened friction coefficient	0.1154	0.1154	0.1154
Cohesion, C (MPa)	10	20	10
Softened cohesion, C (MPa)	2	4	2
Pre-exponential factor, A (MPa^{-n} s^{-1})	6.60693e-8	10e-2	1600
Stress exponent, n	3.1	3.2	3.5
Activation energy, E (kJ mol^{-1})	135	244	520
Activation volume, V (m^3 mol^{-1})	0	0	23e-6
Water fugacity	0	0	1000
Water fugacity exponent	0	0	1.2
Melt viscous softening factor	1e-3	1e-3	1e-1
Melt fraction range for viscous softening	0.2 - 0.3	0.2 - 0.3	0 - 0.02

Code and Experiment Inputs

Numerical code used

The version of *Underworld* used can be found at:

https://github.com/OlympusMonds/EarthByte_Underworld

This version of *Underworld* is a fork of *Underworld 1.8*, with some extras plugins to work more smoothly with the *Lithospheric Modelling Recipe*.

We recommend new users of *Underworld* should use *Underworld 2.0*, found here:
https://github.com/underworldcode/underworld2

Experiment Inputs

The experiments were designed based off the *Lithospheric Modelling Recipe* (the *LMR*), which is a set of pre-defined *Underworld* input files and a script framework to help run them. The *LMR* can be found here:
https://github.com/OlympusMonds/lithospheric_modelling_recipe

The input files used in this experiment can be found here:
https://github.com/OlympusMonds/lmondy-et-al-3D-Rifting-Experiments

References

Crameri, F., Schmeling, H., Golabek, G., Duretz, T., Orendt, R., Buiter, S., May, D., Kaus, B., Gerya, T., and Tackley, P., 2012, A comparison of numerical surface topography calculations in geodynamic modelling: an evaluation of the 'sticky air' method: Geophysical Journal International, v. 189, no. 1, p. 38-54.

Demouchy, S., Tommasi, A., Ballaran, T. B., and Cordier, P., 2013, Low strength of Earth's uppermost mantle inferred from tri-axial deformation experiments on dry olivine crystals: Physics of the Earth and Planetary Interiors, v. 220, p. 37-49.

Dziewonski, A., Chou, T. A., and Woodhouse, J., 1981, Determination of earthquake source parameters from waveform data for studies of global and regional seismicity: Journal of Geophysical Research: Solid Earth, v. 86, no. B4, p. 2825-2852.

Ekström, G., Nettles, M., and Dziewoński, A., 2012, The global CMT project 2004–2010: Centroid-moment tensors for 13,017 earthquakes: Physics of the Earth and Planetary Interiors, v. 200, p. 1-9.

Ellis, S. M., Little, T. A., Wallace, L. M., Hacker, B. R., and Buiter, S. J. H., 2011, Feedback between rifting and diapirism can exhume ultrahigh-pressure rocks: Earth and Planetary Science Letters, v. 311, no. 3-4, p. 427-438.

Floyd, J. S., Tolstoy, M., Mutter, J. C., and Scholz, C. H., 2002, Seismotectonics of mid-ocean ridge propagation in Hess Deep: Science, v. 298, no. 5599, p. 1765-1768.

Hasterok, D., and Chapman, D., 2011, Heat production and geotherms for the continental lithosphere: Earth and Planetary Science Letters, v. 307, no. 1, p. 59-70.

Hirth, G., and Kohlstedt, D., 2003, Rheology of the upper mantle and the mantle wedge: A view from the experimentalists: Inside the subduction Factory, p. 83-105.

Koopmann, H., Brune, S., Franke, D., and Breuer, S., 2014, Linking rift propagation barriers to excess magmatism at volcanic rifted margins: Geology, v. 42, no. 12, p. 1071-1074.

McKenzie, D., and Bickle, M., 1988, The volume and composition of melt generated by extension of the lithosphere: Journal of petrology, v. 29, no. 3, p. 625-679.

Paterson, M., and Luan, F., 1990, Quartzite rheology under geological conditions: Geological Society, London, Special Publications, v. 54, no. 1, p. 299-307.

Rey, P., and Müller, R., 2010, Fragmentation of active continental plate margins owing to the buoyancy of the mantle wedge: Nature Geoscience, v. 3, no. 4, p. 257-261.

Van Wijk, J. W., and Blackman, D. K., 2005, Dynamics of continental rift propagation: the end-member modes: Earth and Planetary Science Letters, v. 229, no. 3-4, p. 247-258.

Wang, Y., Zhang, J., Jin, Z., and Green, H., 2012, Mafic granulite rheology: Implications for a weak continental lower crust: Earth and Planetary Science Letters, v. 353, p. 99-107.

Watremez, L., Burov, E., d'Acremont, E., Leroy, S., Huet, B., Pourhiet, L., and Bellahsen, N., 2013, Buoyancy and localizing properties of continental mantle lithosphere: Insights from thermomechanical models of the eastern Gulf of Aden: Geochemistry, Geophysics, Geosystems, v. 14, no. 8, p. 2800-2817.

Zhong, S., and Watts, A., 2013, Lithospheric deformation induced by loading of the Hawaiian Islands and its implications for mantle rheology: Journal of Geophysical Research: Solid Earth, v. 118, no. 11, p. 6025-6048.

Article 3

Lithospheric Modelling Recipe: A numerical modelling workflow of lithospheric processes for geologists

Luke S. Mondy[1], Patrice F. Rey[1], Guillaume Duclaux[2]

[1]*Earthbyte Group, School of Geosciences, The University of Sydney, Sydney NSW 2006, Australia*

[2]*Université Côte d'Azur, CNRS, OCA, IRD, Géoazur, 06560 Valbonne, France.*

1. Abstract

The use of numerical modelling in geosciences has increased dramatically over the past 3 decades. However, uptake among field geologists has not kept pace with other fields. In this paper, we look at common issues and barriers that inhibit new users from adopting numerical geodynamic modelling as part of their workflows. We then present a strategy in the form of a toolbox called the Lithospheric Modelling Recipe (*LMR*) to address these issues for the geodynamic modelling software *Underworld*. *LMR* is a set of pre-built, numerically stable, customizable and high-resolution 2D and 3D coupled thermo-mechanical model of lithospheric extension. Through its flexible design, it aims to facilitate user engagement via the rapid production of generic numerical experiments. We evaluate the effectiveness of our solutions, and compare them to existing open-source numerical modelling software.

2. Introduction

Over the past decade, the growing availability of high-performance computing (HPC) and community codes have driven the adoption of numerical modelling beyond primarily quantitative disciplines, such as geodynamics and geophysics, and into field-based disciplines. In the discipline of metamorphic petrology, the adoption of thermodynamic modelling is well established thanks to the availability of free, well-documented and tested codes such as *Thermocalc* (Holland & Powell, 1998; Powell and Holland, 1988; Powell et al., 1998), *Perple_X* (Connolly and Petrini, 2002) and *Theriak-Domino* (de Capitani C. and Petrakakis K., 2010). In contrast, despite a long record of pioneering works in computational tectonics (e.g., Chery et al., 1991; Bassi, 1991; Poliakov et al., 1993; Beaumont et al., 1994; Govers and Wortel, 1995), it is only relatively recently that open-source thermo-mechanical codes for tectonic modelling such as *Ellipsis3D* (Moresi et al., 2003; O'Neill et al., 2006), *Underworld* (Moresi et al., 2007), DynEarthSol2D (Choi, et al., 2013), and *ASPECT* (Kronbichler et al., 2012; Heister et al.,

2017; Bangerth et al., 2019), were made available to the broader community. Nevertheless, tectonicists' engagement with scientific computing is still rather limited. As noted by Gerya (2009), although the basic principles at the core of numerical modelling are accessible to science graduates (e.g., linear algebra, fluid mechanics, etc), geologists interested in adding numerical modelling into their workflow must have a strong motivation to develop the understanding needed to produce useful results.

This paper first summarizes the common difficulties non-expert users face when confronted with computational modelling. These include technical difficulties in relation to the compilation and installation of codes on local or high-performance computers, the highly technical documentation and opaque input formats, and the difficulty in relating mathematical entities of model outputs, such as stress and strain rate tensors, to observational data such as rock fabrics.

With the aim to facilitate access to computational modelling to field geologists, we present a

pre-built, user-friendly toolbox addition to *Underworld 1.8* called the *Lithospheric Modelling Recipe* (*LMR*). By embedding *Underworld* and the *LMR* into an ready-to-use *Docker* container, and through a number of design choices, we iron out some of the most pernicious difficulties to enable smooth and accessible workflow for the testing of conceptual tectonic models within a physically robust framework. We hope that by enabling a greater diversity of users, this workflow will promote the adoption of computational tectonics and facilitate more reproducible sciences.

3. Issues facing non-expert users engaging with computational tectonics

The knowledge that structural geologists and tectonicists require to understand and interpret field datasets is not different to that needed to design thermo-mechanical models. These include an understanding of the relationship between strain and stress; the rheology of rocks and its dependence on temperature; the role of shear-heating, melt and recrystallisation as strain localization agents; an understanding of how heat is transferred through the lithosphere; and the role kinematic and/or dynamic boundary conditions play in driving deformation. Nevertheless, field geologists face many difficulties when engaging for the first time with computational modelling. These issues can be broadly linked to i/ limited understanding of the various purposes and approaches of modelling; ii/ the belief that one has to be an expert in computational fluid dynamics to engage in computational tectonics; iii/ the difficult task of compiling thermo-mechanical codes against the suite of libraries providing specialized functionalities to run numerical experiments efficiently on high-performance computers; and iv/ a lack of familiarity regarding common scripting languages used to design the input scripts that describe the model and its boundary conditions.

3.1. Modelling purposes and approaches: simulation vs experiments vs modelling

For most geologists, numerical modelling means to reproduce to the highest level of realism the temporal evolution of a particular geological setting. They often approach modelling after completing the acquisition and the interpretation of their field datasets, with the hope to confirm via "computational simulation" the physical robustness of their conceptual models. Although this motivation is perfectly valid, this is a numerical simulation, since it aims to entirely reproduce the Earth, rather than a model, which instead aims to extract valuable information about Earth processes. Simulation is not necessarily the best way to approach computational tectonics, as it requires tremendous computational resources, and the outputs can be as difficult to understand as the real world - however, newcomers are often disappointed when their numerical modelling outputs do not conform with their conceptual expectations of simulation. Indeed, the thermo-mechanic of natural systems are highly non-linear and therefore highly unpredictable.

Fortunately, computational tectonics doesn't have to necessarily account for the complexity of nature in minute details to deliver transformative understanding - indeed too much complexity can hamper identifying key parameters and processes. For instance, our understanding of collisional processes in Asia was transformed by a simple - even simplistic - analogue experiment in which a rigid rectangular block representing India was forced into a block of plasticine representing Asia (Tapponnier et al., 1982). The experiment failed to deliver first order features characteristic of collisional orogens, including something resembling a plateau, or even a mountain belt. And yet, this simple analogue experiment has changed our understanding of collisional tectonics. Hence, simple experiments, analogue or numerical, using a minimum of input parameters with no ambition to reproduce nature can deliver important insights into tectonic processes (e.g. propagating lateral extrusion) even though our models always fail at capturing nature in all its complexity.

Numerical modelling sits at mid-distance between numerical experiment and numerical

simulation. It often starts following a first set of numerical experiments the purpose of which is to isolate the main controlling parameters. Although the model is still a much simplified version of the world, it accounts for an array of realistic thermal and mechanical parameters and processes, with the aim to deliver sets of structures and behaviors that can be broadly compared to some natural examples. One of the difficulties new user faces is that the numerical code itself often struggles to accommodate realistic thermal and mechanical parameters due to the vast numerical range involved from 1e-15 (e.g. strain rate) to 1e20 (e.g. viscosity), which can lead to large gradients across the finite computational grid. Designing models that are numerically stable often requires trading numerical resolution for faster numerical convergence, in a way that impacts heavily on the modelling outcomes. This often requires a time-consuming trial and error approach. *LMR* has been designed to provide numerical stability for an acceptable resolution cost.

3.2. How much expertise in computational fluid mechanics does one need?

Geodynamic processes affecting the Earth's interior can be understood in terms of mass and heat transfer (Richter, 1978). These can be described by the Stokes equation (Navier-Stokes equation simplified for low-Reynolds number that characterises slow moving fluids), coupled to the equations describing conservation of energy, and the constitutive equations describing the relationship between the strain rate tensor and the stress tensor. Most tectonicists are not familiar with these physical constructs and even less with their computational translation. Hence, computational tectonics has been hitherto the domain of geophysicists. Though we rarely question geophysicists' lack of field-based expertise necessary to interpret model outcomes (e.g. structural geology, tectonics and metamorphic petrology), some expert modellers seem concerned when computational modelling is performed by field geologists using sophisticated codes as a "black-box". This concern

is misplaced. This is akin questioning the ability of a geologist for using a microprobe because he/she is not an engineer. The expertise needed to design and assemble numerical frameworks for the purpose of exploring Earth's fluid dynamic processes is fundamentally different to that needed to run models and interpret their outcomes. Hence, the lack of expertise in fluid-dynamics and numerical methods should not deter field geologists from engaging with computational tectonics, as they have the knowledge to assess the relevance of their model outcomes. Nevertheless, access to an expert in numerical methods can be helpful in avoiding common pitfalls.

3.3 How much expertise in computer science and administration does one need?

Sophisticated open-source scientific software are built on top of a scaffold of well-tested open-source numerical libraries such as *PETSC*, for solving partial differential equations in parallel; MPI, a communication and synchronization protocol to run parallel codes; and HDF5, a hierarchical data format to store large amounts of data outputs - with each of these packages coming with their own set of dependencies. The process of compiling this complex numerical framework is a significant and frustrating barrier to new users, as it requires either practical experience with compilation of large codes, or finding someone to do it for them. Over the past two decades, a number of technological solutions have been developed to circumvent these issues by pre-compiling or automating compilation, or even embedding the precompiled framework into a downloadable virtual container. The recent popularity of Docker containers has changed the landscape of software distribution. Software can be precompiled in its own self-contained environment, and runs largely isolated from the host computer, reducing the maintenance burden on developers and eliminating the difficulties of deploying manually the numerical framework. Containers are easily distributable, and often can be used on supercomputer clusters. This paradigm shift means that any modelling code that

provides Docker containers for distribution significantly reduces the level of expertise in computer science and administration required to engage with computational tectonics.

3.4. Opaque input scripts

Modellers communicate their model designs to executable codes through input scripts. These input scripts are often (but not always) written in textual languages (e.g. XML, JSON, or a simple text file) describing the model's geometry and internal architecture, the mechanical and thermal properties of material involved and how they evolve through important metamorphic reactions (e.g. eclogitization, granulitization, serpentinization and partial melting), and the boundary conditions that a model must obey (temperature or heat flow, velocity or stress).

These scripts also include a large amount of information that makes little sense to tectonicists, unless they are familiar with computational fluid mechanics and finite element (or finite difference) numerical methods. They include information on the type of element making the computational grid, details about solvers and their options, and many other important aspects of how the code links to the libraries necessary to make the code run in parallel on high-performance computers. Input scripts often consist in one single file, which can be dozens of pages long, only a small fraction of which is understandable to non-expert. For many new users, this is enough to impede and even prevent serious engagement with computational modelling.

The confusion from verbose and technical input scripts can be compounded by the fact that thermo-mechanical codes are often designed by experts who are less familiar with the type of field data and observations that geologists care about (e.g. foliations, lineations, finite strain, incremental strain, PTt paths, etc). Additionally, many codes present new users with relatively abstract benchmark examples or "toy" models, such as a ball sinking through a viscous liquid. While such models are essential for benchmarking and testing numerical

modelling codes against analytical solutions of simple problems, or for teaching Stokes flow, they are not particularly relevant to geologists. Having access to input scripts designed to explore more realistic geological problems may be more useful to encourage new users to adopt numerical modelling as part of their workflow.

3.5. Reproducible science

The larger the community of scientists engaging with open source scientific computing, the more robust the science outputs, as results can be easily duplicated and verified. Reproducibility demands that codes and input scripts are made freely available, with all the details necessary to make numerical experiments reproducible. This is far from being always the case, with often only textual descriptions of experiments being provided (e.g., Ioannidis et al., 2009; Merali, 2010). Unfortunately, even for experienced modellers it is difficult - if not impossible - to reproduce a model from text descriptions provided in published papers (Faniel and Jacobsen, 2010). This can be frustrating to experienced and new users, and there is a need to facilitate the distribution of input files, not only for reproducibility, but also to help new users to engage with numerical modelling.

3.6. Summary

The adoption of computational modelling by field geologists and tectonicists can be facilitated by providing these communities with a few generic, customizable and ready-to-use numerical experiments, which are numerically stable and use a format which is easy to read and in which parameters can be easily identified and varied. To minimize errors due to a lack of expertise with numerical methods, the numerical engineering should be accessible, but not directly presented to new users. Finally, adoption of computational modelling by field geologists could be made easier by providing a lightweight virtual computer containing the compiled framework and ready-to-use models. The following section shows an example of this approach based on the *Underworld* numerical

modelling framework.

4. Underworld 1.8 and the Lithospheric Modelling Recipe

The *Lithospheric Modelling Recipe (LMR)* is a framework that sits on top of *Underworld 1.8*, a robust thermo-mechanical code (Moresi et al, 2002, 2003). The *LMR* simplifies access to *Underworld* by supplying ready to use 2D and 3D models. It also gives clear pathways to customize these models by providing simple access to boundary conditions (extension velocity, basal temperature, etc.), a library of rheologies, and modules to add processes such as partial melting, and surface processes.

In what follows, we briefly summarize *Underworld 1.8* and describe how the *LMR* provides a field-geologist-friendly platform to access *Underworld*.

4.1. Underworld 1.8

Underworld 1.8 is a modular, open-source, multi-platform and parallel numerical framework that can be used for computational tectonics involving coupled thermal and mechanical processes (Moresi et al., 2003, 2007). *Underworld* can tackle a very large range of problems, from small-scale rock mechanics, to the deformation of tectonic plates and mantle convection. It is built on top of a stack of open-source standard libraries optimised to handle computational meshes, particles (tracking time-dependent rocks properties), parallelism, and numerical solvers.

Underworld 1.8 takes in XML files as input. These XML files describe all aspects of a model, including the mesh architecture, finite element types, the solving methods, controlling material tracking particles, the layout of the material within the model domain, the rheology of each material (including thermal properties), and the thermal and velocity boundary conditions applied at the boundaries of the computational grid. This large amount of information necessitates a few thousand lines of code, written using the relatively simple XML

language. A typical *Underworld 1.8* model input XML script is built by selecting pre-defined XML chunks, and importing a reference to each segment at the top of the file. These predefined segments can define variables, such as the numerical solver parameters or boundary conditions, but can also be fully-designed models. The remainder of the file usually either modifies sections imported from the predefined segments, or provides geological information, such as the layout of rock materials. Important components, such as controlling and tuning the solver parameters, and the number of CPUs, are specified on the command line.

Model output files from *Underworld* are stored in HDF5 files, delivered with XDMF format files readable by *Paraview*. *Paraview* is an open-source code for the visualisation and processing of data volumes, and is used interactively to explore data, and can visualise both particle field and gridded field data generated by *Underworld*.

4.2. The Lithospheric Modelling Recipe

To mitigate many of the issues identified above and to streamline the production of new models, we have developed the *LMR* framework around *Underworld*. The purpose of the *LMR* is to provide a 2D or 3D, ready-to-use, customizable, generic continental rifting model. The *LMR* is made up of three parts: a set of XML input files that define the model of rifting; a Python script that coordinates the XML files, and handles complex tasks automatically; and a series of compiled additional features for *Underworld*, such as new rheology types and geodynamic processes, known as 'earthbyte_additions'. The *LMR* files and scripts are all available on GitHub: "https://github.com/LukeMondy/lithospheric_modelling_recipe". Here we will describe in detail the model of continental rifting itself, followed by the steps taken to ensure it is setup to be as friendly to new users and geologists as possible.

4.2.1. Model of continental rifting

The *LMR* delivers a ready-to-use 2D or 3D lithospheric model of continental rifting (as shown
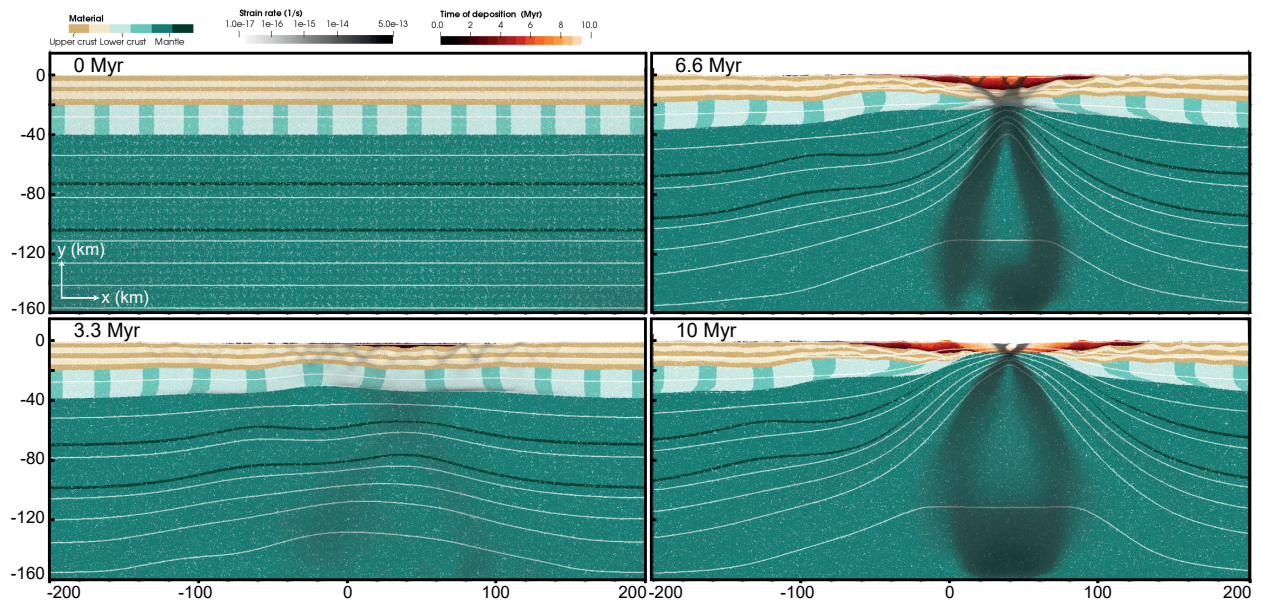
Figure 1. *The evolution of the default LMR model, from time = 0 Myr to 10 Myr. White lines show isotherms every 200 °C, from 30 °C to 1330 °C. Black semi-transparent areas show high strain-rates. Distributed faulting can be seen in the upper crust at time = 3.3 Myr, which localises with lithospheric necking by time = 6.6 Myr. Sedimentary basins form in the subsiding area, until break-up occurs at time = 10 Myr.*

in Figure 1). The default 2D model is setup in a domain 400 km wide (x_{min} = -200 km , x_{max} = 200 km) and 175 km tall (y_{min} = -160 km, y_{max} =15 km). In 3D, the model is extruded out from the 2D plane to be 400 km deep (z_{min} = -200 km, z_{max} = 200 km), so that the XZ plane at y = 0 km and represents the surface of the crust. The lithosphere is made up of laterally homogeneous layers. Starting from y = 0 km, the upper crust is 20 km thick, and uses a wet quartzite rheology from Peterson and Luan (1990). The lower crust is 20 km thick, and uses a dry mafic granulite from Wang et al. (2012). The mantle defines the rest of the domain down to -160 km depth, and has the rheology of wet olivine from Hirth and Kohlstedt (2003). The asthenosphere is not explicitly defined as a separate material, instead with the lithosphere-asthenosphere boundary being defined by the ~1300 °C isotherm. Finally, the lithosphere is covered with a 15 km thick air layer, a low viscosity material that allows topography to develop at the surface of the model (Crameri et al., 2016). The model includes some random damage in the centre of the domain, where the crustal material has been pre-weakened, which ensures that deformation occurs approximately in the centre of the

domain. Every material includes a deviatoric stress limiter of 300 MPa, to take into account pseudo-plastic behavior which limits the strength of the lithosphere (Ord and Hobbs, 1989; Zhong and Watts, 2013). The full list of parameters set for each material is defined in Table 1.

The applied extension velocity is set to 2 cm/yr (1 cm/yr at each vertical wall), using a free slip boundary condition (i.e., the wall allows material to move up and down freely with no friction). The bottom of the model uses an isostatic boundary condition, which attempts to keep the lateral pressure constant by injecting or removing mantle material. As the surface of the model evolves, air material flows freely in and out of the top of the domain. The temperature at the top of the model is fixed to 20 °C, and the bottom is fixed to 1330 °C.

A number of additional geodynamic processes are taken into account in the *LMR* models. A model of partial melting, based on McKenzie and Bickle (1988), is included, which incorporates the appropriate energy consumption and transfer caused by melting, and associated reduction in viscosity and density. This model does not include melt
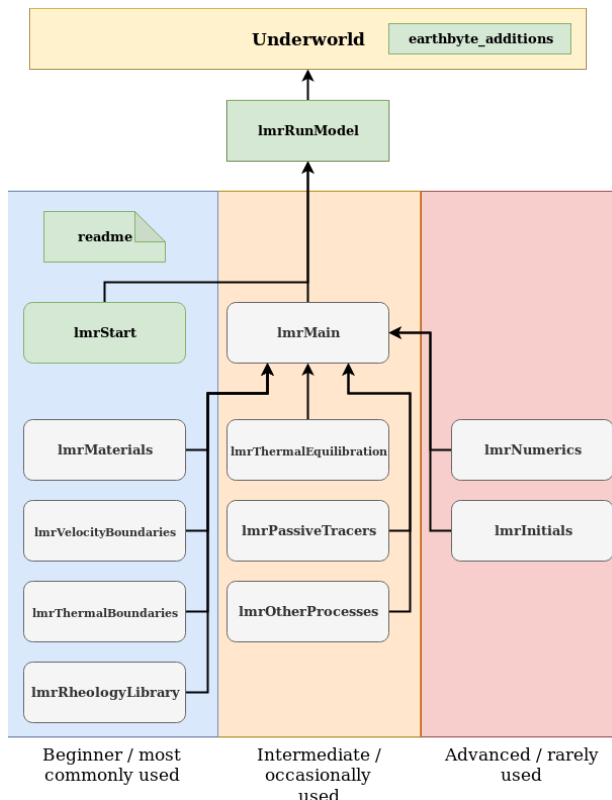
Figure 2. *The LMR framework and its relationship to Underworld. Grey boxes show the XML input files. Green boxes show code and files written to enable the LMR to function with Underworld. Black arrows how the model information flows into Underworld: all the grey XML files are tied together by lmrMain; lmrRunModel then reads both lmrStart and lmrMain, and processes them; finally lmrRunModel invokes Underworld (and some of the additional functions written in earthbyte_additions), and the model runs.*

segregation and transport, so melt is always held within its source. A simple approximation of sedimentation and erosion is also included. It involves transforming rock particles into air particles (erosion), when rock particles reach an imposed elevation threshold; and transforming air particles into sediment particles (deposition), when air particles reach an imposed depth level. Any 'deposited' materials record their time of deposition, allowing for basic stratigraphic analysis.

Figure 1 shows the evolution of the default *LMR* model. Early in the model evolution, distributed faulting in the upper crust dominates, with mostly pure shear type deformation occurring in the lithospheric mantle. As lithospheric necking occurs, deformation becomes more localised in the

rift centre, and the surface subsides, allowing sediments to be deposited. Finally as break-up occurs, all deformation is localised at the mid-ocean ridge, and the rift flanks drift apart as separated plates. The model, by default, runs at 2 km element resolution, so that the model can run relatively quickly on desktop or laptop computers.

The parameters chosen for this model are representative of experiments produced in recent geodynamic publications, and provide a solid foundation from which new models can be derived. The *LMR* model can easily be modified to explore different rifting settings, subduction, and collisional processes, by changing the internal distribution of materials, and the boundary conditions.

The 2D version of the LMR model is capable of being run on desktop computer, with the results of the first timestep usually being output within about 10 minutes. To reach full continental breakup, the model may take 12 to 24 hours, depending on the computer. The 3D version of the LMR model can also be run on a desktop computer, however only at very low resolution. For high-resolution models, using a super-computer is required.

4.2.2. Structure of the *Lithospheric Modelling Recipe*

The flexibility of *Underworld*, which allows tackling a very large range of thermal and mechanical problems (coupled or not), on a very broad range of length and temporal scales, explains the large selection of predefined input XML files users can choose from. However, since our purpose is to model continental rifting, the *LMR* removes this choice and instead provides a set of input XML files tailored to this setting, with each file clearly delineating which aspect of the model it controls. Here, we describe each component of the *LMR*, and detail how they are used together.

LMR XML files

The *LMR* uses eleven commented *Underworld* XML inputs files. The files have a flat layout,

meaning there is no hierarchy between them (with the exception of lmrMain.xml, which only ties the other files together). Each file controls a particular aspect of the model:

• **lmrMaterials.xml** controls the model layout and includes the thermo-mechanical details defining each material involved in the model (i.e., density, thermal expansivity, radiogenic heat production, heat capacity, heat diffusivity, visco-plastic rheology parameters, etc). To keep the length of this file manageable, thermo-mechanical properties are called from the lmrRheologyLibrary file.

• **lmrRheologyLibrary.xml** is a library of published visco-plastic rheologies users can select from, and even add to. This library also includes densities, the solidus and liquidus for each material, how the melt fraction impacts on the thermo-mechanical properties of the material via the latent heat of fusion, and weakening due to the presence of melt.

• **lmrVelocityBoundaries.xml** controls the extensional velocities imposed on the vertical walls and the isostatic boundary condition at the bottom. Velocity boundary conditions may be time- or space-dependent.

• **lmrThermalBoundaries.xml** controls the temperature boundary conditions, which can also be time- or space-dependent.

• **lmrThermalEquilibration.xml** automates and controls the process of getting an initial temperature field (typically, but not necessarily, a steady-state geotherm).

• **lmrPassiveTracers.xml** defines a set of passive particles tracking density interfaces important to tectonicists, including the surface of the model, the boundary between the upper and lower crust (when they are made of different materials), and the moho. Other passive tracers can be included for the purpose of recording pressure and temperature through time (useful to extract PT paths), or recording finite strain

ellipses or ellipsoids.

• **lmrOtherProcesses.xml** controls the activation of additional processes important to tectonicists, such as partial melting, shear heating, erosion and deposition.

• **lmrNumerics.xml** defines what parameters to output, fundamental definitions (e.g., calculating the buoyancy force), and setting up other numerical parameters.

• **lmrInitials.xml** is used in conjunction with the thermal equilibration process to automatically handle setting up the initial conditions of a model.

• **lmrStart.xml** controls options such as whether the model is 2D or 3D, its resolution, whether to run the thermal equilibration mode or the coupled thermal-mechanical mode, details about the output directory, and other meta-model parameters.

• **lmrMain.xml** stitches together all *LMR* XML input files. This file is then passed to Underworld.

Figure 2 shows the layout of the XML files and their role within the *LMR*.

lmrRunModel Python script

The lmrStart.xml file and lmrMain.xml are read by the Python script lmrRunModel.py. This Python script evaluates the requested options from lmrStart.xml and builds the final *Underworld* XML input file. This includes evaluating which solver parameters to use - smaller models use *MUMPS,* a faster but a more memory-intensive direct solver, while large models use a multigrid solver with a direct *MUMPS* solve at the coarsest level of the multigrid stack. Users simply run 'python lmrRunModel.py' and the script handles running *Underworld*, masking this administrative and numerical complexity from the user.

<u>Included scripts and the earthbyte_additions toolbox</u>

The *LMR* comes with a number of scripts that make preprocessing and postprocessing *Underworld* models easier. For example, a Python script is included for generating finite strain ellipsoids as finite strain markers within the *Underworld* model, and a script for showing the semantic difference between two XML input files (for comparing two different models to each other). For postprocessing, *LMR* includes a number of scripts for cleaning up *Underworld* output files, and splitting output files into more manageable segments. It also includes *Paraview* macros, which are small scripts to automate *Paraview* functions. The macros enable the calculation of the principal stress axes and the tectonic stress regime classifier used in Mondy et al., 2017.

The earthbyte_additions toolbox is a plugin for *Underworld* itself, written in C. It adds a number of visco-plastic rheologies, and additional processes including: isostasy, partial melting, and simple surface-processes.

<u>4.2.3. Designed workflow</u>

The run the 2D or 3D LMR model, the first step is to generate the initial temperature field associated with the model at time t_0. The temperature field is created by activating the option *Thermal_Equilibration* in the lmrStart file, which runs the *LMR* over several hundred million years, during which only the energy equation is solved to produce a steady-state temperature field. Only a coarser resolution is needed to solve for the temperature field, which is then stored in its own folder (*initialcondition_192x96x0_laterally_homog*), and can be reused for multiple experiments. This operation takes only a few minutes on a typical laptop.

Once an appropriate initial temperature field has been calculated, the user switches off the *Thermal_Equilibration* option in the lmrStart script, and runs the model again. The *LMR* now runs a fully coupled thermo-mechanical model at

the default grid resolution of 2 km. The model runs over 20 million years, which delivers 400 kilometers of extension, producing the output shown in Figure 1. With the Stoke flow computations and higher resolution, the full model may take a number of hours to run - however, within a few minutes users will receive the first outputs in the form of a suite of .h5, .dat, .xmf and .xdmf files per timestep. These outputs can be examined on-the-fly within *Paraview* by loading the .xdmf files. Users may stop the model run at any time, and restart it from where it left off or from any timestep before. This workflow is described by the included *readme* file that comes with the *LMR* XML files. It also guides users to start making changes to the model, such as changing the velocity boundary conditions.

5. Design choices to address common issues and improve user experience

5.1. Pre-compiled software embedded into a Docker containers

Underworld is dependent on a number of external libraries, each with its own list of dependent libraries, as well as the earthbyte_additions toolbox, that need to be compiled before being able to run *Underworld*. As mentioned above, a major and immediate barrier for new users of computational modelling is the compilation of software and its various dependencies. This is a time consuming, convoluted process with many potential pitfalls. Out of date documentation, mis-typing or mis-copying commands, coupled with confusing error messages, all drastically affect users experience.

To iron-out this issue, the *LMR* is supplied within a *Docker image* in which all the dependencies and *Underworld* have been pre-compiled. The *Docker images* are accessible via a web browser *Docker Hub* or via a desktop program called *Kitematic*. With *Underworld-LMR* distributed via a *Docker image*, new users are given a much more consistent and engaging first experience with

```
<struct name="basal_heat_flow">
    <!-- Heat flow at _moho_ ranges from ~10 to ~20 mW/m^2
         See Jaupart and Mareschal, Treatise on Geophysics, 2007
         Adjust for depth to the base of your model. -->
    <param name="Type"> Ppc_Constant </param>
    <param name="Value" units="mW/(m*m)"> 20 </param>
</struct>
<!-- NOTE: The meltFraction functions are defined as:
         supersolidus = ( ( T - solidusT ) / ( liquidusT - solidusT ) ) - 0.5
         meltFraction = 0.5 + supersolidus + ( supersolidus^2 -0.25 ) *
                                             ( 0.4256 + 2.988 * supersolidus )
         As per McKenzie and Bickle, 1988.

         This has been modified as part of the EarthByte_Additions toolbox, so
         the melt fraction can be artificially limited. -->
<struct name="melt_fraction">
    <param name="Type">Ppc_PartialMelt_Limited</param>
    <param name="LiquidusTag"> LiquidusProperty </param>
    <param name="SolidusTag">  SolidusProperty </param>
    <param name="TemperatureTag"> temperature_ppc_wrapper </param>
    <param name="MeltLimitTag"> MeltFractionLimitProperty </param>
</struct>
```

Figure 3. *Examples of in-line comments that provide education for users about how certain functions behave. Commonly they are accompanied with references to give context to the values selected.*

computational tectonics. *Docker* provides also a number of additional benefits: it imposes no performance cost when running on Mac or Linux (as opposed to running virtual machines); *Docker images* can be deployed on some super-computing clusters; and *Docker images* can be tagged online, so the same environment can be used without being affected by newer versions or code changes, which enhances reproducibility.

5.2. Providing realistic and relevant models by default

Experience with new users has shown that including a fully-developed model of continental rifting by default helps new users to better understand the modelling workflow and its outputs. This is primarily because model outputs are familiar to geologists and tectonicists who are used to diagrams of continental rifting. Conversely, models that are numerically and geologically more simple, (e.g., a Rayleigh-Taylor instability, or a ball sinking through fluid), tend to abstract users away from the geological applications of numerical modelling. Giving users access to geologically realistic and relevant models is more engaging, and provides them with a clearer path towards reproducing other models they may have seen in the literature.

This approach further provides a compromise between new users' expectations of modelling and

the goal of using simple models. It is generally preferable that geodynamic models be as simple as possible in capturing the processes they are modelling, so as to avoid additional complexity potentially confounding interpretations or results. While this principle still holds true, the standard of a 'simple' model in modern geodynamic modelling publications has advanced to the point where a model like that provided by the *LMR* can be considered relatively simple.

5.3. Managing complexity via a layered exposure

The cost of supplying users with a fully-developed geologically realistic model is that they may feel overwhelmed with the amount of information needed for its design, and become unsure how to progress. The *LMR* uses a number of techniques to ensure the complexity users are exposed to progressively increases from a starting point at which modelling outputs can be produced quickly with minimum difficulties. With experience, and as new users want to go beyond the default *LMR* models, they will be gradually exposed to more complex settings, which may involve for instance time-dependent boundary conditions, or the introduction of processes such as shear-heating.

The *LMR's* modular XML input structure was designed to help new users compartmentalise the complexity of model, without necessarily hiding it from them. Each file tends to silo off a particular aspect of the model (Fig. 2), and new users are encouraged to focus on a small number of key XML files, and as they become more comfortable, start to explore other files covering more complex aspects. A similar strategy is also applied within the context of each XML input files, in which the most critical aspects of the model are placed at the top of the file. As the user scrolls down, the complexity increases.

This layered exposure to complexity is coordinated with detailed, informative, and research-relevant commentary within the XML files. Each of the input files comes with brief inline explanatory comments on the purpose of a particular section, the choice of default parameter values,(with

```
<struct>
    <!-- The pressure calibration plugin is used to ensure
         Underworld uses real-world pressure values (appr-
         oximately). Stokes flow only has a pressure grad-
         iant term, so the calibration plugin is used to
         ensure that the pressure at the surface is appro-
         ximately 0 Pa. This is important for rheologies
         that rely on the lithostatic pressure (e.g.,
         Drucker-Prager brittle faulting).
         The plugin calculates the average pressure across
         the top of the model, and removes that value from
         everywhere in the model. -->
    <param name="Type"> Underworld_PressureCalibration </param>
    <param name="Context"> context </param>
    <param name="UsingTopPressure"> True </param>
    <param name="ReferenceHeight"> maxY </param>
</struct>
```

Figure 4. *An example of a default setting that may never need to be adjusted. The additional context rewards users exploring other LMR files, even if they may never need to modify the parameter.*

accompanying references), and the calculation performed. It allows users not comfortable with exploring source codes to grasp why calculations are performed (Merali, 2010). For example, Figure 3 shows an example of explanation in relation to basal heat flow and partial melting.

Finally, the *readme* file that comes with the *LMR* gives a description of the workflow discussed in Section 4.2.3, and advises users to focus on three XML input files in particular: lmrVelocityBoundaries.xml, lmrThermalBoundaries.xml, and lmrMaterials.xml, as well as suggestions for how to modify them. For example, it suggests that users double the rate of extension for lmrVelocitiyBoundaries.xml and increase the basal temperature for lmrThermalBoundaries.xml. In both cases, the changes suggested are focused around the geological aspects of the model - tectonicists and structural geologists can hypothesise the outcome of each change (e.g., a narrow rift from the increase in divergent velocity, and a wide rift from the increased temperature (Buck et al., 1999)), and then observe the model outputs to test their predictions.

5.4. Setting reasonable defaults numerics for stable models

Certain parameters and functions must be tuned in *Underworld* to produce geologically robust and numerically stable models. For example, the *LMR*

sets the tolerances for both linear and non-linear solvers (the software tools used to compute the fluid flow) to 1e-6 and 1e-3, respectively, and enforces a minimum number of non-linear iterations. Furthermore, the *LMR* imposes a stricter time-stepping condition than the default in *Underworld*. Together, these values allows *LMR* to produce numerically stable models - meaning that each timestep converges rapidly, and the model outputs do not have any velocity 'flickering', where velocities (and correspondingly, strain-rates) jump up and down with each timestep. Similarly, by default the *LMR* imposes a pressure calibration step, where at the end of each calculation, the pressure field is adjusted to ensure the top of the domain is approximately 0 Pa, as shown in Figure 4. As the comment states, since Stokes flow only uses a pressure gradient term, the absolute pressure value is not important in computing flow. However, many rheologies rely on the lithostatic pressure, and so having a geologically meaningful pressure value is useful.

In both example cases, the defaults selected by the *LMR* are set so they will produce robust model results - but any intrepid users exploring the XML files can educate themselves as they progress.

To be able to produce high-resolution 2D or 3D models in a reasonable amount of time, an appropriate mathematical solver a set of options must be selected, and an appropriate element type (Q1P0, Q2Q1, Q2P1, etc.) must be chosen. The underlying solver software *PETSc* offers a large selection of solvers, but their effectiveness and the implications for choosing one over another are difficult to discern, even for experienced users. The *LMR* uses a set of solvers and options that have been intensively tested, and automatically makes a selection based on the size of the model, and on the configuration of a typical *LMR* model. This approach has been particularly effective, with most users never having to fine tune solver options, and is capable of performing well even when running large 3D experiments (Rey et al., 2017; Mondy et al., 2017).

```
<!-- === Example Ppc function for wallVC ============= -->
<!-- The following structs define a time dependent wall VC, where between
     t=0 and t=1myr, the wall velocity increases from 0.2 to -2.0 cm/yr.
     Note that the speed increase is linearly interpolated between one
     case to the next (hence the 'l' for linear in the "Interpolate"
     param).

     To use this function, change the left wallVC "type" to be "func", and
     set the "value" to be "left-wall-VC" (and get rid of any units). -->

<struct name="components" mergeType="merge">
    <struct name="current_time" mergeType="replace">
        <param name="Type"> Ppc_Current_Time </param>
    </struct>

    <struct name="left-wall-VC">
        <param name="Type"> Ppc_Switch </param>
        <param name="Field"> current_time </param>
        <param name="Interpolate"> l </param>
        <list name="CaseList">
            <struct>
                <param name="Case" units="Myr"> 0 </param>
                <param name="Value" units="cm/yr"> -0.2 </param>
            </struct>
            <struct>
                <param name="Case" units="Myr"> 1 </param>
                <param name="Value" units="cm/yr"> -2.0 </param>
            </struct>
        </list>
    </struct>
</struct>
```

Figure 5. *An example of a useful alternative. This XML block demonstrates how to implement a more complex velocity boundary condition, and makes it clear how to use it.*

5.5. Providing alternatives boundary conditions and rheologies

Comments within the XML are also used to highlight alternative functions users can choose from and implement. For example, the following comment and XML block is defined towards the end of the lmrVelocityBoundaries.xml file (Figure 5), and describes how to implement a time-dependent velocity boundary condition. By including comments and pre-defined alternative options, users are able to implement more advanced features.

Similarly, converting rheological parameters from published literature experiments can be challenging for new users. Parameters are often expressed in different units between publications, and may not use SI units in calculations. The *LMR* provides large range of viscous flow rheologies (accessible within the lmrRheologyLibrary.xml file) derived from published works, using a homogeneous set of units.

5.6. Automating special tasks

Some operations in *Underworld* require a workflow involving a number of steps, two examples being the production of the initial temperature field, and the restarting of a model from a given timestep. Thermal equilibration of a model requires configuring *Underworld* to remove the Stokes flow solvers, imposing a number of internal and boundary thermal conditions, and changing the model resolution to reach quickly a solution. Furthermore, to use the thermally equilibrated model as initial condition for the thermo-mechanical model, a number of parameters in XML must be adjusted. Performing this task manually can be tedious and error-prone, particularly for new users. Instead, the *LMR* uses the Python framework controlled by lmrStart.xml file to perform these operations. Similarly, while restarting a model in *Underworld* is not necessarily complex (it requires two command line arguments), it can be error-prone, and may overwrite data if performed incorrectly. In *LMR*, users can set a flag in lmrStart.xml to perform a restart, and the *LMR* performs the necessary operation, while saving a copy of the current state of the input files in a separate folder to ensure no data is lost.

As part of the *LMR*, certain functions, such as a simple surface processes, required some modifications to *Underworld*. Most of these modifications are stored as part of the "earthbyte_additions" toolbox. The toolbox sits within the *Underworld* source code and compiles against it. The toolbox provides four new rheology types (including differential stress limiters), and nine additional components (including the surface processes function).

5.7. Enabling field-like measurements

The *LMR* also comes with a number of scripts to: insert finite strain ellipsoids within *Underworld* models, and calculate tectonic stress regimes and extract PT paths. The purpose of these tools is to provide avenues for users to map observable most relevant to field geologists.

5.8. Summary

Exposing new users the full complexity of a lithospheric-scale model is not necessarily a barrier to entry, but must be managed in explicit ways (e.g, telling the user to focus on specific files, providing alternative options) and implicit ways (e.g.,

splitting up input files, ordering file contents from simple to complex). The *LMR* allows interesting and useful models to develop quickly and encourages deeper and iterative exploration of the *LMR*, thus keeping users engaged.

6. Impact of **LMR** on new users

The use of the *LMR* eases and reduces the training time, and new *Underworld* users can become mostly independent in 2-3 weeks, being able to reproduce a well-described published model. The decrease in training time is also enabling the use of *Underworld* in postgraduate research and undergraduate teaching. So far, the *LMR* has been used to support 5 Ph.D. theses, 5 Honours theses, and an undergraduate course on computational tectonics. While the overall goal of the *LMR* is to enable geologists to incorporate numerical modelling as part of their 'toolkit', it has enabled new users of Underworld to produce a number of research papers (e.g. Rey et al., 2017; Korchinski et al., 2018; 3 additional papers in prep.), and over 12 conference presentations.

7. Comparison to other codes

The only freely available, accessible, open-source geodynamic modelling codes we are aware of, besides *Underworld 1.8* and the *LMR*, are currently: *Underworld* 2.0 with the *UWGeodynamics* framework, *ASPECT*, *pTatin3D*, and *LaMEM*. Here we discuss how each one appeals to new users, based on the design choices described above.

7.1. Underworld 2.0 and UWGeodynamics

Underworld 2.0 (*UW2*) (Moresi et al., 2007; Mansour et al., 2019; https://github.com/underworldcode/underworld2) is the latest version of *Underworld*, and implements a Python-only interface to define and run models, instead of XML. *UW2's* Python interface provides a powerful way to programmatically design models, allowing fine grained control of both the numerical and geological definitions. This produces very transparent models, since almost every aspect controlling the

dynamics is 'on show' to a user reading an input script. However, it produces quite large input files that are not simple to split up, with the top of the files usually containing fundamental descriptions of the model setup, such as the gravitational body force definition, and the geological setup much further down.

Using Python (or any programming language) as a way to describe models can be very powerful, but does have drawbacks. Programming languages are typically designed to transform data, whereas markup languages (e.g., XML, HTML, or markdown) are used to describe and present data. Since most aspects of numerical model setup involve describing data (e.g., the shape of the domain, the shape of materials within the domain, which rheologies apply to each material, and the rheological parameters), using a markup language is a natural fit. Markup inputs also tend to be much easier for new users to learn and understand, compared to programming languages.

However, markup languages can result in very verbose inputs, particularly when required to define similar repeated structures (such as stratigraphic layers). Furthermore, any definitions that require calculations, for example, computing the temperature of oceanic crust using its age, need to have that functionality defined within the modelling code itself, as markup languages typically cannot perform such operations. Using a programming language avoids these issues by using functions and for-loops to minimise repetitive definitions, and can calculate any required data on the fly.

A new framework, *UWGeodynamics* (Beucher et al., 2019; Appendix III; https://github.com/underworldcode/UWGeodynamics), has recently been developed to sit on top of *Underworld 2.0*. It was inspired by, and uses data and functionality derived from the *LMR* (isostasy, finite strain markers, etc). The new *UWGeodynamics* framework aims to provide a similar service as the *LMR* by allowing users to focus more on the geological aspects of the model, and allowing numerical aspects to be

```
subsection Function
  set Variable names       = x,y,z
  set Function constants  = cm=0.01, year=1
  set Function expression =  if (x<56e3 && y<=48e3 | x<72e3 && y>48e3, -1*cm/year, 1*cm/year) ; 0 ; 0
end
```

Figure 6. *A function defined within an ASPECT input file, which allows users to use basic programmatic syntax to dynamically control aspects of the model.*

handled by the framework. The framework attempts to mitigate the challenges of using a programming language as input by making the Python input file more similar to a markup language. It uses a single module called 'Model' as data storage. Parameters can be passed to the Model module, and once it is completely constructed, it is passed to *UW2* to run. Similarly, the Model module handles tedious functions, like model restarts and thermal equilibration. The *UW2* and *UWGeodynamics* source codes both come with a number of example models, tutorials, guides, and inputs from published papers. There are a number of different approaches new users can take, with some taking users through the basics of *UW2* itself, some with more abstract models, and some with simplified models of geological settings. In each case, the input files are *Jupyter Notebooks*, which are Python programs that allow for formatted text and figures to be displayed along with code. *UW2* and *UWGeodynamics* both come with *Docker* images with built in *Jupyter Notebook* server, removing the need for users to compile *UW2*, and providing them with a web interface to run models. The markup/programming language hybrid within *UWGeodynamics* works well, but can still be challenging to inexperienced users, as they are required to learn Python (Merali, 2010).

7.2. ASPECT

ASPECT (Kronbichler et al., 2012; Heister et al., 2017; Bangerth et al., 2019; https://aspect. geodynamics.org) is a recent geodynamics code designed to simulate problems in thermal convection. It solves the same fundamental equations of Stokes flow and energy conservation using the same finite element method as *Underworld 1.8* and *Underworld 2.0*, but its usage, design, implementation, and dependent software stacks are entirely different (e.g., *PETSc* for *Underworld*, *deal.ii* for *ASPECT*). *ASPECT* also provides advanced numerical features, such as adaptive mesh refinement, which enables larger scale models to run in shorter processing times.

ASPECT uses a simple markup language to define models, most notable for its clear English, e.g., "set Angle of internal friction = 30". Model input files are typically short (~130 lines) and clear, and tend to focus heavily on the geological aspect of the model. It is also capable of simple programmatic functions (Figure 6) to define for example boundary or initial conditions. *ASPECT* has a large comprehensive manual and a folder of example models, known as cookbooks. The manual provides much details (over 250 pages) about the underlying physics and numerical modelling aspects of the framework, as well as walking users through many of the cookbook entries. The cookbooks themselves also come with some inline comments, explaining the basics of each code blocks. *ASPECT* models are generally new-user friendly, due to their simple and clear input markup. However, the manual and provided cookbooks tend to focus more on abstract models, and doesn't necessarily point new users to the more geologically relevant models that are available. Furthermore, it can be confusing for new users when and why different solver methods are introduced for certain models. *ASPECT* follows an approach that exposes new users to the technical and mathematical aspects of geodynamic modelling first, and the running of models later.

ASPECT comes with pre-built *Docker* images, and so means new users do not need to deal with compilation of the complex underlying software. Furthermore, because of its many numerical optimizations (e.g., adaptive mesh refinement),

ASPECT typically produces model outputs more quickly, allowing users to experiment more rapidly, and increasing the reproducibility of the models (Claerbout, 2006)).

7.3. pTatin3D

pTatin3D (May et al., 2014; https://bitbucket. org/ptatin/ptatin3d) is a highly scalable geodynamic modelling software for simulating large 3D problems. Similar to *Underworld*, it uses finite-elements with the underlying PETSc package. It is written specifically to run efficiently on very large supercomputers, since 3D problems are extremely resource intensive.

pTatin3D uses C files to define models, rather than using input files, and so must be compiled to produce a new program for each model. It also requires a number of PETSc options, often provided as files, to control the numerical solution of the problem.

pTatin3D comes with a number of example inputs and a manual to guide users - however, the use of C (a much more difficult language than for example Python), along with the largely undocumented numerous numerical PETSc options, and no supporting *Docker* image, indicates that this tool is not designed for new users to interact with easily.

7.4. LaMEM

LaMEM (Lithosphere and Mantle Evolution Model) (Popov and Kaus, 2013; https://bitbucket. org/bkaus/lamem) is a 2/3D thermomechanical code with a number of built in extras, such as a gravity solver, fluid pressure and Darcy flow, and simple surface processes. Unlike the other codes discussed here, it uses finite-difference to solve the underlying equations. It also uses PETSc, and is capable of scaling from a laptop to extremely large supercomputers.

LaMEM has a range of different input file formats: an English-like dat file format; Matlab scripts; and the ability to use external tool to create 3D model designs. The dat files typically contain

comments with brief explanations for each line. *LaMEM* also comes with a number of scripts to generate data for models, such as for creating an initial geotherm. These scripts are written in a mix of Matlab, Python, and C.

LaMEM comes with an online wiki, with a number of examples that guide the user from a 3D ball sinking through viscous fluid, to a subduction experiment, then a rifting experiment. The wiki is clearly laid out, with interesting experiments, and explains options users should change to see different results. While this gives new users a pleasant first experience, the lack of context around some of the input files, particularly in choosing the solvers, as well as needing to write scripts to setup input data, can be an intimidating second step. *LaMEM* also does not come with a *Docker* image, making compilation another potential stumbling block.

8. Discussion

The *LMR* framework presented here enables tectonicists and structural geologists to incorporate geodynamic modelling into their 'toolkit', to test their conceptual models and experiment with new hypotheses. There are, however, risks for new users modifying the default experiment to produce experiments that either a) reinforce their desired results ("garbage in, garbage out"), or b) unknowingly produce results they believe are useful, but are instead numerical artefacts, or geologically meaningless.

Gerya warns against this: "... Just be aware that numerical geodynamic modelling is not 'pressing the button and automatically obtaining results' but knowing in depth what you and your code are doing. So, don't play a lottery by starting your numerical career by immediately using these codes as research tools… there is a big risk that your 'automatically obtained results' appearing after 'pressing the button' will be EXTREMELY WRONG." (Gerya, 2009, p.269). He instead advises users to study carefully how numerical modelling is performed to understand the advantages and limitations of

different numerical modelling techniques.

While these concerns are valid, they may also be the reason we have seen less uptake of such tools with tectonicists and structural geologists. Many new users, for example, will gravitate to using existing tools, such as *Underworld* or *ASPECT*, both of which are written and optimised for performance (and not necessarily understandability), rather than initially attempting to write their own tools or reach for a textbook. As experience with *LMR* has shown, allowing new users to rapidly produce robust models motivates users to learn more about numerical aspects of geodynamic modelling. However, making a code user-friendly does not mean it is a license to produce nonsensical results. The modeller has the responsibility to develop a knowledge base sufficient to understand what goes into the model, which equations are being solved, and how to assess and interpret the numerical validity of model outputs. Tectonicists and structural geologists are the people best placed to evaluate the geological pertinance of these model outputs, and so ensuring these tools are accessible to them is critical.

Another benefit of engaging tectonicists and structural geologists is diversifying the peer-review community (Munafò et al., 2017). This will allow a wider community to a) be more critical readers (Hatton, 1997; Gil et al., 2016), b) encourage transparency by encouraging the publication of input files (Piwowar et al., 2007; Vandewalle, 2012), and c) to promote reproducibility.

The benefits of engaging non-technical users has been demonstrated with the introduction of Google Earth (Lisle, 2006). Google Earth greatly simplified access to both geographical information tools (e.g., Patterson, 2007), and interactions with very large datasets (e.g., Gorelick et al., 2017) to audiences outside the traditional user-base of GIS specialists and geoscientists (Yu, L. and Gong, P., 2012). While geodynamic numerical modelling may not require such a similarly broad explosion in use, progress towards user-friendliness for

non-expert users can hopefully spawn a similar revolution in how these tools are applied.

9. Conclusion

Engaging tectonicists and structural geologists in numerical geodynamic modelling has a number of benefits: they are empowered to test their ideas in a self-consistent tectonic framework; they are able to better interpret and review claims made about geodynamic models; and they diversify and enrich the field of numerical geodynamic modelling. A number of approaches have been examined in this paper that seek to reduce the barriers of entry to numerical geodynamic modelling for users, and how the *LMR*, in particular, solves many of them by tailoring the experience of users with *Underworld*. We encourage other geoscientific tool creators to engage in similar user-friendly design choices.

10. Acknowledgements

11. References

Bangerth, W., Dannberg, J., Gassmoeller, R., and Heister, T., 2019, April 29. ASPECT v2.1.0. Zenodo. https://doi.org/10.5281/zenodo.2653531

Bassi, G., 1991. Factors controlling the style of continental rifting: insights from numerical modelling: Earth and Planetary Science Letters, v. 105, p. 430–452, doi: 10.1016/0012-821X(91)90183-I.

Beaumont, C., Fullsack, P., and Hamilton, J., 1994. Styles of crustal deformation caused by subduction of the underlying mantle. Tectonophysics, 232, 119-132.

Beucher, R., Moresi, L., Giordani, J., Mansour, J., Sandiford, D., Farrington, R., Mondy, L., Mallard, C., Rey, P., Duclaux, G. and Kaluza, O., 2019. UWGeodynamics: A teaching and research tool for numerical geodynamic modelling. *Journal of Open Source Software*, *4*(36), p.1136.

Buck, W.R., Lavier, L.L. and Poliakov, A.N., 1999. How to make a rift wide. Philosophical Transactions of the Royal Society of London. Series A: Mathematical, Physical and Engineering Sciences, 357(1753), pp.671-693.

Chery, J. Vilotte, J.-P. and Daignieres, M., 1991. Thermomechanical evolution of a thinned continental lithosphere under compression: Implications for the Pyrenees. Journal of Geophysical Research: Solid Earth 96 (B3), p. 4385-4412

Choi, E., Tan, E., Lavier, L.L. and Calo, V.M., 2013. DynEarthSol2D: An efficient unstructured finite element method to study long□term tectonic deformation. Journal of Geophysical Research: solid earth, 118(5), pp.2429-2444.

Claerbout, J., 2006, Preface to SEP report 124, Technical Project Report, Stanford Exploration Project, 22 February 2006. [Available at http://sepwww.stanford. edu/data/media/public/sep//jon/repropreface.html.]

Connolly J.A.D., and Petrini K., 2002. An automated strategy for calculation of phase diagram sections and retrieval of rock properties as a function of physical conditions. Journal of Metamorphic Geology, v. 20, p. 697-708.

Crameri, F., Schmeling, H., Golabek, G.J., Duretz, T., Orendt, R., Buiter, S.J.H., May, D.A., Kaus, B.J.P., Gerya, T.V. and Tackley, P.J., 2012. A comparison of numerical surface topography calculations in geodynamic modelling: an evaluation of the 'sticky air'method. Geophysical Journal International, 189(1), pp.38-54.

Demouchy, S., Tommasi, A., Ballaran, T. B., and Cordier, P., 2013, Low strength of Earth's uppermost mantle inferred from tri-axial deformation experiments on dry olivine crystals: Physics of the Earth and Planetary Interiors, v. 220, p. 37-49.

de Capitani C. and Petrakakis K., 2010. The computation of equilibrium assemblage diagrams with Theriak/ Domino software. American Mineralogist, v.95, p. 1006-1016

Faniel, I.M. and Jacobsen, T.E., 2010. Reusing scientific data: How earthquake engineering researchers assess the reusability of colleagues' data. Computer Supported Cooperative Work (CSCW), 19(3-4), pp.355-375.

Garrett, R. (2014) Modelling the Impact of Salt's Thermal Conductivity on Temperature Distribution in the Context of Salt Tectonics [Bachelor of Arts/Bachelor of Science (Adv)(Hons): University of Sydney

Gerya, T., 2009. Introduction to numerical geodynamic modelling. Cambridge University Press.

Gerya, T., and Tackley, P., 2012, A comparison of

numerical surface topography calculations in geodynamic modelling: An evaluation of the 'sticky air' method: Geophysical Journal International, v. 189, no. 1, p. 38-54.

Gil, Y., David, C.H., Demir, I., Essawy, B.T., Fulweiler, R.W., Goodall, J.L., Karlstrom, L., Lee, H., Mills, H.J., Oh, J.H. and Pierce, S.A., 2016. Toward the geoscience paper of the future: best practices for documenting and sharing research from data to software to provenance. Earth and Space Science, 3(10), pp.388-415.

Gorelick, N., Hancher, M., Dixon, M., Ilyushchenko, S., Thau, D. and Moore, R., 2017. Google Earth Engine: Planetary-scale geospatial analysis for everyone. Remote Sensing of Environment, 202, pp.18-27.

Govers, R., and Wortel, M.J.R., 1995. Extension of stable continental lithosphere and the initiation of lithospheric scale faults. Tectonics, v. 14-4, p. 1041-1055.

Hatton, L., 1997. The T-experiments: errors in scientific software. In Quality of Numerical Software (pp. 12-31). Springer, Boston, MA.

Heister, T., Dannberg, J., Gassmöller, R., and Bangerth, W., 2017, "High Accuracy Mantle Convection Simulation through Modern Numerical Methods – II: Realistic Models and Problems." Geophysical Journal International 210 (2) (May 9): 833–851. doi:10.1093/ gji/ggx195. http://dx.doi.org/10.1093/gji/ggx195.

Hirth, G., and Kohlstedt, D., 2003, Rheology of the upper mantle and the mantle wedge: A view from the experimentalists: Inside the subduction Factory, p. 83-105.

Holland, T.J.B., and Powell, R., 1998. An internally-consistent thermodynamic dataset for phases of petrological interest. Journal of Metamorphic Geology 16, 309-344.

Ioannidis, J.P., Allison, D.B., Ball, C.A., Coulibaly, I., Cui, X., Culhane, A.C., Falchi, M., Furlanello, C., Game, L., Jurman, G. and Mangion, J., 2009. Repeatability of published microarray gene expression analyses. Nature genetics, 41(2), p.149.

Korchinski, M., Rey, P.F., Mondy, L., Teyssier, C. and Whitney, D.L., 2018. Numerical investigation of deep-crust behavior under lithospheric extension. Tectonophysics, 726, pp.137-146.

Kronbichler, M., Heister, T., and Bangerth, W., 2012. High accuracy mantle convection simulation through modern numerical methods. Geophysical Journal International, v. 191, p. 12-29. doi:10.1111/j.1365-246x.2012.05609.x

Lisle, R.J., 2006. Google Earth: a new geological resource. Geology today, 22(1), pp.29-32.

Mansour, J., Kaluza, O., Giordani, J., Beucher, R., Farrington, R., Kennedy, G., Moresi, L., Velic, M., Beall, A., Laik, A., Sandiford, D., Mather, B., 2019. underworldcode/underworld2: v2.8.1b. doi:10.5281/zenodo.3384283

May, D.A., Brown, J. and Le Pourhiet, L., 2014, November. pTatin3D: High-performance methods for long-term lithospheric dynamics. In Proceedings of the international conference for high performance computing, networking, storage and analysis (pp. 274-284). IEEE Press.

McKenzie, D., and Bickle, M., 1988, The volume and composition of melt generated by extension of the lithosphere: Journal of petrology, v. 29, no. 3, p. 625-679.

Merali, Z., 2010. Computational science: Error, why scientific programming does not compute. Nature, 467(7317), pp.775-777.

Mondy, L.S., Rey, P.F., Duclaux, G. and Moresi, L., 2017. The role of asthenospheric flow during rift propagation and breakup. Geology, 46(2), pp.103-106.

Moresi, L., Dufour, F., and Muhlhaus, H.B., 2002, Mantle convection modeling with viscoelastic/brittle lithosphere: Numerical methodology and plate tectonic modeling: Pure And Applied Geophysics, v. 159, no. 10, p. 2335–2356, doi: 10.1007/s00024-002-8738-3.

Moresi, L., Dufour, F., and Muhlhaus, H.B., 2003. A Lagrangian integration point finite element method for large deformation modeling of viscoelastic geomaterials: Journal of Computational Physics, v. 184, no. 2, p. 476–497.

Moresi, L., Quenette, S., Lemiale, V., Meriaux, C., Appelbe, B., and Mühlhaus, H.-B., 2007, Computational approaches to studying non-linear dynamics of the crust and mantle: Physics of the Earth and Planetary Interiors, v. 163, no. 1, p. 69-82.

Munafò, M.R., Nosek, B.A., Bishop, D.V., Button, K.S., Chambers, C.D., Du Sert, N.P., Simonsohn, U., Wagenmakers, E.J., Ware, J.J. and Ioannidis, J.P., 2017. A manifesto for reproducible science. Nature human behaviour, 1(1), p.0021.

O'Neill, C., Moresi, L., Mueller, R. D., Albert, R. and Dufour, F., 2006. Ellipsis 3D: a particle-in-cell finite-element hybrid code for modelling mantle convection and lithospheric deformation. Computer and Geosciences, v. 32, p. 1769-1779.

Ord, A., Hobbs. B., 1989. The strength of the continental crust, detachment zones and the development of plastic instabilities. Tectonophysics, v.158, p. 269-289.

Paterson, M., and Luan, F., 1990, Quartzite rheology under geological conditions: Geological Society,

London, Special Publications, v. 54, no. 1, p. 299-307.

Patterson, T.C., 2007. Google Earth as a (not just) geography education tool. Journal of Geography, 106(4), pp.145-152.

Piwowar, H.A., Day, R.S. and Fridsma, D.B., 2007. Sharing detailed research data is associated with increased citation rate. PloS one, 2(3), p.e308.

Poliakov, A.N.B., Van Balen, R., Podladchikov, Y., Daudre, B., Cloetingh, S.A.P.L. and Talbot, C., 1993. Numerical analysis of how sedimentation and redistribution of surficial sediments affects salt diapirism. Tectonophysics, 226(1-4), pp.199-216.

Popov, A. and Kaus, B., 2013, April. LaMEM (Lithosphere and Mantle Evolution Model): advancing a staggered-grid finite difference version of the code. In EGU General Assembly Conference Abstracts (Vol. 15).

Powell, R., and Holland, T.J.B., 1988 An internally consistent thermodynamic dataset with uncertainties and correlations: 3: application methods, worked examples and a computer program. Journal of Metamorphic Geology 6, 173-204.

Powell, R., Holland, T.J.B., and Worley, B., 1998. Calculating phase diagrams involving solid solutions via non-linear equations, with examples using THERMOCALC Journal of Metamorphic Geology 16, 577-588.

Rey, P., and Müller, R., 2010, Fragmentation of active continental plate margins owing to the buoyancy of the mantle wedge: Nature Geoscience, v. 3, no. 4, p. 257-261.

Rey, P.F., Mondy, L., Duclaux, G., Teyssier, C., Whitney, D.L., Bocher, M. and Prigent, C., 2017. The origin of contractional structures in extensional gneiss domes. Geology, 45(3), pp.263-266.

Richter, F. M. (1978). Mantle convection models. *Annual Review of Earth and Planetary Sciences*, *6*(1), 9-19.

Tapponnier, P., Peltzer, G., Le Dain, A.Y., Armijo, R., and Cobbold, P., 1982. Propagating extrusion tectonics in Asia: New insights from simple experiments with plasticine. Geology, v.10, p. 611-616.

Vandewalle, P., 2012. Code sharing is associated with research impact in image processing. Computing in Science & Engineering, 14(4), pp.42-47.

Wang, Y., Zhang, J., Jin, Z., and Green, H., 2012, Mafic granulite rheology: Implications for a weak continental lower crust: Earth and Planetary Science Letters, v. 353, p. 99-107.

Yu, L. and Gong, P., 2012. Google Earth as a virtual globe tool for Earth science applications at the global scale: progress and perspectives. International Journal of Remote Sensing, 33(12), pp.3966-3986.

Zhong, S. and Watts, A. B., 2013. Lithospheric deformation induced by loading of the Hawaiian Islands and its implications for mantle rheology. Journal of Geophysical Research, v. 118, 1–24.

Table 1. Parameters used in the default LMR model.

Parameter	Description	Air	UC	LC	Mantle
Reference density, ρ_r (kg m^{-3})	The density of material at room temperature. Note that the LMR uses the Boussinesq approximation, meaning a material's density may change without changing its volume.	1	2800	2900	3300
Thermal expansivity, α (K^{-1})	Controls the density response to temperature via $\rho = \rho_r * (1 - (\alpha * (\text{temperature} - \text{room temperature})))$	3.00E-05			
Heat capacity, C_p (J K^{-1} kg^{-1})	The amount of energy required to heat a unit of rock material per unit of temperature.	1000	1000	1000	1000
Thermal diffusivity, α (m^2 s^{-1})	A measure of the rate of heat transfer through a material.	1.00E-05	1.00E-06	1.00E-06	1.00E-06
Latent heat of fusion, L_f (kJ kg^{-1})	A measure of the energy consumed during a phase change from solid to liquid. Used in the calculation of partial melting.	n/a	300	300	300
Radiogenic heat production, A (W m^{-3})	The amount of heat produced by the decay of radioactive elements in this material.	0	1.20E-06	6.00E-07	2.00E-08
Melt density change fraction, M $\Delta\rho r$	The fraction that the density of a material reduces by when fully melted.	n/a	0.13	0.13	0.13
Liquidus term 1, t1 (K)	A term used in calculating the liquidus, derived from lab experiments in McKenzie and Bickle (1988)	n/a	1493	1493	2013
Liquidus term 2, t2 (K Pa^{-1})	See above	n/a	-1.20E-07	-1.20E-07	6.15E-08
Liquidus term 3, t3 (K Pa^{-2})	See above	n/a	1.60E-16	1.60E-16	3.12E-18
Solidus term 1, t1 (K)	See above	n/a	993	993	1393.661
Solidus term 2, t2 (K Pa^{-1})	See above	n/a	-1.20E-07	-1.20E-07	1.33E-07
Solidus term 3, t3 (K Pa^{-2})	See above	n/a	1.20E-16	1.20E-16	-5.10E-18
Softening strain	The amount of finite strain a material has to accumulate to become fully weakened.	n/a	0.2	0.2	0.2
Friction coefficient	Part of the Drucker-Prager yield criterion for brittle deformation. The friction coefficient represents the measure of a material to withstand a shear stress, and controls fault angles.	n/a	0.577	0.577	0.577
Softened friction coefficient	Once a material faults, the material is weakened. As the finite strain accumulates, the material's friction coefficient reduces to this value until fully weakened.	n/a	0.1154	0.1154	0.1154

Cohesion, C (MPa)	Part of the Drucker-Prager yield for brittle deformation. The cohesion represents the component of shear strength not related to the friction of particles within the rock, and instead processes such as cementation.	n/a	10	20	10
Softened cohesion, C (MPa)	Once a material faults, the material is weakened. As the finite strain accumulates, the material's cohesion reduces to this value until fully weakened.	n/a	2	4	2
Pre-exponential factor, A ($MPa^{-n}\ s^{-1}$)	A mediating parameter describing the relationship between stress and strain in a rock. Derived from laboratory experiments. Commonly additional parameters are combined into this variable, such as water fugacity or grain size. This is used in the calculation of viscous flow behavior.	n/a	6.61E-08	1.00E-01	1600
Stress exponent, n	The non-linearity of the strain response to applied stress. Derived from laboratory experiments. This is used in the calculation of viscous flow behavior.	n/a	3.1	3.2	3.5
Activation energy, E (kJ mol^{-1})	Required thermal energy input to allow chemical reactants to transform into products. Defines part of the rheological behavior relating to temperature. This is used in the calculation of viscous flow behavior.	n/a	135	244	520
Activation volume, V ($m^3\ mol^{-1}$)	Defines part of the rheological behavior relating to the pressure. This is used in the calculation of viscous flow behavior.	n/a	0	0	2.30E-05
Water fugacity	Parameter regarding the availability of water within the system, and how this affects the stress-strain relationship of a rock.	n/a	0	0	1000
Water fugacity exponent	The non-linearity of the water fugacity.	n/a	0	0	1.2
Melt viscous softening factor	The factor that a material's viscosity should drop by. This models the partial melt being fully connected, and so allowing mineral grains to slip past each other.	n/a	1.00E-03	1.00E-03	1.00E-01
Melt fraction range for viscous softening	The melt fraction at which melt begins to become fully connected, and hence become weaker.	n/a	0.2 - 0.3	0.2 - 0.3	0 - 0.02

Discussion and Conclusions

Despite the overall extensional kinematics of continental rift systems, the occurrence of non-extensional (i.e., contractional or transcurrent) deformation, such as reverse faults, strike-slip faults and low amplitude folds, and basin depth inversions, is a common feature of many passive margins around the world (Boldreel and Andersen, 1993; Withjack et al., 1998; Schlische et al., 2003; Cloetingh et al., 2008; Lundin and Doré, 2011; Holford et al., 2014). The ubiquity of these basin inversion features implies that, whatever is the process behind this inversion, it must be operating at most rift margins, and not dependent on unusual conditions. It has long been suspected that the upwelling asthenosphere, during active or passive rifting, can impose a significant stress onto developing continental margins, induced by the buoyancy force between the colder, denser rift flanks and the hotter, lighter asthenospheric upwelling (Le Pichon et al., 1982; Turcotte and Emerman, 1983; Le Pichon and Alvarez, 1984). The role of 'rift-push' in developing continental margins, however, has received relatively little detailed attention (Davis and Kusznir, 2002). Because of the complex dynamics and the non-linear processes at work during continental rifting, it has remained unclear how large a role rift-push plays in causing or mediating contractional or transcurrent deformation observed at passive margins, or in explaining basin depth inversion.

The experiments performed in Chapters 3 and 4 use high-resolution thermo-mechanical numerical models to investigate the role buoyancy forces play within continental rifting. To do so, we map Andersonian stress regimes throughout the entire domain, to reveal areas in tectonic extensional, compressional, or transcurrent stress. The experiments confirm the results of a number of previous studies. They show that at the onset of the exhumation of the asthenosphere, the stress acting on the lithospheric mantle in the rift flanks rapidly switches from extensional to compressional, as the rift-push force is somewhat resisted by the imposed kinematic boundary conditions (Turocotte and Emerman, 1983; Huismanns et al, 2001; Davis and Kusznir, 2002). As rifting progresses, the experiments also show a build-up of excess gravitational potential energy (GPE) in the asthenospheric dome, with respect to adjacent rift flanks (Chapter 4, Pascal and Cloetingh, 2009). Notably, experiments with higher rifting velocities (>2 cm/yr) produce zones of compression in the crust inboard of the developing continental margin well before breakup (Chapter 3). In these experiments, the maximum stress reaches approximately 30 MPa in the fastest experiments, with an average of 10 to 20 MPa. This level of deviatoric stress is compatible with the relatively small-scale contractional structures found on passive margins (Withjack et al., 1998; Schlische et al., 2003). The variation in magnitude between slow and fast extension experiments may be explained by the variation in the density of the upwelling asthenosphere, with slower rift velocities resulting in a cooler, and more dense asthenosphere that leads to a correspondingly smaller rift-push force. This

result builds upon the work by Newman and White (1999) and Huismanns et al. (2001), both showing some compression acting on rift flanks, though due to the numerical resolution available at the time, upper crustal and basin structures cannot be resolved, and tend to show much higher values (up to 100 MPa).

The introduction of simple surface processes in our experiments, accounting for accumulation of sediments on the continental margins and the formation of rift basins, shows that basins tend to localise compressional stress. We attribute this localisation to the combination of the regional rift-push and local crustal buoyancy forces that derive from the presence of large volumes of the less dense sediments (e.g. Le Pichon and Alvarez, 1984). Furthermore, the sediments filling the basins acts in opposition to both the thinning of the lithosphere as well as the upwelling of the asthenosphere, delaying break up (Burov and Poliakov, 2001). When the sediment supply stops however, our experiments show the upwelling asthenosphere is less restrained and capable of inducing a significant basin depth inversion of around 1 to 2 km, which may explain the formation of the break-up unconformity documented on many passive margins.

It is hypothesised that the diachronous break-up of the continental lithosphere along a rift axis, either via an active mantle upwelling or through the kinematics of plate movements on a sphere, has a number of impacts on margin development, including volcanism, basin depth changes, and syn-rift margin deformation (Withjack et al., 1998; Schlische et al., 2003; Franke, 2013; Lundin et al., 2014). In Chapter 4 of this thesis, we test this idea by modelling a continental rift system close to an Euler pole. Kinematically, the divergent velocity of a rift increases as a function of the distance to the Euler pole, and so break-up and asthenospheric doming occurs earlier further from the Euler pole, and later to close to it. In these experiments, the velocity of extension increases along the rift axis, from the slow end at 0.5 cm/yr (close to the Euler pole) to the fast end at 5 cm/yr (distal to the Euler pole). They show, as per Chapter 3, that a component of the rift-push force is acting orthogonal to the rift axis, and is able to induce compressional stress in the passive margins. However, a component of rift-push force is also acting parallel to the rift axis, since the hot upwelled asthenosphere at the fast end is juxtaposed along the rift axis against the relatively unthinned, cold continental lithosphere at the slow end. The result of the interaction of the two components of rift-push force is a transition from extensional to transcurrent stress within the rift flanks, with some areas in the stretched margin crust showing compressional stress. These experiments confirm the idea that diachronous rifting along a margin can induce non-extensional deformation in the rift system. However, our experiments show that the rift-parallel gravitational force induces a velocity component of asthenospheric flow in the direction of the Euler pole, and a deviatoric stress promoting the self-propagation of the rift along its strike, indicating that deep mantle processes (e.g. deep mantle upwelling, or mantle plume) may not be necessary to explain non-extensional structures observed on passive margins (Withjack et al., 1998; Schlische et al., 2003). The experiments also reproduce a number of features found in nature, including the distinct pattern of extensional, to compressional, to transcurrent stress regimes with increasing distance from the Euler pole; matching patterns seen in earthquake focal mechanisms in regions rifting close to Euler poles, such as the Woodlark Basin, and the Galapagos Rise (Taylor et al., 1995; Floyd et al., 2002).

The experiments performed in Chapters 3 and 4 confirm that buoyancy forces from the upwelling mantle are a significant contributor to the structural evolution of passive margins, and explain many observations that do not conform to plate tectonics kinematic models of continental rifting and oceanization. This is reinforced by the work done in Appendix I and II, that demonstrate a similar effect within metamorphic core complexes. These works show how buoyancy forces acting on a relatively weak lower crust can produce, during extension, contractional structures in the form of double-dome structures. The resulting structural pattern involves high-strain contractional structures sandwiched between extensional domains that form contemporaneously, despite the applied divergent boundary condition.

As illustrated in this thesis, numerical modelling is becoming an important contributor to modern geosciences. In Chapter 5, we presented the design a more accessible, field geologist-friendly numerical modelling framework, called the *Lithospheric Modelling Recipe* (*LMR*). We detailed the specific design choices used to lower the barrier to entry to new users, and compare our work to other numerical modelling codes. We find that the inclusion of a realistic and customizable model improves the engagement of new user. Coupled with clear avenues for new users to engage with modifying this model, the LMR reduces the training time required for new users to become self-sufficient.

Including a broader range of people into geodynamics has a number of benefits, including: giving geoscientists the tools to test and experiment with their ideas in a self-consistent framework; diversifying and enlarging the community able to critically assess numerical modelling outputs; and enabling the community most familiar with natural structures and processes to assess the relevance and pertinence of model outputs.

FUTURE WORK

This thesis has used numerical modelling to investigate and quantify some of the geodynamic processes involved in continental rifting. However, in all experiments, we have generated tectonic force via the imposition of kinematic boundary conditions. While this is a commonly accepted approach for driving far-field tectonic forces, it implies that processes emerging within the rift system, and the magnitude of the all the acting forces, must also obey the imposed kinematic boundary conditions. Measuring the tectonic force resulting from the kinematic boundaries shows that at the beginning of an experiment, when the lithosphere is at its strongest, the magnitude of the force required to initiate rifting at the imposed velocity is high. As the lithosphere weakens through deformation and thinning, the magnitude of the force required to pull at the same imposed velocity goes down. This is further complicated by the evolving dynamics of the model. Indeed, as the mantle transition from a passive to an active role, the boundary conditions get in the way of the dynamic of the system, since the active mantle may induce a velocity higher than allowed by the boundary condition, and hence generate local compressive stresses.

This kinematic approach to far-field tectonic force was tested by Brune et al. (2016), where they instead used a dynamic boundary condition to rift the continental lithosphere. Since the amount of force is fixed, the velocity of rifting changes through time. The experiments showed that while the lithosphere is still strong, rifting velocity is low; and that as deformation and thinning occur, and correspondingly the lithosphere weakens, the rift velocity

accelerates. These experiments demonstrate realistic rift development, that matches the evolution of many natural passive margins.

An issue with these experiments, as identified by the authors, is that once the lithosphere is sufficiently weak, rift velocities become unrealistically fast, since the same amount of force applied at the start of the experiment is now pulling on a much weaker system. In reality, it is more likely that the magnitude of force a subducting slab is able to provide to a rift system changes as a function of the length of the subducted slab, as well as its interaction with the 660 km mechanical transition. Recent global 2D models of mantle convection confirm this, showing that the force available to rifting changes as subduction evolves (Ulvrova et al., 2019).

Investigating how rifting affects the broader plate tectonic dynamics, and the feedbacks it may produce, is an interesting future research direction. As described, the experiments performed in both Chapters 3 and 4 show that the buoyant forces in the mantle can exceed the applied tectonic boundary conditions, resulting in compressional and transcurrent stresses - but it is unclear how a system including the subducting slab would react to this, for example, the switch to active rifting may instead increase sinking velocity of the slab, rather than induce compression in the rift margins. Of particular interest is how the experiments of rifting near an Euler pole in Chapter 4 would evolve with dynamic boundary conditions. The boundary conditions applied in the experiment dictate the location of the Euler pole at a fixed position; however, in nature, the Euler pole location is determined by the overall force balance that results in the final plate movements, indicating they are able to move and migrate (e.g., Lundin et al., 2014).

The force required to rift in these experiments changes along the margin and through time. At the beginning of the experiment, more force is required to rift at the fast end of the model than at the slow end, since the imposed rift velocity is higher at the fast end (and the lithosphere is homogeneous along the rift axis). However, since the fast end reaches break-up earlier, the force required to continue to pull it at the imposed extension velocity is greatly reduced compared to the relatively unthinned slow end of the model. Furthermore, the rift-push force induced by the upwelling asthenosphere at the fast end further reduces the required force to pull orthogonal to the rift.

Future experiments using dynamic force boundary conditions, or within a whole Earth model, would allow the investigation of these complex force dynamics. While it is likely that the Euler pole would migrate away from the rift, unzipping the continental plate, the complexities of the dynamic feedbacks on to the slabs driving this process make it difficult to predict (Brune, 2018).

Performing such experiments will likely require new tools, to both perform the high resolution tectonic models required, and to incorporate additional relevant processes, such as surface processes. It is therefore critical to ensure that these tools are as usable and approachable as possible, not only for the scientific robustness and reproducibility it encourages (as discussed in Chapter 5), but also because the breadth of knowledge required to design inputs, and understand the outputs, of such models is likely to require a team with a broad range of field expertise. Ensuring a broader spectrum of geoscientists can experiment, investigate,

explore, and verify the processes in and outside their expertise is therefore an important part of building numerical tools.

REFERENCES

Boldreel, L.O. and Andersen, M.S., 1993, January. Late Paleocene to Miocene compression in the Faeroe–Rockall area. In Geological Society, London, Petroleum Geology Conference series (Vol. 4, No. 1, pp. 1025-1034). Geological Society of London.

Brune, S., Williams, S.E., Butterworth, N.P. and Müller, R.D., 2016. Abrupt plate accelerations shape rifted continental margins. Nature, 536(7615), p.201.

Brune, S., 2018. Forces within continental and oceanic rifts: Numerical modeling elucidates the impact of asthenospheric flow on surface stress. Geology, 46(2), pp.191-192.

Burov, E. and Poliakov, A., 2001. Erosion and rheology controls on synrift and postrift evolution: Verifying old and new ideas using a fully coupled numerical model. Journal of Geophysical Research: Solid Earth, 106(B8), pp.16461-16481.

Cloetingh, S., Beekman, F., Ziegler, P.A., van Wees, J.-D., and Sokoutis, D., 2008. Post-rift compressional reactivation potential of passive margins and extensional basins, in Johnson, H., et al., eds., The Nature and Origin of Compression in Passive Margins. Geological Society of London Special Publication 306, p. 27–70, https://doi.org/10.1144/SP306.2.

Davis, M., and Kusznir, N., 2002, Are buoyancy forces important during the formation of 204

rifted margins?: Geophysical Journal International, v. 149, p. 524–533, 205 https://doi.org/10.1046/j.1365-246X.2002.01666.x.

Floyd, J.S., Tolstoy, M., Mutter, J.C. and Scholz, C.H., 2002. Seismotectonics of mid-ocean ridge propagation in Hess Deep. Science, 298(5599), pp.1765-1768.

Franke, D., 2013. Rifting, lithosphere breakup and volcanism: Comparison of magma-poor and volcanic rifted margins. Marine and Petroleum geology, 43, pp.63-87.

Holford, S.P., Tuitt, A.K., Hillis, R.R., Green, P.F., Stoker, M.S., Duddy, I.R., Sandiford, M., and Tassone, D.R., 2014. Cenozoic deformation in the Otway Basin, southern Australian margin: Implications for the origin and nature of post breakup compression at rifted margins. Basin Research, v. 26, p. 10–37, https://doi.org/10.1111/bre.12035.

Huismans, R.S., Podladchikov, Y.Y. and Cloetingh, S., 2001. Transition from passive to active rifting: Relative importance of asthenospheric doming and passive extension of the lithosphere. Journal of Geophysical Research: Solid Earth, 106(B6), pp.11271-11291.

Le Pichon, X., Angelier, J. and Sibuet, J.C., 1982. Plate boundaries and extensional tectonics. Tectonophysics, 81(3-4), pp.239-256.

Le Pichon, X. and Alvarez, F., 1984. From stretching to subduction in back-arc regions: Dynamic considerations. Tectonophysics, 102(1-4), pp.343-357.

Lundin, E.R. and Doré, A.G., 2011. Hyperextension, serpentinization, and weakening: A new paradigm for rifted margin compressional deformation. Geology, 39(4), pp.347-350.

Lundin, E.R., Redfield, T.F., Péron-Pindivic, G. and Pindell, J., 2014, January. Rifted continental margins: Geometric influence on crustal architecture and melting. In 33rd Annual GCSSEPM Foundation Bob F. Perkins Conference. Sedimentary Basins: Origin, Depositional Histories, and Petroleum Systems. Gulf Coast Section SEPM, Houston, TX (Vol. 18, p. 53).

Newman, R. and White, N., 1999. The dynamics of extensional sedimentary basins: constraints from subsidence inversion. Philosophical Transactions of the Royal Society of London. Series A: Mathematical, Physical and Engineering Sciences, 357(1753), pp.805-834.

Pascal, C. and Cloetingh, S.A., 2009. Gravitational potential stresses and stress field of passive continental margins: Insights from the south-Norway shelf. Earth and Planetary Science Letters, 277(3-4), pp.464-473.

Schlische, R.W., Withjack, M.O., and Olsen, P.E., 2003. Relative timing of CAMP, rifting, continental breakup, and basin inversion: Tectonic significance, in Hames, W.E., et al., eds., The Central Atlantic

Magmatic Province: Insights from Fragments of Pangea. American Geophysical Union Geophysical Monograph 136, p. 33–59, https://doi.org/10.1029/136GM03.

Taylor, B., Goodliffe, A., Martinez, F. and Hey, R., 1995. Continental rifting and initial sea-floor spreading in the Woodlark Basin. Nature, 374(6522), p.534.

Turcotte, D.L. and Emerman, S.H., 1983. Mechanisms of active and passive rifting. In Developments in Geotectonics (Vol. 19, pp. 39-50). Elsevier.

Ulvrova, M.M., Brune, S. and Williams, S., 2019. Breakup without borders: how continents speed up and slow down during rifting. Geophysical Research Letters, 46(3), pp.1338-1347.

Withjack, M.O., Schlische, R.W., and Olsen, P.E., 1998. Diachronous rifting, drifting, and inversion on the passive margin of central eastern North America: An analog for other passive margins. American Association of Petroleum Geologists, Bulletin, v. 82, p. 817–835.

Appendix I

The origin of contractional structures in extensional gneiss domes

P.F. Rey[1], L. Mondy[1], G. Duclaux[2], C. Teyssier[3], D.L. Whitney[3], M. Bocher[4], and C. Prigent [5]

[1]School of Geosciences, University of Sydney, Sydney, NSW 2006, Australia

[2]Department of Earth Science, University of Bergen, Bergen 5007, Norway

[3]Department of Earth Sciences, University of Minnesota, Minneapolis, Minnesota 55455, USA

[4]Laboratoire de Géologie de Lyon, Université Claude Bernard, Lyon 1, F-69622 Villeurbanne, France, and Ecole Normale
 Supérieure de Lyon, F-69342 Lyon, France

[5]Université Grenoble Alpes, CNRS, ISTerre, F-38000 Grenoble, France

ABSTRACT

The juxtaposition of domains of shortening and extension at different scales in orogens has fueled many debates about driving forces and tectonic interpretations, including timing of deformation. At the orogen scale, gravitational collapse and mass transfer from orogenic plateaux to forelands explain some of these juxtapositions. At a regional scale, structures in gneiss domes are commonly contractional yet are coeval with regional extension and denudation. Here we use three-dimensional numerical experiments to show that crustal flow in orogenic domains does not necessarily conform to plate motion. We document contractional crustal flow associated with the formation of a gneiss dome in an orogenic pull-apart setting where localized extension and crustal thinning focus the exhumation of deep crust. We show that the flow field results in a complex strain pattern in which an extensional strain regime that is collinear with the direction of plate motion is partitioned into the shallow crust, whereas contractional structures and fabrics at a high angle to the direction of imposed transport develop in the deep crust. Advective mass transfer across regions of contrasting yet coeval strain regimes leads to a polyphase tectonic history. We observe structural features remarkably similar to those documented in some natural gneiss domes such as the Montagne Noire, which developed in a dextral pull-apart domain at the southern margin of the French Massif Central.

INTRODUCTION

In the 1980s, gravitational collapse of orogenic crust was proposed to explain regions of surface extension in zones of active convergence (Molnar and Chen, 1982; Coney and Harms, 1984; Dewey, 1988; England and Houseman, 1989). Under warm crustal conditions (i.e., Moho temperature, T_{Moho} > ~700 °C), superposition of the tectonic far-field stress related to displacement of neighboring plates and the gravitational stress generated by lateral variations in gravitational potential energy can lead to contrasting strain regimes in orogenic plateau and adjacent foreland regions (e.g., Sonder et al., 1987; Jones et al., 1996; England and Houseman, 1989; England and Molnar, 1997; Flesch et al., 2000; Rey et al., 2010). Strong vertical strain partitioning also develops during heterogeneous thinning of the upper crust, as convergent flow forces the ductile lower crust into gneiss domes in which contractional strain dominates while boundary-driven extension develops in the shallow crust (e. g. Wdowinski and Axen, 1992; Axen et al., 1998; Mancktelow and Pavlis, 1994; Rey et al., 2011; Le Pourhiet et al., 2012; Whitney et al., 2013; Molnar, 2015). Hence, gneiss domes represent prime targets to document and understand complex three-dimensional (3-D) flow through time.

Here, we simulate a dextral pull-apart basin through a set of 3-D coupled thermal-mechanical experiments that document complex flow and strain patterns. The pull-apart basin geometry is a simple 3-D setting capable of partitioning deformation between the brittle upper crust and the ductile lower crust, as well as horizontally across various domains where simple shear, extension, or contraction dominate. In the upper crust, we observe divergence and rigid translation collinear to the imposed kinematic conditions that are applied at the margin of the model. In contrast, flow of the warm ductile crust involves a curvilinear convergent motion toward the zone of pull-apart basin extension in the upper crust. Consequently, extension in the upper crust is coeval with contractional structures and fabrics in the lower crust. We compare the resulting structures to that of the Montagne Noire, a gneiss dome formed in a dextral pull-apart basin domain at the southern edge of the French Massif Central (Variscan orogen).

EXPERIMENTAL SETUP AND NUMERICAL METHODS

A block of continental lithosphere with dimensions 256 × 256 × 128 km is mapped over a computational mesh consisting of 192 × 192 × 96 elements (Fig. 1). The model includes, from top to bottom, an 8-km-thick layer of compressible air-like material, a layer of continental crust (40 km or 60 km thick), and a layer of mantle. Two non-overlapping, parallel and vertical faults are embedded into the upper part of the continental crust
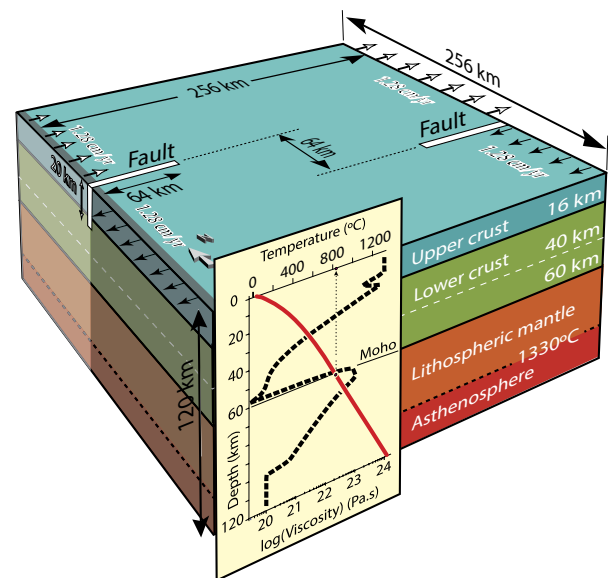
Figure 1. Experimental setup. Kinematic boundary conditions are applied on two opposite vertical walls via inflow and outflow of material driving overall dextral motion, opposite lithospheric blocks moving laterally at velocity of 1.28 cm yr⁻¹ (i.e., total relative velocity of 2.56 cm yr⁻¹). Graph in front of model shows geotherm (solid curve) and viscosity profile (dashed curve) at time *t* = 0 yr.
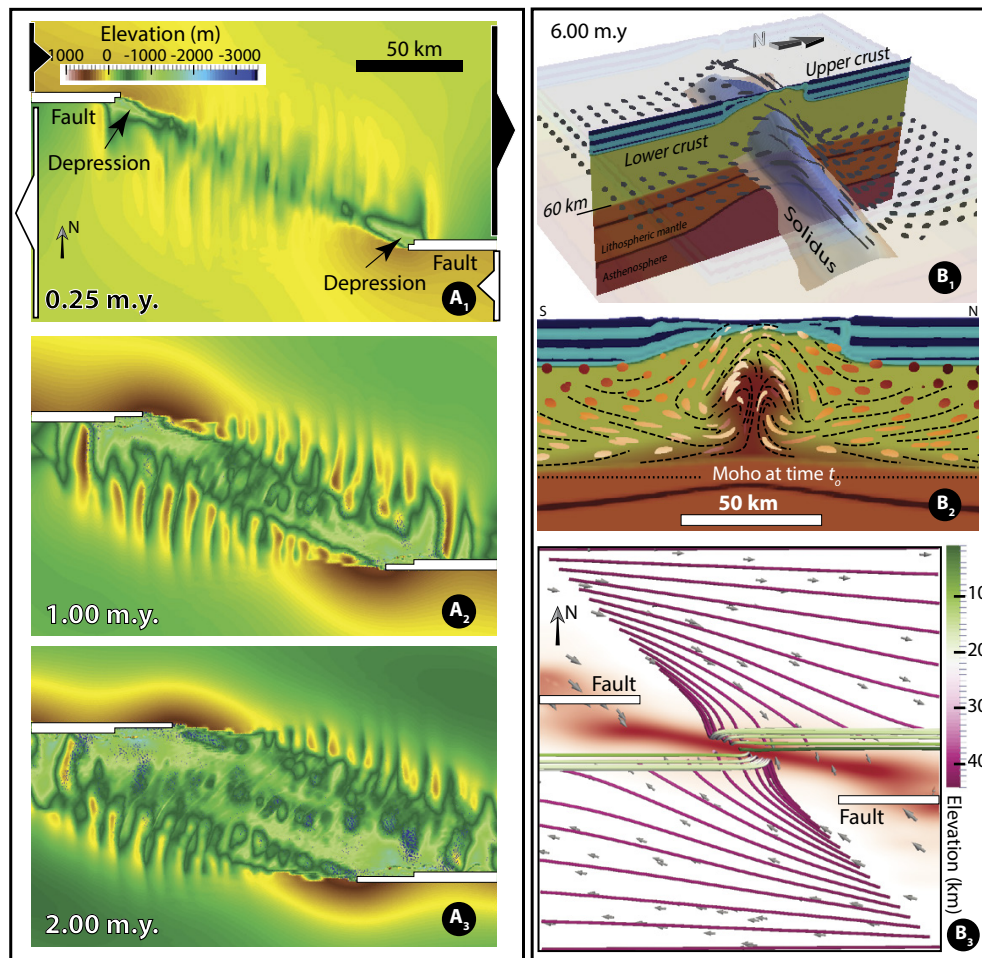
Figure 2. Strain fields for decoupled experiment. A: Maps of topographic surface showing evolution of deformation through time. B: Ductile strain field and flow field at 6 m.y. B_1: Three-dimensional view showing location of cross-section in panel B_2. Blue envelope shows solidus colored for temperature (blue is cold). Strain markers, initially spherical, are in dark gray. They were initially located at ~42 km depth before exhumation into upper crust (see also Fig. DR4 [see footnote 1]). B_2: Cross-section showing deformed strain markers in lower crust (hue varies with increased finite strain) and foliation trajectories (dashed lines). Red shading in lower crust shows melt fraction up to maximum of 18%. B_3: Streamlines colored for elevation starting at 44 km depth on horizontal northwest-southeast diagonal. They are aligned with direction of plate motion in shallow crust. Grey arrows show velocity vectors at 44 km depth.

(Fig. 1). The faults, made of material of weaker rheology (Table DR1 in the GSA Data Repository[1]), extend from the surface to 20 km depth and laterally over a distance of 64 km from the two opposite vertical walls. Kinematic boundary conditions drive divergence at a total velocity of 2.56 cm yr^{-1} (Fig. 1) promoting the formation of a pull-apart basin.

The density of all rocks varies with temperature and melt fraction when temperature $T > T_{solidus}$ (Fig. 1; Table DR1). The rheology of crust and mantle follows a visco-plastic formulation, which incorporates a strain-weakening term (see the Data Repository and Table DR1) and a term taking into account the presence of partial melt (e.g., Rey and Müller, 2010). The geotherm derives from imposing radiogenic heat production in the crust, mantle heat flow at the base of the model (20 mW m^{-2}), and constant temperature in the uppermost air-like layer (20 °C). At the base of the model, the asthenosphere is allowed to flow in or out of the model to maintain a constant basal lithostatic pressure. A free slip boundary condition is imposed on the front and back vertical walls, and outflow or inflow on the left and right walls.

The open-source code Underworld (Moresi et al., 2003, 2007) solves the Stokes equation for a very low Reynolds number on a fixed regular

Cartesian grid. Lagrangian particles (~212 × 10^6 in total) carrying material properties are advected through the grid at the nodes of which pressure and velocity are solved. We explore two contrasting settings in which the mantle is either mechanically coupled to, or decoupled from, the upper crust. Keeping the same initial temperature field for both sets of experiments, coupling or decoupling is achieved by considering a crust of normal thickness (i.e., 40 km, T_{Moho} ~630°C) or a thicker crust (60 km, T_{Moho} ~830°C). The lower section of the thicker crust is therefore warmer and weaker, which results in decoupling the strong upper crust from the strong lithospheric mantle.

RESULTS

In both coupled and decoupled experiments, the early stage of deformation is characterized by the development of a set of en échelon extensional fractures (Figs. 2A1–2A3; Fig. DR1 and Figs. DR2A1–2A3 in the Data Repository) perpendicular to the direction of regional divergence. The resulting damaged zone helps focus deformation in the region limited by the two master faults (i.e., step-over region). At the tip of each master fault, a depression develops bounded by a set of conjugate normal faults. As extension proceeds, the two sets of conjugate normal faults and associated depressions propagate toward the center of the step-over region to form a pull-apart basin (Fig. 2A). Extension progressively focuses in the central depression where thinning of the brittle upper crust via normal faulting controls the flow of lower crust toward the pull-apart region (Fig. 2B).


A cross-section perpendicular to the central depression (Figs. 2B$_1$–2B$_2$) reveals a finite strain pattern in the ductile crust that depends on the mechanical coupling between the mantle and the upper crust. In the case of strong lower crust (40-km-thick crust), strain partitioning is moderate (Fig. DR2B$_2$). In the experiment with a 60-km-thick crust, the weak lower crust flows within a subhorizontal channel toward the region below the developing pull-apart basin (Figs. 2B$_1$–2B$_2$). The convergent, isostatically driven deep crustal flow mitigates crustal thinning, and the Moho remains more or less flat (Fig. 2B$_2$); this contrasts with the more prominent Moho exhumation in the coupled experiment (Figs. DR2B$_2$ and DR3A).

Below the pull-apart basin a gneiss dome develops, assisted by decompression melting (decreased viscosity) during ascent of flowing crust (Figs. 2B$_2$–2B$_3$). The long axis of the dome is aligned with the direction of the damaged zone in the upper crust. In the deep crust, the subhorizontal velocity streamlines curve clockwise, converging toward the region below the pull-apart basin, where they become sub-perpendicular to the direction of plate motion (Fig. 2B$_3$). As deep crust flows into the growing dome, the streamlines rotate upward before becoming subhorizontal upon reaching the base of the stronger shallow crust. Streamlines in the shallow crust remain horizontal and collinear with the direction of plate motion (Fig. 2B$_3$). In the mechanically coupled experiment, streamlines largely conform to the imposed velocity boundary condition (Figs. DR2B$_3$–DR2BC).

In the decoupled experiment (60-km-thick crust), strain markers reveal a strongly partitioned strain regime between the shallow and the deep crust (Fig. 2B$_2$). Extensional deformation with shallowly dipping foliation develops just below the brittle-ductile transition (Fig. 2B$_2$). In contrast, contractional structures with steeply dipping foliation in a high-strain planar zone separate two folds of foliation that develop in the ductile crust below the pull-apart basin where deep crustal rocks are exhumed (Figs. 2B$_2$, 3B). This double fold is wrapped by a broad domical foliation fold that is elongated in the direction joining the tips of the master faults at an angle to the imposed velocity direction. In the deep crust, away from the pull-apart region, the stretching lineation is perpendicular to the velocity direction imposed at the margins of the model (Fig. 3A1). This lineation rotates in the region underneath the pull-apart basin to become locally prominent (constrictional strain) and broadly aligned with the imposed velocity direction (Figs. 2B$_3$, 3A). This stretching lineation makes an angle with the direction of the overarching dome and, as a consequence, plunges in opposite directions on both of its flanks (Fig. 3A). These structural features are far less prominent when the upper crust is coupled to the upper mantle (Figs. DR2B$_2$ and DR3).

DISCUSSION

In the experiment in which the warm lower crust decouples the upper crust from the mantle, the finite strain field suggests a polyphase tectonic history. The early flat-lying, high-grade foliation and lineation (D1) are folded into two upright anticlinal folds (D2$_a$). The intervening syncline evolves into a high-strain zone (D2$_b$). These deep structures are exhumed underneath an extensional brittle-ductile detachment zone (D3$_a$) above which a set of normal faults (D3$_b$) accommodates thinning of the upper crust. Tectonic structures and fabrics are commonly directly related to tectonic regimes and therefore to plate motions or far-field boundary conditions. Accordingly, one may be tempted to conclude that a phase of convergence responsible for D2 structures preceded a phase of divergence resulting in D3 structures. However in our numerical experiments the far-field boundary conditions remain constant, and D1 to D3 structures develop at the same time but in different domains of contrasting yet coeval strain regimes. Importantly, the shallow part of the gneiss dome (<5 km depth) includes rocks exhumed from the base of the lower crust as shown by the passive strain markers (Fig. 2B; Fig. DR4). During their exhumation, these deep rocks traveled through contrasting strain domains where they potentially recorded D1 through D3 flattening to constrictional fabrics.
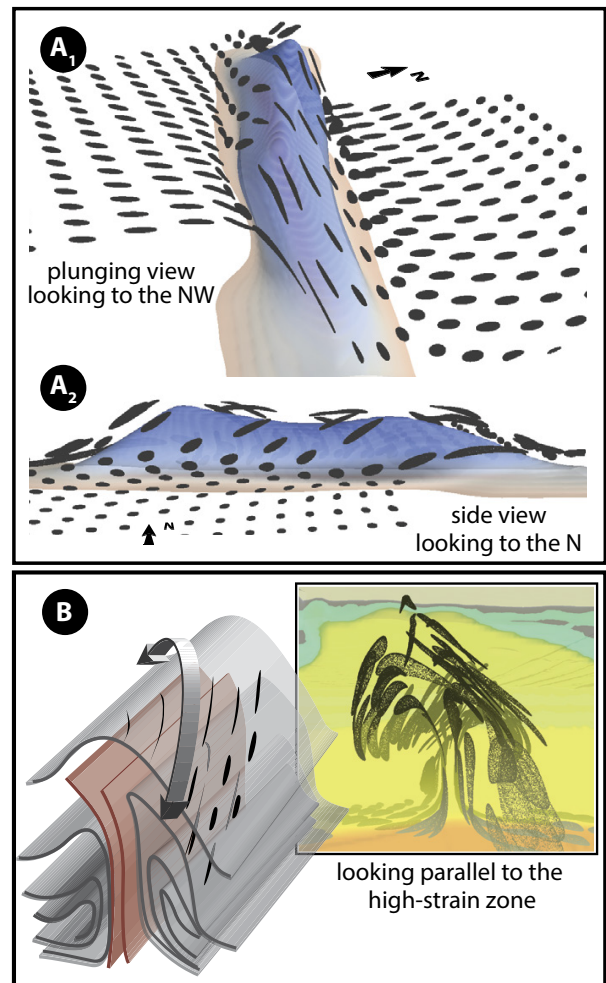
Figure 3. Internal structure and stretching lineation in decoupled experiment. A: Strain markers at 6 m.y. Markers were initially located at 42 km depth. B: Tectonogram illustrating double fold of foliation separated by high-strain zone (in red shading) underneath overarching foliation fold carrying stretching lineation curving over fold axis (black strain markers and curved arrows).

The structures and metamorphic association described above (Figs. 2B$_2$ and 3B) is remarkably similar to that documented in the Montagne Noire gneiss dome, which was exhumed between two dextral strike-slip faults at the southern end of the French Massif Central (Echtler and Malavieille, 1990; Roger et al., 2015). Detailed regional structural maps (e.g., Rabin et al., 2015) show that the Montagne Noire consists of a double dome, with the Agout-Espinouse dome to the north and the Nore-Caroux dome to the south, separated by a steeply dipping high-strain zone (Rey et al., 2011). The regional stretching lineation, locally constrictional, is oriented northeast-southwest at an angle to the ENE-WSW orientation of the Montagne Noire dome. The lineation plunges northeastward at the northeastern end of the dome, and southwestward at the southwestern end. Crystallization of migmatite and granite was coeval with the formation of the dome and has been dated at 315–305 Ma (Roger et al., 2015). Eclogite dated at ca. 315 Ma was exhumed from ~1.4 GPa to shallow crustal levels in <10 m.y. (Whitney et al., 2015), consistent with our experiment results showing rapid, large-scale exhumation of the deep crust in domes (Fig.

DR4B). Our numerical experiments confirm that the main structures of the Montagne Noire are compatible with a double dome emplaced into a dextral pull-apart basin (e.g., Echtler and Malavieille, 1990; Demange, 1999; Doublier et al., 2015; Roger et al., 2015). Similar double-dome structures occur in other orogens (e.g., Naxos dome, Aegean Sea; Aston-Hopitalet dome, Pyrenees; Entia dome, Alice Springs orogen, Australia).

CONCLUSIONS

In orogenic crust, localized thinning of the upper crust forces convergent flow in the lower crust leading to the formation and denudation of a gneiss dome. The flow field follows a complex pattern that is not conforming with imposed far-field motions. Contractional structures in the core of the dome develop coevally with extensional structures in the shallow part of the dome. Our 3-D experiments explain the upright, double foliation folds (double dome) separated by a steeply dipping high-strain zone and the strong shallowly plunging stretching lineation oblique to the dome axis observed in the Montagne Noire gneiss dome. The advective transfer of deep crust across regions of contrasting yet coeval strain regimes results in a polyphase tectonic history that developed during steady far-field motion.

REFERENCES CITED

Axen, G., Selverstone, J., Byrne, T., and Fletcher, J.M., 1998, If the strong lower crust leads, will the weak crust follow?: GSA Today, v. 8, no. 12, p. 1–8.

Coney, P.J., and Harms, T.A., 1984, Cordilleran metamorphic core complexes: Cenozoic extensional relics of Mesozoic compression: Geology, v. 12, p. 550–554, doi:10.1130/0091-7613(1984)12<550:CMCCCE>2.0.CO;2.

Demange, M., 1999, Evolution tectonique de la Montagne Noire: Un modèle en transpression: Comptes Rendus de l'Académie des Sciences de Paris, Series IIA: Earth and Planetary Science, v. 329, p. 823–829, doi:10.1016/S1251-8050(00)88638-3.

Dewey, J.F., 1988, Extensional collapse of orogens: Tectonics, v. 7, p. 1123–1139, doi:10.1029/TC007i006p01123.

Doublier, M.P., Potel, S., and Wemmer, K., 2015, The tectono-metamorphic evolution of the very low-grade hangingwall constrains two-stage gneiss dome formation in the Montagne Noire example (southern France): Journal of Metamorphic Geology, v. 33, p. 71–89, doi:10.1111/jmg.12111.

Echtler, H., and Malavieille, J., 1990, Extensional tectonics, basement uplift and Stephano-Permian collapse basin in a late Variscan metamorphic core complex (Montagne Noire, southern Massif Central): Tectonophysics, v. 177, p. 125–138, doi:10.1016/0040-1951(90)90277-F.

England, P.C., and Houseman, G., 1989, Extension during continental convergence, with application to the Tibetan Plateau: Journal of Geophysical Research, v. 94, p. 17,561–17,579, doi:10.1029/JB094iB12p17561.

England, P.C., and Molnar, P., 1997, Active deformation of Asia: From kinematics to dynamics: Science, v. 278, p. 647–650, doi:10.1126/science.278.5338.647.

Flesch, L.M., Holt, W.E., Haines, A.J., and Bingming, S.-T., 2000, Dynamics of the Pacific–North American plate boundary in the western United States: Science, v. 287, p. 834–836, doi:10.1126/science.287.5454.834.

Jones, C.H., Unruh, J., and Sonder, L.J., 1996, The role of gravitational potential energy in active deformation in the southwestern United States: Nature, v. 381, p. 37–41, doi:10.1038/381037a0.

Le Pourhiet, L., Huet, B., May, D.A., Labrousse, L., and Jolivet, L., 2012, Kinematic interpretation of the 3D shapes of metamorphic core complexes: Geochemistry Geophysics Geosystems, v. 13, Q09002, doi:10.1029/2012GC004271.

Mancktelow, N.S., and Pavlis, T.L., 1994, Fold-fault relationships in low-angle detachment systems: Tectonics, v. 13, p. 668–685, doi:10.1029/93TC03489.

Molnar, P., 2015, Gravitational instability of mantle lithosphere and core complexes: Tectonics, v. 34, p. 478–487, doi:10.1002/2014TC003808.

Molnar, P., and Chen, W.P., 1982, Seismicity and mountain building, in Hsu, K. J. ed., Mountain Building Processes: New York, Academic Press, p. 41–57.

Moresi, L.N., Dufour, F., and Mühlhaus, H.B., 2003, A Lagrangian integration point finite element method for large deformation modelling of viscoelastic geomaterials: Journal of Computational Physics, v. 184, p. 476–497, doi:10.1016/S0021-9991(02)00031-1.

Moresi, L., Quenette, S., Lemiale, V., Meriaux, C., Appelbe, B., and Mühlhaus, H.B., 2007, Computational approaches to studying non-linear dynamics of the crust and mantle: Physics of the Earth and Planetary Interiors, v. 163, p. 69–82, doi:10.1016/j.pepi.2007.06.009.

Rabin, M., Trap, P., Carry, N., Fréville, K., Cenki-Tonk, B., Lobjoie, C., Goncalves, Ph., and Marquer, D., 2015, Strain partitioning along the anatectic front in the Variscan Montagne Noire massif (southern French Massif Central): Tectonics, v. 34, p. 1709–1735, doi:10.1002/2014TC003790.

Rey, P.F., and Müller, R.D., 2010, Fragmentation of active continental plate margins owing to the buoyancy of the mantle wedge: Nature Geoscience, v. 3, p. 257–261, doi:10.1038/ngeo825.

Rey, P.F., Teyssier, C., and Whitney, D.L., 2010, Limit of channel flow in orogenic plateaux: Lithosphere, v. 2, p. 328–332, doi:10.1130/L114.1.

Rey, P.F., Teyssier, C., Kruckenberg, S.C., and Whitney, D. L., 2011, Viscous collision in channel explains double domes in metamorphic core complexes: Geology, v. 39, p. 387–390, doi:10.1130/G31587.1.

Roger, F., Teyssier, C., Respaut, J.-P., Rey, P.F., Jolivet, M., Whitney, D.L., Paquette, J.-L., and Brunel, M., 2015, Timing of formation and exhumation of the Montagne Noire double dome, French Massif Central: Tectonophysics, v. 640–641, p. 53–69, doi:10.1016/j.tecto.2014.12.002.

Sonder, L., England, P.C., Wernicke, B.P., and Christiansen, R.L., 1987, A physical model for Cenozoic extension of western North America, in Coward, M.P., et al., eds., Continental Extensional Tectonics: Geological Society of London Special Publication 28, p. 187–201, doi:10.1144/GSL.SP.1987.028.01.14.

Wdowinski, S., and Axen, G.J., 1992, Isostatic rebound due to tectonic denudation: A viscous flow model of a layered lithosphere: Tectonics, v. 11, p. 303–315, doi:10.1029/91TC02341.

Whitney, D.L., Teyssier, C., Rey, P.F., and Buck, W.R., 2013, Continental and oceanic core complexes: Geological Society of America Bulletin, v. 125, p. 273–298, doi:10.1130/B30754.1.

Whitney, D.L., Roger, F., Teyssier, C., Rey, P.F., and Respaut, J.-P., 2015, Syn-collapse eclogite metamorphism and exhumation of the deep crust in a migmatite dome: The P-T-t record of the youngest Variscan eclogite (Montagne Noire, French Massif Central): Earth and Planetary Science Letters, v. 430, p. 224–234, doi:10.1016/j.epsl.2015.08.026.

Appendix II

Contents lists available at ScienceDirect

Tectonophysics

journal homepage: www.elsevier.com/locate/tecto

Numerical investigation of deep-crust behavior under lithospheric extension

Megan Korchinski[a,*], Patrice F. Rey[b], Luke Mondy[b], Christian Teyssier[a], Donna L. Whitney[a]

[a] *Department of Earth Sciences, University of Minnesota, Minneapolis, MN, USA*
[b] *EarthByte, School of Geosciences, University of Sydney, Sydney, Australia*

ARTICLE INFO

ABSTRACT

What are the conditions under which lithospheric extension drives exhumation of the deep orogenic crust during the formation of gneiss domes? The mechanical link between extension of shallow crust and flow of deep crust is investigated using two-dimensional numerical experiments of lithospheric extension in which the crust is 60 km thick and the deep-crust viscosity and density parameter space is explored. Results indicate that the style of extension of the shallow crust and the path, magnitude, and rate of flow of deep crust are dynamically linked through the deep-crust viscosity, with density playing an important role in experiments with a high-viscosity deep crust. Three main groups of domes are defined based on their mechanisms of exhumation across the viscosity-density parameter space. In the first group (low-viscosity, low-density deep crust), domes develop by lateral and upward flow of the deep crust at $km \, m.y^{-1}$ velocity rates (i.e. rate of experiment boundary extension). In this case, extension in the shallow crust is localized on a single interface, and the deep crust traverses the entire thickness of the crust to the Earth's near-surface in 5 m.y. This high exhuming power relies on the dynamic feedback between the flow of deep crust and the localization of extension in the shallow crust. The second group (intermediate-viscosity, low-density deep crust) has less exhuming power because the stronger deep crust flows less readily and instead accommodates more uniform extension, which imparts distributed extension to the shallow crust. The third group represents the upper limits of viscosity and density for the deep crust; in this case the low buoyancy of the deep crust results in localized thinning of the crust with large upward motion of the Moho and lithosphere-asthenosphere boundary. These numerical experiments test the exhuming power of the deep crust in the formation of extensional gneiss domes.

1. Introduction

Flow of the deep crust is a significant mechanism for the transport of heat and mass during orogeny and is a critical geodynamic process in the chemical and physical evolution of continents. Horizontal flow is one mode of orogenic collapse (Rey et al., 2001) and may contribute to the growth of orogenic plateaus (e.g., Clark and Royden, 2000). Vertical flow in combination with horizontal flow can bring hot, deeply-sourced material to shallower levels (e.g., Burg et al., 2004; Schulmann et al., 2008; Rey et al., 2011; Teyssier and Whitney, 2002), in some cases traversing most of the thickness of the orogenic crust (Whitney et al., 2015) to within a few kilometers of the Earth's surface (Stübner et al., 2013a, 2013b; Toraman et al., 2014).

Vertical flow of hot, deep crust can create crustal-scale structures that are characterized by domal patterns of foliation in high-grade metamorphic rocks. These gneiss domes are exposed in most orogens, from Archean to Cenozoic (Teyssier and Whitney, 2002; Whitney et al., 2004, 2013). Domes are typically cored by migmatite and associated granite, which represent crystallized partial melt and magma, respectively. In many gneiss domes, the P-T paths obtained from layers and lenses of refractory lithologies included in the host quartzofeldspathic gneiss indicate isothermal decompression that was equivalent to at least 10–20 km of exhumation at high temperature (e.g., Augier et al., 2005; Bonev et al., 2005; Caby et al., 2001; de Sigoyer et al., 2004; François et al., 2014; Norlander et al., 2002; Whitney et al., 2004).

Dome formation has been previously investigated in 2D and 3D numerical modeling studies, wherein initial and/or boundary conditions were varied. Parameters varied in models include: (a) the rheology of the crust (e.g. Buck, 1991); (b) the initial geotherm (e.g. Tirel et al., 2004a; Tirel et al., 2008; Wijns et al., 2005); (c) the presence of temperature anomalies in the deep crust (e.g. Burov et al., 2014; Koptev et al., 2017); (d) the presence of partial melt in the deep crust (e.g. Rey et al., 2011; Rey et al., 2009a, 2009b; Schenker et al., 2012); (e) the presence of inherited rheological layers within the crust (e.g. Fayon et al., 2004; Huet et al., 2011; Labrousse et al., 2016; Le Pourhiet et al., 2012; Schenker et al., 2012); (f) the strength and/or presence of

---

an initial weak zone in the crust (e.g. Fayon et al., 2004; Mezri et al., 2015); and (g) the imposed extensional velocity (e.g. Buck, 1991; Rey et al., 2011; Rey et al., 2009a, 2009b; Schenker et al., 2012; Tirel et al., 2004b; Tirel et al., 2008). We present a systematic exploration of the independent impact of the density and viscosity of the deep crust on (1) the mechanical links between the deep and shallow crust during extension, and (2) the conditions and mechanisms of deep-crust exhumation in extensional domes.

This study executed a series of 2D numerical experiments of lithospheric extension in which the viscosity and density of the deep crust were varied systematically. In order to capture the first order relationship between viscosity, strain rate and stress, we utilize a flow law that is representative of the crust to build a framework that can be used to explore the impact of compositional variances observed in nature. We used two starting crustal thicknesses (40 and 60 km), and two extensional velocities, 2 cm yr^{-1} (fast) and 2 mm yr^{-1} (slow), to evaluate the interplay among buoyancy, viscosity, and extension velocities during dome development. Numerical experiments reveal the parameter combinations that favor or suppress the generation of extensional gneiss domes, and demonstrate how the flow of deep crust is dynamically linked to strain localization or distribution in the shallow crust and the mantle.

2. Numerical experiment design

We use *Underworld*, a particle-in-cell finite element code that solves the equations for momentum, energy, and mass for incompressible flow of low Reynolds numbers (Moresi et al., 2007; Moresi et al., 2003) (Appendix A). Experiments are run using the Lithospheric Modelling Recipe: (https://github.com/OlympusMonds/lithospheric_modelling_recipe), a Python wrapper that facilitates efficient experiment design and execution. The reference experiment maps a 360 km long and 160 km deep model over a computational grid with 1 km resolution (Fig. 1). Models include from top to bottom: 10 km air layer, 20 km shallow crust (2620 kg·m^{-3}), 40 km deep crust (2700–3100 kg·m^{-3}), 40 km lithospheric mantle (3370 kg·m^{-3}), and 50 km asthenosphere (3395 kg·m^{-3}) (Fig. 1).

In the shallow crust, a 2 km-thick prism made of weaker material acts as a fault (45° dip) (Fig. 1). The fault forces deformation to localize in the center of the numerical experiment. This facilitates comparison of flow and strain patterns among the different experiments, and mitigates boundary effects (e.g., asymmetric flow) that would occur when a dome develops close to a vertical wall in the model. Similar experiments conducted by Rey et al. (2009b) tested the effect of a dipping weak prism versus a point weakness to force strain localization in the center of the experimental domain and found negligible differences. The dipping heterogeneity is preferred because it provides a geologically realistic asymmetry in the structural development of the dome (Rey et al., 2009b).

Material viscosities are temperature and strain-rate dependent, and plastic rheologies include a strain-weakening function. The visco-plastic rheology of the shallow crust is based on quartzite (Paterson and Luan,

1990), and the visco-plastic rheology of the lithospheric mantle and asthenosphere is based on wet olivine (Fig. 1; Appendix A) (Hirth and Kohlstedt, 2004). The deep crust has visco-plastic rheology based on the dry mafic granulite model of Wang et al. (2012); the starting viscosity of this layer is varied within the experiment suite.

A swarm of circular passive markers gives a qualitative representation of the finite strain field within the deep crust (Rey et al., 2009a). These markers were initially distributed as regularly spaced circles, allowing the evolution of finite strain orientations and strain intensity to be tracked within each experiment, and to be compared, at least qualitatively, across the suite of experiments. Recent 3D experiments (Rey et al., 2017) utilize similar strain markers to track finite strain in domes that develop in pull-apart systems. These 3D models show that dome material displays a double dome of foliation and a strong lineation parallel to the axis of the dome, which cannot be revealed by 2D models (see also Le Pourhiet et al., 2012). However, 2D models produce flow fields that are similar to the flow fields observed in the cross section projection of 3D models, as well as similar flow velocities, exhumation velocities, and thermal structure. Therefore, the computationally economical models presented here, although they limit strain within 2D, are nevertheless helpful for comparing flow fields within the deep crust across a wide spectrum of parameters.

The initial thermal state of each experiment is calculated using a period of thermal evolution under null extension, crustal radiogenic heating, basal heat flow, and constant surface temperature (Table 1; Appendix A). The resulting initial geotherm is characterized by a Moho temperature of ~850 °C (Fig. 1; Appendix A).

The starting reference density of deep crust is varied systematically from 2700 to 3100 kg·m^{-3} by increment of 100 kg·m^{-3}. Within each experiment, density depends on temperature and melt fraction when present (see below); the coefficient of thermal expansion is kept constant across all experiments.

The reference viscosity of the deep crust is also systematically varied by changing the pre-exponential factor (A; $\eta = \frac{1}{2} \cdot A^{-1/n} \cdot \exp\left[\frac{Q}{n \cdot R \cdot T}\right] \cdot \varepsilon^{(1-n)/n}$; Appendix A) (Rey et al., 2009b, 2011). The reference viscosities are hereafter referred to as *weak* (1.0E19 Pa·s), *intermediate* (1.0E20 Pa·s), and *strong* (1.0E21 Pa·s). These values describe the viscosity at the base of the crust (immediately above Moho) at the initial time step.

The presence of melt in a dome facilitates the upward advection of heat and material (Rey et al., 2009b). In order to account for the mechanical and thermal effects of partial melting, a heuristic function is included (Rey et al., 2009a, 2009b). The melt fraction is a function of the supersolidus temperature (McKenzie and Bickle, 1988) (Appendix A). The solidus and liquidus for the crust and mantle are both temperature- and pressure-dependent and are described by polynomial functions (Fig. 1); a partial melt layer exists at the start of experiments where the geotherm crosses the solidus. The maximum partial melt fraction is 0.3, which is in line with melt fractions inferred in many gneiss (migmatite) domes (Whitney et al., 2004). The reference density of the crust decreases linearly to a maximum of 13% (Clemens and Droop, 1998), and material viscosity decreases linearly by three orders
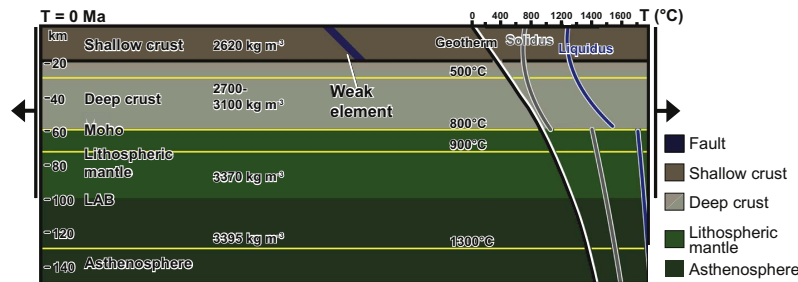

Fig. 1. Experiment input parameters, boundary conditions, and geometry. Yellow lines delineate the initial depth of isotherms. The weak element (i.e. detachment fault) is 2 km wide and is outlined in blue. The fault has the same density of the shallow crust and a Newtonian viscosity (1.0E19 Pa·s). Black arrows show applied extension velocity. LAB: lithosphere-asthenosphere boundary. (For interpretation of the references to color in this figure legend, the reader is referred to the web version of this article.)

Table 1
Rheological parameters.

Parameter	Shallow crust	Deep crust	Lithosph. mantle	Asthenosph. mantle
Reference temperature (K)	293			
Dislocation creep viscous rheology	Wet quartzite[a]	Dry mafic granulite[b]	Wet olivine[c]	Wet olivine[c]
Reference density (kg·m^{-3})	2620	2700–3100	3370	3395
Heat capacity (J K^{-1} kg^{-1})	1000			
Thermal diffusivity (m^2 s^{-1})	1.0E − 6			
Latent heat of fusion (kJ kg^{-1})	300			
Radiogenic heat production (W m^{-3})[d]	0.7E − 6	0.4E − 6	0.02E − 6	0.02E − 6
Melt fraction density change (M$_{\Delta pr}$)[e]	0.13			
Solidus term 1 (K)	993	993	1393.661	1393.661
Solidus term 2 (K Pa^{-1})	− 1.2E7	− 1.2E7	1.32899E − 7	1.32899E − 7
Solidus term 3 (K Pa^{-2})	1.2E16	1.2E16	− 5.104E − 18	− 5.104E − 18
Liquidus term 1 (K)	1493	1493	2013	2013
Liquidus term 2 (K Pa^{-1})	− 1.2E7	− 1.2E7	6.15E − 8	6.15E − 8
Liquidus term 3 (K Pa^{-2})	1.6E16	1.6E16	3.12E − 18	3.12E − 18
Friction coefficient	0.577			
Softened friction coefficient	0.1154			
Softened cohesion (MPa)	2	4	2	2
Pre-exponential factor (MPa^{-n} s^{-1})	6.60692E − 8	10E − 2	1600	1600
Stress exponent	3.1	2.8–3.6	3.5	3.5
Activation energy (kJ mol^{-1})	135	244	520	520
Activation volume (m^3 mol^{-1})	0	0	23E − 6	23E − 6
Water fugacity	0	0	1000	1000
Water fugacity exponent[f]	0	0	1.2	1.2
Melt viscous softening factor	1.0E − 3	1.0E − 3	1.0E − 2	1.0E − 2
Viscous softening melt fraction	0.2–0.3	0.2–0.3	0.03–0.08	0.03–0.08

[a] Parameters were derived from Paterson and Luan (1990).
[b] Parameters were derived from Wang et al. (2012).
[c] Parameters were derived from Hirth and Kohlstedt (2004).
[d] Parameters were derived from Hasterok and Chapman (2011).
[e] Melt and other parameters were derived from Rey and Muller (2010).
[f] A zero value denotes that this effect on the viscous flow law is incorporated into the pre-exponential factor.

of magnitude across a critical melt fraction range between 0.2 and 0.3. Previous numerical experiments of the development of extension-driven domes have shown that the melt fraction increases to its maximum value over a few kilometers as the solidus is translated upward through the deep crust (Rey et al., 2009b). Therefore, numerical experiments are not significantly impacted by decreasing the critical melt fraction to lower values (i.e. 2–12%) (Rey et al., 2009b; Rosenberg and Handy, 2005). Melt does not segregate from the host rock in the experiments; this *en masse* movement of partially molten material is consistent with observations of migmatite-cored metamorphic core complexes in which only a relatively small volume of leucogranite is extracted from the partial melt layer (Teyssier and Whitney, 2002).

Experiments are run at two extension velocities: 2.0 and 0.2 cm yr^{-1}. The velocity boundary conditions are applied to the vertical walls down to the base of the lithosphere (Fig. 1). A function at the base of the model allows inflow of asthenosphere to isostatically balance the extension-related outward flow of material at the sides.

3. Experimental results

The experiments systematically explore flow and deformation within the lithosphere as a function of the density and viscosity of the deep crust. Selected experiment outputs are presented as two main suites: *fast* extension (2 cm yr^{-1}; Fig. 2a) and *slow* extension (0.2 cm yr^{-1}; Fig. 2b). We describe first-order results across the parameter space, and then focus on how the flow of deep crust varies across the experiment suite, noting the strain and kinematic patterns that describe the flow. We present and compare experimental results after 5 m.y. for fast extension and 50 m.y. for slow extension, corresponding to 28% extension. Appendix B presents the fast and slow experiment suites experimental results at 39% and 55% extension (unless otherwise noted in Appendix B), as well as the effective viscosity and strain rate of the fast and slow experiment suites at 28%, 39%, and 55% extension.

3.1. Exhumation of deep crust and strain localization in shallow crust

3.1.1. Fast extension

Crustal-scale vertical transport of deeply sourced crustal material to the near-surface occurred across the entire experiment suite (Fig. 2a). Experimental results show that the magnitude of exhumation of deep material is primarily dependent on the ability of deformation to localize in the shallow crust. In experiments with a weak deep crust (Fig. 2a$_3$), strong localization of strain on the initial weak element results in boudinage of the shallow crust, which creates space and allows rapid upward flow of deep, low-viscosity material into a broad (up to 100 km wide) core complex. Crust that was partially molten at the start of the experiment remains partially molten to depths < 15 km, while temperature remains within 100 °C of the maximum temperature (T$_{max}$) at peak pressure.

In experiments with a strong or intermediate deep crust (Fig. 2a$_{1–2}$), the mechanical coupling between the shallow crust and the deep crust is stronger, and localization of deformation in the shallow crust is less efficient. Strain initially localizes along the original normal fault and newly formed conjugate faults (Fig. 2a$_1$) before migrating > 30 km away from the imposed weak element (Fig. 2a$_1$).

Vertical flow within the dome is markedly different across experiments with differing deep crustal viscosities. Material sourced from a weak deep crust is transported vertically up to 5 km of the Earth's surface after 5 m.y. (28% extension; Fig. 2a$_3$). In experiments with an intermediate and strong deep crust, rocks from the deep crust are transported up to 20 km of the Earth's surface at 28% extension, resulting in significantly less exhumation than in the weak experiments.

The magnitude of exhumation is less dependent on the density of the deep crust (Fig. 2a). For example, for weak deep crust at 28% extension, the difference in total vertical transport (Δz) between experiments with a low density deep crust and high density deep crust is only ~4 km (Fig. 2a$_3$). This is an order of magnitude lower than the variation of vertical transport achieved across experiments by contrasting
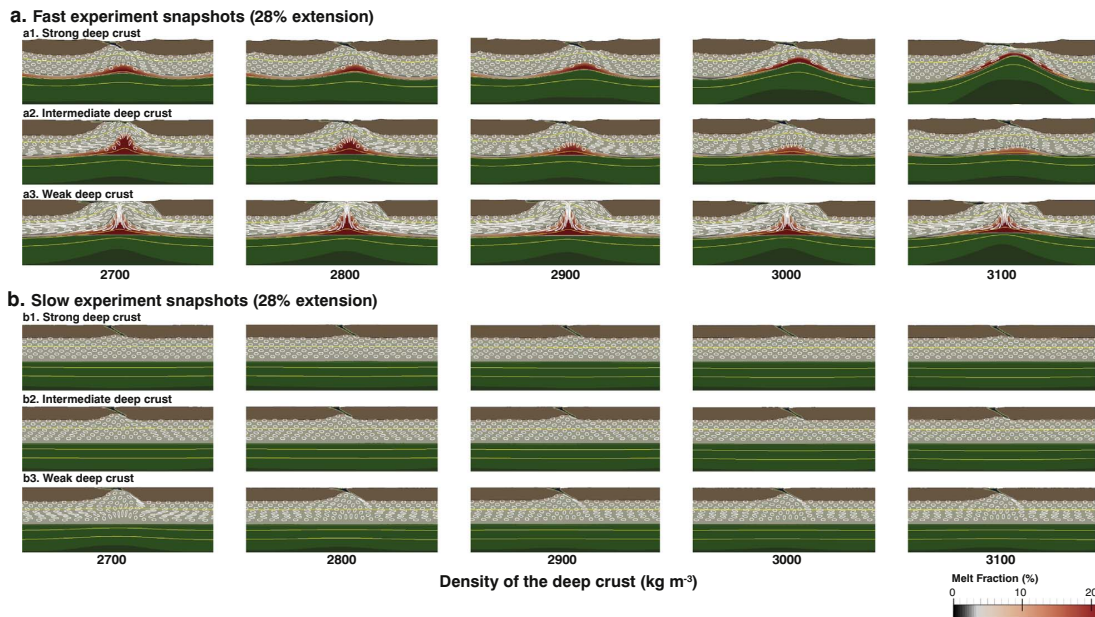
M. Korchinski et al.

Fig. 2. Experimental snapshots illustrating crustal geometry and strain patterns in the deep crust. (a) Fast extension experiments (2 cm yr^{-1}). Strain ellipses are shown in white within the deep crust. These markers start out as circles, and become deformed as the experiment proceeds thereby recording the intensity and direction of strain. Note that the melt fraction in the deep crust is shown as a red shading. (b) Slow extension experiments (0.2 cm yr^{-1}). Complete experimental results are presented in Appendix B. (For interpretation of the references to color in this figure legend, the reader is referred to the web version of this article.)

deep crustal viscosities.

3.1.2. Slow extension

Vertical transport of deeply sourced rocks is minimal in the slow-extension experiment suite, regardless of the physical parameters used for the deep crust (Fig. 2b). Localization of strain occurs on a single fault in the weak, low-density experiments, but it is significantly less than the localization that occurs in experiments with fast extension. Decompression melting of the deep crust occurs in the weak, low-density experiments; however, the predicted melt fraction in these experiments is negligible relative to that present in the equivalent fast-extension experiment (Fig. 2b; Fig. B1.7–B1.9, Appendix B).

3.2. Deep crust strain patterns

The passive markers inserted in the deep crust record the various strain patterns that develop across the parameter space, and can be compared to foliation trajectories within and around natural domes.

3.2.1. Fast extension

At one end of the viscosity-density parameter space (weak deep crust, 2700 kg·m^{-3}) strain markers highlight the partitioning of strain across a décollement channel in the deep crust (Fig. 2a$_3$). The lowest viscosity deep crust flows horizontally inward, toward the zone of extension, while the upper layer of deep crust moves away from the center of the experiment, consistent with the imposed extension boundary conditions. The inward flow in the low-viscosity channel is bounded above and below by sub-horizontal high-strain zones with opposite senses of shear. Inward flow of the deep crust is nearly symmetrical about the center of the experiment and results in the viscous collision of material directly below the zone of shallow crust thinning. This collision leads to the development of a vertical high-strain zone (horizontal contraction) between two subdomes of foliation ('double dome'; Gessner et al., 2007; Labrousse et al., 2016; Rey et al., 2011; Schenker et al., 2012). Substantial upward flow is accommodated within the

subdomes resulting in considerable exhumation of the deep crust. As the deep crust reaches shallow depths (< 10 km), flow transitions from dominantly vertical to dominantly horizontal and outward, away from the dome core (Fig. 2a$_3$).

In the parameter space, the double dome geometry is best exemplified in the weak, low-density experiment, and the main features of this geometry (double dome, vertical high-strain zone) persist across all investigated densities from 2700 to 3100 kg·m^{-3} (Fig. 2a$_3$). The double dome geometry is also present in the intermediate viscosity experiments (Fig. 2a$_2$), particularly for low densities (2700 and 2800 kg·m^{-3}). Increasing density suppresses the upward flow of deep crust and limits the development of double domes. Nevertheless, vertical foliation still develops directly below the zone of upper crust thinning (center of experiment) in the higher density, intermediate viscosity deep crust cases (Fig. 2a$_2$), indicating some degree of deep crust inward flow and viscous collision during extension.

In the case of strong deep crust (Fig. 2a$_1$), no pronounced inward flow develops in the deep crust. The strain ellipses reveal uniform thinning with a zone of localized necking in the center of the experiment, creating substantial relief of both the Moho and the lithosphere-asthenosphere boundary (LAB). Necking is amplified when the density increases from 2700 to 3100 kg·m^{-3} (Fig. 2a$_1$). The substantial exhumation of strong deep crust in experiments with a high density deep crust (3100 kg·m^{-3}; Fig. 2a$_1$) is caused primarily by localized thinning of the crust (i.e. Moho depths of 15 km), indicating that high-viscosity, high-density thick crust could be rifted exposing deep crust and mantle sections at the surface.

3.2.2. Slow extension

Strain ellipses show that the deep crust undergoes uniform strain (Fig. 2b). Extension of the lithosphere results in overall vertical shortening and horizontal lengthening of deep crust material (Fig. B1.7–B1.9, Appendix B). The exceptions to this pattern are the weak, low-density experiments in which up to 5 km of upward flow of deep crust material (over 5 m.y. experiment duration) is present as a result of
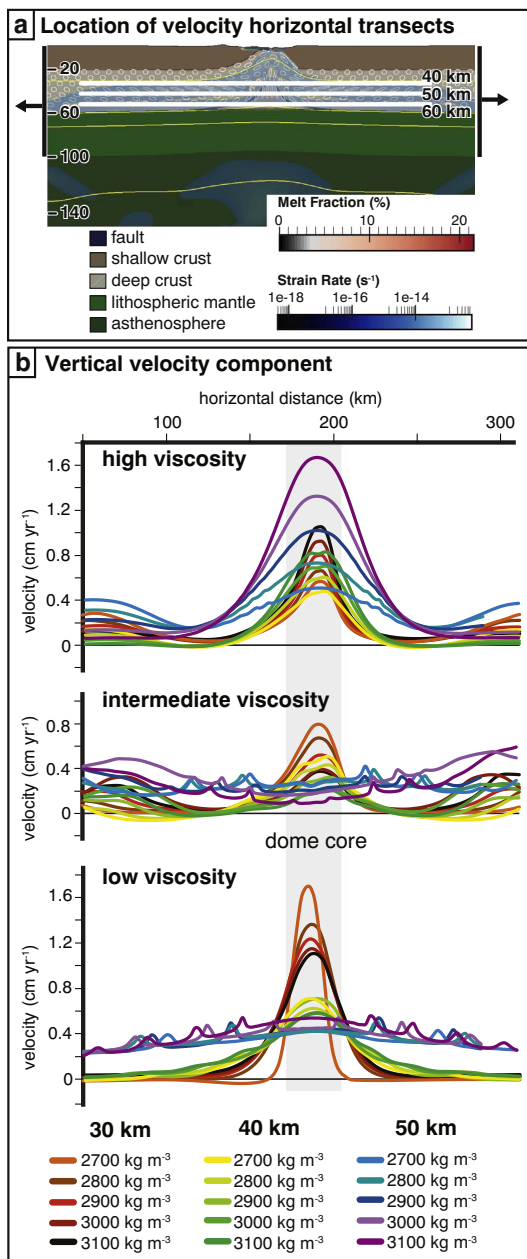
M. Korchinski et al.

Fig. 3. Vertical component of the velocity field along three horizontal profiles. (a) Velocity profiles at 30, 40 and 50 km depth located in the low viscosity, low density (2700 $kg\cdot m^{-3}$) experiment. Velocity profiles were extracted at 11% extension (2 m.y. experiment time; 2 $cm\ yr^{-1}$ extension rate). (b) Profiles of the vertical component of velocity for various deep crust viscosity and densities. The approximate location of the dome core shown in grey.

boudinage of the shallow crust (Fig. B1.7, Appendix B). In this case, strain ellipses in the core of the dome initially track horizontal shortening, followed by vertical shortening caused by bulk lithospheric extension (Fig. B1.7, Appendix B). This evolution represents the initiation and subsequent suppression of a double dome (Fig. 2b₃).

The upward motion of the Moho and LAB is the result of uniform

crustal thinning in the slow experiment suite, with no significant Moho and LAB relief (Figs. 2b; B1.7–B1.9, Appendix B). A slight upward deflection of the Moho and LAB exists at the sides of experiments in the case of high-density, intermediate-strong deep crust.

4. Horizontal and vertical flow of deep crust

The results of the numerical experiments provide information about the flow field across the experimental parameter space, including the magnitude of horizontal and vertical flow components, the latter being critical to the assessment of the exhuming power of domes. In this section, we focus on the fast experiment suite, in which horizontal and vertical flow varies significantly. For all values of viscosity and density, we take a snapshot of the magnitude, distribution, and velocity of horizontal and vertical flow at 2 m.y. (11% extension; Fig. 3, 4).

4.1. Vertical flow

Vertical component of velocity, evaluated across the experiment at depths of 30, 40, and 50 km (Fig. 3), shows that exhumation dynamics varies significantly as a function of depth and viscosity. In the dome-core area, rapid exhumation is achieved for all combination of densities and viscosities; however the maximum flow varies horizontally (Fig. 3b). Results show that weak deep crust achieve exhumation velocity approaching the driving extension velocity (1.7 $cm\ yr^{-1}$, Fig. 3b). However, peak vertical velocity varies considerably for different viscosity-density scenarios and also varies across each experiment for different sites relative to the shallow-crust localizing element (fault) and the underlying dome-core that develops. Interestingly, two exhumation modes emerge: (1) exhumation of the deep crust occurs without development of significant relief on the Moho (e.g., 2a₃), and (2) exhumation of the deep crust is coeval with substantial (~40 km) exhumation of the Moho and little flow of the deep crust (Fig. 2a₁, 3100 $kg\cdot m^{-3}$).

4.2. Horizontal flow

During lithospheric extension, the magnitude of horizontal flow in the deep crust is primarily dependent on its viscosity, and to a less extend to its density (Fig. 4). The horizontal component of the velocity field (positive when particles move to the right) varies from the value of the driving extensional velocity in the rigid parts of the lithosphere, to opposite but similar values in low-viscosity and low-density experiments (Fig. 4b profiles at 30 km). Experiments with high-viscosity and high-density deep crust, however, experience little flow as deformation is dominated by upwards translation of the deep crust (Fig. 4b). Closer to the experiment center, intermediate- and low-viscosity deep crust experiences strong convergent flow towards the developing 'dome'.

5. Exhumation of deep crust

The 2D experimental suite provides insight into the dynamics of gneiss domes that develop under extension. Exhumation of the deep crust in a domal structure occurs in the fast-extension suite of experiments and, to a lesser extent, under slow extension in the weak deep crust experiments.

In the fast-extension suite of experiments, domes are common (Fig. 2a). In many cases, the material that feeds the dome is deeply sourced and flows horizontally over tens of kilometers and flows vertically toward the surface. Under fast extension, the viscosity of the deep crust exerts the primary control on the amount of exhumation of deeply sourced material in the dome, on the strain patterns in the deep crust, and on whether deformation in the shallow crust is distributed or localized. The density of the deep crust has a minor influence in cases of low-viscosity deep crust but significantly influences the behavior of high-viscosity deep crust (Fig. 2a₁).
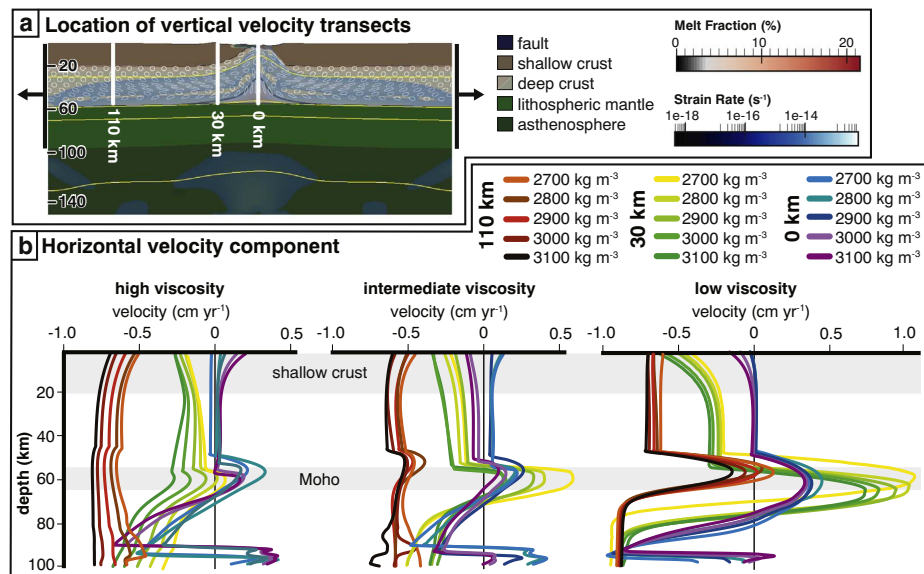
M. Korchinski et al.

Fig. 4. Horizontal component of the velocity field along three vertical profiles. (a) Velocity profiles at 0, 30 and 110 km from the center of the model located in the low viscosity, low density (2700 kg·m^{-3}) experiment. Velocity profiles were extracted at 11% extension (2 m.y. experiment time; 2 cm yr^{-1} extension rate). (b) Profiles of the horizontal component of velocity for various deep crust viscosities and densities. The approximate location of the shallow crust, deep crust, and Moho are shown in grey.

Under slow extension, overall thinning of the lithosphere occurs across the entire parameter space (Fig. 2b; Appendix B). Using similar extension velocities, previous numerical studies have produced deep-crustal domes with as little as 13% extension (e.g. extension velocities < 0.6 cm yr^{-1}; Koptev et al., 2017; Mezri et al., 2015). However, as our experiments have no thermal anomaly within the deep crust (i.e. no addition-crustal heat source beyond the background radiogenic heat, and no mantle plume), the lithosphere undergoes thinning without significant faulting within the shallow crust and flow within the deep crust.

5.1. Exhumation modes and velocity

In this section, we explore different modes of exhumation and consider associated exhumation velocities and P-T paths during ascent of deep crust. Three modes of exhumation can be defined across the experiment parameter space (Figs. 2; 5). Mode A comprises cases where the exhumation of deep crust is the result of deep crustal flow with little relief developed on the Moho, extreme thinning of the shallow crust, and the formation of a double dome of foliation (Fig. 5a). Mode B also involves deep crustal flow; however the shallow crust thins uniformly relative to Mode A, and double dome development is limited (Fig. 6a). Mode C corresponds to the case where the deep crust and Moho are exhumed by lithosphere necking owing to the concentration of extension at the center of the model while the lithosphere away from the center undergoes negligible extension (Fig. 6a).

Let us consider a 50-km deep particle located at the center of the model domain, and trace its ascent for all viscosity/density pairs in the parameter space (Fig. 6). In the case of experiments with a weak deep crust, the exhumation velocity of the particle is on the order of 10 km m.y^{-1} and exhibits a slight acceleration with time; exhumation velocities are not dependent on the density of the deep crust. In the case of experiments with an intermediate deep crust, the exhumation velocity of the particle is on the order of 10 km m.y^{-1} in the first few million years, after which exhumation decelerates. This deceleration is positively correlated with the density of the deep crust. The particle remains below ~20 km depth at 28% extension, except in the case of

lowest density deep crust where the particle reaches ~10 km depth. In the case of experiments with a strong deep crust, the particle is exhumed efficiently to within ~25 km from the surface for the low density deep crust and to ~15 km depth for the high density deep crust.

When exhumation velocities for 50 km deep particles are plotted in the density viscosity parameter space, Mode A corresponds to experiments where the exhumation of deep crust is rapid (6–13 km m.y^{-1}) (Fig. 6c). Mode B corresponds to experiments with exhumation velocities of ~5 km m.y^{-1}, and even though double domes do develop, an intermediate to high viscosity deep crust combine with the uniform thinning of shallow crust to suppress deep crust exhumation (Fig. 6a, c). Mode C is restricted to experiments with a high density (> 2900 kg·m^{-3}) and strong deep crust (Fig. 6c). Exhumation is initially isothermal for all three modes, from ~50 km to ~25 km (Fig. 6d). Modes A and B are easily distinguished as Mode B experiences slight cooling and remains at high temperatures and pressures for the initial 5 m.y., whereas Mode A deep crust reaches the near-surface and cools rapidly after 2 m.y. (Fig. 6d). Mode C also shows exhumation of the 50 km deep particle; however, the deep crust also remains at high temperatures and pressures for the initial 5 m.y.

In the case of Mode C, exhumation is achieved by necking of the crust and shearing of the mantle lithosphere; the switch in behavior from the low density to high density cases for the high-viscosity deep crust case merits further scrutiny. Why would denser crust exhume faster than less dense crust? If one considers the entire extent of each high-viscosity model (5 models) (Fig. 2a$_1$), one realizes that the lithosphere undergoes limited thinning away from the center of the experiment in the case of a high density deep crust (> 2900 kg·m^{-3}), which yields an increase in the stretching (B) factor at the center of the experiment (Fig. 7). Therefore, given that the experiment boundaries are pulled at the same velocity for all fast experiments, the thinning deficit in the overall lithosphere with dense deep crust is achieved in a more limited region in the center of the model, and therefore the velocity of exhumation is greatest when the deep crust is denser. This is made possible by the localization of conjugate normal shearing through the crust in the center of the experiment that is controlled by the initial model fault; the end result is efficient upward motion of the Moho and
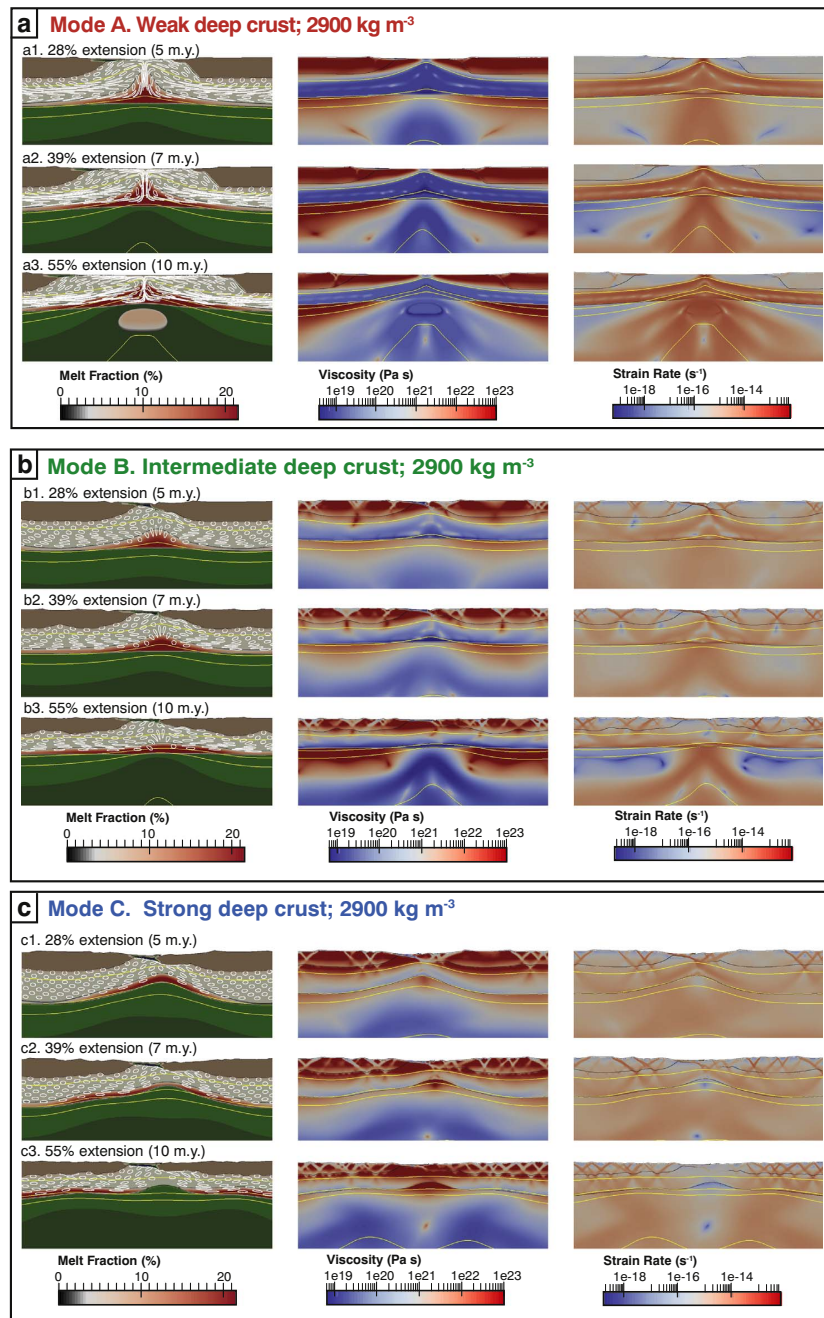
Fig. 5. Experiment snapshots, effective viscosity, and strain rate of Mode A (panel a), Mode B (panel b), and Mode C (panel c) exhumation mechanisms for the fast experiment suite. Results are presented for 28%, 39%, and 55% extension. Complete experimental results, along with effective viscosity and strain rate, for the fast and slow experiment suite are presented in Appendix B.

shearing of the underlying lithosphere. More generally, one can surmise that a dense, horizontally extensive deep crust favors lithospheric necking, especially if deformation is localized (pre-existing weakness) and rapid exhumation of the Moho and possibly the mantle.

5.2. Exhumation modes and mechanical coupling of deep and shallow crust

The degree to which shallow and deep crustal layers are mechanically coupled is key in producing Mode A or Mode B domes. In Mode A domes, the upper deep crust is mechanically coupled to the shallow crust, and partially decoupled from the lower deep crust across a
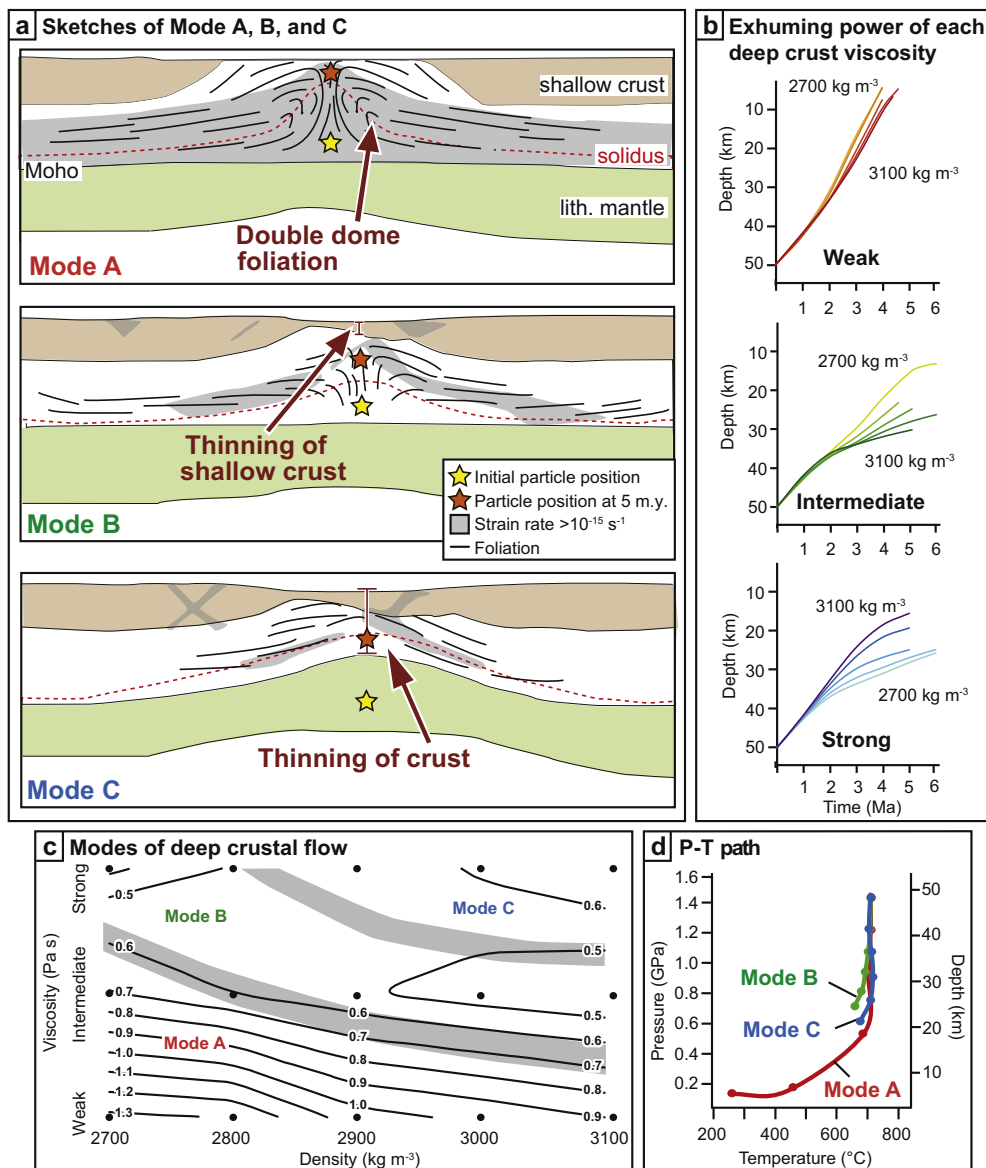
Fig. 6. (a) Sketches of mode A, B, and C exhumation mechanisms at 5 m.y. (28% extension). (b) dz/dt for various deep crust viscosities (fast experiment suite). Each set of curves is colored by density of the deep crust and shows the vertical path of the particle or passive tracer denoted in panel (a) as a yellow star. (c) Viscosity density parameter space contoured for the average exhumation velocity (cm yr^{-1}) over 5 m.y. of the particle shown in panel (a). See text for more information. (d) Pressure-temperature path for the particle shown in panel (a) for mode A, B, and C exhumation mechanism over the initial 5 m.y. (28% extension; 2 cm yr^{-1} extension rate). Each dot on P-T path represents 1 m.y. (For interpretation of the references to color in this figure legend, the reader is referred to the web version of this article.)

décollement (Fig. 5a). The normal fault breaks apart the shallow crust, and the lower deep crust undergoes vertical transport into space previously occupied by the shallow crust and the upper deep crust (Fig. 3, 4). The inward horizontal flow of the lower deep crust and the outward horizontal flow of the shallow crust/upper deep crust results in widespread high stain ($> 10^{-14}$ s^{-1}) across the entire deep crust (Fig. 5a), with a mid-crustal shear zone characterized by high finite strain. By comparison, the Mode B deep crust exhibits high-viscosity, low strain-rate regions, each of which corresponds to a set of conjugate faults in the shallow crust (Fig. 5b). These regions represent mechanical coupling between the shallow crust and the deep crust, which reduces the

horizontal and vertical flow of the deep crust in Mode B compared to Mode A domes (Fig. 4c), and thins the shallow crust without breaking it apart completely (Fig. 6a).

5.3. Insights from numerical experiments on convergent deep-crustal flow in extensional gneiss domes

The horizontal and vertical flow of the deep crust in experiments that yield Mode A and B exhumation mechanisms creates a "double dome" cored by a steep vertical zone (Figs. 5b, 6a). In nature, double domes of foliation have been described in the high-grade (gneiss,
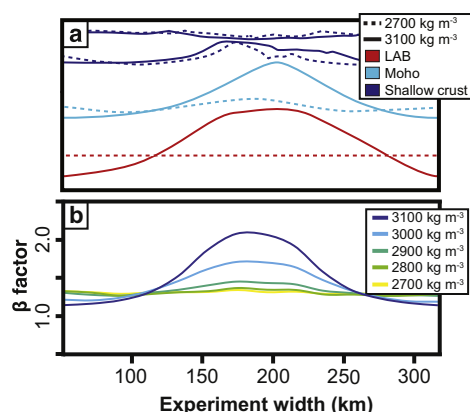
Fig. 7. (a) Lithological boundaries for a strong deep crust and two deep crust densities (28% extension). (b) Horizontal β factor profile with a strong deep crust and range of deep crust density (28% extension). Please see text for the explanation of why a denser lower crust records a higher β factor.

migmatite) cores of metamorphic core complexes (Rey et al., 2011). These are comprised of a steep high-strain zone flanked by subdomes that have experienced complex flow, including horizontal flow at upper structural levels (Kruckenberg and Whitney, 2011; Rey et al., 2011, 2017; Whitney et al., 2013).

As a result of efficient vertical mass transport, Mode A domes yield the highest exhumation velocities in the fast-extension parameter space (Fig. 5a), and are characterized by tens of kilometers of vertical transport of deep crust (Fig. 5d). These experiments therefore predict that the formation of double domes in nature involves the exhumation of high-pressure rocks to shallow crustal depths. For example, a north-south cross-section through the east-west elongated Montagne Noire double dome of the southern French Massif Central (Rey et al., 2011) resembles the cross sections of our low- and intermediate viscosity experiments (Figs. 2b$_2$, 3b$_3$, 6b). This double-dome contains eclogite that records maximum P-T conditions of ∼1.4 GPa at 725 °C, corresponding to a depth of > 40 km in the orogenic crust. These eclogite units were exhumed shortly after their crystallization in the eclogite facies, during a single exhumation event along with host migmatite and granite that record crystallization at low-pressure conditions (≤ 10 km) (Whitney et al., 2015).

6. Conclusions

Results of 2D numerical experiments show that during fast extension (2 cm yr^{-1}) of the lithosphere, the viscosity and density of the deep crust exerts a first-order influence on the magnitude of exhumation experienced by rocks exposed in the core of extensional gneiss domes. Across the range of viscosity-density values in this study, under no set of conditions is the upward flow of the deep crust completely suppressed: exhumation of the deep crust occurs in every experiment. However, the mechanism and velocity of exhumation and the geometry of the extended region varies as a function of viscosity and density of the deep crust. Flow of deep crust is primarily driven by one of two mechanisms: (1) feedback between normal faulting in the upper crust and flow in the deep crust to fill the space created by the extending upper crust (for low to intermediate viscosity deep crust), creating a double-dome structure within a core complex, or (2) a passive response to relief generated on the Moho and lithosphere asthenosphere boundary during thinning of the crust and shearing of the mantle lithosphere, creating a single antiform or dome of foliation in a core complex. Slow extension (mm yr^{-1}) results in negligible exhumation of the deep crust.

Appendix A. Supplementary data

Supplementary data to this article can be found online at https://doi.org/10.1016/j.tecto.2017.12.029.

References

Augier, R., Agard, P., MoniÉ, P., Jolivet, L., Robin, C., Booth-Rea, G., 2005. Exhumation, doming and slab retreat in the Betic Cordillera (SE Spain): in situ ^{40}Ar/^{39}Ar ages and P–T–d–t paths for the Nevado-Filabride complex. J. Metamorph. Geol. 23 (5), 357–381.

Bonev, N., Burg, J.-P., Ivanov, Z., 2005. Mesozoic–Tertiary structural evolution of an extensional gneiss dome—the Kesebir–Kardamos dome, eastern Rhodope (Bulgaria–Greece). Int. J. Earth Sci. 95 (2), 318–340.

Buck, W.R., 1991. Modes of continental lithospheric extension. J. Geophys. Res. Solid Earth 96 (B12), 20161–20178.

Burg, J.-P., Kaus, B.J.P., Podladchikov, Y.Y., 2004. Dome structures in collision orogens: Mechanical investigation of the gravity/compression interplay. Geol. Soc. Am. Spec. Pap. 380, 47–66.

Burov, E., Francois, T., Yamato, P., Wolf, S., 2014. Mechanisms of continental subduction and exhumation of HP and UHP rocks. Gondwana Res. 25 (2), 464–493.

Caby, R., Hammor, D., Delor, C., 2001. Metamorphic evolution, partial melting and Miocene exhumation of lower crust in the Edough metamorphic core complex, west Mediterranean orogen, eastern Algeria. Tectonophysics 342 (3–4), 239–273.

Clark, M.K., Royden, L.H., 2000. Topographic ooze: building the eastern margin of Tibet by lower crustal flow. Geology 28 (8), 703–706.

Clemens, J.D., Droop, G.T.R., 1998. Fluids, P–T paths and the fates of anatectic melts in the Earth's crust. Lithos 44 (1–2), 21–36.

Fayon, A.K., Whitney, D.L., Teyssier, C., 2004. Exhumation of orogenic crust: diapiric ascent versus low-angle normal faulting. In: Whitney, D.L., Teyssier, C., Siddoway, C.S. (Eds.), Gneiss Domes in Orogeny, vol. 380: Boulder, Colorado. Geological Society of America Special Paperpp. 129–139.

François, C., Philippot, P., Rey, P.F., Rubatto, D., 2014. Burial and exhumation during Archean sagduction in the East Pilbara Granite-Greenstone Terrane. Earth Planet. Sci. Lett. 396, 235–251.

Gessner, K., Wijns, C., Moresi, L., 2007. Significance of strain localization in the lower crust for structural evolution and thermal history of metamorphic core complexes. Tectonics 26 (2).

Hasterok, D., Chapman, D., 2011. Heat production and geotherms for the continental lithosphere. Earth Planet. Sci. Lett. 307 (1), 5970.

Hirth, G., Kohlstedt, D., 2004. Rheology of the upper mantle and the mantle wedge: a view from the experimentalists, inside the subduction factory. Am. Geophys. Union 83–105.

Huet, B., Le Pourhiet, L., Labrousse, L., Burov, E., Jolivet, L., 2011. Post-orogenic extension and metamorphic core complexes in a heterogeneous crust: the role of crustal layering inherited from collision. Application to the Cyclades (Aegean domain). Geophys. J. Int. 184 (2), 611–625.

Koptev, A., Burov, E., Gerya, T., Le Pourhiet, L., Leroy, S., Calais, E., Jolivet, L., 2017. Plume-induced continental rifting and break-up in ultra-slow extension context: insights from 3D numerical modeling. Tectonophysics. http://dx.doi.org/10.1016/j.tecto.2017.03.025. (in press).

Kruckenberg, S.C., Whitney, D.L., 2011. Metamorphic evolution of sapphirine- and orthoamphibole-cordierite-bearing gneiss, Okanogan dome, Washington, USA. J. Metamorph. Geol. 29 (4), 425–449.

Labrousse, L., Huet, B., Le Pourhiet, L., Jolivet, L., Burov, E., 2016. Rheological implications of extensional detachments: Mediterranean and numerical insights. Earth Sci. Rev. 161, 233–258.

Le Pourhiet, L., Huet, B., May, D.A., Labrousse, L., Jolivet, L., 2012. Kinematic interpretation of the 3D shapes of metamorphic core complexes. Geochem. Geophys. Geosyst. 13 (9).

M. Korchinski et al.

McKenzie, D., Bickle, M.J., 1988. The volume and composition of melt generated by extension of the lithosphere. J. Petrol. 29 (3), 625–679.

Mezri, L., Le Pourhiet, L., Wolf, S., Burov, E., 2015. New parametric implementation of metamorphic reactions limited by water content, impact on exhumation along detachment faults. Lithos 236, 287–298.

Moresi, L.N., Dufour, F., Mühlhaus, H.B., 2003. A Lagrangian integration point finite element method for large deformation modelling of viscoelastic geomaterials. J. Comput. Phys. 184, 476–497.

Moresi, L., Quenette, S., Lemiale, V., Meriaux, C., Appelbe, B., Mühlhaus, H.B., 2007. Computational approaches to studying non-linear dynamics of the crust and mantle. Phys. Earth Planet. Inter. 163, 69–82.

Norlander, B.H., Whitney, D.L., Teyssier, C., Vanderhaeghe, O., 2002. Partial melting and decompression of the Thor-Odin dome, Shuswap metamorphic core complex, Canadian Cordillera. Lithos 61 (3–4), 103–125.

Paterson, M.S., Luan, F.C., 1990. Quartzite rheology under geological conditions. Geol. Soc. Lond., Spec. Publ. 54 (1), 299–307.

Rey, P.F., Muller, R.D., 2010. Fragmentation of active continental plate margins owing to the buoyancy of the mantle wedge. Nat. Geosci. 3 (4), 257–261.

Rey, P., Vanderhaeghe, O., Teyssier, C., 2001. Gravitational collapse of the continental crust: definition, regimes and modes. Tectonophysics 342 (3–4), 435–449.

Rey, P.F., Teyssier, C., Whitney, D.L., 2009a. Extension rates, crustal melting, and core complex dynamics. Geology 37 (5), 391–394.

Rey, P.F., Teyssier, C., Whitney, D.L., 2009b. The role of partial melting and extensional strain rates in the development of metamorphic core complexes. Tectonophysics 477 (3–4), 135–144.

Rey, P.F., Teyssier, C., Kruckenberg, S.C., Whitney, D.L., 2011. Viscous collision in channel explains double domes in metamorphic core complexes. Geology 39 (4), 387–390.

Rey, P.F., Mondy, L., Duclaux, G., Teyssier, C., Whitney, D.L., Bocher, M., Prigent, C., 2017. The origin of contractional structures in extensional gneiss domes. Geology 45 (3), 263–266. http://dx.doi.org/10.1130/G38595.1.

Rosenberg, C.L., Handy, M.R., 2005. Experimental deformation of partially melted granite revisited: implications for the continental crust. J. Metamorph. Geol. 23 (19–28).

Schenker, F.L., Gerya, T., Burg, J.P., 2012. Bimodal behavior of extended continental lithosphere: modeling insight and application to thermal history of migmatitic core complexes. Tectonophysics 579, 88–103.

Schulmann, K., Lexa, O., ŠTÍPskÁ, P., Racek, M., TajČManovÁ, L., KonopÁSek, J., Edel, J.B., Peschler, A., Lehmann, J., 2008. Vertical extrusion and horizontal channel flow of orogenic lower crust: key exhumation mechanisms in large hot orogens? J. Metamorph. Geol. 26 (2), 273–297.

de Sigoyer, J., Guillot, S., Dick, P., 2004. Exhumation of the ultrahigh-pressure Tso Morari unit in eastern Ladakh (NW Himalaya): a case study. Tectonics 23 (3).

Stübner, K., et al., 2013a. The giant Shakhdara migmatitic gneiss dome, Pamir, India-Asia collision zone: 2. Timing of dome formation. Tectonics 32 (5), 1404–1431.

Stübner, K., et al., 2013b. The giant Shakhdara migmatitic gneiss dome, Pamir, India-Asia collision zone: 1. Geometry and kinematics. Tectonics 32 (4), 948–979.

Teyssier, C., Whitney, D.L., 2002. Gneiss domes and orogeny. Geology 30 (12), 1139–1142.

Tirel, C., Brun, J., Burov, E., 2004a. Thermomechanical modeling of extensional gneiss domes. In: Whitney, D.L., Teyssier, C., Siddoway, C.S. (Eds.), Gneiss Domes in Orogeny, Volume 380: Boulder, Colorado. Geological Society of Americal Special Paper.

Tirel, C., Brun, J.-P., Burov, E., 2004b. Thermomechanical modeling of extensional gneiss domes. Geol. Soc. Am. Spec. Pap. 380, 67–78.

Tirel, C., Brun, J.-P., Burov, E., 2008. Dynamics and structural development of metamorphic core complexes. J. Geophys. Res. Solid Earth 113 (B4).

Toraman, E., Teyssier, C., Whitney, D.L., Fayon, A.K., Thomson, S.N., Reiners, P.W., 2014. Low-temperature thermochronologic record of Eocene migmatite dome emplacement and late Cenozoic landscape development, Shuswap core complex, British Columbia. Tectonics 33 (8), 1616–1635.

Wang, Y.F., Zhang, J.F., Jin, Z.M., Green Ii, H.W., 2012. Mafic granulite rheology: implications for a weak continental lower crust. Earth Planet. Sci. Lett. 353–354, 99–107.

Whitney, D.L., Teyssier, C., Vanderhaeghe, O., 2004. Gneiss domes and crustal flow. In: Whitney, D.L., Teyssier, C., Siddoway, C.S. (Eds.), Gneiss Domes in Orogeny, Volume 380: Boulder, Colorado. Geological Society of America Special Paperpp. 15–33.

Whitney, D.L., Teyssier, C., Rey, P., Buck, W.R., 2013. Continental and oceanic core complexes. Geol. Soc. Am. Bull. 125 (3–4), 273–298.

Whitney, D.L., Roger, F., Teyssier, C., Rey, P.F., Respaut, J.P., 2015. Syn-collapse eclogite metamorphism and exhumation of deep crust in a migmatite dome: the P–T–t record of the youngest Variscan eclogite (Montagne Noire, French Massif Central). Earth Planet. Sci. Lett. 430, 224–234.

Wijns, C., Weinberg, R., Gessner, K., Moresi, L., 2005. Mode of crustal extension determined by rheological layering. Earth Planet. Sci. Lett. 236 (1–2), 120–134.

Appendix III

UWGeodynamics: A teaching and research tool for numerical geodynamic modelling

Romain Beucher[1], **Louis Moresi**[1], **Julian Giordani**[1], **John Mansour**[2], **Dan Sandiford**[1], **Rebecca Farrington**[1], **Luke Mondy**[3], **Claire Mallard**[3], **Patrice Rey**[3], **Guillaume Duclaux**[4], **Owen Kaluza**[2], **Arijit Laik**[5], and **Sara Morón**[1]

1 School of Earth Science, The University of Melbourne, Melbourne, Australia **2** Monash eResearch Centre, Monash University, Clayton, Australia **3** School of Geosciences, Earthbyte Research Group, The University of Sydney, Australia **4** Laboratoire Géoazur, Université Nice Sophia Antipolis, Nice, France **5** Department of Earth Science, Faculty of Science, Vrije Universiteit, Amsterdam

Summary

The UWGeodynamics module facilitates development of 2D and 3D thermo-mechanical geodynamic models (Subduction, Rift, Passive Margins, Orogenic systems etc.). It is designed to be used for research and teaching, and combined the flexibility of the Underworld Application Programming Interface, (Moresi, Dufour, & Mühlhaus, 2002, Moresi, Dufour, & Mühlhaus (2003), Moresi et al. (2007)) with a structured workflow.

Designing geodynamic numerical models can be a daunting task which often requires good understanding of the numerical code. UWGeodynamics provides a simple interface with examples to get you started with development of numerical models. Users can start designing their models without any pre-existing knowledge of programming. Expert users can easily modify the framework and adapt it to more specific needs. The code can be run in parallel on multiple CPUs on personal computers and/or High Performance Computing systems.

Although UWGeodynamics has been primarily designed to address geodynamic problems, it can also be used to teach fluid dynamics and material mechanics.

UWGeodynamics uses the flexibility of the Python language and the Jupyter Notebook environment, which allows leveraging the wide range of scientific libraries available from the Python community. It also facilitates the coupling with existing scientific Python modules such as Badlands (Salles, Ding, & Brocard, 2018).

The functionalities include:

- Dimensional input values, using user's choice of physical units.
- Automated and transparent scaling of dimensional values.
- Sets of predefined geometries that can be combined to define the initial geometry of a model.
- Handles Newtonian and non-Newtonian rheologies (Viscous, Visco-plastic and Visco-elasto-plastic).
- Database of common rheologies used in geodynamics, which can be personalised / extended by users.
- Simple definition of kinematic, stress, and thermal boundary conditions.
- Lithostatic pressure calculation.
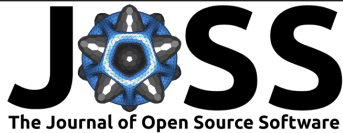
- Thermal equilibrium (steady-state) calculation.
- Pseudo Isostasy using a range of kinematic or stress boundary conditions.
- Partial melt calculation and associated change in viscosity / heat production.
- Simple definition of passive tracers and grid of tracers.
- Simple Phase changes
- 2-way coupling with the surface processes model pyBadlands (Salles et al., 2018).

UWGeo comes with a series of examples, benchmarks and tutorial setups that can be used as cookbook recipes. They provide a wide range of teaching materials useful to introduce numerical geodynamic modeling to students.

New functionalities are constantly being added to the code and contributions are more than welcomed. You can access the full documentation online at https://uwgeodynamics.readthedocs.io

Audience

The module is directed towards a large audience, including earth-science students, structural geologists, expert numerical geodynamicists and industry research and development teams. It is used as a research and teaching tool at the University of Melbourne and the University of Sydney.

Acknowledgments

References

Moresi, L., Dufour, F., & Mühlhaus, H.-B. (2002). Mantle Convection Modeling with Viscoelastic/Brittle Lithosphere: Numerical Methodology and Plate Tectonic Modeling. *Pure and Applied Geophysics*, *159*(10), 2335–2356. doi:10.1007/s00024-002-8738-3

Moresi, L., Dufour, F., & Mühlhaus, H.-B. (2003). A Lagrangian integration point finite element method for large deformation modeling of viscoelastic geomaterials. *Journal of Computational Physics*, *184*(2), 476–497. doi:10.1016/S0021-9991(02)00031-1

Moresi, L., Quenette, S., Lemiale, V., Mériaux, C., Appelbe, B., & Mühlhaus, H.-B. (2007). Computational approaches to studying non-linear dynamics of the crust and mantle. *Physics of the Earth and Planetary Interiors*, *163*(1-4), 69–82. doi:10.1016/j.pepi.2007.06.009

Salles, T., Ding, X., & Brocard, G. (2018). PyBadlands: A framework to simulate sediment transport, landscape dynamics and basin stratigraphic evolution through space and time. *PLOS ONE*, *13*(4), 1–24. doi:10.1371/journal.pone.0195557

Appendix IV

Finding the forces in continental rifting

Luke Mondy - edited by Grace Shephard · February 28, 2018 · Geodynamics 101 · Comments Closed
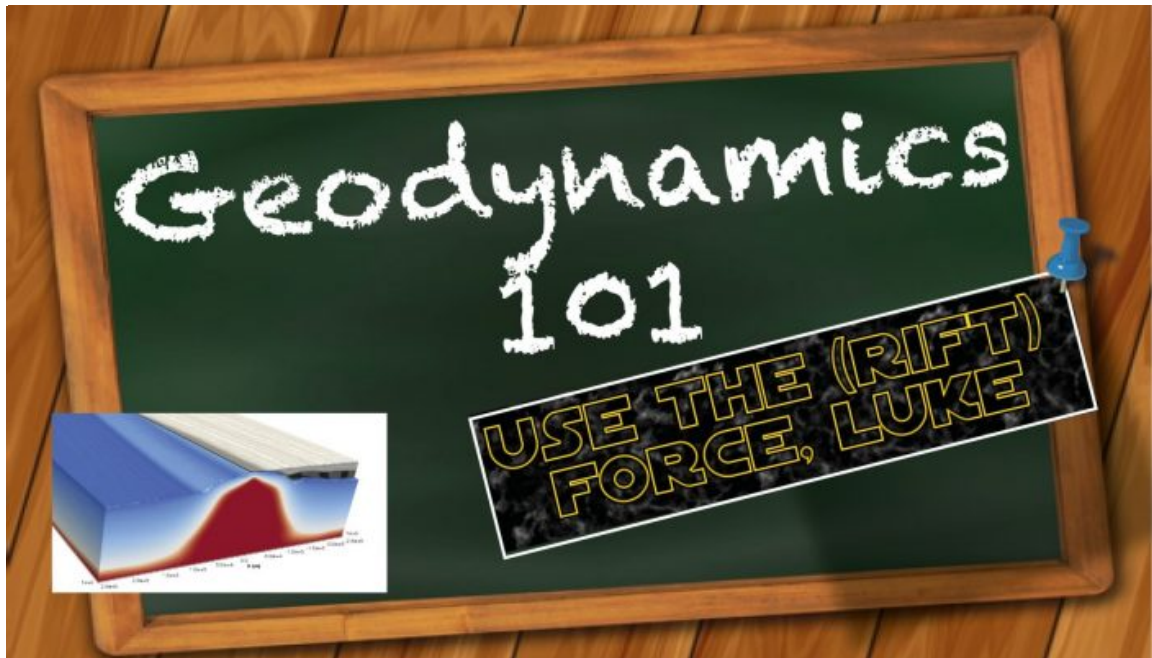
This week's Geodynamics 101 is on rifting and is by PhD padawan Luke Mondy (had to utilize some editorial license and go for the Star Wars puns). Font generated from flamingtext.com

Luke Mondy

The Geodynamics 101 series serves to showcase the diversity of research topics and methods in the geodynamics community in an understandable manner. We welcome all researchers – PhD students to Professors – to introduce their area of expertise in a lighthearted, entertaining manner and touch upon some of the outstanding questions and problems related to their fields. For our latest 'Geodynamics 101' post, PhD candidate Luke Mondy from the EarthByte Group at the University of Sydney blogs about some impressively high-resolution numerical models of 'rotational rifting,' and the role of gravity. Luke also shares a bit about the journey behind this work, which recently appeared in Geology.

In geodynamic modelling, we're always thinking about forces. It's a balancing act of plate driving forces potentially interacting with the upwelling mantle, or maybe sediment loading, or thermal relaxation… the list goes on.
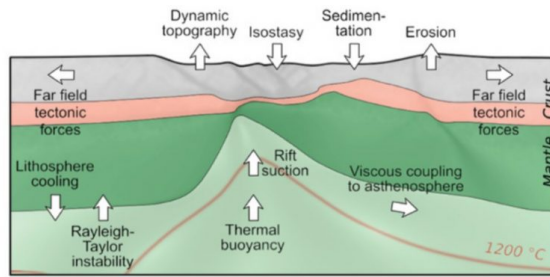
Figure 1: A summary of the forces interacting during continental rifting, from Brune, 2018.

But the thing that underpins all of these forces, fundamentally, is our favourite but oft forgotten force: gravity. Here, I'll tell the story of investigating a numerical model of continental rifting and discovering – or rather, rediscovering – the importance of gravity as a fundamental force in driving Earth dynamics.

How it started – a side project!

A few years ago, my colleagues and I were granted access to not just one, but two, big supercomputers in Australia: Raijin, and Magnus. Both were brand new and raring to go – but we needed something big to test them out on. At the time, 3D geodynamic models were typically limited to quite low resolution, since they can be so computationally demanding, but since we had access to this new power, we decided to see how far we could push the computers to address a fundamentally 3D problem.

2D vs 3D

Historically, subduction and rifting have been ideal settings to model as they can be constrained to two dimensions while still retaining most of their characteristic properties.
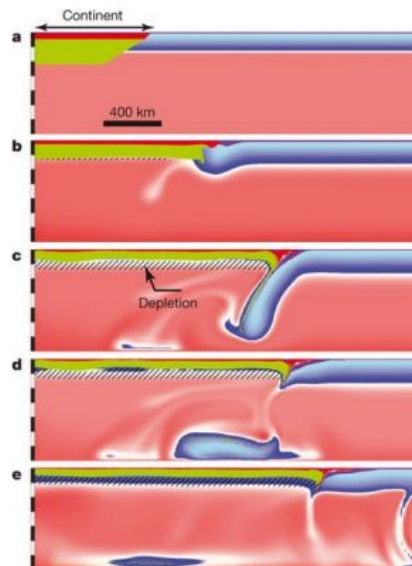

Figure 2. A 2D subduction model. Despite being 'only' two dimensions, the fundamental and interesting aspects of the problem are still captured by the model. Figure from Rey et al., 2014.

However, as tremendously useful as these models have been, many interesting problems in geodynamics are fundamentally three dimensional. The obvious example is global mantle convection, but we are starting to see more and more papers addressing both rifting and subduction problems that require 3D contexts, for example: continental accretion (Moresi et al., 2014), metamorphic core complex formation (Rey et al., 2017), or oblique rifting (Brune et al., 2012).

Typically when we model a rift in 2D, the dimensionality implies that we are looking at orthogonal rifting – that the plates move away from each other perpendicular to the rift axis. Since 2D models cannot account for forces in the third dimension, they are only suitable for when the applied tectonic forces pull within the plane of the model – that is, when the 2D model lies along a small circle of an Euler pole.

Euler poles have another interesting geometric property – the velocity of extension between two plates changes as we move closer or further away from the Euler pole: zero velocity at the pole itself, and fastest at the equator to the pole (Lundin et al., 2014).
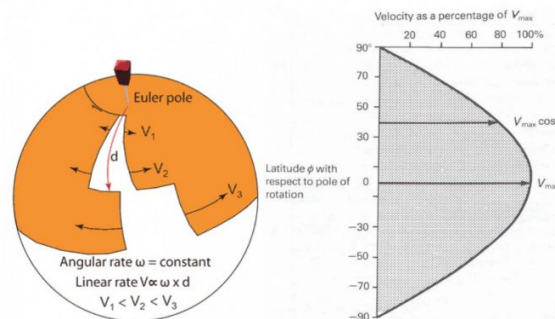

Figure 3. Left: From Lundin et. al. (2014), the figure shows the geometric relationship of increasing rifting velocity as the distance from the pole increases. Right: the same relationship graphed out, showing the cosine curve (Kearey et.al. 2009).

This leads to differing extension velocities along the length of the rift axis. Extension velocities are a huge control on the resulting geodynamics (e.g., Buck et al., 1999). Employing a series of 2D models along a rift axis (Brune et al., 2014) has been used to show how these dynamics change, but misses out on the three-dimensionality of the problem – how do these differing and diachronous dynamics interact with each along other the rift margin as it forms?

Rotational Rifting

We decided to attempt to model this sort of rifting, as we termed it "rotational rifting". Essentially we linked up the 2D slices along the rift axis into one big 3D model – so that we have slow extension towards the Euler pole, and fast extension away from it.

To do this, we ended up using the code *Underworld* (at the time version 1.8 – but their 2.0 version is the best place to start!), and a framework developed inside the EarthByte group at the University of Sydney called the 'Lithospheric Modelling Recipe', or LMR.

Using the LMR, we set up two 3D experiments: both are 1000 km by 500 km along the surface, and 180 km deep. The 'orthogonal' experiment is modelled at the equator to the pole – so the velocities along the walls are the same all the way along the rift axis. The 'rotational' experiment is very close to the Euler pole (where the rate of extension velocity change is greatest), from 89 degrees to 79 degrees (90 degrees being the Euler pole), which gives an
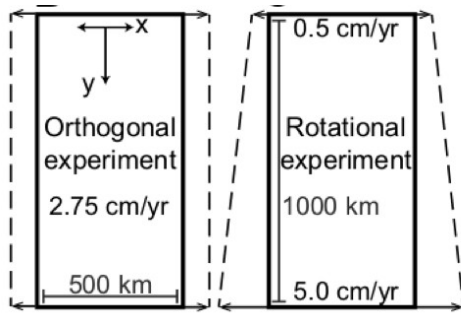
Figure 4. Map view of the two experiments. Arrows show the velocity boundary conditions applied. Note they are perpendicular to the model domain – we thought long and hard about this choice, and explain it fully in the Data Repository.

imposed velocity at the slow end (89 degrees) of 0.5 cm/yr and at the fast end (79 degrees) 5.0 cm/yr.

Since we wanted to stress test the supercomputers, we ran these experiments at just under 2 km grid resolution (256 x 512 x 96). This meant each experiment ended up using about 2.5 **billion** particles to track the materials! The 2 km grid size is an important milestone – to properly resolve faulting, sub-2 km grid sizes are required (Gerya, 2009).

The results!

So we ran the experiments, and compared the results! To give a broad overview of what we found, here's a nice animation:
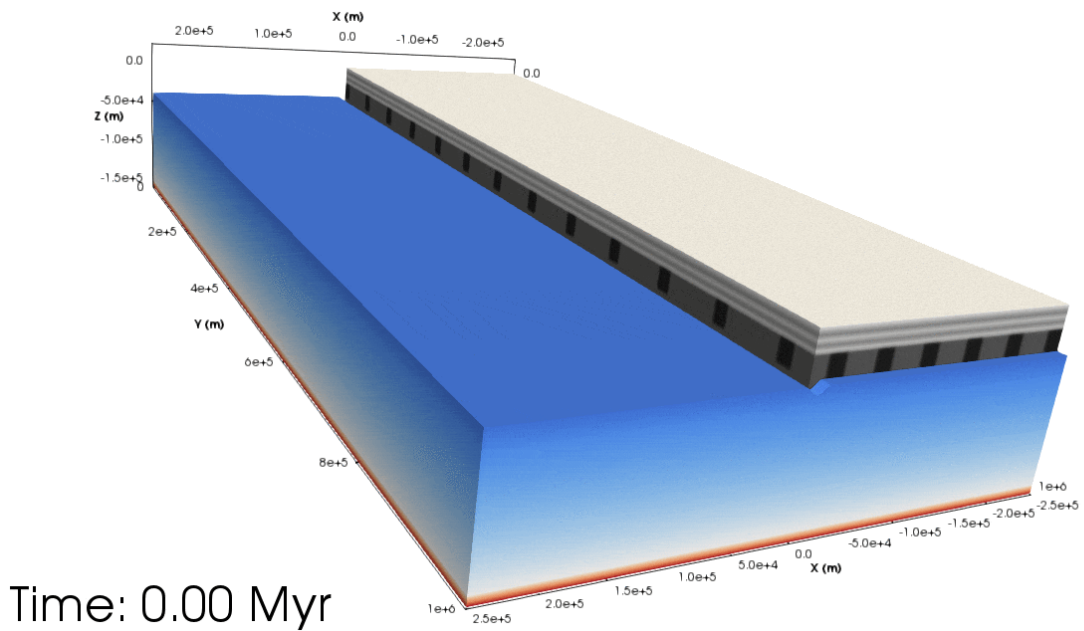
Time: 0.00 Myr
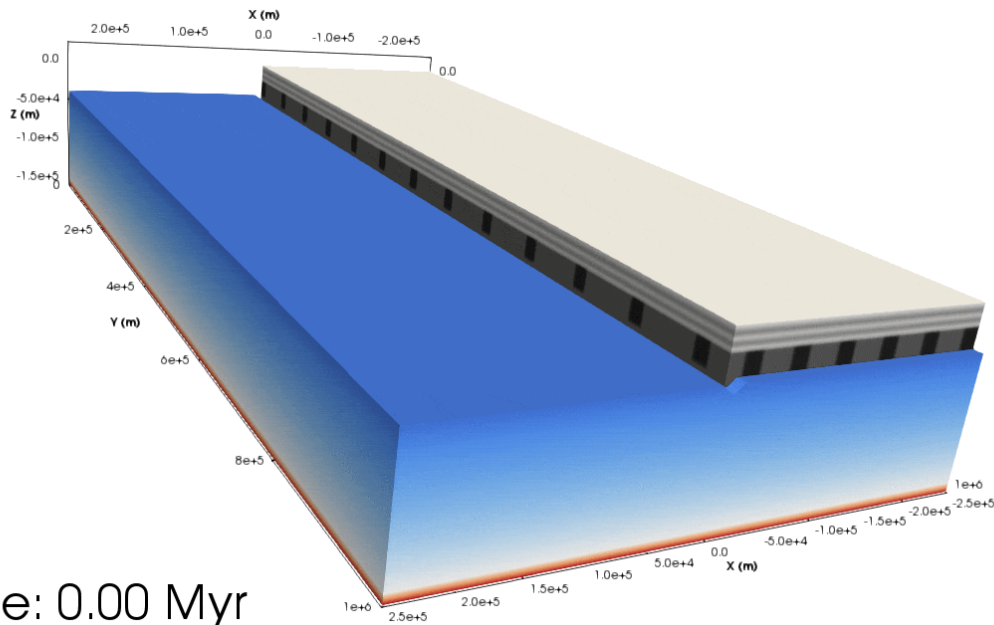
Figure 5. Top: Animation showing the orthogonal experiment from a south-west perspective (with the Euler pole being the 'north' pole). The light grey layers show the upper crust, dark grey the lower crust. Half of the crust has been removed to show the lithospheric mantle topography. The blue to the white colours show the lithospheric mantle temperature, and from white to red shows the asthenospheric temperature. Bottom: As above but for the rotational experiment. Notice that the asthenospheric dome migrates along the rift towards the Euler pole.

What to do now?

Cool looking experiments, of course! The supercomputers had been able to handle the serious load we put on them (it took about 2 weeks per experiment, on ~800 cpus), so that part of the project was a success. But what about the experiments themselves – did switching to 3D actually tell us anything useful?

What we expected...

The things we expected were there. The orthogonal experiment behaved identically to a 2D model. For the rotational experiment, we found the style of faulting changed and evolved along the rift axis, and seemed to match up nicely with the 2D work about differing extension rates. We were able to identify phases of rifting via strain patterns, which were similar to those described by Lavier and Manatschal (2006), and seemed to match the outputs of the series of 2D models along a rift axis.
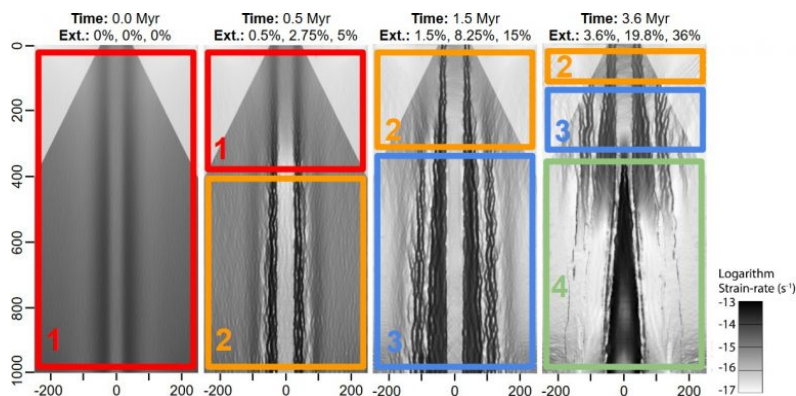

Figure 6. Map view of strain-rate of the rotational experiment through time. The phases (1 through 4, representing different modes of deformation) migrate along the rift towards the

Euler pole.

What we didn't expect...

Almost on a whim, we decided to start looking into the tectonic regime. Using the visualization program *Paraview*, we calculated the eigenvectors of the deviatoric stress and assigned a tectonic regime (blue for extension, red for compression, green for strike-slip, and white for undetermined), following a similar scheme to the World stress map (Zoback, 1992). Apologies to colour blind folk!

Here's what a selected section of the orthogonal experiment surface looks like through time:
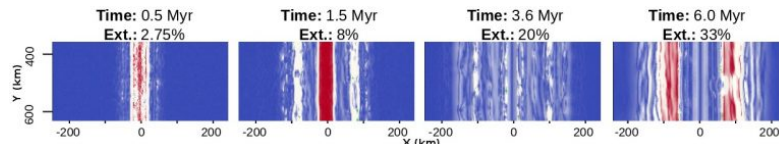

Figure 7. The stress regimes at the surface of the orthogonal experiment (clipped to y = ~400 to ~600 km).

Not really that surprising – we found mostly extension everywhere, with a bit of compression when the central graben sinks down and gets squeezed. However, it was a little bit surprising to see the compression come back on the rift flanks.

But when we applied the same technique to the rotational experiment, we found this on the surface:
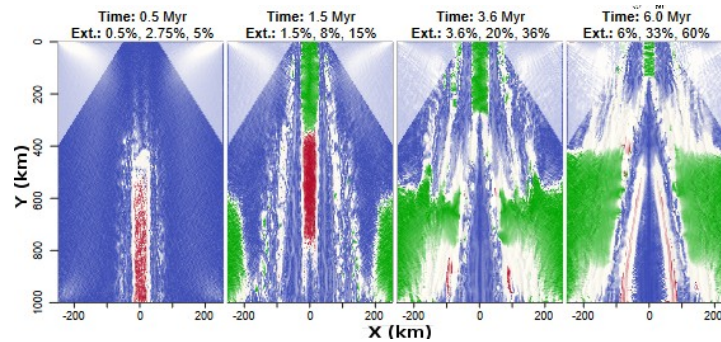

Figure 8. The stress regimes at the surface of the rotational experiment. The three numbers at the top represent the total extension at y = 0 km, 500 km, and 1000 km respectively.

Now all of a sudden we're seeing strike-slip stress regimes in different areas of the experiment!

The above figures displaying the stress in the experiments so far have been of the surface – where one of the principal stress axes must be vertical – but our colouring technique does not limit us to just the surface. We noticed when looking at cross-sections that the lithospheric mantle was also showing unexpected stress regimes!
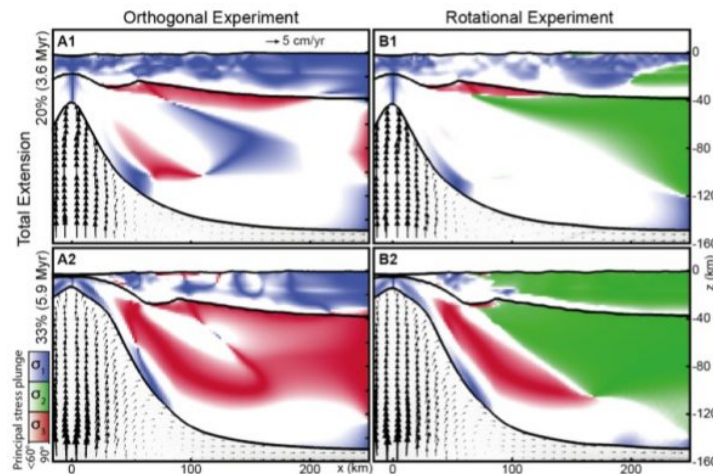
Figure 9. Slices at y = 500 km across the rift axis (right in the middle). Coloured areas show where the plunge of one principal stress axis is >60 degrees. Both experiments have the same applied extension velocity at y = 500 km, and so total extension is equivalent between experiments.

In most of the lithosphere, the strain rate is still very small, not enough to notice much deformation (1e-16 to 1e-18 1/s). But a few puzzling questions were raised: why do we see compressional tectonic regimes in the orthogonal experiment; and why do we also see strike-slip regimes in the rotational experiment?

Gravitational Potential Energy (GPE)

It quickly became apparent that these stress changes were related to the upwelling asthenosphere, as the switch between regimes was well timed to when the asthenosphere would approach the Moho – about 40 km depth. This gave us the hint that perhaps buoyancy forces were at play. We used *Paraview* again to calculate the gravitational potential energy at each point on the surface (taking into account all the temperature dependent densities, detailed topography, and so on), and produced these maps:
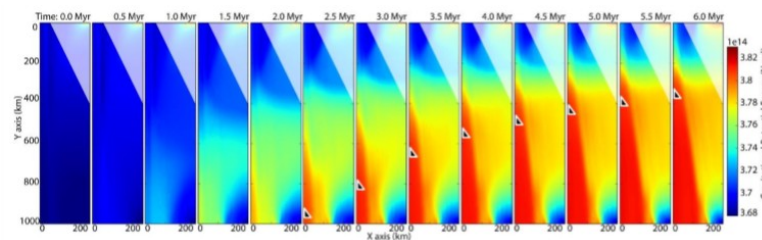

Figure 10. A time series showing the gravitational potential energy (GPE) at each point on the surface of the rotational experiment. Only half the surface is shown because it is symmetrical. The small triangle notch is where we determined the rift tip to be located (where 1/(beta factor) < 0.2).

What we saw confirmed our suspicions – the rise of the asthenospheric dome induces a gravitational force that radiates outwards. The juxtaposition of the hot, yet still quite heavy, asthenospheric material, next to practically unthinned crust on both the rift flanks and ahead of the rift tip, produces a significant force.

But why the switch to compression or strike-slip tectonic regimes in an otherwise extensional setting? In the case of the orthogonal model, the force (aka the difference in GPE) is perpendicular to the rift axis, since the dome rises synchronously along the axis. When this force overcomes the far-field tectonic force (essentially the force required to drive our experiment boundary conditions), the stress regime changes from extension to compression.

However, in the rotational experiment, the dome is larger the further away from the Euler pole, and so instead the gravitational force radiates outwards from the dome. Now the stress in the lithospheric mantle has to deal with not only the force induced from the upwelling asthenosphere right next to it, but also from along the rift axis (have a look at the topography of the lithospheric mantle in Fig. 5). These combined forces end up rotating the principal stresses such that sigma_2 stands vertical and a strike-slip regime is generated.

We also see the gravitational force manifest in other ways. Looking at the along axis flow in the asthenosphere, the experiment initially predicts a suction force towards the rapidly opening end of the model (away from the Euler pole), similar to Koopmann et al. (2014). But once the dome is formed, we see a reversal of this flow, back towards the Euler pole, driven by gravitational collapse. This flow appears to apply a strong stress to the crust surrounding the dome, reaching upwards of 50 MPa in some places.
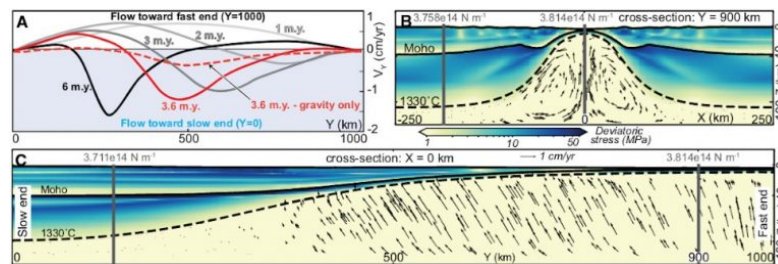

Figure 11. A: The direction of flow at the lithosphere-asthenosphere boundary in the centre of the rift. Early in the experiment, we see suction towards the fast end of the rift, while later in the experiment, we see a return flow. The dashed line shows the flow after the tectonic boundary conditions have been removed. B,C: cross-sections showing stress and velocity arrows from the experiment just after the tectonic boundary conditions have been removed.

How do we know it's gravity?

To test this idea further, we ran some additional experiments. First, we let the rotational experiment run for about 3.6 Million years, and then 'stopped' the tectonics (changed the side velocity boundary conditions to 0 cm/yr) – leaving gravity as the only driving force. We saw that the return flow towards the Euler pole was still present (though reduced). By running some more rotational experiments with either doubled or halved Euler pole rotational rate, we saw that the initial suction magnitude correlates with the change in opening velocity, but the return flow to the Euler pole is almost identical, giving further evidence that this is gravity driven.

What about the real world?

We numerical modellers love to stay in the world of numbers – but alas sometime we must get our hands dirty and look at the real world – just to make sure our models actually tell us something useful!

Despite our slightly backwards methodology (model first, check nature second), it did give us an advantage: our experiments were producing predictions for us to go and test. We had our hypothesis – now to see if it could be validated.

So we went out and looked for examples of rifting near an Euler pole, and the two most notable we found were in the Woodlark Basin, Papua New Guinea, and the Galapagos Rise in the Pacific. Despite the 'complications' of the natural world (things like sediment loading, pre-existing weakness in the crust, etc. – things that get your hands dirty), we found a striking first order relationship between the earthquake focal mechanisms present in both areas, and what our experiments predicted:

Furthermore, much work has been done investigating the Hess deep, a depression that sits ahead of the rift tip in the Galapagos. We found in our rotational experiment a similar 'deep' that moves ahead of the rift tip through time,
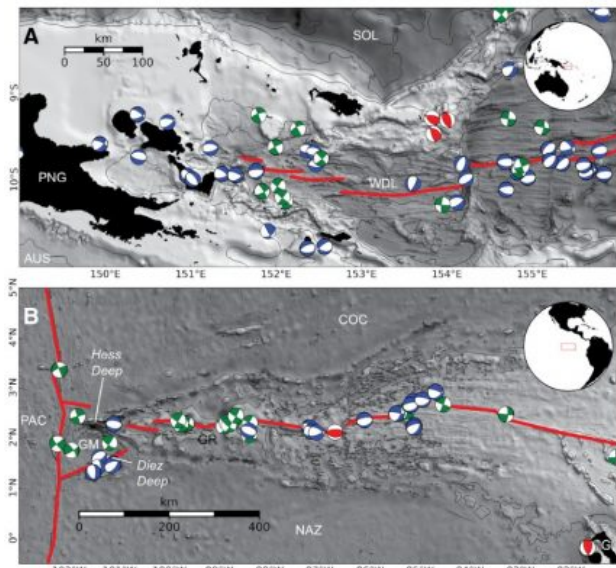
Figure 12. Top: the Woodlark Basin, PNG. Bottom: the Galapagos Rise. Both show earthquake focal mechanisms, coloured the same way as our experiments: blue for extension, red for compression, and green for strike-slip.

giving us greater confidence in our experimental predictions.

Takeaways

There are a few things I've taken away from this experience. The first is that it's important to remember the fundamentals. I've found that, generally, geodynamicists initially think about the force-balances going on in a particular setting, but gravity was staring me in the face for a while before I understood its critical role.

The second take-away was that exploratory modelling – playing around with experiments just for fun – is a great thing to do. Probably most of us do this anyway as part of the day-to-day activities, but putting aside some time to think about what sort of things to try out allowed us to find something really interesting. Furthermore, we then had a whole host of predictions we could go out and look for, rather than trying to tweak out experiment parameters to match something we already had found.

Finally, the 3D revolution we're going through at the moment is exciting! Now that there are computers available to us that are able to run these enormous calculations, it gives us a chance to explore these fundamental problems in a new way and hopefully learn something about the world!

If you would like to checkout our paper, you can see it here. We made all of our input files open-source (and the code *Underworld* is already open-source), so please check them out too!

```
References

Brune, S., Popov, A. A., & Sobolev, S. V. (2012). Modeling suggests that oblique
extension facilitates rifting and continental break-up. Journal of Geophysical Research:
Solid Earth, 117(B8).

Brune, S., Heine, C., Pérez-Gussinyé, M., & Sobolev, S. V. (2014). Rift migration
explains continental margin asymmetry and crustal hyper-extension. Nature
Communications, 5, 4014.

Brune, S. (2018). Forces within continental and oceanic rifts: Numerical modeling
elucidates the impact of asthenospheric flow on surface stress. Geology, 46(2), 191-192.

Buck, W. R., Lavier, L. L., & Poliakov, A. N. (1999). How to make a rift wide.
Philosophical Transactions - Royal Society of London Series A, Mathematical Physical and
Engineering Sciences, 671-689.
```

Gerya, T. (2009). Introduction to numerical geodynamic modelling. Cambridge University Press.

Kearey, P. (Ed.). (2009). The Encyclopedia of the solid earth sciences. John Wiley & Sons.

Lundin, E. R., Redfield, T. F., Péron-Pindivic, G., & Pindell, J. (2014, January). Rifted continental margins: geometric influence on crustal architecture and melting. In Sedimentary Basins: Origin, Depositional Histories, and Petroleum Systems. 33rd Annual GCSSEPM Foundation Bob F. Perkins Conference. Gulf Coast Section SEPM (GCSSEPM), Houston, TX (pp. 18-53).

Koopmann, H., Brune, S., Franke, D., & Breuer, S. (2014). Linking rift propagation barriers to excess magmatism at volcanic rifted margins. Geology, 42(12), 1071-1074.

Lavier, L. L., & Manatschal, G. (2006). A mechanism to thin the continental lithosphere at magma-poor margins. Nature, 440(7082), 324.

Mondy, L. S., Rey, P. F., Duclaux, G., & Moresi, L. (2018). The role of asthenospheric flow during rift propagation and breakup. Geology.

Moresi, L., Betts, P. G., Miller, M. S., & Cayley, R. A. (2014). Dynamics of continental accretion. Nature, 508(7495), 245.

Rey, P. F., Coltice, N., & Flament, N. (2014). Spreading continents kick-started plate tectonics. Nature, 513(7518), 405.

Rey, P. F., Mondy, L., Duclaux, G., Teyssier, C., Whitney, D. L., Bocher, M., & Prigent, C. (2017). The origin of contractional structures in extensional gneiss domes. Geology, 45(3), 263-266.

Zoback, M. L. (1992). First-and second-order patterns of stress in the lithosphere: The World Stress Map Project. Journal of Geophysical Research: Solid Earth, 97(B8), 11703-11728.